UNIVERSITY OF CALIFORNIA SAN DIEGO
SAN DIEGO STATE UNIVERSITY

Toward high-frequency deterministic simulations: source, path and site effects

A dissertation submitted in partial satisfaction of the
requirements for the degree
Doctor of Philosophy

in

Geophysics

by

Zhifeng Hu

Committee in charge:

University of California San Diego

Joel Conte
Peter Shearer

San Diego State University

Kim Olsen, Chair
Steven Day
Daniel Roten
Samuel Shen

2021

The dissertation of Zhifeng Hu is approved, and it is acceptable in quality and form for publication on microfilm and electronically.

University of California San Diego

San Diego State University

2021

DEDICATION

To my family

Xiaoyang, Xiuhong and Fei

EPIGRAPH

You must know that a person's ability to discern the truth
is directly proportional to his knowledge.
— Cixin Liu, The Three-Body Problem

There are only the pursued, the pursuing, the busy and the tired.
— F. Scott Fitzgerald, The Great Gatsby

Never confuse education with intelligence,
you can have a PhD and still be an idiot.
— Richard P. Feynman

TABLE OF CONTENTS

Dissertation Approval Page . . . iii

Dedication . . . iv

Epigraph . . . v

Table of Contents . . . vi

List of Figures . . . ix

List of Tables . . . xvii

Acknowledgements . . . xviii

Vita . . . xxi

Abstract of the Dissertation . . . xxii

Chapter 1 Introduction . . . 1
1.1 Motivation . . . 1
1.2 Model Characteristics in High-Frequency Simulations . . . 3
1.2.1 Near Surface Low Velocity . . . 4
1.2.2 Topography . . . 5
1.2.3 Anelastic attenuation . . . 6
1.2.4 Small-scale Heterogeneities . . . 7
1.3 Site Amplification . . . 9
1.4 Near-source Plasticity . . . 11

Chapter 2 Calibration of the Near-surface Seismic Structure in the SCEC Community Velocity Model Version 4 . . . 13
2.1 Introduction . . . 14
2.2 Numerical Approach . . . 18
2.3 Simulation Results . . . 20
2.4 Velocity Taper Method . . . 21
2.5 SH1D Theoretical Analysis . . . 24
2.6 3D Numerical Simulations . . . 26
2.7 Discussion and Conclusions . . . 27
Acknowledgements . . . 31
Tables and Figures . . . 32
Appendix . . . 49

Chapter 3 0-5 Hz Deterministic 3D Ground Motion Simulations for the 2014 La Habra, California, Earthquake . . . 51
3.1 Introduction . . . 52
3.2 Model Features and Computational Aspects . . . 55
3.2.1 Numerical method for simulating ground motions . . . 55
3.2.2 Velocity Model . . . 56
3.2.3 Small-scale Heterogeneities . . . 56
3.2.4 Topography . . . 57
3.2.5 Anelastic Attenuation . . . 58
3.2.6 Near-surface Geotechnical Layer . . . 59
3.2.7 Ground Motion Simulations . . . 59
3.2.8 Data Processing . . . 60
3.2.9 Intensity Measures . . . 60
3.3 Results . . . 61
3.3.1 Source Models . . . 61
3.3.2 Minimum V_S . . . 61
3.3.3 Topography . . . 62
3.3.4 Anelastic Attenuation . . . 63
3.3.5 Small-scale heterogeneities . . . 65
3.4 Discussion and Conclusions . . . 66
Acknowledgements . . . 70
Tables and Figures . . . 71
Appendix . . . 87

Chapter 4 Modeling of Empirical Transfer Functions with 3D Velocity Structure . . . 114
4.1 Introduction . . . 115
4.2 Data . . . 118
4.3 TFs . . . 118
4.4 Model Construction . . . 120
4.4.1 Numerical simulations . . . 121
4.5 GVDA . . . 123
4.6 TKCH05 . . . 125
4.7 Discussion . . . 127
4.8 Summary and Conclusions . . . 130
Acknowledgements . . . 132
Tables and Figures . . . 134
Appendix . . . 147

Chapter 5 Kinematic Source Models for Earthquake Simulations with Fault-zone Plasticity . . . 152
5.1 Introduction . . . 153
5.2 Method . . . 154
5.2.1 Simulations of Dynamic Rupture . . . 154

5.2.2 Peak Slip Rate–Depth Profile 156
5.2.3 Kinematic Source Model 157
5.3 Comparison of Ground Motion Simulations for Linear, Nonlinear and EKS models 157
5.3.1 Comparison of Ground Motions 157
5.3.2 Nonlinear Reduction of Ground Motion Extremes 158
5.3.3 Rupture Direction 159
5.3.4 Off-Fault Regions 159
5.4 Discussion and Conclusions 160
Acknowledgements 160
Tables and Figures 161

Appendix 171
A Von Kármán Autocorrelation Function 171

Bibliography 173

LIST OF FIGURES

Figure 2.1: Simulation region for the La Habra event and locations of 259 strong ground motion stations (circles represent type A sites with surface V_S < 1000 m/s and red triangles represent type B sites with surface V_S >= 1000 m/s). The following maps (Figs. 2.5, 2.10 and 2.11) will only show the simulated domain (black rectangle), whose dimensions and geographical coordinates are listed in Table 2.1, The named sites (triangles with black edge) are selected for further comparisons in Figure 2.12. The star depicts the epicenter of the La Habra earthquake. 35

Figure 2.2: Description of the selected source model used in this study. (a) Moment distribution (shading). The contours represent rupture time at a 0.4 s interval starting from 0. (b) and (c) represent the sum of the moment rates for all subfaults and the Fourier amplitude spectrum, respectively. A Brune-type ω^{-2} decay source (Brune, 1970) that fits the source spectrum is plotted for reference. 36

Figure 2.3: (a) Top 150 m and (b) 0-4000 m V_S profiles at the 259 stations. The black and red curves represent type A (surface $V_S < 1000$ m/s) and type B (surface $V_S >= 1000$ m/s) sites, respectively. The darker curves denote the sites with farther distance from the source. 37

Figure 2.4: FAS derived from the records (black) and CVM-S (blue) for the (a) east-west component, (b) north-south component and (c) vertical component. The left and right columns represent type A and B sites, respectively. The solid line is the median of FAS over the site group, the narrow band is the 95% confidence interval of the median, and the dashed lines depict the standard deviation centered at the median. 38

Figure 2.5: (a) Surface V_S extracted from CVM-S, and (b) V_{S30} from Thompson (2018) in our model domain (values in the left bottom corner are not available). The star denotes the epicenter. 39

Figure 2.6: Representative V_S profiles for (a) type A sites and (b) type B sites from CVM-S. The thick black curves depict the averaged velocity profiles for all 220 type A and 39 type B sites directly extracted from CVM-S. The thin lines show the V_S profiles resulting from our proposed method for different z_T depths between 200 m and 1500 m. The dashed curve shows the V_S profile calculated using the Equation (2.2) tapers from our preferred z_T of 1000 m (note that because the tapers are applied as upper bounds to V_S, they typically only affect the type A V_S structure at depths exceeding 350m, where the GTL in CVM-S ceases and causes the abrupt discontinuity). 40

Figure 2.7: The SH1D response for the refined profiles using various z_T depths for average (a) type A and (b) type B sites, divided by the response obtained with the averaged type A and type B profiles from CVM-S. 41

Figure 2.8: Bias of FAS for the two horizontal components averaged over all (a) type A and (b) type B sites for CVM-S at all 259 stations, superimposed with the corresponding SH1D response. The black curves denote CVM-S and other labeled curves represent various tapering depths using SH1D results. 42
Figure 2.9: Bias of FAS on the (a) east-west, (b) north-south and (c) vertical components, calculated from 3D simulations in CVM-S and with tapering depth of 350 m, 700 m, and 1000 m. A positive (negative) value depicts overprediction (underprediction). The left (right) column shows type A (B) sites. The solid line is the median of FAS, where the narrow band is the 95% confidence interval of the median, and the dashed lines depict the standard deviation centered at the median. 43
Figure 2.10: Maps of interpolated log10-based FAS bias between four 3D models and data: (a) CVM-S, and CVM-S with tapering depth of (b) 350 m, (c) 700 m and (d) 1000 m, calculated from the synthetics and records at 259 stations. The warm (cool) colors represent overprediction (underprediction). The circles (triangles) depict type A (B) sites. Note the log10-based colorbar. 44
Figure 2.11: Maps of interpolated log10-based FAS bias for two 3D CVMs and data. (a) CVM-S with velocity tapering depth of 350 m and $Q_S = 0.15V_S$, and (b) CVM-S with velocity tapering depth of 1000 m and $Q_S = 0.05V_S$. Warm (cool) colors represent overprediction (underprediction). Circles depict type A sites and triangles show type B sites. 45
Figure 2.12: Cumulative kinetic energy and Fourier velocity spectra at six type B sites. The subtitles show the names of the sites and their hypocentral distance. . 46
Figure 2.13: Type B site V_S profiles from CVM-S, and CVM-S and CVM-H with (default) Ely *et al*. (2010) GTL taper depth of 350 m. 47
Figure 2.14: (a) V_S profile sample locations in California. Circles denote type A sites and triangles denote type B sites, and (b) extracted V_S profiles. The top panel zooms into the top 500 m. 48
Figure A2.1: Bias of FAS of the (a) east-west, (b) north-south and (c) vertical component, calculated from 3D simulations in CVM-S with V_S tapering depths of 350 m and 1000 m along with attenuation models $Q_S = 0.05V_S$, $Q_S = 0.1V_S$, and $Q_S = 0.15V_S$. A positive (negative) value means overprediction (underprediction). The left (right) columns show type A (B) sites. The solid line is the median of FAS, where the narrow band is the 95% confidence interval of the median, and the dashed lines depict the standard deviation centered at the median. 49
Figure A2.2: Averaged FAS bias for frequencies between 0.15-1 Hz at poorly constrained sites plotted as a function of site surface V_S for (a) three-component average, (b) east-west, (c) north-south and (d) vertical components. The shades represent 95% confidence intervals estimated using bootstrap. 50

Figure 3.1: Simulation domain for the La Habra earthquake (purple solid rectangle) and locations of 259 strong motion stations (black triangles). The star denotes the epicenter. The geographical coordinates of the corners of the simulated domain is listed in Table 3.1, which is used in subsequent map views. . . . 73
Figure 3.2: Illustration of the imprint of small-scale heterogeneities at the surface. (a) V_S extracted from the CVM-S. (b) Same as (a) but superimposed with a statistical model of heterogeneities with a correlation length of 100 m, anisotropy factor of 5, Hurst number of 0.05 and standard deviation of 5%. Topography is removed in (b) for clarity. The epicenter for the La Habra earthquake is depicted with a star. 74
Figure 3.3: Description of the selected source model used in this study. (a) Slip distribution (shading), with contours representing rupture time at a 0.4 s interval starting from 0. (b) and (c) represent the sum of the moment rates for all subfaults and the Fourier amplitude spectrum, respectively. A Brune-type ω^{-2} decay source (Brune, 1970) that fits the source spectrum is plotted for reference. 75
Figure 3.4: Illustration of the SH1D method used to include the effects of material with V_S less than 500 m/s in our 3D simulations for an example site. (a) V_S profile extracted from CVM-S (red dashed curve) and clamped at 500 m/s (blue). (b) SH1D response ratio between the profiles without clamping and with clamping of $V_S = 500$ m/s. (c) Synthetics from a 3D simulation using $V_S = 500$ m/s, with and without the SH1D response ratio. (d) Fourier amplitude spectra corresponding to the waveforms in (c). 76
Figure 3.5: Percent difference of PGV (the first row) and DUR (the second row) at the surface determined by the model with topography and the model without topography for (left) 0.15-1 Hz, (center) 1-2.5 Hz, and (right) 2.5-5 Hz. Positive (negative) values colored in red (blue) indicate amplification (deamplification). The star denotes the epicenter. 77
Figure 3.6: Comparison of interpolated PGVs measured at 259 stations, depicted by triangles, for (a) data and (b) synthetics using Model 1 (including topography, 1000 m shallow velocity refinement and frequency-dependent attenuation $Q_S = 0.1 V_S f^{0.6}$, $Q_P = 2Q_S$; see Table 3.2). The star denotes the epicenter. (c) PGV against R_{hypo} for data and synthetics. The left and right columns show band-limited results for 0.15-2.5 Hz, and 2.5-5 Hz, respectively. . . . 78
Figure 3.7: FAS computed from records and models with various attenuation models (blue: Model 1, violet: Model 3, red: Model 4, green: Model 5). The left (right) column shows results for the horizontal (vertical) components. The top row shows the FAS amplitudes and the bottom show shows the FAS bias between models and records, calculated as the 10-based log between simulations and data. The solid lines depict the median FAS over all 259 stations. The shading shows the 95% confidence interval (CI) and the dashed lines denote one standard deviation centered at the median. 79

Figure 3.8: (a-c) Spatial distribution of the three-component bias for PGV, band pass filtered between 2.5 and 5 Hz. The bias values are computed as the base 10 logarithm of the ratio between simulations and records at each strong motion site. Positive (negative) values represent overprediction (underprediction). (d) Moving average of the bias of PGV using a 20-point window from the three Q models (red: Model 1, green: Model 3, blue: Model 4; see Table 3.2) shown in (a-c) versus hypocentral distance. 80
Figure 3.9: Bias of (a-b) PGV and (c-d) DUR for passbands (left) 0.15-2.5 Hz and (right) 2.5-5 Hz at all 259 stations. The bias is calculated in the same way as for Figure 3.7. The solid lines depict the moving average of the bias using a 20-point window for each of the Q models (blue: Model 11, red: Model 10, green: Model 3, orange: Model 1; see Table 3.2) versus hypocentral distance. 81
Figure 3.10: Difference in (top row) PGV and (bottom) DUR (bottom row) from Model 16, including SSH with $\sigma = 5\%$ and $a = 5000$ m, versus Model 1 (no SSHs). Left (right) columns show results for bandwidths 0.15-2.5 Hz (2.5-5 Hz). The star depicts the epicenter. 82
Figure 3.11: Probability density histogram of the difference between Model 16, including SSH with $\sigma = 5\%$ and $a = 5000$ m, and Model 1 (no SSHs). The definition of percent difference (x-axis) is the same as in Figure 3.5. 83
Figure 3.12: Bias of (top row) PGV and (center row) DUR and (bottom row) GOF for bandwidths (left column) 0.15-2.5 Hz and (right column) 2.5-5 Hz at all 259 stations for Model 6 (see Table 3.2 for a list of model features). The bias is calculated in the same way as for Figure 3.9. The solid line depicts the moving average using a 20-point window. The shading denotes the standard deviation centered at the mean. 84
Figure 3.13: Bias of FAS on the (a) east-west, (b) north-south and (c) vertical components, calculated from models labeled by their IDs. A positive (negative) value depicts overprediction (underprediction). The left and right columns shows type A and B sites, respectively. The solid lines depict the median of FAS, where the narrow band is the 95% confidence interval of the median, and the dashed lines depict the standard deviation centered at the median. 85
Figure 3.14: Density of PGV change for models with topography relative to models without topography for bandwidths of (left column) 0.15-2.5 Hz and (right column) 2.5-5 Hz, and models with (top row) and without (bottom row) modified shallow velocities. The y-axis depicts topographic curvature smoothed using a 2-D window of dimensions 640 m $\times$ 640 m. Values toward the top right (bottom left) denote strong amplification at steep topography (deamplification at flat topography). Note that density intervals do not correspond to constant bin sizes. 86

Figure A3.1: Shear-wave quality factor (Q_S) plotted against V_S (m/s) for several attenuation models widely used in the literature (e.g., Olsen *et al*., 2003; Taborda and Bielak, 2014; Savran and Olsen, 2019; Withers *et al*., 2019) and investigated here. The inset figure in the upper left corner zooms into $V_S <= 1600$ m/s, denoted by the dashed black box. Note that these Q_S relations are valid for constant Q models, or frequency-dependent Q models for frequencies below 1 Hz. 87
Figure A3.2: Description of three candidate source models used in this study. (top) Slip distribution (shading) for sources 1, 2 and 3 (left to right), characterized by their hypocentral depths at 5, 5.5 and 6 km, respectively. Contours depict rupture time at a 0.4 s interval starting from 0. (bottom) (left) sum of the moment rates for all subfaults and (right) Fourier amplitude spectrum, respectively. Sources 1, 2 and 3 (from left to right in the first row) are characterized by their hypocentral depths at 5, 5.5 and 6 km, respectively. The contours represent rupture time at a 0.4 s interval starting from 0. Source 1 is the default source model used elsewhere in this chapter. 88
Figure A3.3: PGVs for sources 1, 2 and 3 (from left to right; see Fig. 3.3). The top and bottom rows represent the band-pass filtered results for 0.15-2.5 Hz and 2.5-5 Hz, respectively. The star denotes the epicenter. 89
Figure A3.4: Probability density histogram of the PGV difference caused by SSH effects, between Models 12-14 with Model 6 (blue, green and red) , and Model 16 with Model 2 (cyan). The definition of percent difference (x-axis) is the same as in Figure 3.11. 90
Figure A3.5: Density of PGV change for models with topography relative to models without topography for bandwidths of (left column) 0.15-2.5 Hz and (right column) 2.5-5 Hz, and models with (top row) and (bottom row) without modified shallow velocities. The y-axis depicts topographic curvature smoothed using a 2-D window of 120 m $\times$ 120 m. Values toward the top right (bottom left) denote strong amplification at steep areas (deamplification at flat areas). Note that density intervals do not correspond to constant bin sizes. 91
Figure A3.6: GOF scores for a subset of the metrics used in this study, for frequency bands 0.15-1 Hz, 1-2.5 Hz, and 2.5-5 Hz. Model IDs are listed in Table 3.2. . . . 92
Figure A3.7: Bias of (top row) PGV and (middle row) DUR and GOF (bottom row) for bandwidths of (left column) 0.15-2.5 Hz and (right column) 2.5-5 Hz at all 259 stations for Model 1 (see Table 3.2 for model features). The bias is calculated in the same way as Figure 3.9. The solid line depicts the moving average of the bias of PGV using a 20-point window versus hypocentral distance. The shading denotes the standard deviation centered at the mean. 93
Figure A3.8: Same as Figure A3.7, but for Model 2. 94
Figure A3.9: Same as Figure A3.7, but for Model 3. 95
Figure A3.10:Same as Figure A3.7, but for Model 4. 96
Figure A3.11:Same as Figure A3.7, but for Model 5. 97
Figure A3.12:Same as Figure A3.7, but for Model 7. 98

Figure A3.13:Same as Figure A3.7, but for Model 8. 99
Figure A3.14:Same as Figure A3.7, but for Model 9. 100
Figure A3.15:Same as Figure A3.7, but for Model 10. 101
Figure A3.16:Same as Figure A3.7, but for Model 11. 102
Figure A3.17:Same as Figure A3.7, but for Model 12. 103
Figure A3.18:Same as Figure A3.7, but for Model 13. 104
Figure A3.19:Same as Figure A3.7, but for Model 14. 105
Figure A3.20:Same as Figure A3.7, but for Model 15. 106
Figure A3.21:Same as Figure A3.7, but for Model 16. 107
Figure A3.22:Same as Figure A3.7, but for Model 17. 108
Figure A3.23:Same as Figure A3.7, but for Model 18. 109
Figure A3.24:Same as Figure A3.7, but for Model 19. 110
Figure A3.25:Same as Figure A3.7, but for Model 20. 111
Figure A3.26:Same as Figure A3.7, but for Model 21. 112
Figure A3.27:Same as Figure A3.7, but for Model 22. 113

Figure 4.1: Site map of Garner Valley Downhole Array (GVDA), denoted by the star. The rectangle depicts the extent of the modeling domain, where the contours depict elevation in meters. The triangle denotes a nearby outcrop site GVAR. The color version of this figure is available only in the electronic edition. . 136
Figure 4.2: (a) Multiresolution index of valley bottom flatness (MRVBF) and (b) the bedrock depth map surrounding GVDA, which is depicted by a triangle in both figures. (c) The mapping function from MRVBF to bedrock depth, with GVDA marked with an asterisk. The color version of this figure is available only in the electronic edition. 137
Figure 4.3: Cross sections of V_S in the 3D mesh (see Fig. 4.2) intersecting GVDA along (a) A–A' and (c) B–B'; the downhole accelerometer is denoted with the asterisk. (b) The 1D V_S profile, with its location denoted by the dashed line in the left panels, obtained from the borehole log, and used in the SH1D model. The color version of this figure is available only in the electronic edition. . 138
Figure 4.4: Comparison between the theoretical transfer functions (TTFs) computed using the 3D model and the SH1D model at GVDA, with the two-sigma scatter of empirical transfer functions (ETFs) shaded in gray. The color version of this figure is available only in the electronic edition. 139
Figure 4.5: Site map of TKCH05, denoted by the star. The rectangle depicts the extent of the modeling domain, where the contours depict elevation in meters. The color version of this figure is available only in the electronic edition. 140
Figure 4.6: (a) Borehole log at TKCH05 (from Thompson *et al*. 2012). (b) Borehole V_S profiles at TKCH05 and HKD090, as well as for our simplified 1D model. The color version of this figure is available only in the electronic edition. . 141

Figure 4.7: (a) Comparison between TTFs and the two-sigma scatter of the ETF for 3D and 1D models at TKCH05. Solid and dashed lines without markers are the 3D and 1D models based on the borehole log profile, respectively; solid and dashed lines with diamond markers depict the 3D and 1D models, based on the simplified downhole profile. (b,c) Comparison of 1.5–8 Hz observed east–west component surface ground motions with those obtained from convolution of the downhole records with the TTFs from models using the simplified profile for the (b) 3D model and (c) 1D model. The color version of this figure is available only in the electronic edition. 142
Figure 4.8: (a) MRVBF and (c) depth to bedrock in the vicinity of TKCH05, with the site location denoted by the triangle. (b) West–east A–A' and (d) north–south B–B' cross sections intersecting TKCH05, the downhole sensor is marked with the asterisk. The color version of this figure is available only in the electronic edition. 143
Figure 4.9: (a) The Gibbs and Steller velocity profiles at GVDA, in which the bedrock depth is 64 (solid line) and 88 m (dashed line), respectively. (b) Comparison between the two-sigma scatter of the ETFs (gray shaded) and the TTFs from the 3D models assembled with the Gibbs and Steller profiles, respectively. The color version of this figure is available only in the electronic edition. . 144
Figure 4.10: Comparison between the median ensemble ETF, the TTF from the 3D model without and with small-scale heterogeneities (SSHs) at TKCH05. The gray shaded region is the range of maximum and minimum values encountered in TTFs from these realizations of SSHs. The color version of this figure is available only in the electronic edition. 145
Figure 4.11: Energy on the (a) horizontal and (b) vertical components at the site TKCH05. (c) Total energy along depth using the simplified velocity profile at TKCH05 with different incidence angles. The gray horizontal line, at around 100 m depth, depicts the downhole site depth. The color version of this figure is available only in the electronic edition. 146
Figure A4.1: (a) Map of events (purple triangles) used for computing the ETFs at GVDA. The red triangle depicts the event used in simulations. (b) Recorded accelerations (normalized) along West-East direction at 10 randomly selected sites. The maximum amplitude is shown to the left of each line. 148
Figure A4.2: (a) Map of events (purple triangles) used for computing the ETFs at TKCH05. The red triangle depicts the event used in simulations. (b) Recorded accelerations (normalized) along West-East direction at 10 randomly selected sites. The maximum amplitude is shown to the left of each line. 149
Figure A4.3: Snapshots of V_X at TKCH05 along the A-A' cross section in Figure 4.8c, bandpass filtered between 4.5 and 5 Hz. (a), (c) and (e) display snapshots of the 3D model, where the gray contour lines represent interfaces between bulks with difference Vs; the green star denotes the downhole site and the green line marks its depth. (b), (d) and (f) are for the 1D model. 150
Figure A4.4: Same as Figure A4.3, except along the B-B' cross section in Figure 4.8c. . 151

Figure 5.1: Peak slip rate (PSR) simulated on the fault for ShakeOut scenario, with the surface PSR (in m/s) shown in the panel above each subplot. (a) linear, (b) sandstone (nonlinear), and (c) shale (nonlinear) results. Black contours indicate rupture time in 1 s intervals from 0. 161
Figure 5.2: Peak slip rate (PSR) averaged along strike against depth (left panel of each subplot) for sandstone (nonlinear) and linear models and their ratio (right panel of each subplot). (a)-(c) depit three realizations for the sandstone models with stress drop of 7, 8, and 10 MPa, respectively. Dashed red lines indicate the curves fitting the nonlinear to linear PSR ratios using Equation (5.2.2). 162
Figure 5.3: (a) STF on a representative subfault from the linear model. (b) Time-domain scaling factors from the shape function computed by Equation (5.2.2). (c) STFs for the nonlinear model and EKS model. The black dashed lines in (a) and (b) indicate the peak time of the STF and shape functions. 163
Figure 5.4: PGV distribution for the southern San Andreas fault region, obtained for (a) linear, (b) sandstone and (c) EKS model. The red rectangle depicts the LA basin region for further ground motion comparisons in Figure 5.10. 164
Figure 5.5: Cumulative distribution of PGVs for linear models with stress drop of 7 (a and c) and 10 (b and d) MPa, as well as nonlinear models and the corresponding EKS models. The top row (a and b) depicts models with sandstone and the bottom row (c and d) shows models with shale. 165
Figure 5.6: Same as Figure 5.5, but for SA-5s comparisons. 166
Figure 5.7: Same as Figure 5.5, but for SA-3s comparisons. 167
Figure 5.8: Same as Figure 5.5, but for SA-2s comparisons. 168
Figure 5.9: Same as Figure 5.8, but the rupture direction is reversed to NW-SE for all models. 169
Figure 5.10: Probability density (P.D.) histograms of PGVs in the Los Angeles Basin area. The models for each subfigure are the same as in Figure 5.8 170

LIST OF TABLES

Table 2.1: Simulation parameters used for the deterministic ground motion simulations of the 2014 La Habra earthquake. 32
Table 2.2: Type B site information 33
Table 2.3: Average FAS biases for all three components for various models. 34

Table 3.1: Simulation parameters used for the deterministic ground motion simulations of the 2014 La Habra earthquake. 71
Table 3.2: Summary and main features of the models used in this study. 72

Table 4.1: Earthquakes Used to Compute the Empirical Transfer Functions at Garner Valley Downhole Array (GVDA) 134
Table 4.2: Earthquakes Used to Compute the Empirical Transfer Functions at TKCH05 135

ACKNOWLEDGEMENTS

First and foremost, I would like to express my deepest sense of gratitude to my supervisor, Professor Kim Olsen, for his invaluable supervision, support, and tutelage during the course of my PhD studies. Kim always gives me the freedom to explore problems, allows me to try different approaches, and re-directs me every time I move in a wrong direction. He is always responsive to asking and patient to answering, even if my questions are naive. His suggestions and comments are so detailed and constructive that they easily refresh my thoughts and guide me in the right direction. I am always impressed by his skills in applying physical sense in solving problems and providing relevant knowledge in a timely manner. He emphasizes the big picture in seismology, while at the same time taught me how to present scientific findings, polish academic reports and communicate with the community. I appreciate the wealth of knowledge he has given me.

It is my privilege to thank my committee members for their great mentorship and guidance. I thank Professor Steve Day, who is always supportive and encouraging. Even during the most difficult times, I feel encouraged thinking of his optimistic attitude and enthusiasm in life. He is rigorous to scientific problems but open to explore different possibilities, to which he always provides valuable comments and insights. It was an honor to attend his retirement ceremony in person and see how a life of contribution to science is remembered and respected. Professor Peter Shearer is the person leading me to this field by his popular course "Introduction to Seismology", which is still an important source of answers in my research. He showed me that science can be elegant yet fun. I thank Professor Samuel Shen for his valuable help in mathematics in our discussions. I also thank Professor Joel Conte for his kind suggestions and comments. Dr. Daniel Roten is extraordinarily supportive in Kim's group, who taught me the details in research practice from the beginning. I cannot overstate how much I learned from him, and it is my privilege to work with someone as versatile, brilliant, and productive as Daniel. I am also grateful to Professor Shuo Ma at SDSU for sharing his experience and life advice.

I am grateful to all the professors at Scripps Institution of Oceanography (SIO) and SDSU,

who taught a wide series of courses that prepared me for my research, including Professor Duncan Agnew, Professor Adrian Borsa, Professor Catherine Constable, Professor Steven Constable, Professor Yuri Fialko, Professor Guy Masters, Professor David Sandwell, Professor Peter Shearer, and Professor Dave Stegman at Scripps Institution of Oceanography at UCSD; Professor Michael Holst in the Department of Mathematics at UCSD; and Professor Shuo Ma and Professor Kim Olsen at SDSU.

My research achievements would not be possible without the help and communication from my coauthors and collaborators from the Southern California Earthquake Center. I thank Kim Olsen, Steven Day, Daniel Roten, Christine Goulet, Robert Graves, Fabio Silva, Scott Callaghan, and Kevin Milner for their incredible collaborations and discussions.

I appreciate the support and friendship from my incredible fellows and friends: Nan Wang, Te-Yang Yeh, Yongfei Wang, Shiying Nie, Qian Yao, Wei Wang, Zefeng Li, Yuxiang Zhang, Bill Savran, Kyle Withers, Drake Singleton, Rumi Takedatsu, Xiaohua Xu, Kang Wang, Wenyuan Fan, Zhao Chen, Yuval Levy, Zeyu Jin, Yue Du, Zheng Fang, Junlong Hou, Mingda Li, and Yuan Huang. Thank you for making my time at San Diego a wonderful memory. I also appreciate the administrative advisors and staff, including Gilbert Bretado, Wayne Farquharson, Paul Dean, and Sara Miceli at UCSD; Irene Occhiello, Pia Parrish, Heather Webb, Susan Langsford, and Pat Walls at SDSU, for their consistent and timely assistance.

Finally, I would also like to extend my deepest gratitude to my parents, Xiaoyang and Xiuhong, for always listening to me, supporting me, and encouraging me. Lastly but most importantly, I thank Fei for being there for me, for always believing in me, and for enriching my life in numerous amounts of ways.

Chapter 2, in full, is a reformatted version of a paper currently being prepared for submission for publication: Hu, Z., Olsen, K.B., and Day S.M. (2021). Calibration of the Near-surface Seismic Structure in the SCEC Community Velocity Model Version 4. The dissertation author was the primary investigator and author of this paper.

Chapter 3, in full, is a reformatted version of a paper currently in preparation for submission for publication: Hu, Z., Olsen, K.B. and Day, S.M. (2021), 0-5 Hz Deterministic 3D Ground Motion Simulations for the 2014 La Habra, California, Earthquake. The dissertation author was the primary investigator and author of this paper.

Chapter 4, in full, is a reformatted version of the material as it appears in Bulletin of the Seismological Society of America: Hu, Z., Roten, D., Olsen, K.B. and Day, S.M. (2020). Modeling of Empirical Transfer Functions with 3D Velocity Structure. *Bulletin of the Seismological Society of America*. The dissertation author was the primary investigator and author of this paper.

Chapter 5, in full, is a reformatted version of a report to the Southern California Earthquake Center: Hu, Z., Roten, D., Olsen, K.B., and Day, S.M. (2021). Kinematic Source Models for Earthquake Simulations with Fault-zone Plasticity. The dissertation author was the primary investigator and author of this manuscript.

VITA

2015	B.S. in Geophysics, Peking University
2015-2021	Graduate Teaching/Research Assistant, San Diego State University
2021	Ph.D. in Geophysics, University of California, San Diego and San Diego State University

PUBLICATIONS

Hu, Z., Roten, D., Olsen, K.B., and Day, S.M. (2021) Kinematic Source Models for Earthquake Simulations with Fault-zone Plasticity. *In preparation for publication*.

Hu, Z. and Olsen, K.B. (2021). 0-5 Hz Deterministic 3D Ground Motion Simulations for the 2014 La Habra, California, Earthquake. *To be submitted for publication*.

Hu, Z., Olsen, K.B., and Day, S.M. (2021). Calibration of the Near-surface Seismic Structure in the SCEC Community Velocity Model Version 4. *To be submitted for publication*.

O'Reilly O., Yeh, T. Olsen, K.B., **Hu, Z.**, Breuer, A.N., Roten D., Goulet C. (2021). A High-order Finite Difference Method on Staggered Curvilinear Grids for Seismic Wave Propagation Applications with Topography, *Bulletin of the Seismological Society of America*. *Accepted for publication, June 10, 2021*.

Hu, Z., Roten, D., Olsen, K.B., and Day, S.M. (2020). Modeling of Empirical Transfer Functions with 3D Velocity Structure. *Bulletin of the Seismological Society of America*. doi:10.1785/0120200214.

ABSTRACT OF THE DISSERTATION

Toward high-frequency deterministic simulations: source, path and site effects

by

Zhifeng Hu

Doctor of Philosophy in Geophysics

University of California San Diego, 2021
San Diego State University, 2021

Kim Olsen, Chair

High-frequency (here defined for a maximum frequency (f_{max}) larger than about 1 Hz) ground motions are closely relevant to building response associated with small structures of engineering interests. Gaining a deeper understanding of the propagation of high-frequency seismic waves and characteristics of the resulting ground motions is therefore a principal goal for seismologists and earthquake engineers. Earthquake simulations, in particular those based on physics-based and deterministic models, have drawn significant attention from the seismic community in the most recent decades as a valuable supplement to recorded data. With the potential ability to accurately characterize broadband wavefields, numerical simulations have

their own limitations, in particular difficulty in characterizing the underlying physical parameters to a sufficient resolution and computationally accommodating regional-scale models for seismic hazard analysis. The primary objective of this dissertations is to explore and rate the effects on high-frequency ground motions from various model features, which sheds light on their individual and mixed contributions and importance for future modelers. Chapter 1 is an introduction, providing background and motivation for each of the following chapters. Chapters 2 and 3 focus on model characteristics that govern the high-frequency ground motions. Chapter 2 proposes a calibration approach that enhances the near-surface velocity structure that is insufficiently resolved in community velocity models. In Chapter 3, we simulate a series of models to investigate the effects of topography, small-scale heterogeneities, frequency-dependent attenuation, and low near-surface velocities on the resulting wavefields and ground motions as the frequency extends up to 5 Hz. In Chapter 4, we propose a method to incorporate surface topography in constraining the 3D subsurface structure to predict site response. Chapter 5 studies nonlinear effects using dynamic simulations and proposes an equivalent kinematic source generator to emulate near-source plasticity in terms of the resulting peak ground velocities and spectral accelerations.

Chapter 1

Introduction

1.1 Motivation

Earthquakes, caused by energy release from the Earth's interior during short time span, constitute one of the most catastrophic natural hazards to human society. While the majority of earthquakes are too small to be felt by humans, their recordings from expanding sensor deployments increasingly contribute to our understanding of seismology. Major earthquakes with magnitude greater than 7 occur globally more than once per month. The timing of these events remains unpredictable, with limited progress expected in the near future. On the other hand, considerable progress has been made in estimation of the spatial distribution of ground motions for future damaging earthquake scenarios, an important ingredient in seismic hazard analysis.

Ground motion prediction is central to seismic hazard analysis, because ground shaking from major earthquakes is oftentimes the most dominant source of direct damage, as well as responsible for secondary effects, such as tsunamis, landslides, liquefaction and fires. A conventional approach to ground motion estimation is to perform statistical analysis from earthquake records, incorporating correlations between earthquake characteristics and measurements. This method is referred to as ground motion models (GMMs) or ground motion prediction equations

(GMPEs; e.g., Abrahamson *et al*., 2014; Boore *et al*., 2014; Campbell and Bozorgnia, 2014; Chiou and Youngs, 2014; Idriss, 2014), typically providing median values with uncertainty estimates. However, due to lack of records for large earthquakes, particularly at near-fault sites (e.g., less than about 10 km), estimates of strong ground motions using GMPEs suffer from large uncertainty. Here, physics-based numerical methods represent viable alternatives to produce ground motion estimates for large earthquakes and near-fault distances required for accurate seismic hazard analysis, public earthquake emergency preparedness, and the design of seismic-resistant structures in civil engineering.

As analytical solutions for wave propagation in 3D velocity structures are often intractable, physics-based deterministic simulations solving the elastodynamic equations numerically are required to obtain ground motion estimates for realistic scenarios. A variety of deterministic numerical methods have been developed for ground motion prediction, including finite-difference, finite-element, boundary element, spectral element and pseudo-spectral methods (e.g., Sánchez-Sesma *et al*., 1982; Frankel and Vidale, 1992; Olsen *et al*., 1995; Graves, 1996; Bao *et al*., 1998; Seriani, 1998; Käser and Dumbser, 2006; Chaljub *et al*., 2006). These numerical methods differ from each other with individual advantages or disadvantages in terms of accuracy, efficiency and ranges of applicability. Based on extensive verification and validation, though under various simplifications and assumptions due to insufficiently resolved parameters and computational limitations, these methods have been developed and applied successfully in a series of meaningful research exercises (e.g., ShakeOut, PetaShake, M9 Cascadia; for more details readers are referred to Cui *et al*., 2009a; Cui *et al*., 2009b; Olsen *et al*., 2009; Marafi *et al*., 2019). Among these methods, finite difference is the most widely used method in large-scale three-dimensional (3D) simulations considering its simplicity in mesh generation and GPU parallelization, efficiency and scalability. Finite-difference methods are able to support nonlinear soil behavior, frequency-dependent anelastic attenuation, discontinuous mesh discretization and irregular surface topography (e.g., Roten *et al*., 2017b; Nie *et al*., 2017; Zhang *et al*., 2012;

O'Reilly *et al*., 2021).

Armed with increased availability of high-performance computing resources, researchers have achieved considerable progress in higher-frequency ground motion simulations in the last two decades (Graves *et al*., 2008; Olsen *et al*., 2009; Bielak *et al*., 2010; Roten *et al*., 2012; Savran and Olsen, 2019; Withers *et al*., 2019). Despite of this progress, it is critical to continually refine the temporal and spatial characteristics of broadband seismic wave propagation simulations, in order to make further advances in mitigating life and property in future damaging earthquakes. State-of-the-art deterministic earthquake simulations lend themselves to explore the relative effects of features such as rupture nucleation, rock failure, plastic deformation, anelastic attenuation and scattering, 3D path effects, low-velocity amplification, etc. This thesis explores the relative contributions to ground motion estimation from a series of physics-based model features, introduced in the following.

1.2 Model Characteristics in High-Frequency Simulations

State-of-the-art velocity models used in seismic wave propagation simulations are typically based on geological, geotechnical and geophysical information, and the accuracy of these velocity models are critical in minimizing systematic uncertainties in the resulting ground motion predictions. In the past decades, most large-scale deterministic earthquake simulations have focused on low-frequency ($f_{max} \leqslant 1$ Hz) seismic waves, which only requires relatively coarse quantification of model properties. Generally, these simulations excluded surface topography, small-scale spatial heterogeneities and frequency-dependent attenuation, along with the minimum velocity clamped at often unrealistically high values to alleviate computational costs. However, these model features are expected to play an increasingly important role when entering the high-frequency bandwidth, along with trade offs complicating their relative contributions to the resulting ground motion estimates. For example, scattering increasing the envelope duration and

often lowering the peak amplitudes is generated by both topography and velocity heterogeneities Lai *et al*. (2020). In the following sections, we briefly discuss the physics-based deterministic simulation features and how they can be accommodated in high-frequency deterministic simulations.

1.2.1 Near Surface Low Velocity

The presence of near-surface low-velocity layers can have a dramatic effect on the simulated ground motion, mainly by scattering seismic waves (e.g., Dodge and Beroza, 1997; Vernon *et al*., 1998; Imperatori and Mai, 2013; Imperatori and Mai, 2015). Previous studies have shown that low near-surface material properties, in particular the shear-wave velocity V_s, can lead to significant amplification, especially at higher frequencies (Boore and Joyner, 1997; Poggi *et al*., 2011). In addition, low-velocity layers can increase coda wave amplitude and duration by trapping energy close to the free surface (Imperatori and Mai, 2013). Unfortunately, many large-scale deterministic simulations, in particular those using uniform grid approaches, have had to adopt larger than realistic surface low velocities, because of limitations on the computational resources.

Due to the oftentimes significant amplification effects, characterization of shallow material properties is an important task for ground motion estimation. Numerous well-established techniques have been applied for local characterization of the shallow velocities, including seismic borehole logging, surface-wave dispersion surveys, cone penetration tests, gravity observations and oil-well samples. Regional-scale characterization of near-surface material variability is, however, technically infeasible and financially prohibitive.

The Southern California Earthquake Center (SCEC) maintains several popular and widely-used Community Velocity Models (CVMs). The CVM velocities below the top 1-2 kilometers are generally relatively well-constrained from tomographic inversions (e.g., Lee *et al*., 2014a; Shaw

et al., 2015), while the near-surface ($<$ 300 m) velocity information consists of a combination of geotechnical information and the S-wave velocity in the very uppermost 30 m (V_{S30}) when available, along with empirical functions, derived from features such as topography (e.g., Wald and Allen, 2007; Thompson *et al*., 2014). However, the velocities between the top 300 m and the tomographic constraints, which have disproportionately strong influence over intermediate to high frequencies (e.g. $>$ 0.5 Hz Day, 1996), are relatively poorly resolved. Ely *et al*. (2010) proposed a method to include the V_{S30} information into the CVMs via tapering to the values at a fixed threshold depth. We find that this threshold depth is poorly determined, and we propose an update to this method for the greater Los Angeles basin based on our modeling of the 2014 M5.1 La Habra, CA, earthquake (see Chapter 2).

1.2.2 Topography

Probably the most prominent effect of surface topography on seismic motions is to amplify ground motions at mountain ridges and peaks, as evidenced from both observational and numerical studies (Çelebi, 1987; Kawase and Aki, 1990; Massa *et al*., 2010; Burjánek *et al*., 2014). However, a key challenge in exploring topographic effects is to isolate the contribution of local relief from other factors, such as stratigraphy, the presence of fault damage zones or low-velocity surface layers. For example, the assumption that the near-surface geology is consistent across areas with simple and highly irregular topography (Çelebi, 1987; Geli *et al*., 1988; Chávez-García and Faccioli, 2000) is difficult to make. Numerical simulations provide a convenient means to circumvent such assumptions and isolate topographic amplification (Boore, 1972; Sánchez-Sesma and Campillo, 1991; Lovati *et al*., 2011; Hartzell *et al*., 2017).

A wide range geomorphic parameters have been used to describe topography geometry, including slope, curvature, relative elevation, and surface roughness (Ashford and Sitar, 1997; Nguyen and Gatmiri, 2007; Bouckovalas and Papadimitriou, 2005). These studies found that

smoothed curvature and relative elevation, which are linearly correlated with each other, are key parameters controlling topographic amplification (Maufroy *et al*., 2015; Rai *et al*., 2017). Because the characteristic length is critical and dependent on frequency, the topographic effects behave differently in different frequency bands. The conventional assumption is that topography has negligible effects below 1 Hz (Boore, 1972; Pischiutta *et al*., 2010), with increasing effects for higher frequencies. Some recent studies, however, indicate that topography can cause factor-of-two effects on peak ground motions at frequencies as low as 0.5 Hz, in the presence of a broad mountain range with significant relief (e.g., Ma *et al*., 2007). Also, topography can be a major source of scattering, especially when the source location is shallow and surface waves are excited (Lee *et al*., 2009b; Imperatori and Mai, 2015). Here, we will use the support for topography in our numerical modeling code to further isolate topographic amplification of ground motion for the greater Los Angeles basin due to the 2014 M5.1 La Habra, CA, earthquake.

1.2.3 Anelastic attenuation

Anelastic (intrinsic) attenuation of seismic waves propagating through Earth's crust can be described by the quality factor Q as the fractal energy loss per cycle: $Q^{-1}(\mathbf{x}, f) = \delta E/2\pi E$, where $\mathbf{x}$ is the position, f is the circular frequency, E is the total energy and δE is the energy loss (O'Connell and Budiansky, 1978). Intrinsic attenuation is caused by internal dissipation and scattering from crustal and mantle heterogeneities (Sato and Fehler, 2009), which become prominent at high frequencies ($f \geqslant 1$ Hz; e.g., Sato *et al*., 2012). As indicated by its nature, Q primarily affects the ground motion amplitudes, but can also prolong the shaking duration, especially for surface waves excited by shallow events (Imperatori and Mai, 2015; Lai *et al*., 2020). Different tectonic regions are generally characterized by different anelastic attenation regimes. For southern California studied here, a tectonic active area, anelastic attenuation is generally stronger compared to techtonically stable areas (Frankel *et al*., 1990; Erickson *et al*.,

2004). The near-surface crustal material experiences more attenuation, where Q can be as low as 10 in soft sediments (Aster and Shearer, 1991; Abercrombie, 1997).

At low frequencies (i.e., less than about 1 Hz), anelastic attenuation is normally modeled as a frequency-independent phenomenon (Aki and Richards, 2002). However, observational evidence shows that Q values appear to increase with frequency at higher frequencies (e.g., Aki, 1980; Atkinson, 1995; Erickson *et al*., 2004), at least in some regions. Withers *et al*. (2015) developed an efficient numerical approach to implement frequency-dependent anelastic attenuation $Q(f)$ in 3D deterministic simulations, and showed that $Q(f)$ models generally predict ground motions better than constant Q models. As simulations are pushed to higher frequencies, anelastic attenuation becomes increasingly important because of the added wave cycles within the simulated domain, and is critical for accurate estimation of earthquake ground motions.

1.2.4 Small-scale Heterogeneities

The heterogeneous nature of Earth's crust, at different scales, is another important factor governing the propagation of seismic wavefields (Levander and Holliger, 1992; Levander *et al*., 1994; Bean *et al*., 1999; Helffrich and Wood, 2001; Hedlin *et al*., 1997). Changes in material properties can lead to amplitude decay and dispersive effects, known as scattering. The most prominent effects of scattering on the resulting ground motions is the generation of coda waves, including envelope broadening (Sato, 1989), waveform variation and travel time shift (Flatté and Wu, 1988). Multiple theoretical studies have been developed to explain the nature of wave scattering (Aki, 1969; Wu, 1985; Aki and Chouet, 1975; Zeng *et al*., 1991; Zeng, 1993; Zeng *et al*., 1995).

Stochastic numerical simulations, typically computationally less demanding than the deterministic counterparts, have been carried out using radiative transfer theory (Gusev and Abubakirov, 1996; Przybilla *et al*., 2006) or Markov approximation (Saito *et al*., 2002; Sawazaki

et al., 2011) to capture scattering processes. For ground motion predictions and earthquake engineering, hybrid techniques are sometimes applied to include scattering statistics, mainly at high frequencies, with parameters constrained by observed seismograms and ground motion prediction models (Liu *et al*., 2006; Graves and Pitarka, 2010; Mai *et al*., 2010). Despite being more computationally expensive, deterministic simulations have been used to study scattering processes, distributions of heterogeneities and scattering characteristics by comparing the synthetic results to seismic records or theoretical predictions (Frankel and Clayton, 1986; Roth and Korn, 1993; Shapiro and Kneib, 1993; Thybo *et al*., 2003). Recent availability of high-performance computing resources is increasing the potential for extending these studies to higher frequencies, where scattering processes tend to play a larger role.

As sufficient coverage of direct measurement constraints for meter-scale mapping of small-scale heterogeneities is prohibitively expensive, statistical methods have been used to parameterize crustal heterogeneities. For example, perturbations of crustal material properties, such as seismic velocities and densities, can be superimposed onto a reference velocity model via a spatially random field, such as the bandlimited von Kármán correlation function (Frankel and Clayton, 1986; Hartzell *et al*., 2010; Appendix A). Other correlations functions, such Gaussian and exponential formulations, have been less favored for this purpose, as they are unable to match some key scattering phenomena (Frankel and Clayton, 1986). The parameters that control the distributions of heterogeneities have been constrained by data from borehole analysis, reflection seismic experiments and sonic logs (e.g., Holliger, 1996; Dolan and Bean, 1997; Bean *et al*., 1999; Savran and Olsen, 2016) as well as by numerical simulation estimates (Thybo *et al*., 2003; Nielsen and Thybo, 2006; Przybilla *et al*., 2009; Imperatori and Mai, 2013; Imperatori and Mai, 2015), but remain somewhat uncertain.

1.3 Site Amplification

The amplitude of seismic waves is increased when propagating from stiff bedrock into the lower-velocity soils near the surface due to the impedance contrast (Boore, 1986; Silva and Darragh, 1995). The effects of soft soils on ground motions, referred to as site response, site effects, or site amplification, have been documented and studied for more than 100 years (e.g., Wood, 1908; Reid, 1910; Gutenberg, 1957). For example, Gutenberg (1957) found that the amplitude of ground motions between 0.67 to 1 Hz were about 5 times larger at dry alluvium sites than at crystalline rock sites. Different soil types respond differently when excited by ground motions in various frequency bands, dependent on the thickness of the soil column (Aki, 1993). One of the most outstanding examples of site amplification due to local geological structure was observed during the 1985 M 8.1 Michoacan, Mexico, Earthquake, where the ground motions on soft lake sediments were amplified by up to 50 times compared to nearby rock sites (Singh and Ordaz, 1993). Since metropolitan regions are often located on top of soft sediments, the study of local site conditions and the resulting amplification is a fundamental task for earthquake engineering.

The accuracy of site response estimates depends on the accuracy of the subsurface model used, which is usually controlled by the uncertainty of the site properties, and in particular, the shear-wave velocity, V_s (e.g., Barani *et al*., 2013; Griffiths *et al*., 2016). V_s is generally considered to be the most important parameter for conventional 1D site amplification estimation, which uses an approximation of horizontally polarized plane S waves propagating through a stack of homogeneous, planar layers (e.g., Kramer, 1996). This modeling procedure (SH1D) ignores the lateral complexity of often heterogeneous geology and subsurface structure and is, therefore, not able to capture 2D or 3D amplification effects (e.g., Roten *et al*., 2008; Thompson *et al*., 2012). Zhu *et al*. (2018) performed numerical analysis on 2D sedimentary basins and found that a constant spectral aggravation factor (Chávez-García and Faccioli, 2000), which quantifies the

discrepancy between 1D and 2D/3D models, insufficiently identify basin effects, in particular for regions close to the edge of shallow basins. In addition, ground motions computed in 1D models lack realistic spatial variability, caused by complex wave propagation such as basin amplification, surface-wave generation, and scattering. For this reason, 1D models are unable to capture spatial correlations, which is important for risk calculations, in particular concerning regional-scale infrastructure (e.g., Olsen and Schuster, 1995; Boore, 2004). Although recent efforts have attempted to reduce velocity uncertainties in site effect estimation (Matavosic and Hashash, 2012; Teague *et al*., 2018), these methods either require prohibitively complex processing or are developed for specific cases only.

It is impractical to characterize subsurface structure over a broad region to the resolution required for accurate ground-motion estimation to high frequencies (e.g., 10 Hz, on the order of meters to tens of meters). Instead, some studies choose to use simple proxies, based on broad site classes to supplement estimates of soil properties and spatial site characteristics, for example, the National Earthquake Hazards Reduction Program (NEHRP) soil classification (BSSC, 2003; Akkar and Bommer, 2010) or a weighted average of V_s in the uppermost 30 m (V_{S30}, e.g., Abrahamson and Silva, 2008; Idriss, 2014). Thompson *et al*. (2012) proposed a scheme to classify surface-downhole site pairs by the extent of interevent variability and goodness of fit between 1D modelling and empirical site response, which can be used to calibrate the constitutive models and guide specific site studies. Despite the use of these characterizations in some generic seismic hazard estimates, for instance, via ground-motion prediction equations, recent work has pointed out the importance of considering site-to-site amplification variability (Atkinson and Boore, 2006; Atik *et al*., 2010). These studies show that, even within a single NEHRP or V_{S30} class, the variability of site amplification and spatial correlations is sufficiently strong to induce large uncertainty into the resulting ground-motion estimates.

In Chapter 4, we propose a method using surface topography to improve estimation of site response and the associated uncertainty, and 3D wave propagation effects via high-resolution

numerical simulations. The simulations naturally take advantage of 3D geotechnical information and are able to capture complicated, spatially varying amplification effects.

1.4 Near-source Plasticity

A number of densely populated regions are located close to major faults where extreme earthquakes are likely to occur, e.g., Los Angeles, San Francisco, Tokyo, Istanbul and others. Seismic hazard analysis and building code design for these regions are particularly affected by the poorly constrained database of near-source ground motions which leads to large uncertainty of the high ground motion levels at low exceeding probability (e.g., Hanks *et al*., 2005; Bommer and Abrahamson, 2006). Oftentimes, large-scale simulations are limited to linear deformation for modeling simplicity (Olsen *et al*., 2008; Molnar *et al*., 2014), despite pervasive evidence of nonlinear effects during large earthquakes, which typically decreases the peak ground motions close to the fault (Andrews *et al*., 2007; Ma, 2008; Duan and Day, 2010; Templeton *et al*., 2010; Dunham *et al*., 2011b). The occurrence of inelastic deformation near the fault damage zone is supported by the fact that the central fault core zone is composed of ultra-cataclasites from microcracks to secondary faults. Though the exact generation of fault damage zones is still unresolved (Mitchell and Faulkner, 2009), considering plastic deformation is important in numerical simulations to avoid the otherwise abnormally high slip velocities and accumulative stress around the bends of the fault (Noda *et al*., 2009; Dunham *et al*., 2011a).

Physics-based numerical simulations have the potential to complement the sparse observations, particularly in the near-fault regions. Several studies have incorporated the inelastic deformation in earthquake models with continuum plasticity using specific yielding functions and flow rules (e.g. Mohr-Coulomb or Drucker–Prager formulations; Andrews, 2005; Ma and Beroza, 2008; Duan and Day, 2010; Dunham *et al*., 2011b; Roten *et al*., 2014). While nonlinear soil effects are traditionally found for frequencies above 1 Hz based on 1D analysis (Field *et al*.,

1998), Roten *et al*. (2014) showed from 3D deterministic simulations that visco-plastic rheology can reduce the peak amplitudes of long-period (<1 s) ground motions from large southern San Andreas earthquake scenarios by up to 70% in the Los Angeles Basin compared to the response obtained with visco-elastic models, primarily due to plastic yielding near the fault.

As large-scale earthquake simulations with plasticity are computationally expensive, in particular as frequencies increase, we explore the efficacy of an approximate linear method to include nonlinear effects in the ground motions. The method, involving an "Equivalent Kinematic Source (EKS)", uses results from a series of linear and plastic simulations to formulate a modified source description that optimally emulates the response of an equivalent nonlinear rheology.

Chapter 2

Calibration of the Near-surface Seismic Structure in the SCEC Community Velocity Model Version 4

The near-surface seismic structure (to a depth of about 1000 m), particularly the shear-wave velocity (V_S), can strongly affect the propagation of seismic waves, and therefore must be accurately calibrated for ground motion simulations and seismic hazard assessment. The V_S of the top ($<$ 300 m) crust is often well-characterized from borehole studies, geotechnical measurements, and water and oil wells, while the velocities of the material deeper than about 1000 m are typically determined by tomography studies. However, in regions lacking information on shallow lithological stratification, typically rock sites outside the sedimentary basins, the material parameters between these two regions are typically poorly characterized due to resolution limits of seismic tomography. When the alluded geological constraints are not available, models, such as the Southern California Earthquake Center Community Velocity Models (CVMs), default to regional tomographic estimates that do not resolve the uppermost V_S values, and therefore deliver unrealistically high shallow V_S estimates. A widely-used method for incorporating the

near-surface earth structure is implemented in CVMs by applying a generic overlay based on measurements of time-averaged V_S in top 30 m (V_{S30}) to taper the upper part of the model to merge with tomography at certain depth (e.g., 350 m). However, our 3D simulations of the 2014 M_w 5.1 La Habra earthquake in the Los Angeles area using the CVM-S4.26.M01 model significantly underpredict low-frequency (< 1 Hz) ground motions at sites subject to the generic overlay ("taper"). On the other hand, extending the V_{S30}-based taper of the shallow velocities down to a depth of about 1000 meters improves the fit between our synthetics and seismic data at those sites, without compromising the fit at well constrained sites. We explore various tapering depths, demonstrating increasing amplification as the tapering depth increases, and the model with 1000 m tapering depth yields overall favorable results. Effects of varying anelastic attenuation are small compared to effects of velocity tapering. Although a uniform tapering depth is adopted in the models, we observe some spatial variabilities that may further improve our method.

2.1 Introduction

Ground motion amplification due to the near-surface structure is widely accepted and well-studied (e.g., Gilbert *et al*., 1907; Field, 2000), and needs to be incorporated in numerical simulations of earthquakes to produce accurate ground motion results. Theoretical analyses have shown that the near-surface shear-wave velocity (V_S) can exert strong control on spectral amplification (Joyner *et al*., 1981; Boore and Joyner, 1991; Anderson *et al*., 1996; Day, 1996). The time-averaged shear-wave velocity in the upper 30 m (V_{S30}) is routinely used as a representation of the site condition in ground motion prediction models and building codes (Borcherdt, 1994; Bozorgnia *et al*., 2014; International Code Council, 2014). Several methods have been proposed for estimating V_{S30} from topography (Wald and Allen, 2007), supplemented with near-surface geological information (Thompson *et al*., 2014; Wills *et al*., 2015). However, despite the continuing advancement in the V_{S30}-based methodologies by the seismic hazard community

(e.g., Thompson *et al*., 2014; Heath *et al*., 2020), estimating V_{S30} at high resolution remains a difficult task and it is noted that V_{S30} is not a good single proxy for the estimation of site amplification (e.g., Steidl, 2000; Lee and Trifunac, 2010; Shingaki *et al*., 2018). Other empirical methodologies provide additional predictive capability for shallow low-velocity amplification, normally constrained by sediment depth, which is parameterized using the depth to the 1 km/s (z_1) or 2.5 km/s ($z_{2.5}$) V_S horizon (e.g., Abrahamson *et al*., 2014; Boore *et al*., 2014; Campbell and Bozorgnia, 2014). Nonetheless, these empirical methods, oftentimes dependent on V_{S30}, have similar limitations with V_{S30} that depth-dependent and lateral velocity variations are insufficiently accounted for.

While the current approximations to correct for site effects represent great progress in ground motion estimation, a fully physics-based approach to computing ground motion offers opportunities for further improvements. The physics-based approach entails difficult challenges as well, and remains a long-term goal. In such an approach, the full wavefield is computed deterministically, to maximum frequencies that are sometimes up to 5 Hz or higher, using a 3D velocity model that includes observationally constrained heterogeneities (Savran and Olsen, 2019; Withers *et al*., 2019; Hu *et al*., 2021a). A necessary ingredient in producing accurate synthetic seismograms using physics-based simulations is an accurate velocity model for the model region. Community Velocity Models (CVMs) have been developed for such purpose, e.g., the Southern California Earthquake Center (SCEC) CVMs (Small *et al*., 2017), the Cascadia CVM (Stephenson *et al*., 2017) and the Subsurface Structure Model maintained by the Japan Seismic Hazard Information Station (Fujiwara *et al*., 2017). These velocity models are often generated by combining 3D tomographic inversion from seismic waves (Tape *et al*., 2009; Tape *et al*., 2010; Lee *et al*., 2014b) with shallow geotechnical information (e.g., V_{S30}). The spatial resolution of large-scale tomographic studies is generally limited by the density of ray paths, distribution of high-quality measurements, or intrinsic nonuniqueness of inversion, particularly in the upper ~1000 m of the crust. For example, Lin *et al*. (2007) had a vertical grid spacing of 3 km

and only resolved $>$ 1 km velocity contrasts in their tomographic inversion using P and S wave arrival time, the full-3D seismic waveform tomography conducted by Lee *et al*. (2014b) can reach at best 1 km resolution in the center of the inverted region, and Qiu *et al*. (2019) found the top 3 km is poorly constrained in their Eikonal tomography using ambient noise cross correlations.

Shallow velocity structure, e.g. S-wave impedance and scattering, has an significant role in modifying ground motion amplification and duration (e.g., Graves, 1995; Anderson *et al*., 1996; Imperatori and Mai, 2013). Specifically, 1D theoretical analysis by Day (1996) suggests that the smoothed amplification spectrum is principally determined by shallow V_S, above roughly the depth of half the smoothing bandwidth expressed as a wavelength. Over a ~0.5 Hz bandwidth and typical Southern California rock site V_S values, the analysis predicts that the V_S structure above about 1000 m will have a disproportionately strong effect on ground motion. Therefore, resolving the shallow velocity structure is essential in accurate predictions of ground motions. In SCEC CVMs, velocities and densities in the top 300 m within the basins are constrained by geotechnical and geophysical data, such as seismic reflection surveys, borehole seismic records and gravity data, and in the deeper basins are estimated either from empirical age- and depth-consolidation rules based on water and oil wells and geological studies, or sonic logs and reflection/refraction profiles from the oil industry (Magistrale *et al*., 1996; Magistrale *et al*., 2000; Süss and Shaw, 2003). Unfortunately, outside and below the basins (typically rock sites), CVMs simply assign interpolated results from regional tomography studies. Additional data constraints on shallow velocity structure, including seismic refraction studies (e.g., Teague *et al*., 2018) or borehole logs (e.g., Steller, 1996; Thompson *et al*., 2012) are rare in these regions.

Where location-specific constraints are lacking, previous studies have attempted to use generic models to bridge the gap between data constraints at shallow (< ~30 m) and deeper (> ~1000 m) depths. For example, Boore and Joyner (1997) generated a continuous depth-dependent V_S function based on 3 different intervals. The V_S profile in the upper 30 m was constructed from interpolated shallow average arrival times. At depths below 4 km, V_S was estimated from the

P-wave velocity (V_P), measured from earthquake location studies and velocity surveys, on the assumption of a fixed Poisson ratio at 0.25. Finally, the shallow and deeper V_S were connected using two power-law functions. Ely *et al.* (2010) proposed a generalized method that derives the surface V_S by linearly scaling V_{S30} and then interpolates velocities with depths until converging to the original tomography model at a certain depth, a scheme which has been implemented in some of the SCEC CVMs. We will use the term "tapering" to denote the replacement of (poorly constrained) site-specific CVM values by a generic function of depth that merges smoothly with the original CVM at some depth z_T. Ely *et al.* (2010) proposed a value of 350 m for z_T, based on qualitative comparison between synthetic and seismic records from the 2008 M_w 5.4 Chino Hills, CA, earthquake.

In this study, we quantify the accuracy of ground motion simulations based upon comparisons to the 2014 M_w 5.1 La Habra, CA, earthquake, and interpret the results in terms of the representation of crustal V_S in the top 1000 m. The chapter is organized as follows: we first briefly introduce our numerical approach to obtain the simulated ground motions, present an approximate 1D analysis of site amplification to evaluate the potential to improve site amplification at poorly constrained sites, and finally evaluate different generic tapers using 3D wave propagation simulations. The proposed tapering method amplifies the ground motions as the tapering depths increase, which generates up to 3 times (less than 10%) increase in the spectral amplitudes at poorly (well) constrained locations, compared to the original (i.e., untapered) CVM. We also discuss the limitations of this study, in particular the neglect of spatial variation of the taper depths, which will be a future objective to investigate, using more validation metrics and higher frequencies.

2.2 Numerical Approach

We perform 0-1 Hz wave propagation simulations of the 2014 M_w 5.1 La Habra earthquake to explore the accuracy of ground motion predictions in terms of the shallow velocity structure. The simulations use the SCEC velocity model CVM-S4.26-M01 (hereafter referred to as CVM-S). Figure 2.1 shows the computational domain and strong motion seismic stations in the greater Los Angeles area used in this study. We discretize a 148 km $\times$ 140 km $\times$ 58 km region from CVM-S and the computational domain is rotated 39.9° clockwise to reduce the mesh size while optimizing the data coverage in our region of interest. Table 2.1 lists the simulation parameters.

The GPU-supported staggered-grid finite difference code AWP-ODC (Anelastic Wave Propagation - Olsen, Day, and Cui, from the authors of the code; Cui *et al*., 2010) with discontinuous mesh (Nie *et al*., 2017) was used for the simulations analyzed in this study. We used spatial grid spacings of 20 m and 60 m in the grid partitions above and below 7.5 km, respectively, and a minimum V_S of 500 m/s. To facilitate the use of these simulations in a companion, high-frequency study (Hu *et al*., 2021a), we computed frequencies up to 5 Hz. However, we restrict our analysis to a maximum frequency of 1 Hz in this study, which precludes some of the complicating effects that may become important at higher frequencies, e.g. topography, frequency-dependent attenuation, etc. Anelastic attenuation is incorporated with the quality factors given by linear velocity-dependent relations $Q_S = 0.1V_S$ (V_S in m/s) and $Q_P = 2Q_S$, as suggested by previous literature (e.g., Bielak *et al*., 2010; Withers *et al*., 2019). We applied sponge zones (Cerjan *et al*., 1985) with a width of 64 nodes at the exterior grid boundaries (except at the flat free surface) to limit artificial reflections.

The 2014 M_w 5.1 La Habra earthquake was well recorded by broadband strong motion sensors. We selected 259 stations with the epicentral distance up to 90 km and signal-to-noise larger than 3 dB for our study. The assessment of the ground motion synthetics is made using the Fourier amplitude spectra (FAS) of accelerations at all 259 stations, and the goodness of fit to

data is described by the FAS bias between model and data:

$$Bias(frequency, site) = \log_{10}\left(\frac{FAS_{\text{model}}}{FAS_{\text{data}}}\right) \tag{2.1}$$

We used a kinematic source description generated following Graves and Pitarka (2016) which creates finite-fault rupture scenarios with stochastic characteristics optimized for California events. The focal mechanism was taken from the U.S. Geological Survey (strike=233°, dip=77°, rake=49°; USGS, 2014) with a moment magnitude 5.1, fault area of 2.5 km $\times$ 2.5 km, and a hypocentral depth of 5 km (0.5 km below the top of the finite fault). The source was selected from a series of 40 realizations with different random seeds from comparison between spectral accelerations with records at stations within 31 km to the epicenter (R. Graves, Personal Communication, 03/04/2020; see Fig. 2.2). The rupture duration is less than 2 s, and the source model was sampled at an interval of 0.001 s, identical to the time step used in our simulations.

The V_S profiles extracted from CVM-S beneath all 259 stations selected for the La Habra event are shown in Figure 2.3. For most stations, the unmodified CVM-S gives low surface V_S (< 500 m/s, see Fig. 2.3a), while a small portion (15%) of the stations have significantly larger surface V_S (> 1500 m/s, up to 4650 m/s). Such large V_S, typically representative of much larger depths, are highly unrealistic at the surface in western North America, even for rock sites in the presence of weathering (note that shallow velocities can be much higher in mid-continent and eastern North America where the surface weathered soils are stripped off by glacial erosion). Additionally, the fact that the V_S values remain constant between the surface and about 500 m depth (Fig. 2.3) indicates a poorly constrained near-surface V_S at these stations. We separate all sites into two classes: type A sites where CVM-S provides meaningful near-surface velocities based on geological and geophysical constraints and type B sites where shallow velocities are typically higher than realistic near-surface velocities due to their derivation from relatively low-resolution seismic tomography. The two types of stations fall into two distinct CVM-S surface V_S

classes, ~200-300 m/s and ~1500-4650 m/s, respectively (Fig. 2.3). Type B represents sites with poor constraints in velocities and thus constitute our main target for calibration in this study (see Table 2.2 for type B site information from the original, untapered CVM-S; note the unrealistically large surface V_S). There are many indications that the near-surface V_S values at type B sites in CVM-S are anomalously high. CVM-S includes a geotechnical layer (GTL) by recovering the basin information from geological and geophysical data, which are typically confined to the top 300 m in basin areas only (Magistrale *et al*., 1996; Magistrale *et al*., 2000). In addition, CVM-S cuts off the GTL at 350 m depth when it is merged with the background velocity model, leading to a sharp contrast at that depth when the background model has high velocity (as at type B sites). Note, that the mean values of each of the two groups of profiles become similar below a depth of 2000 m. The hypocentral-distance distributions for the respective site types (A and B) are similar, though type B sites are typically located outside the basins and thus of relatively larger distance.

2.3 Simulation Results

We calculate the Fourier amplitude spectra (FAS) of accelerations for both recorded and synthetic time series, both processed in the following way: (1) low-pass filtering with a corner frequency of 10 Hz using a 4^{th}-order zero-phase Butterworth filter; (2) interpolating linearly to a uniform time step; (3) tapering at the last 2 seconds using the positive half of a Hanning window; and (4) padding with 5 seconds of zeros. Horizontal components for both data and synthetics were rotated to east-west (E-W) and north-south (N-S) directions, and the data were synchronized to the rupture time. Furthermore, if needed, records were padded with zeros to obtain a duration of 120 s relative to the rupture time. Finally, we calculated the FAS of the accelerations from the time derivatives of the velocities for the synthetics and records, which were bandpass filtered between 0.15 Hz and 1 Hz using a 4^{th}-order zero-phase Butterworth filter. The lower cut-off frequency of 0.15 Hz was selected to avoid noise interference.

Figure 2.4 shows a comparison of median FAS, taken over the two types of stations, of ground accelerations for synthetics from unmodified CVM-S and recordings. The FAS at type A sites are well predicted, especially below 0.7 Hz, with a small underprediction between 0.7 Hz and 1 Hz on the horizontal components. At type B sites, however, significant underprediction is observed for all three components for frequencies as low as 0.2 Hz on the horizontal components. Also, as the frequency increases toward 1 Hz, the difference in FAS between data and synthetics increases rapidly, leaving the FAS from the simulated results outside of the 95% confidence interval of the data. The relatively good match at type A sites indicates that the source description is not likely to be a significant source of the misfit. Furthermore, more complicated path and site effects from topography, small-scale heterogeneities and frequency-dependent attenuation are expected to be negligible at frequencies below 1 Hz. For example, topographic relief mostly affects a frequency band that scales inversely with the characteristic dimensions of the relief (e.g., Boore, 1972; Bouchon and Barker, 1996; Durand *et al*., 1999), and that band is generally observed to be above 2 Hz (e.g., Pischiutta *et al*., 2010; Massa *et al*., 2014). Frequency dependence of anelastic Q will also be unimportant of the narrow band considered here (e.g., Liu *et al*., 1976; Fehler *et al*., 1992). Small-scale velocity perturbations likewise have are usually found to have a relatively small effect at frequencies below 1 Hz (Hartzell *et al*., 2010). The fact that the large underprediction in Figure 2.4 is confined to the type B sites and is most marked at frequencies of ~0.5-1.0 Hz, strongly suggests that it is principally controlled by the artificially high shallow Vs in the CVM-S at those sites.

2.4 Velocity Taper Method

Ely *et al*. (2010) proposed a method for tapering shallow velocities in SCEC CVMs. The method first multiplies the V_{S30} by a uniform constant (the coefficient a in Equation (2.2), determined by trial and error) to derive the surface V_S, which is used to infer the V_P and density

following the scaling laws of Brocher (2005). It should be noted that this method may not preserve the original V_{S30}, albeit the deviation is generally small. V_P, V_S and density at the transition depth are directly extracted from the velocity model. V_P and V_S are independently interpolated between the surface and the transition depth, and density is again calculated via the Nafe-Drake law (Ludwig *et al*., 1970). The revised velocities, as a function of depth, are obtained by:

$$\begin{aligned} z &= z'/z_T \\ f(z) &= z + b\left(z - z^2\right) \\ g(z) &= a - az + c\left(z^2 + 2\sqrt{z} - 3z\right) \\ V_S(z) &= f(z)V_{ST} + g(z)V_{S30} \\ V_P(z) &= f(z)V_{PT} + g(z)P\left(V_{S30}\right) \\ \rho(z) &= R\left(V_P\right) \end{aligned} \tag{2.2}$$

where z' is the depth, z_T is the transition (taper) depth, z is a normalized depth used in the following calculations, and $f(z)$ and $g(z)$ are functions defined for formulating the resulting V_P and V_S. V_{ST} and V_{PT} are the S- and P-wave velocities extracted from the velocity model at z_T, respectively, and P and R are the Brocher (2005) V_P scaling law and Nafe-Drake law, respectively. The coefficient a controls the ratio of surface V_S to V_{S30}, and b and c control the overall and near-surface curvature, respectively. The method generates a profile as a function of depth minimally parameterized by V_{S30}, properties at the transition depth and three empirical coefficients only, which greatly simplifies the introduction of the model modifications into the velocity mesh. The coefficients ($a = 1/2$, $b = 2/3$, $c = 3/2$) proposed by Ely *et al*. (2010) are calibrated to match the generic rock profiles of Boore and Joyner (1997) and Magistrale *et al*. (2000).

V_{S30} is one of the key parameters, along with z_T, controlling the profile generated using the method proposed by Ely *et al*. (2010). The V_{S30} values adopted by Ely *et al*. (2010) were

obtained from the geology-based V_{S30} map of Wills and Clahan (2006) for California and the topography-based estimations by Wald and Allen (2007) outside California. Thompson *et al*. (2014) proposed a V_{S30} map for California based on regression kriging to incorporate multiple constraints from geology, topography and site-specific V_{S30} measurements at various spatial scales based on the method by Wills and Clahan (2006), and later updated to the V_{S30} map by Wills *et al*. (2015). This approach is adopted by the US. Geological Survey (Thompson, 2018) for California, which we adopt to calibrate near-surface velocities in CVM-S.

Figure 2.5 shows a comparison of surface V_S values extracted from CVM-S to the V_{S30} values from Thompson (2018) in our model domain. For type B sites, it is clear that surface velocities are unrealistically high compared to the V_{S30} values. This discrepancy motivated the V_S tapering method by Ely *et al*. (2010), which replaces the original velocities from the surface to the transition depth z_T, while leaving velocities below z_T unchanged. Note, that the Ely *et al*. (2010) method does not necessarily maintain low velocities in the original model, which are always overwritten by the calculated profile. For type B sites, where the surface velocities in CVM-S are typically much larger than the corresponding V_{S30} values, this velocity tapering works as intended to lower unrealistically large shallow V_S values. However, for type A sites, the benefits of this method are less clear, as the shallow V_S values in CVM-S are close to, or sometimes smaller than the V_{S30} from Thompson (2018). In addition, the near-surface velocities at type A sites are derived from a combination of detailed well logs and other geotechnical information (Magistrale *et al*., 2000; Small *et al*., 2017), often different and likely more accurate than the result of the Ely *et al*. (2010) GTL.

For the reasons mentioned above, we propose and test the following variant of the Ely *et al*. (2010) method for assigning the shallow velocities in our model domain. We adopt V_{S30} values from the most recent map (i.e., Thompson, 2018), across the entire domain. Between the surface and a specified maximum depth, z_T, we replace the V_S values in CVM-S by Equation (2.2) whenever the former exceeds the latter. Figure 2.6 illustrates the application of our method to the

average type A and type B velocity profiles, respectively. At type B sites, V_S is reduced (relative to original CVM-S values) at all depths above z_T. At type A sites, the effect is more variable. Since CVM-S already includes a low-velocity GTL (from geological measurements and borehole data) down to 350 m in part of California (notice the abrupt discontinuity in Fig. 2.6), the typical type A profile is mostly unaffected when z_T is small (e.g., for the two smallest z_T values, in the case shown in Fig. 2.6). For larger values of z_T, type A sites velocities are typically reduced only for depths between 350 m and z_T. Note that, because we impose Equation (2.2) as an upper bound rather than as an equality, we can apply the method to the CVM-S without explicitly identifying type A and type B sites a priori (e.g., we do not have to worry about Eq. (2.2) inadvertently overwriting low sediment velocities at type A sites, as illustrated by the purple dashed curve in Fig. 2.6).

2.5 SH1D Theoretical Analysis

Before performing computationally expensive 3D numerical simulations, we use a theoretical approach to estimate the threshold depth z_T. We model vertically-incident SH waves in a horizontally-layered halfspace (hereafter referred to as "SH1D" modeling) to obtain a preliminary estimate the effect of the velocity taper. SH1D is widely used in theoretical (e.g., Day, 1996) and numerical (e.g., Thompson *et al*., 2012) analysis of elastic site response.

Figure 2.7 shows the 1D site amplification functions for tapered V_S profiles from CVM-S (shown as FAS ratios of the tapered to untapered case), grouped into type A and type B sites. The various curves indicate the effect of tapering depth z_T on site amplification (in the 1D approximation). As the tapering depth increases, the shallow velocity decreases, generating larger amplification. For type A sites, amplification (i.e., FAS ratio greater than one) is only obtained for z_T larger than 350 m. Amplification is generated below 0.5 Hz and above ~0.8 Hz, with deamplification in between these frequencies. Deeper tapering depths tend to further decrease

near-surface velocities and produce stronger amplification. The narrow band of deamplification appears only for profiles with tapering depth greater than 350 m, where the sharp discontinuity starts to subside. The deamplification band gets narrower as the tapering depth increases, leaving the profiles smoother near 350 m depth. We therefore attribute the deamplification seen in some of the type A sites to the removal of the velocity contrast at 350 m depth. In general, the changes at type A sites are relatively small, with less than 10% amplification or deamplification for tapering shallower than 1000 m. The amplification at type B sites, on the other hand, increases monotonically with the tapering depth, as expected from the pattern of velocity reduction in Figure 2.6. The type B amplifications can be quite large; for example, they exceed a factor of 2 in the 0.5-1.0 Hz range for a taper depth of 1000 m.

We further examined the effects on the resulting synthetics from applying these velocity tapers; we did so by combining the 3D simulations (which used the original, untapered CVM) with the SH1D amplification results, as shown in Figure 2.8. At every station, and for each tapered profile, we calculated the FAS of the 3D simulated acceleration, divided by the FAS of the recorded acceleration, and multiplied by the SH1D amplification of the tapered profile. We then averaged across all sites in type A and B site groups, respectively. As expected, the type A sites show limited effects of superimposing the velocity tapering, and larger z_T generally yields more amplification, with the exception of $z_T < 500$ m for 0.7-1 Hz. Unlike the muted effects of the velocity tapering for type A sites, different tapering depths produce much greater amplification effects for type B sites. Deeper tapering depths generate a favorable fit for 0.2-0.4 Hz, but tend to overpredict above 0.4-0.5 Hz for $z_T >= 750$ m. On the other hand, in the 0.5-1.0 Hz range, taper depths in the range 350 m to 750 m appear more favorable. These estimates from SH1D encourage us to explore tapering depths in the range 350 to 1000 m using 3D simulations in the next section.

2.6 3D Numerical Simulations

We carried out three additional 3D simulations using CVM-S, with z_T of 350 m (default in Ely *et al*., 2010), 700 m, and 1000m, respectively. Figure 2.9 shows the resulting FAS bias for all three components at both type A and B sites. There is a negligible visual difference at type A sites for all components because our velocity tapering method leaves the original low velocities virtually unchanged. On the other hand, these models show significant differences at type B sites, where the original near-surface V_S are deemed too large. Both the 700 m and 1000 m tapering models eliminate the critical underprediction from CVM-S for the two horizontal components. However, between these two models, the 1000 m model produces a better fit below 0.5 Hz while slightly overpredicting above 0.5 Hz for the horizontal components. Effects of the velocity taper are smaller for the vertical component, where the 1000 m model again is superior with a slight underprediction above 0.2 Hz. Thus, the 1000 m velocity tapering model provides the best fit across almost the entire frequency band.

It is helpful to quantify the results using a single goodness of fit (GOF) metric, which we define as the average of the median bias over (a group of) sites:

$$GOF(model, component) = \frac{1}{nfreq} \sum_{i=1}^{nfreq} \text{median}(Bias(frequency_i, site)), \qquad (2.3)$$

where $nfreq$ is the number of discrete frequencies in the FAS calculation. We prefer using the median of the bias over stations to minimize the effects of outliers. Table 2.3 lists the bias for different components and the single GOF value, averaged for the three components, for various tapering models. Resulting biases are -0.22, -0.154, -0.041, and 0.016 (corresponding to amplitude underpredictions of 40%, 30%, 10%, and overprediction of 4%), for taper depths of 0, 350, 700, and 1000m, respectively.

Figure 2.10 shows a map of interpolated horizontal FAS bias for CVM-S and our three

models with tapering depths of 350 m, 700 m, 1000 m. The large basin areas with very low near-surface velocities, including the central Los Angeles and Chino basins, show almost no variability among these models. Despite the fairly large spatial variability, the median FAS ratio in the basins is generally small and insensitive to the tapering depth. More importantly, we see significant improvement of the bias outside of the basins. For example, the Santa Ana mountains (see Fig. 2.1 for location) suffer strong underpredictions in CVM-S, and the GOF improves as the tapering depths increase to 1000 m.

2.7 Discussion and Conclusions

A taper depth z_T of 1000 m provides the largest improvement in FAS bias (as measured by GOF, Eq. (2.3)) for type B sites that we could find using a single generic taper over the region of interest (Fig. 2.1). This value is substantially different than the 350 m value of Ely *et al*. (2010). The spatial distribution of FAS bias in Figure 2.11 suggests that additional improvements may be possible by permitting spatial variations of the V_S tapering. For example, the areas of type B sites with relatively small underprediction remaining in the preferred 1000 m tapering model suggests the need for V_S modification to even larger depths. However, the eastern termination end of the San Gabriel Mountains (see Fig. 2.1 for location) shows underprediction for the 350 m model and overprediction for the 700 and 1000 m models, which indicates the need for tapering with z_T in the 350-700 m range. We also notice a slightly degraded fit at type B sites east of the Chino Basin (see Fig. 2.5 for location). Possible reasons for this degraded fit include the fact that this area features a relatively abrupt separation of regions with low and high velocities right at the boundary, which complicates a fixed, overall tapering depth. In addition, the accuracy of the topography-based V_{S30} estimation in this area may be decreased by relatively high elevation and limited surface topographic slopes, which may induce less accurate topography-based V_{S30} estimation.

The optimal tapering depth may also be affected by the anelastic attenuation. We parameterize anelastic attenuation as a function of local V_S, a commonly accepted procedure for ground motion estimation (e.g., Olsen *et al.*, 2003; Savran and Olsen, 2019; Lai *et al.*, 2020). Our choice of the relation $Q_S = 0.1V_S$ (for V_S in m/s; $Q_P = 2Q_S$) relation is based on the results from modeling the 2008 M_w 5.4, Chino Hills, earthquake by Savran and Olsen (2016). However, to examine whether the overprediction in the valleys (underpredictions in the mountain areas) diminishes with lower (higher) Q, we tested two additional models: (1) CVM-S with z_T of 1000 m using $Q_S = 0.05V_S$ and (2) CVM-S with z_T of 350 m with $Q_S = 0.15V_S$ (see Fig. 2.11). Although reducing the overprediction in the valleys, the $Q_S = 0.05V_S$ model reduces the FAS below the levels observed in the data as distance increases. In addition, the $Q_S = 0.05V_S$ model increasingly degrades the fit on the vertical component at type A sites (see Table 2.3), as the frequency increases toward 1 Hz (see Fig. A2.1) and likely beyond. On the other hand, the $Q_S = 0.15V_S$ model increases the FAS, mostly above the basins and provides little improvement at type B sites. For these reasons, we prefer the $Q_S = 0.1V_S$, $Q_P = 2Q_S$ model.

Figure 2.12 compares three-component FAS and cumulative kinetic energy (defined as $\int_0^T v(t)^2 dt$, where $v(t)$ is particle velocity as a function of time and T is duration) between the records and synthetics for a subset of 6 out of 39 type B sites in our model domain. The 6 sites are selected throughout the domain, representing the broad range of fit between synthetics and data. Both metrics show amplification on the horizontal components from the velocity tapering that reduces the shallow velocities. The amplifications on the vertical components, however, generally increase less with the tapering depths (e.g., sites CIQ0022 and CISDD), indicating that the horizontal components are more sensitive to site amplification effects, in agreement with previous studies (e.g., Bonilla *et al.*, 1997; Gülerce and Abrahamson, 2011). At almost all type B sites, CVM-S underpredicts the FAS below 1 Hz compared with the records, while the tapered models mitigate the underprediction. Note, however, that different sites show very different peak amplification frequencies, which complicates the definition of a single, domain-wide z_T.

For example, sites CIQ0022 and CE13080 have close surface V_S (see Table 2.2), but CIQ0022 shows significant underprediction and CE13080 shows overprediction for the 1000 m tapering model. Also, the low-frequency (0.2 - 0.3 Hz) FAS peaks present at site CIIPT, CISTG, CIQ0022 and CISDD are likely due to other local site effects. Figure A2.2 shows the FAS bias at all type B sites from different models as a function of surface V_S. All models show the trend that the bias increases with surface V_S, indicating that sites with larger surface V_S need relatively weaker velocity reduction or shallower velocity tapering. In summary, our method introduces first-order improvement in overall type B site amplification, while additional fine-tuning of local amplification requires additional work. Such analysis should include additional GOF metrics, as well as using simulations of multiple events.

Another family of velocity models for southern California, CVM-H, was originally developed by Süss and Shaw (2003) and later improved by Plesch *et al*. (2007), Plesch *et al*. (2009), and Plesch *et al*. (2017) with incorporation of the tomography results from Tape *et al*. (2009) and Tape *et al*. (2010). CVM-H supports the option to include the Ely *et al*. (2010) GTL, with a default transition depth of 350 m, across the entire domain. Taborda *et al*. (2016) performed 3D deterministic simulations of small earthquakes in California and showed that CVM-S consistently provides overall superior fit to records as compared to CVM-H for frequencies up to 1 Hz, with or without the Ely *et al*. (2010) GTL (z_T of 350 m). They also noted that the addition of the Ely *et al*. (2010) GTL generally improved the GOF. Fig. 2.13 shows a comparison of V_S profiles from CVM-S and CVM-H at the recording stations located on type B sites. It is clear that the most poorly constrained site profiles from CVM-S and CVM-H that include the Ely *et al*. (2010) GTL with a transition depth of 350 m are similar. We therefore expect that CVM-H can benefit from a deeper tapering depth (~1000 m) at type B sites, similar to what provided significant improvement for CVM-S.

In Figure 2.14, we uniformly sampled 300 locations in California and queried their velocity profiles from CVM-S and CVM-H. The majority of the type A sites are located in the

west and south and most type B sites in the east. Similar to our simulation domain (Fig. 2.3), the state-wide sampling shows that most type B sites lack sufficient resolution in the top 1000 m, likely requiring calibration of the shallow velocities. For this reason, the application of our proposed tapering depth will likely improve the accuracy of ground motion simulations in other regions of California.

While our analysis was limited to frequencies below 1 Hz, the proposed tapering of the near-surface V_S structure for type B sites in CVM-S will benefit future ground motion predictions to even higher frequencies. As the available computational resources increase, ground motion simulations can be extended to higher frequencies, where model features such as topography, small-scale crustal heterogeneities and frequency-dependent attenuation play an increasingly large role. However, unless the underlying velocity model is sufficiently accurate, these model features may cause trade-offs in the results. For example, unrealistically large near-surface velocities, if present, may trade off with attenuation quality factors to compensate for the underprediction. To further isolate shallow low-velocity effects and examine the efficacy of our velocity tapering method, higher-frequency simulations for multiple earthquakes that resolve the velocity structure in different directions and paths are demanded, along with validations via more ground motion metrics.

Data and Resources

The UCVM program used to extract velocity meshes can be obtained from SCEC on https://github.com/SCECcode/UCVMC (last accessed 12/2020). The simulations were performed on Summit at the Oak Ridge Leadership Computing Facility in Tennessee. Most of the data-processing work was done using Python and the Generic Mapping Tools package (https://www.generic-mapping-tools.org, last accessed 04/2021).

Acknowledgements

This research was supported through the U.S. Geological Survey External Program (award #G19AS00021), as well as the Southern California Earthquake Center (SCEC; Contribution Number xx). SCEC is funded by the National Science Foundation (NSF) Cooperative Agreement EAR-1600087 and the U.S. Geological Survey (USGS) Cooperative Agreement G17AC00047. We thank Robert W. Graves for providing the source models and Fabio Silva for providing the station records of the 2014 La Habra earthquake.

Chapter 2, in full, is a reformatted version of a paper currently being prepared for submission for publication: Hu, Z., Olsen, K.B., and Day S.M. (2021). Calibration of the Near-surface Seismic Structure in the SCEC Community Velocity Model Version 4. The dissertation author was the primary investigator and author of this paper.

Tables and Figures

Table 2.1: Simulation parameters used for the deterministic ground motion simulations of the 2014 La Habra earthquake.

Domain	
Length	147.840 km
Width	140.400 km
Depth	58.000 km
Northwest corner	-118.0154409, 34.8921683
Southwest corner	-118.9774168, 33.9093124
Southeast corner	-117.7401908, 33.0695780
Northeast corner	-116.7729754, 34.0429241
Spatial resolution	
Maximum frequency	5 Hz
Minimum V_S	500 m/s
Points per minimum wavelength	5
Grid discretization	20/60 m
Number of cells	25,092,587,520
Number of GPU processors	960
Wall-clock time	1.5 hr
Temporal resolution	
Time discretization	0.001 s
Simulation time	120 s
Number of timesteps	120,000

Table 2.2: Type B site information

site name	Lon (°)	Lat (°)	R_{hypo} (km)	Surface V_S (m/s)	V_{S30} (m/s)	Elevation (m)
CISRN	-117.79	33.83	17.53	1908.44	351.90	212.32
CIQ0029	-117.75	33.73	27.87	2163.35	293.50	94.84
CE13220	-117.75	33.68	31.99	2090.55	351.90	70.28
CISTG	-117.77	33.66	32.61	1980.29	351.90	47.53
CE13441	-117.78	33.66	32.74	1934.54	447.28	45.87
CIPLS	-117.61	33.80	33.36	2234.93	351.90	1215.81
CE24399	-118.06	34.22	36.28	2597.01	710.10	1724.74
CIMWC	-118.06	34.22	36.28	2596.96	710.10	1727.73
CIQ0034	-117.66	33.69	36.56	2289.27	293.50	324.50
CIQ0009	-117.71	33.61	41.12	1885.40	351.90	106.23
CIQ0022	-117.50	33.77	43.52	2425.56	351.90	362.41
CIBFS	-117.66	34.24	44.01	2270.57	710.10	1301.77
NP707	-117.45	33.85	45.57	2913.91	293.50	407.88
CIQ0026	-117.57	33.64	45.83	2529.13	228.20	375.70
CIQ0005	-117.77	33.53	46.38	1961.18	710.10	42.60
CISDD	-117.66	33.55	48.13	1923.53	351.90	122.19
CIQ0038	-117.43	33.73	51.38	2926.22	293.50	416.98
CE13916	-117.32	33.90	56.71	2893.67	518.90	522.59
CITA2	-117.68	34.38	56.88	2381.10	351.90	2258.42
CILPC	-117.55	34.32	56.89	1970.65	351.90	1344.56
CICJM	-117.42	34.27	61.30	2404.97	228.20	1615.85
CE13080	-117.25	33.97	63.28	2607.63	518.90	542.10
CE23958	-117.65	34.44	63.85	2093.92	447.28	1236.29
CIQ0035	-118.20	34.47	66.03	2428.36	710.10	864.55
CE13096	-117.27	33.70	66.46	4105.94	518.90	426.84
CE23292	-117.54	34.43	66.98	1807.64	710.10	1211.92
CIIPT	-117.29	34.20	67.45	2552.72	228.20	945.86
CIPER	-117.21	33.86	67.67	2880.41	518.90	467.03
CIQ0028	-117.18	33.83	70.30	3197.89	518.90	461.22
CIQ0013	-118.06	34.54	70.31	2620.60	518.90	859.30
CE13927	-117.17	33.92	70.31	2377.65	351.90	494.08
CISOF	-117.56	33.37	70.35	2333.99	351.90	16.09
CILUG	-117.37	34.37	72.20	2080.27	513.69	1136.43
CISBPX	-117.24	34.23	73.34	2310.65	293.50	1872.13
CE13924	-117.13	33.75	76.98	4161.26	351.90	486.31
CIQ0049	-117.13	34.20	80.69	2184.64	710.10	1661.03
CIBBS	-116.98	33.92	88.03	1639.46	518.90	782.79
CE12919	-116.97	33.93	88.77	1559.19	518.90	795.50
CIQ0020	-116.95	33.96	90.66	1588.16	468.40	859.36

Table 2.3: Average FAS biases for all three components for various models.

Model	Type A sites				Type B sites			
	East-west	North-south	Vertical	**Average**	East-west	North-south	Vertical	**Average**
CVM-S*	0.034	0.044	0.009	**0.029**	-0.277	-0.261	-0.136	**-0.225**
CVM-S + 350 m*	0.040	0.048	0.009	**0.033**	-0.171	-0.153	-0.138	**-0.154**
CVM-S + 700 m*	0.055	0.062	0.018	**0.045**	-0.020	-0.015	-0.087	**-0.041**
CVM-S + 1000 m*	0.065	0.073	0.020	**0.053**	0.048	0.055	-0.055	**0.016**
CVM-S + 350 m + $Q_S = 0.05V_S$†	-0.039	-0.027	-0.091	**-0.052**	-0.064	-0.052	-0.156	**-0.091**
CVM-S + 1000 m + $Q_S = 0.15V_S$†	0.085	0.091	0.061	**0.080**	-0.135	-0.120	-0.105	**-0.120**

* $Q_S = 0.1V_S$; $Q_P = 2Q_S$

† $Q_P = 2Q_S$

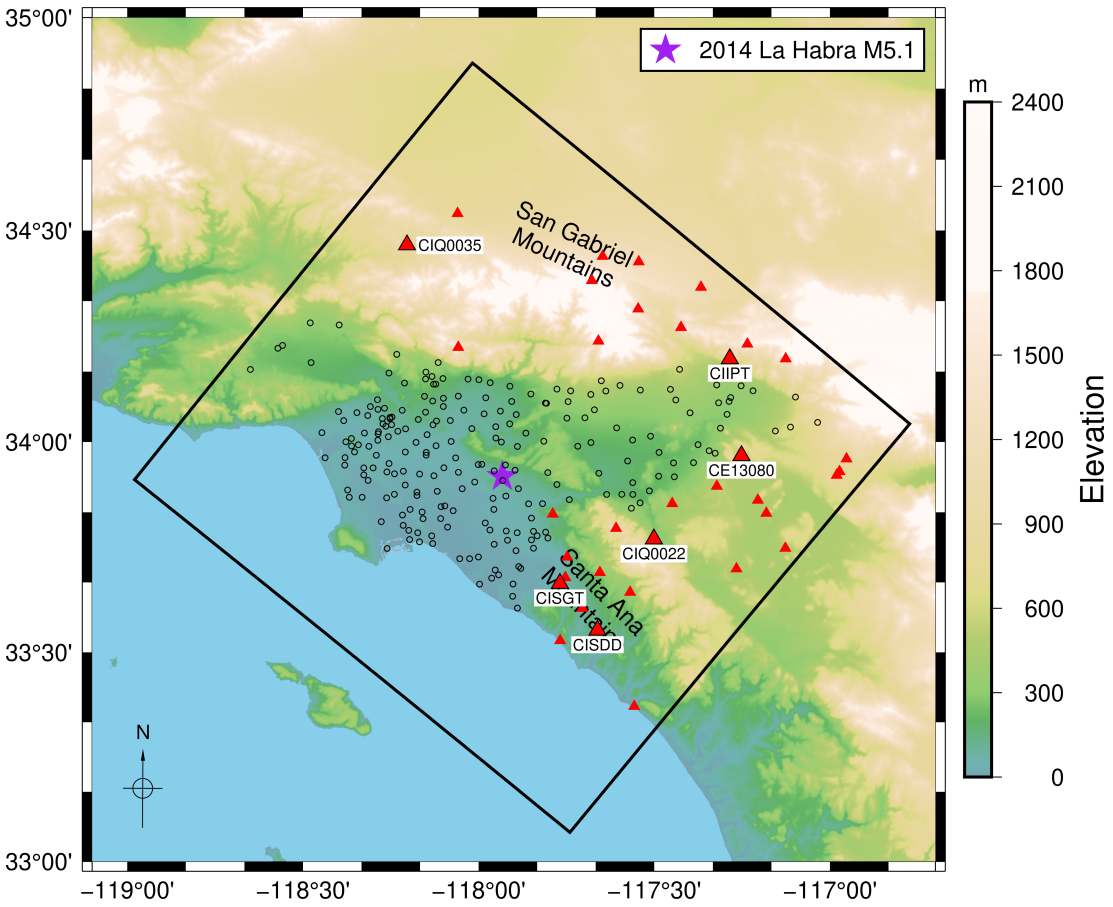

Figure 2.1: Simulation region for the La Habra event and locations of 259 strong ground motion stations (circles represent type A sites with surface V_S < 1000 m/s and red triangles represent type B sites with surface V_S >= 1000 m/s). The following maps (Figs. 2.5, 2.10 and 2.11) will only show the simulated domain (black rectangle), whose dimensions and geographical coordinates are listed in Table 2.1, The named sites (triangles with black edge) are selected for further comparisons in Figure 2.12. The star depicts the epicenter of the La Habra earthquake.

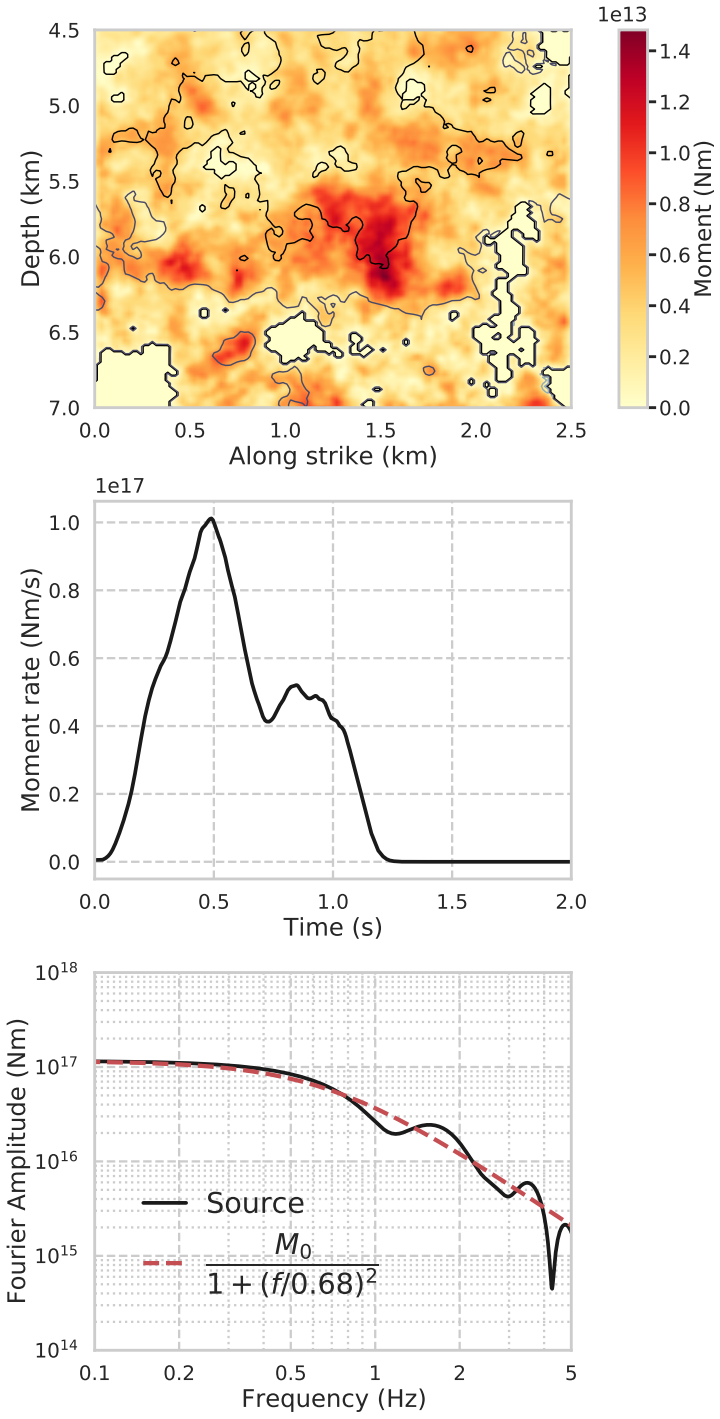

Figure 2.2: Description of the selected source model used in this study. (a) Moment distribution (shading). The contours represent rupture time at a 0.4 s interval starting from 0. (b) and (c) represent the sum of the moment rates for all subfaults and the Fourier amplitude spectrum, respectively. A Brune-type ω^{-2} decay source (Brune, 1970) that fits the source spectrum is plotted for reference.

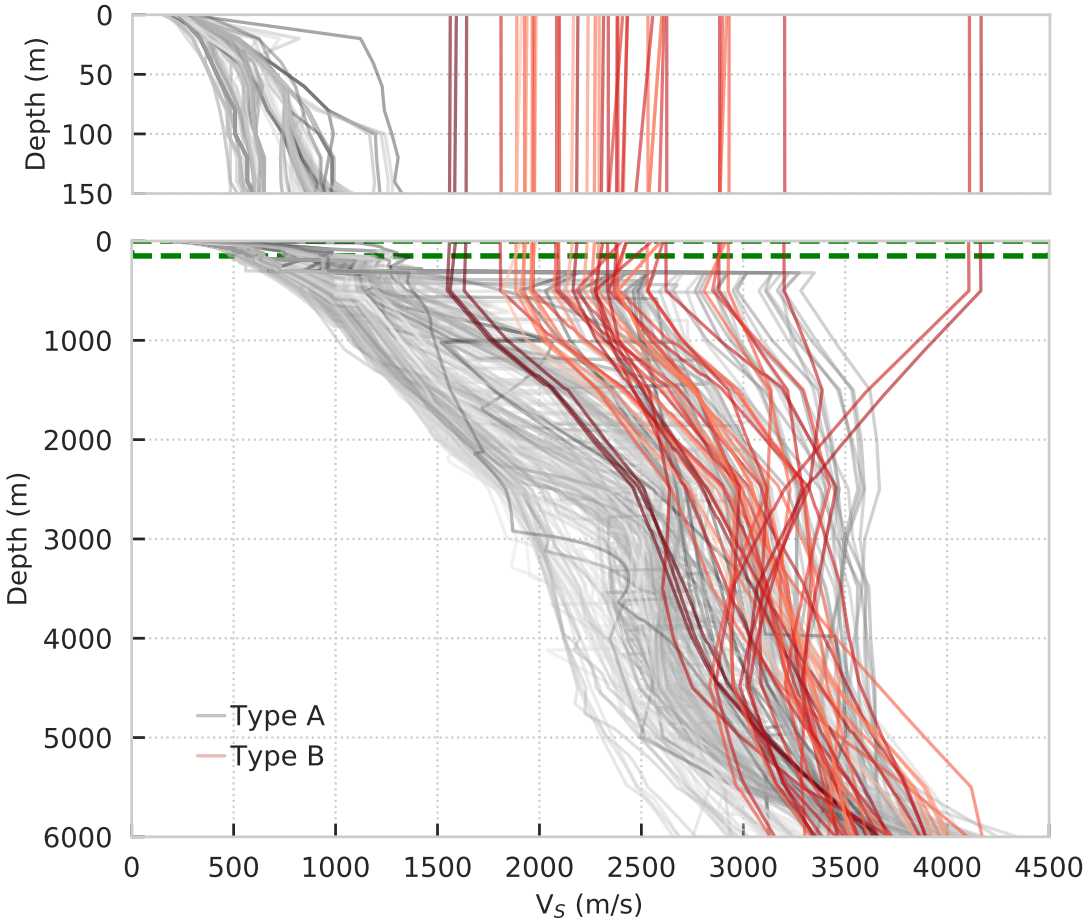

Figure 2.3: (a) Top 150 m and (b) 0-4000 m V_S profiles at the 259 stations. The black and red curves represent type A (surface $V_S < 1000$ m/s) and type B (surface $V_S >= 1000$ m/s) sites, respectively. The darker curves denote the sites with farther distance from the source.

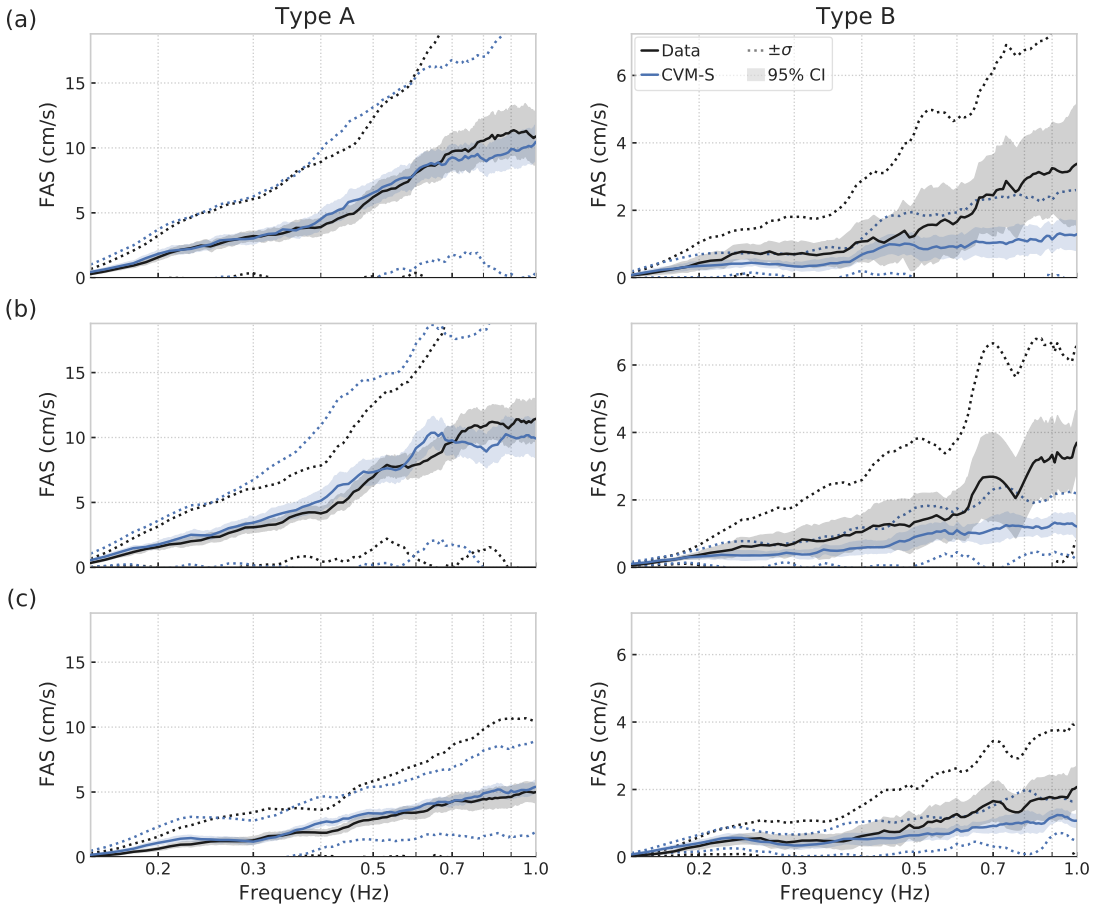

Figure 2.4: FAS derived from the records (black) and CVM-S (blue) for the (a) east-west component, (b) north-south component and (c) vertical component. The left and right columns represent type A and B sites, respectively. The solid line is the median of FAS over the site group, the narrow band is the 95% confidence interval of the median, and the dashed lines depict the standard deviation centered at the median.

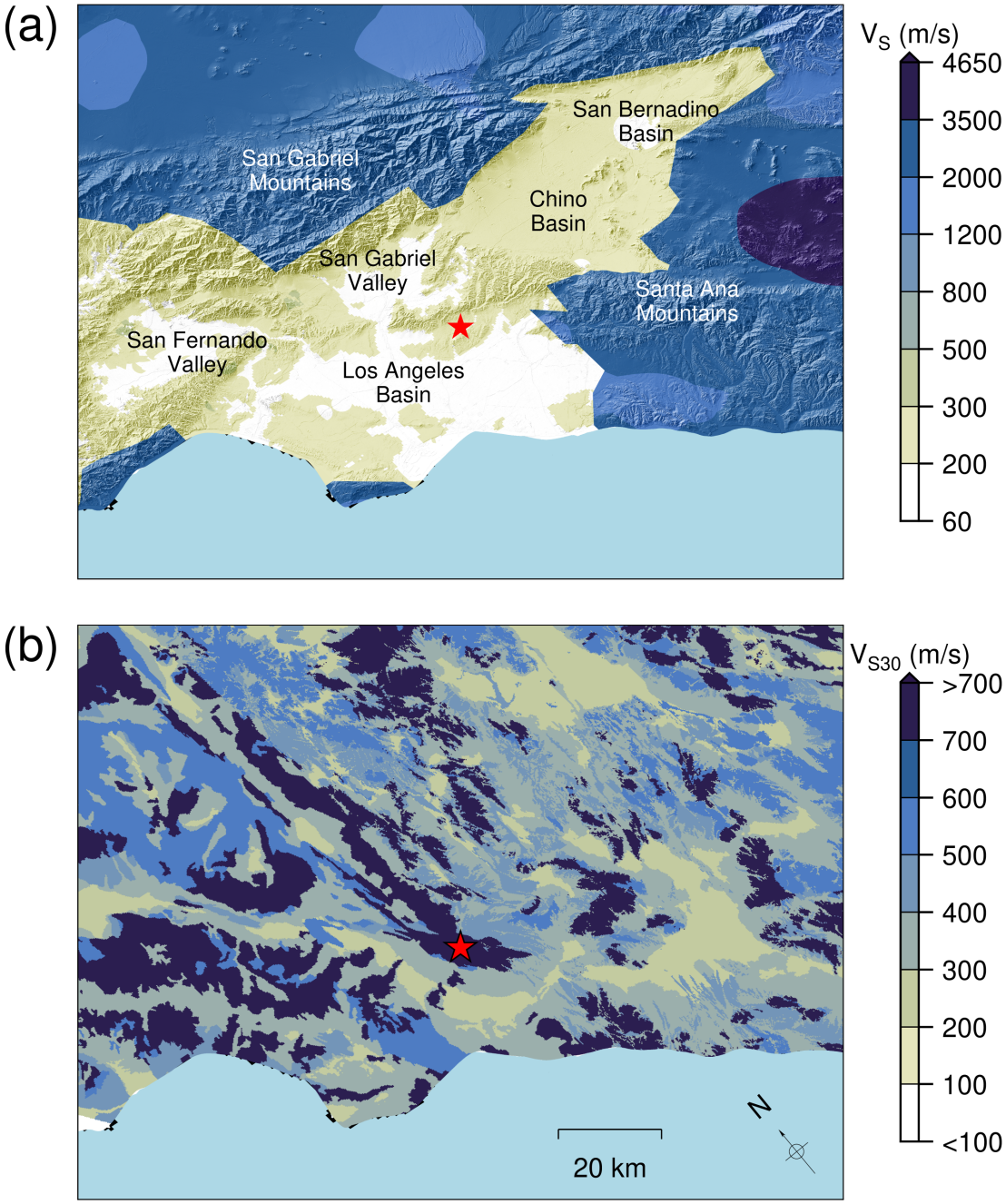

Figure 2.5: (a) Surface V_S extracted from CVM-S, and (b) V_{S30} from Thompson (2018) in our model domain (values in the left bottom corner are not available). The star denotes the epicenter.

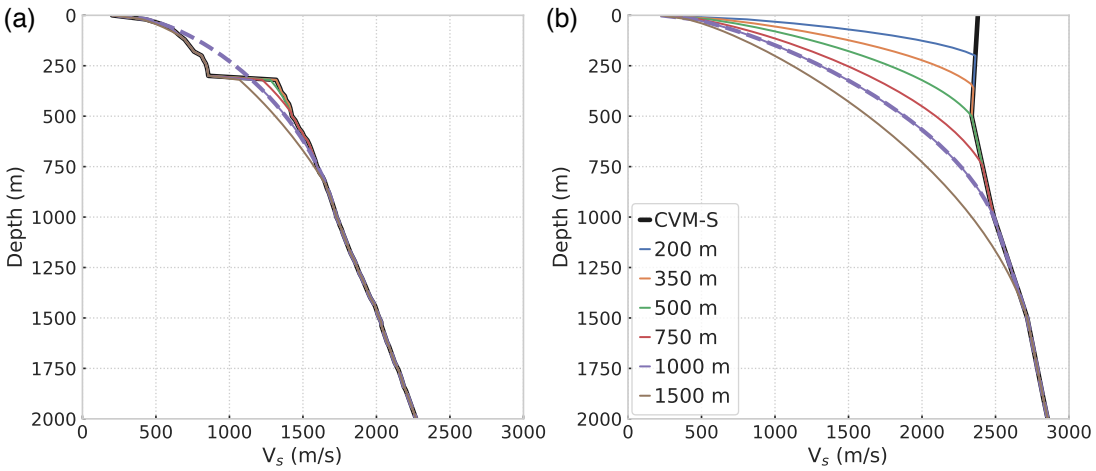

Figure 2.6: Representative V_S profiles for (a) type A sites and (b) type B sites from CVM-S. The thick black curves depict the averaged velocity profiles for all 220 type A and 39 type B sites directly extracted from CVM-S. The thin lines show the V_S profiles resulting from our proposed method for different z_T depths between 200 m and 1500 m. The dashed curve shows the V_S profile calculated using the Equation (2.2) tapers from our preferred z_T of 1000 m (note that because the tapers are applied as upper bounds to V_S, they typically only affect the type A V_S structure at depths exceeding 350m, where the GTL in CVM-S ceases and causes the abrupt discontinuity).

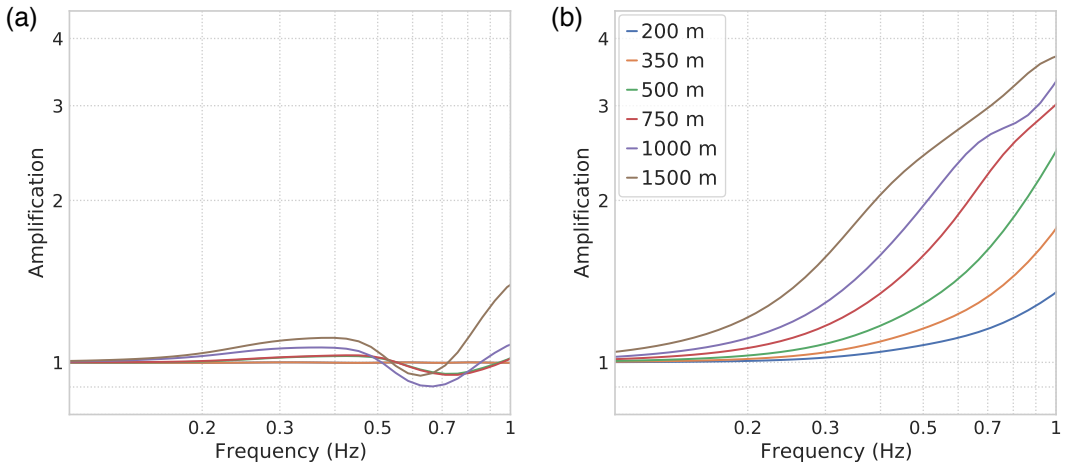

Figure 2.7: The SH1D response for the refined profiles using various z_T depths for average (a) type A and (b) type B sites, divided by the response obtained with the averaged type A and type B profiles from CVM-S.

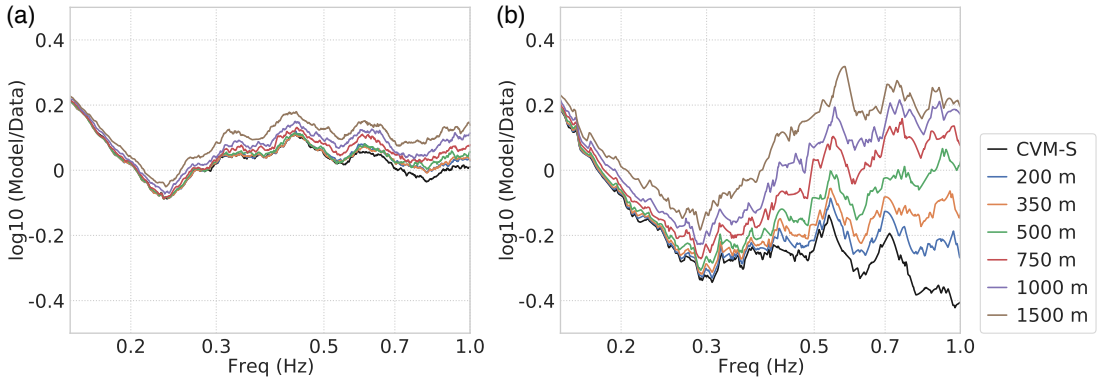

Figure 2.8: Bias of FAS for the two horizontal components averaged over all (a) type A and (b) type B sites for CVM-S at all 259 stations, superimposed with the corresponding SH1D response. The black curves denote CVM-S and other labeled curves represent various tapering depths using SH1D results.

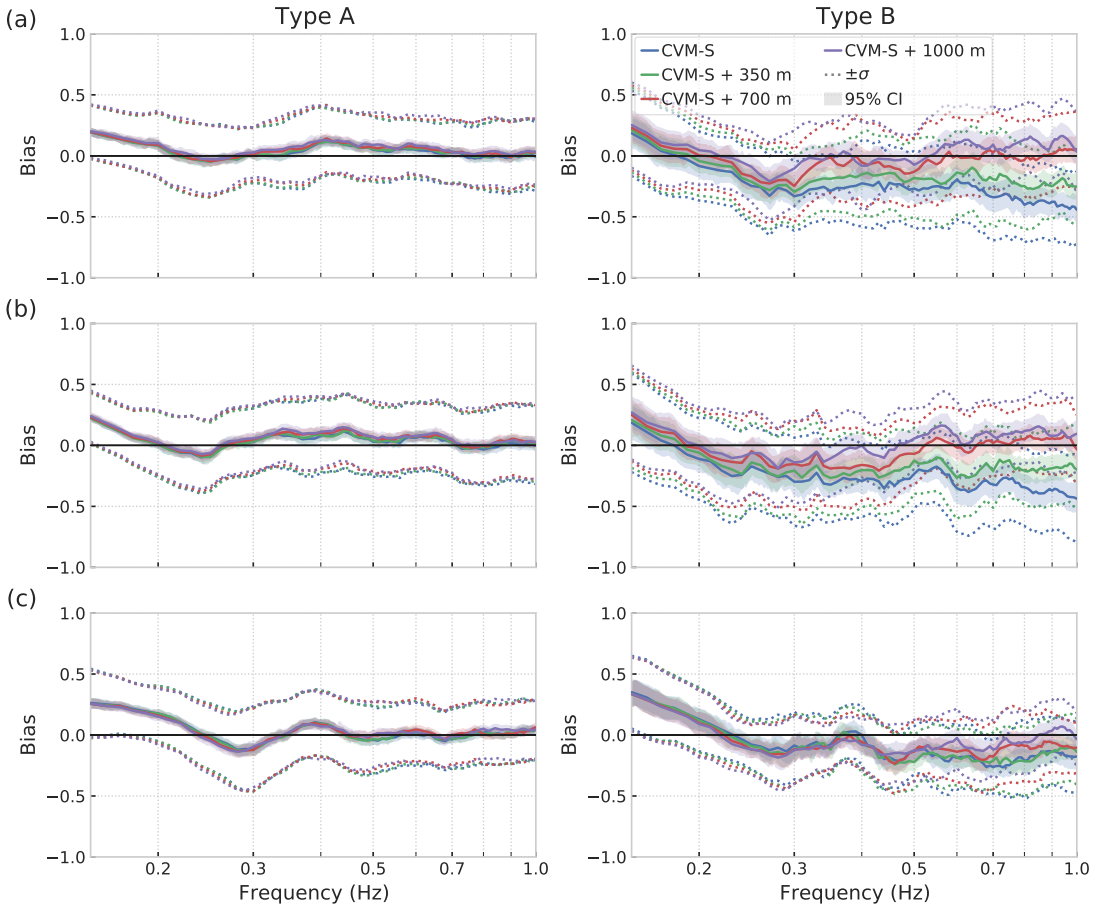

Figure 2.9: Bias of FAS on the (a) east-west, (b) north-south and (c) vertical components, calculated from 3D simulations in CVM-S and with tapering depth of 350 m, 700 m, and 1000 m. A positive (negative) value depicts overprediction (underprediction). The left (right) column shows type A (B) sites. The solid line is the median of FAS, where the narrow band is the 95% confidence interval of the median, and the dashed lines depict the standard deviation centered at the median.

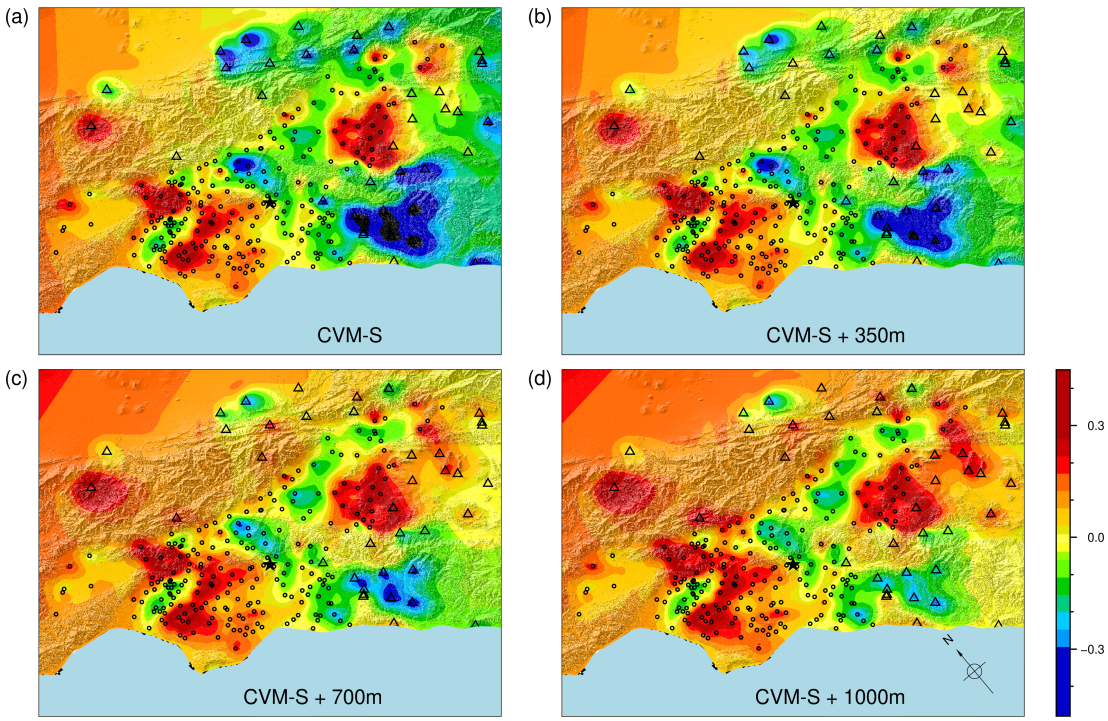

Figure 2.10: Maps of interpolated log10-based FAS bias between four 3D models and data: (a) CVM-S, and CVM-S with tapering depth of (b) 350 m, (c) 700 m and (d) 1000 m, calculated from the synthetics and records at 259 stations. The warm (cool) colors represent overprediction (underprediction). The circles (triangles) depict type A (B) sites. Note the log10-based colorbar.

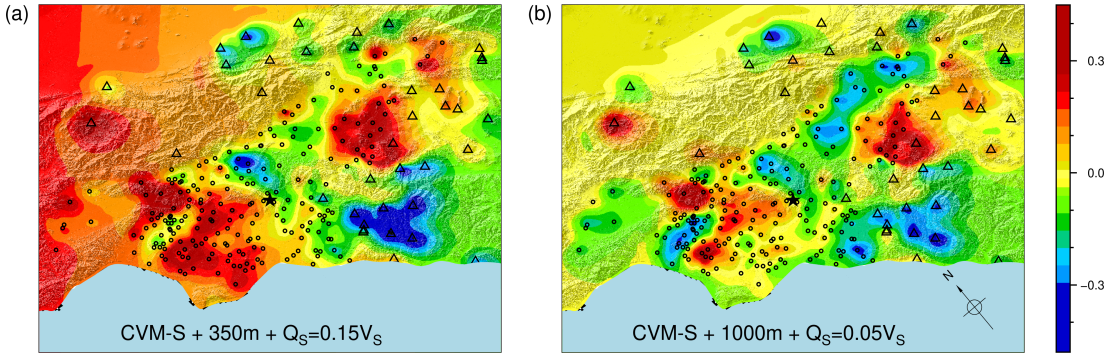

Figure 2.11: Maps of interpolated log10-based FAS bias for two 3D CVMs and data. (a) CVM-S with velocity tapering depth of 350 m and $Q_S = 0.15V_S$, and (b) CVM-S with velocity tapering depth of 1000 m and $Q_S = 0.05V_S$. Warm (cool) colors represent overprediction (underprediction). Circles depict type A sites and triangles show type B sites.

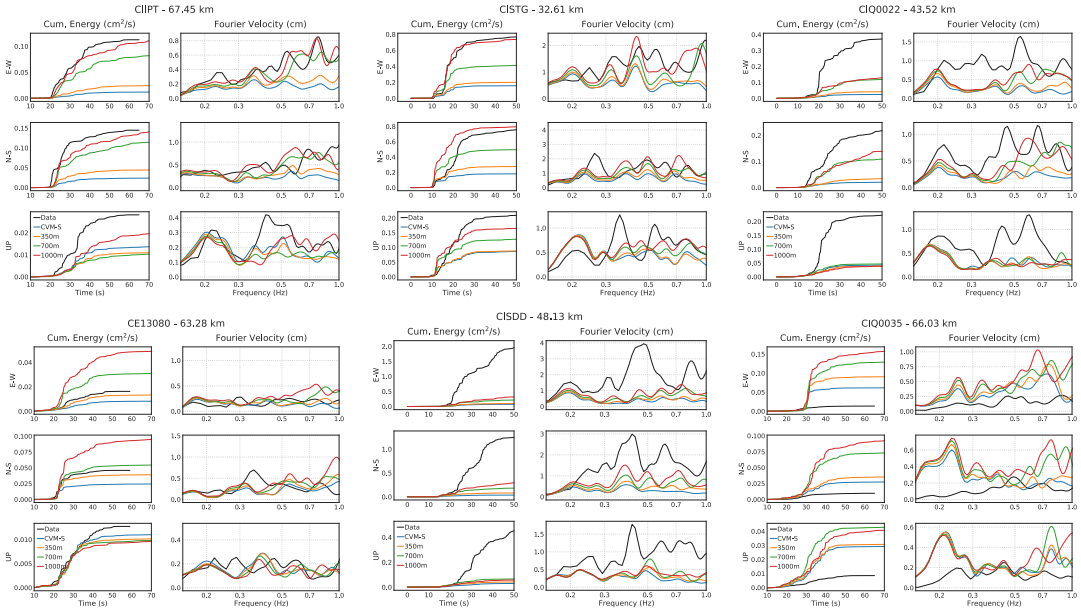

Figure 2.12: Cumulative kinetic energy and Fourier velocity spectra at six type B sites. The subtitles show the names of the sites and their hypocentral distance.

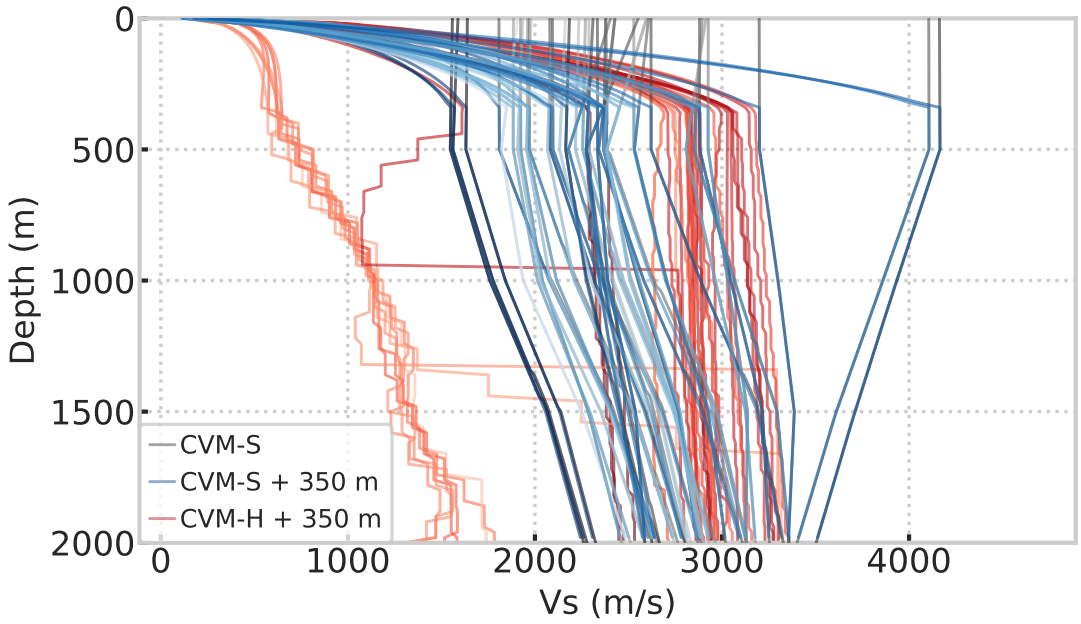

Figure 2.13: Type B site V_S profiles from CVM-S, and CVM-S and CVM-H with (default) Ely *et al*. (2010) GTL taper depth of 350 m.

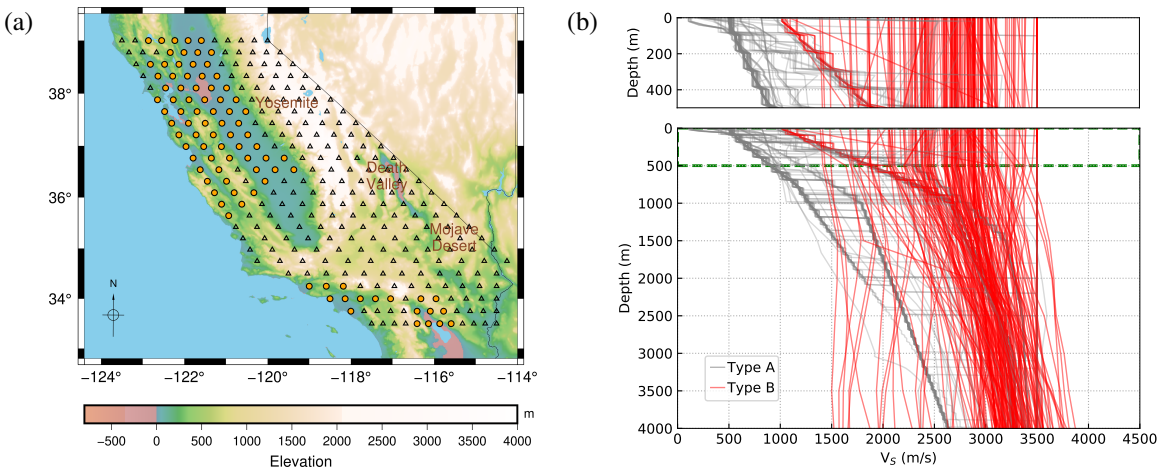

Figure 2.14: (a) V_S profile sample locations in California. Circles denote type A sites and triangles denote type B sites, and (b) extracted V_S profiles. The top panel zooms into the top 500 m.

Appendix

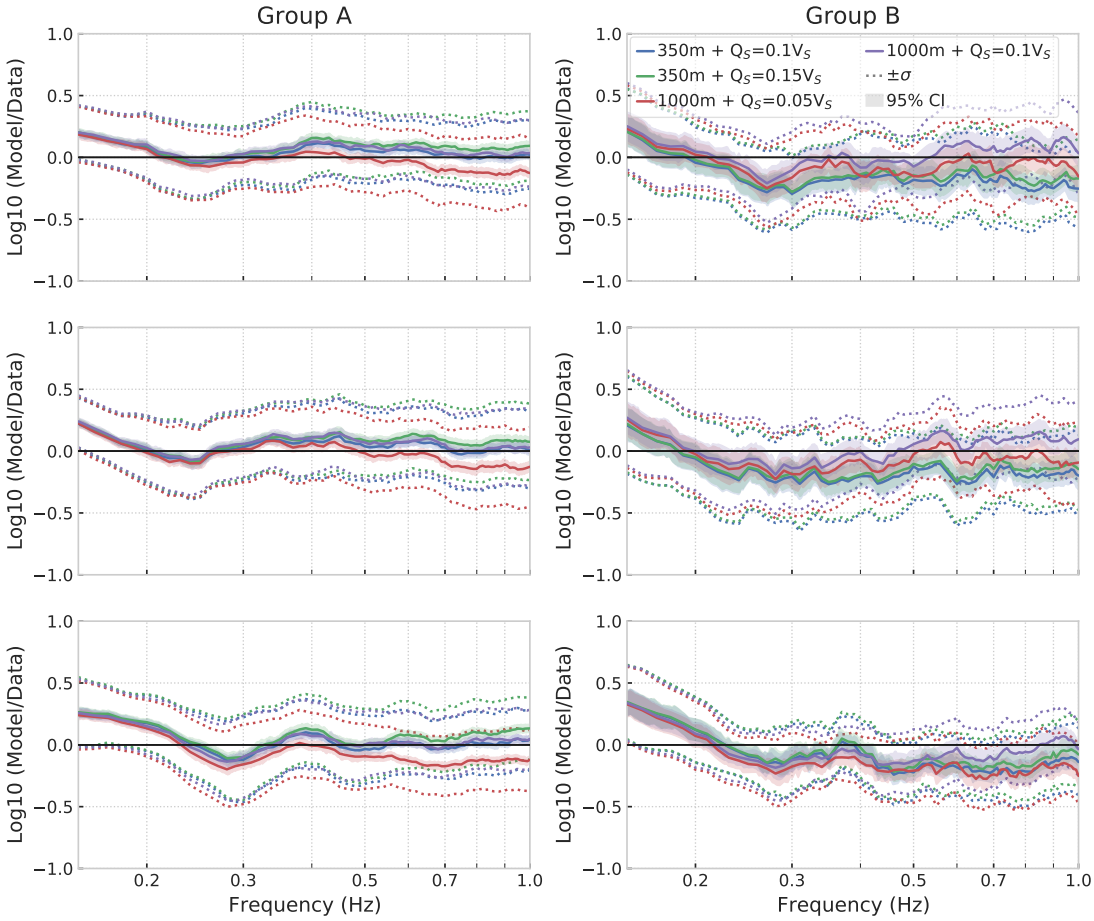

Figure A2.1: Bias of FAS of the (a) east-west, (b) north-south and (c) vertical component, calculated from 3D simulations in CVM-S with V_S tapering depths of 350 m and 1000 m along with attenuation models $Q_S = 0.05V_S$, $Q_S = 0.1V_S$, and $Q_S = 0.15V_S$. A positive (negative) value means overprediction (underprediction). The left (right) columns show type A (B) sites. The solid line is the median of FAS, where the narrow band is the 95% confidence interval of the median, and the dashed lines depict the standard deviation centered at the median.

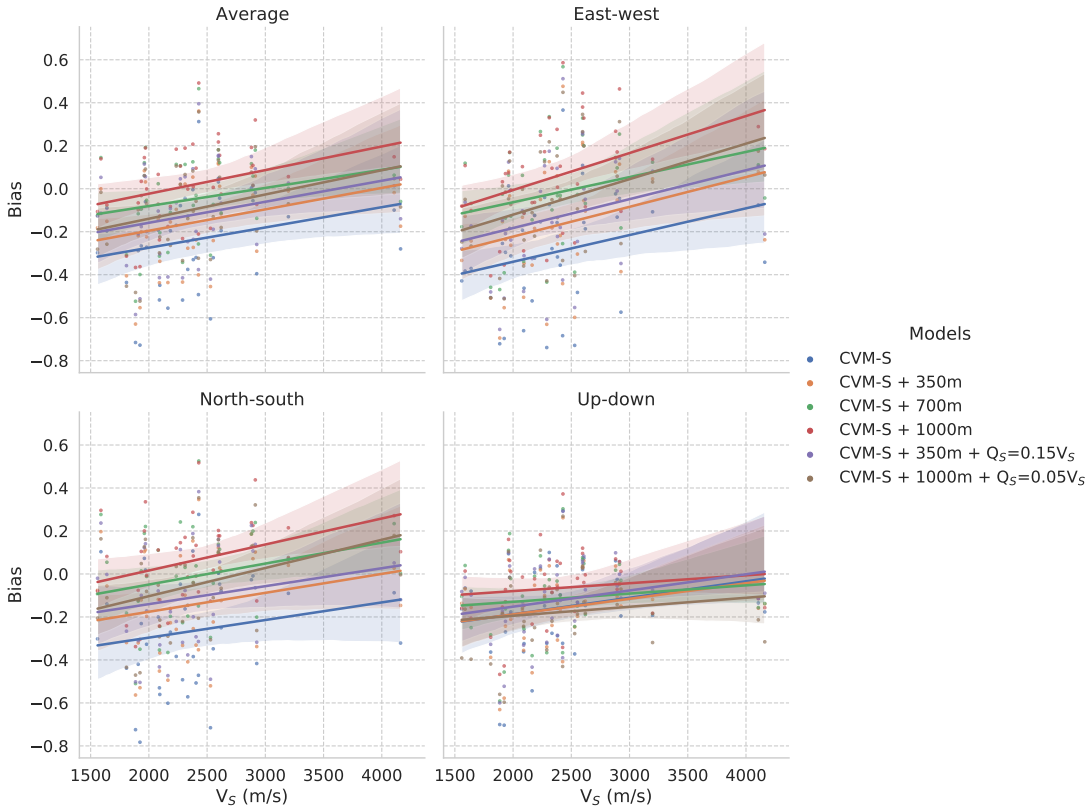

Figure A2.2: Averaged FAS bias for frequencies between 0.15-1 Hz at poorly constrained sites plotted as a function of site surface V_S for (a) three-component average, (b) east-west, (c) north-south and (d) vertical components. The shades represent 95% confidence intervals estimated using bootstrap.

Chapter 3

0-5 Hz Deterministic 3D Ground Motion Simulations for the 2014 La Habra, California, Earthquake

We have simulated 0-5 Hz deterministic simulations for the 2014 M_w 5.1 La Habra, CA, earthquake in a mesh from the Southern California Earthquake Center Community Velocity Model Version S4.26-M01 with a finite-fault source. Our simulations include statistical distributions of small-scale crustal heterogeneities (SSHs), frequency-dependent attenuation $Q(f)$, surface topography, and effects of near-surface low velocity material. Strong motion data at 259 sites within an 148 km by 140 km area are used to validate our simulations. Accuracy of the velocity model, particularly the near-surface low velocities and 3D structure, controls the resolution to which the anelastic attenuation can be determined. We examine parameterizations of low-frequency ($<$1 Hz) shear-wave Q values ($Q_{S,0}$) as a function of shear-wave speed (V_S), where a faster increase of $Q_{S,0}$ for larger V_S generally improves the fit to the seismic data. Power-law exponents γ for high-frequency ($>$1 Hz) frequency-dependent shear-wave Q_S expressed as $Q_S = Q_{S,0} f^{\gamma}$ larger than about 0.6 appear inconsistent with the seismic records. Topography, and

to a lesser extent SSHs, predominantly decrease the peak velocities and significantly increase the duration, by energy redistribution. A weathering layer with realistic near-surface low velocities is found to enhance the amplification at mountain peaks and ridges. Our results show that the effects of, and trade-offs between, near-surface low-velocity material, topography, SSHs and $Q(f)$ become increasingly important as frequencies increase.

3.1 Introduction

It is the ultimate goal for ground motion modelers to deliver their results to engineers and see their work used in applications beneficial for society, such as structural design. This is particularly useful in cases of infrequent observations, such as for large magnitude events at short distances from the fault, where simulations may provide a viable alternative to data. Deterministic ground motion predictions, including features such as three-dimensional (3D) velocity structure and frequency-independent anelastic attenuation are now routinely produced for frequencies up to about 1 Hz with generally satisfactory fit to recorded data (e.g., Graves, 1996; Olsen *et al*., 2009; Roten *et al*., 2012). These simulations have proved to be useful in public earthquake emergency response and seismic hazard management (e.g., the SHAKEOUT scenario; Jones *et al*., 2008), and complementing empirical ground motion prediction models in regions with sparse stations coverage (e.g., Day *et al*., 2008).

While the results of these low-frequency simulations are promising, structural engineers need ground motions with signal content up to 5 Hz and higher for design purposes. Hybrid techniques, combining deterministic low-frequency and stochastic high-frequency signals (e.g., Olsen and Takedatsu, 2015; Graves and Pitarka, 2016) can be used to generate synthetic seismograms with frequency content up to 10 Hz and higher. However, simulating both the lower and higher frequency content using a deterministic approach has the potential to lower part of the epistemic uncertainty in the resulting ground motion estimates. In this study we investigate the feasibility

of increasing the highest frequency for deterministic ground motion predictions to 5 Hz, using simulations and data for the 2014 M_w 5.1 La Habra, CA, earthquake. The La Habra event was chosen due to an abundance of records available in the greater Los Angeles area, while ground motions can be considered linear due to its relatively small magnitude.

As frequencies increase above about 1 Hz, features with increasingly small length scales become important to realistically predict deterministic ground motions. For example, small-scale complexity of both the source and surrounding media, on the order of 10-100s of meters, is expected to increasingly affect ground motion predictions at higher frequencies. Frequency-independent anelastic attenuation, often chosen as proportional to the local velocity structure (e.g., Graves and Pitarka, 2010) is usually a good approximation for lower frequencies (up to ~1 Hz; e.g., Liu *et al*., 1976; Fehler *et al*., 1992). However, models of frequency-independent anelastic attenuation appear to be inconsistent with seismic records at higher frequencies where regional studies indicate that larger Q values may be more accurate (e.g., Withers *et al*., 2015). Finally, ground motion simulations often artificially truncate the lowest near-surface velocities due to computational limitations, which may be a reasonable approximation for lower frequencies (e.g., Olsen *et al*., 2003). However, stronger effects from this near-surface material emerge as frequencies increase and wavelengths decrease (e.g., Pitarka and Ichinose, 2009; Imperatori and Mai, 2013). Here, we quantify the effects of all of these features in our 3D simulations of the La Habra event.

In southern California, two state-of-the-art 3D velocity models, namely the Community Velocity Models (CVM) versions S and H, have been developed through the Southern California Earthquake Center (SCEC). These CVMs have been validated against ground motion data in a series of studies (e.g., Taborda *et al*., 2016; Savran and Olsen, 2019; Lai *et al*., 2020). Ely *et al*. (2010) proposed a method to calibrate the near-surface material based on estimates of the time-averaged velocity in the upper 30 m (V_{S30}), and later improved by Hu *et al*. (2021b), specifically for sites with poor constraints for shallow rock site velocities. Here, we use the SCEC

CVM-S with the update by Hu *et al*. (2021b).

The effects of irregular surface topography on ground motions also play an increasingly large role as frequencies increase (e.g., Liu *et al*., 2020). In recent studies, theoretical and numerical methods have helped clarify the interaction between seismic waves and topography (mainly scattering and trapping of waves, e.g., Imperatori and Mai, 2015; Takemura *et al*., 2015; Rodgers *et al*., 2018), as well as describing the characteristic effects on ground motions. Some of the most notable effects of topography found by these studies are listed in the following. (1) Amplification tends to occur at the top of relatively steep slopes for waves with comparable wavelength to the size of the topographic features; on the other hand, deamplification tends to occur at low-elevation areas (Trifunac and Hudson, 1971; Boore, 1972; Spudich *et al*., 1996; Bouchon and Barker, 1996; Assimaki *et al*., 2005). Amplification can range up to a factor of 10 or more between the crest and base of a topographic feature (Davis and West, 1973; Geli *et al*., 1988; Umeda *et al*., 1987; Gaffet *et al*., 2000). (2) The amplification at mountain tops is systematically larger for incident S compared with P waves, with diminishing effect when the slope decreases or the incidence angle increases (Bard, 1982). (3) Body and surface waves are strongly scattered by irregular topography, thus reducing ground motion amplitudes while prolonging the shaking duration (Sánchez-Sesma and Campillo, 1991; Lee *et al*., 2009a). (4) Topography tends to disrupt the coherency of high-frequency ground motion and thereby distorting the S-wave radiation pattern (Imperatori and Mai, 2015). Notably, 3D models of the topography are necessary to capture the amplification effects, as noted in two-dimensional simulation results (Geli *et al*., 1988; Bouchon and Barker, 1996). While geometrical characteristics, such as smoothed curvature and relative elevation, have been explored to approximate topographic effects (e.g., Maufroy *et al*., 2015; Rai *et al*., 2017), they require critical parameter constraints based on local velocity and target frequency, and are thus difficult to generalize for broadband studies.

It should be noted that previous studies discussed above included only a subset of the model features deemed to be affecting high-frequency ground motions, or omitted validation

of the results. In this study, we simulate ground motions for frequencies up to 5 Hz in the widely-tested SCEC CVM-S4.26M01 including high-resolution topography, and compare to strong-motion data for the 2014 M_w 5.1 La Habra, CA, earthquake, in order to constrain the relative contributions from topography, SSHs, and $Q(f)$ on the ground motions. This chapter is organized as follows. We first describe the velocity model, simulation parameters, processing of the synthetic and recorded ground motions, and the source description. Then the relative effects of model features such as topography, shallow near-surface velocities, small-scale heterogeneities, and $Q(f)$ are quantified through goodness-of-fit (GOF) measures between synthetics and data. Finally, we discuss future research directions based on our results.

3.2 Model Features and Computational Aspects

In this section we describe the simulation method and model setup, and summarize the features included in our model. In addition, we outline the processing parameters for simulations and data, and introduce our goodness-of-fit (GOF) measures to validate our simulations.

3.2.1 Numerical method for simulating ground motions

We use the staggered-grid finite-difference (FD) code AWP-ODC (Anelastic Wave Propagation, Olsen-Day-Cui, from the authors of the code, hereafter denoted by AWP; Cui *et al*., 2010), which is 4^{th}-order accurate in space and 2^{nd}-order accurate in time, to generate ground motion predictions for the La Habra event. AWP has been adapted to GPU accelerators for kinematic sources (Cui *et al*., 2013), and provides support for frequency-dependent viscoelastic attenuation (Withers *et al*., 2015) and topography using a curvilinear grid (O'Reilly *et al*., 2021).

The accuracy of AWP has been thoroughly verified. For example, large-scale earthquake simulations in realistic 3D earth models with strong heterogeneities and complex finite-fault

source descriptions (Bielak *et al*., 2010; Bielak *et al*., 2016), revealed good agreement between AWP, another staggered-grid FD code and a finite-element code. The implementation of frequency-dependent anelastic attenuation was tested by Withers *et al*. (2015) against a frequency-wavenumber solution, and the accuracy of the curvilinear topography implementation (O'Reilly *et al*., 2021) was verified against SPECFEM3D (Komatitsch and Tromp, 2002).

3.2.2 Velocity Model

We used a model domain of lateral dimensions 148 km by 140 km, rotated 39.9° clockwise with a depth extent of 60 km (see Fig. 3.1). The mesh was extracted from the SCEC CVM-S4.26-M01, an updated version of the original CVM-S4 model (Magistrale *et al*., 2000; Kohler, 2003) with iterative 3D tomography inversions in Southern California (Lee *et al*., 2011). The SCEC Uniform Community Velocity Model software framework (V19.4; Small *et al*., 2017) was used for the extraction of seismic P-wave velocity (V_P), V_S and the material density. The choice of CVM-S4.26-M01 (hereafter abbreviated with CVM-S) for this study was based on the results by Taborda *et al*. (2016) who concluded from a comprehensive validation of four velocity models with 30 earthquakes in the greater Los Angeles region that this model consistently yielded the best fit to ground motion data using a variety of metrics. The model includes the near-surface V_S tapering method proposed by Hu *et al*. (2021b).

3.2.3 Small-scale Heterogeneities

Small-scale crustal heterogeneities (on the order of tens to hundreds of meters) are known to exist in nature (e.g., Savran and Olsen, 2016) but are insufficiently resolved in state-of-the-art velocity models. Instead, small-scale heterogeneities are commonly included in numerical simulations via statistical models of property fluctuations (e.g., Imperatori and Mai, 2013; Savran and Olsen, 2019). Here, we superimpose a statistical model of velocity and density perturbations

onto CVM-S, defined via a von Kármán shape function (Frankel and Clayton, 1986):

$$\Phi_{v,a}(r) = \sigma^2 \frac{2^{1-v}}{\Gamma(v)} \left(\frac{r}{a}\right)^v K_v \left(\frac{r}{a}\right) \tag{3.1}$$

which has Fourier transform:

$$P(k) = \frac{\sigma^2 (2\sqrt{\pi}a)^E \Gamma(v + E/2)^{v+E/2}}{\Gamma(v)\,(1 + k^2 a^2)} \tag{3.2}$$

in which k is the wave number and E is the Euclidean dimension, Γ denotes the Gamma function, and K stands for the modified Bessel function of the second kind with order ν. The parameters of the von Kármán autocorrelation function include correlation length a, standard deviation σ and Hurst number ν. This approach generates a random field with zero mean, and the desired standard deviation is guaranteed by scaling the random variable at each computational node. We used a fixed Hurst number of 0.05 and introduced elliptical anisotropy with a ratio of horizontal-vertical correlation lengths of 5, and tested correlation lengths between 100-5000 m, and standard deviation of 5% and 10%, based on previous studies in Southern California (e.g., Nakata and Beroza, 2015; Savran and Olsen, 2016). In our model, the random perturbations extend to a depth of 7.5 km, and then linearly tapered to a standard deviation of 0 at 10 km depth (Olsen *et al.*, 2018). Figure 3.2 shows an example realization of small-scale heterogeneities, compared to the original CVM-S in terms of V_S at the surface.

3.2.4 Topography

While the basins of the greater Los Angeles region, including near the epicentral area of the La Habra event, are characterized by relatively flat topographic relief, the San Gabriel and Santa Ana Mountains bound the area to the north and east, respectively (see Fig. 3.1). To quantify the effects of topography on ground motions from the La Habra event, we use the curvilinear grid

approach by O'Reilly *et al*. (2021). In this version of AWP, surface topography is incorporated by stretching the computational grid in the vertical direction, while keeping the horizontal grid spacing unchanged, so that the surface grid locations conform to the shape of the topography. We include surface topography into our model domain via the $\frac{1}{3}$ arc-second resolution Digital Elevation Model in southern California from the U.S. Geological Survey (USGS, 2020).

3.2.5 Anelastic Attenuation

Anelastic attenuation is needed for accurate simulation of seismic wave propagation through earth models at distances further than the dominant wavelength to account for the loss of intrinsic energy. Frequency-independent attenuation, resulting in identical seismic energy loss per cycle across a frequency bandwidth, has successfully been used to validate ground motion recordings for frequencies up to about 1 Hz (e.g., Olsen *et al*., 2003; Graves and Wald, 2004). However, as frequencies increase above about 1 Hz, data often supports frequency-dependent Q (e.g., Raoof *et al*., 1999; Eberhart-Phillips *et al*., 2014; Wang and Shearer, 2017). To address these findings, Withers *et al*. (2015) developed an efficient coarse-grained memory variable approach to model frequency-dependent attenuation using a power law formulation

$$Q(f) = Q_0 * \left(\frac{f}{f_0}\right)^{\gamma}, \quad f \geq f_0, \tag{3.3}$$

where Q_0 is a frequency-independent Q value applied for $f < f_0$.

A widely-used parameterization of Q_0 is proportional to local seismic velocity, with separate values $Q_{P,0}$ and $Q_{S,0}$ for V_P and V_S quality factors, respectively, producing an expected stronger attenuation for lower velocity material, as pointed out by Hauksson and Shearer (2006). Taborda and Bielak (2014) revised the formula expressed by Brocher (2008) and applied a 6^{th}-order polynomial function for $Q_{S,0}$ from V_S, and $Q_{P,0} = \frac{3}{4}\left(V_P/V_S\right)^2 Q_{S,0}$. We test a variety of these parameterizations of Q_0 for the La Habra event (see Fig. A3.1).

3.2.6 Near-surface Geotechnical Layer

CVM-S includes geotechnical data which integrates geology and geophysics data from surficial and deep boreholes, oil wells, gravity observations, seismic refraction surveys and empirical rules calibrated based on ages and depth estimates for geological horizons in southern California (Magistrale *et al*., 1996; Magistrale *et al*., 2000). While recent validation studies, such as Taborda *et al*. (2016), have shown that the basin structure included in CVM-S is reasonably accurate, unrealistically large surface rock site velocities (see Fig. 3.2) motivated the method by Ely *et al*. (2010) to reduce the V_S in the top 350 m based on available V_{S30} values. Recently, Hu *et al*. (2021b) proposed a method to further adjust the near-surface structure to a depth of 1000 m, resulting in an improved fit between simulated and recorded Fourier spectra below 1 Hz for the La Habra earthquake, which will be used in the simulations in this study.

3.2.7 Ground Motion Simulations

Table 3.1 lists the parameters used in our simulations. All simulations have the same duration of 120 s and resolve wave propagation up to $f_{max} = 5$ Hz by at least 5 points per minimum S-wavelength. We use AWP-topo that supports a uniform regular, curvilinear mesh to model wave propagation in composite models including topography and other features, with the minimum V_S clamped at 500 m/s to reduce computational cost. V_P in the low-velocity material is determined by the V_P/V_S ratio from (the un-clamped) CVM-S. We use a kinematic source generated following Graves and Pitarka (2016), which creates finite-fault rupture scenarios with stochastic characteristics optimized for California events. The focal mechanism was taken from the U.S. Geological Survey (strike=233°, dip=77°, rake=49°; USGS, 2014) with a moment magnitude 5.1.

3.2.8 Data Processing

259 strong-motion seismic stations were used to validate the simulations. The strong motion recordings (velocity time series) are obtained from SCEC (F. Silva, Personal Communication, 07/2020), with hypocentral distance up to 90 km and signal-to-noise ratio above 3 dB. The processing procedure included the following steps: (1) low-pass filtering of the time series below 10 Hz using a zero-phase filter; (2) interpolating the time series linearly to a uniform time step; (3) tapering of at the last 2 seconds using the positive half of a Hanning window; (4) zero padding the last 5 seconds; (5) filtering the seismograms to the desired frequency, and (6) converting velocities to accelerations by a time derivative. Except for the initial 10 Hz low-pass filter, all filters used a low-cut frequency of 0.15 Hz to avoid noise interference (in the data). 4^{th}-order Butterworth filters were used in all cases. Finally, our horizontal synthetic seismograms were rotated 39.9° counter-clockwise.

3.2.9 Intensity Measures

We use 7 different intensity measures to characterize the performance of our ground motion models for the La Habra earthquake, namely peak ground velocity (PGV), peak ground acceleration (PGA), energy duration (DUR), cumulative energy (ENER), response spectral acceleration averaged between 0.1 and 10 s (RS), smoothed Fourier amplitude spectrum (FAS), as well as Arias intensity (AI). We computed the SA at frequencies linearly spaced from 0.2 to 5 Hz. Cumulative energy is calculated as $ENER = \int v(t)^2 dt$. Both ENER and DUR are defined on the interval between the arrival of 5 and 95 percent of the total energy. Arias intensity describes the cumulative energy per unit mass (Arias, 1970), and is defined as $AI = \frac{\pi}{2g} \int a(t)^2 dt$, where $a(t)$ is the acceleration time series, and g is the gravitational acceleration.

3.3 Results

3.3.1 Source Models

Due to the stochastic characteristics of the kinematic source generator by Graves and Pitarka (2016), a series of 40 source realizations with different random seeds are evaluated based on comparisons between spectral accelerations with records at stations with epicentral distance of 31 km or less (R. Graves, Personal Communication, 03/04/2020). The 40 source models, using a fault area of 2.5 km x 2.5 km, were rated based on the average absolute bias between synthetics and data up to 5 Hz for the median pseudo-spectral acceleration rotated over all azimuths (rotD50), from which we selected the three best performing source descriptions with hypocentral depths at 5, 5.5 and 6 km (see Fig. A3.2). The rupture duration of the source descriptions is less than 2 s and sampled at an interval of 0.0006 s, identical to the time step used in our simulations. The three sources tend to generate overall similar patterns of PGV within the same bandwidth of low (< 2.5 Hz) or high (> 2.5 Hz) frequencies (Fig. A3.3). Based on this result, we carry out our analysis with Source 1 (Fig. 3.3) only in order to limit the computational requirements.

3.3.2 Minimum V_S

Southern California features several low-velocity basins where the lowest V_S in CVM-S can be much lower than the minimum value of 500 m/s that we imposed in our models (see Table 3.1). As previous studies have pointed out, soft soils, characterized by lower V_S, have been found to generate significant amplification of ground motions (e.g., Anderson and Hough, 1984). Reducing the minimum V_S will, however, increase the computational cost for the series of 3D numerical simulations needed in our analysis beyond the available resources. For example, clamping the minimum V_S at 200 m/s instead of 500 m/s requires about 40 times more node hours for a single simulation.

For this reason, we use a computationally much less expensive 1D method, which models vertically-incident SH waves in a horizontally-layered halfspace (e.g., Day, 1996; Thompson *et al*., 2012), to account for effects of the material with V_S less than 500 m/s. At each site, we calculated the response from two 1D models, one using the velocity profile from our models, and the other using the same profile but with minimum V_S clamped at 500 m/s. In this way, the ratio of the two 1D results characterizes the effects of the material with V_S less than 500 m/s, which is then convolved with our 3D simulations. Because the SH1D method considers SH waves only, we will apply this calibration to horizontal components only.

Figure 3.4 illustrates the results of applying the SD1D method low-velocity correction for an example site. The two profiles show similar SH1D responses below about 0.3 Hz, above which the SH1D response ratio slowly trends upward with frequency, depicting the amplification from the material with V_S less than 500 m/s. The PGV of the horizontal synthetic with the correction is increased by 32% relative to that with V_S clamped at 500 m/s (Figure 3.4c). The correction leaves the shape of the waveform almost unchanged. The smoothed Fourier spectra (Figure 3.4d) further suggests that clamping V_S at 500 m/s may be reasonable for frequencies up to 0.8-1 Hz. Similar effects are observed for all profiles with near-surface velocity lower than 500 m/s, and we therefore apply this technique to all our 3D simulations with minimum V_S clamped at 500 m/s.

3.3.3 Topography

In this section we investigate the effects of topography, which are often ignored in numerical simulations (e.g., Graves and Wald, 2004; Olsen *et al*., 2006; Savran and Olsen, 2019). Our analysis of topographic effects uses a reference model with topography removed. Figure 3.5 shows the percent difference between models with and without topography for PGV, DUR and AI for bandwidths of 0.15-1 Hz, 1-2.5 and 2.5-5 Hz. It is clear that topography complicates the wavefield pattern significantly, even at frequencies below 1 Hz in terms of DUR and thus AI.

Consistent with previous studies (e.g., Hartzell *et al*., 1994; Lee *et al*., 2009a), we observe a weak deamplification of PGV below 1 Hz in basin areas, while that mountain peaks and ridges may amplify PGV by less than 50%. In addition, we find that PGV is reduced by about 30% in the Chino Basin and northwest of San Gabriel Mountains. These results are in agreement with Ma *et al*. (2007) who found that the San Gabriel Mountains scatter surface waves from a northern rupture on the San Andreas Fault and reduce the PGVs in the LAB by up to 50%. We interpret these results as shielding and focusing effects on the front and back sides of the mountains, respectively, which become more significant at higher frequencies, in agreement with Liu *et al*. (2020). In addition, at frequencies increase above 2.5 Hz, we observe a clear pattern of "amplification-deamplification-amplification" along the N-S (short) axis of the San Gabriel Mountains, which is predicted in numerical experiments by Liu *et al*. (2020).

It is particularly noticeable that DUR within 10 km of the source is strongly amplified for both low and high frequencies, mostly to the north (northwest end of the Santa Ana Mountains). Here, topography seems to act as a significant source of scattering that increases the wave duration on the sides of the mountain facing the incoming wavefields, while DUR is reduced on the "back" sides of the mountain seen from the source location. At further distance from the source, our results show a clear negative correlation between the effects on PGV amplification and DUR lengthening, suggesting that topography redistributes seismic energy from the large-amplitude first arrivals to the adjacent coda waves. These results are in agreement with Lee *et al*. (2009a) who noticed that the effects from topography can interfere with those from path and directivity.

3.3.4 Anelastic Attenuation

Figure 3.6 shows a comparison between PGVs extracted from records and synthetics for a simulation with Model 1, and Figure 3.7 shows the horizontal- and vertical-component FAS and FAS bias from Models 1, 3, 4 and 5 (see Table 3.2). As expected, the frequency-dependent and

constant Q models diverge above 1 Hz. Among the four attenuation models, $Q_S = 0.075V_S f^{0.4}$ (Model 4) fits the vertical component the best, $Q_S = 0.1V_S$ (Model 3) and $Q_S = 0.05V_S f^{0.6}$ (Model 5) provide the best fit to the FAS of the data for horizontal components, though Model 3 (Model 5) underpredicts the vertical component above 3 Hz (below 3 Hz).

As for FAS, the spatial distribution of peak ground motions, e.g. PGV, varies significantly between various $Q(f)$ models (Fig. 3.8). The $Q_S = 0.1V_S f^{0.6}$ model strongly overpredicts the high-frequency (>2.5 Hz) PGVs in the basins toward the south and west, while providing a fairly good match at distances greater than 40 km. The more attenuated $Q_S = 0.075V_S f^{0.4}$ and $Q_S = 0.1V_S$ models, on the other hand, generate moderate overprediction in the near-source regions while underpredicting the PGVs at farther distances.

The consistent overprediction within 40 km for all Q models may be caused by the omission of the near-surface low-velocity material (<500 m/s) when inverting for the source description. Another potential cause of the near-source overprediction could be a very low Q in the shallow sediments (more abundant in the near-source area as compared to larger epicentral distances), as proposed by Hough *et al*. (1988) and examined in the numerical simulations by Withers *et al*. (2019). The presence of such thin, near-surface layer with very low Q would also alleviate at least part of the overprediction of the duration (DUR), as obtained for most models. On the other hand, it is intriguing that the PGVs predicted by all tested Q models appear to decay faster than data beyond 40 km, roughly at the boundaries of the LAB. This observation may suggest unrealistically large contrasts in the shear impedance near the basin boundaries in the CVM, causing excessive entrapment of waves (see Fig. 3.2). Another explanation for the underprediction of ground motions beyond epicentral distances of 40 km could be higher Q in the surrounding mountain areas compared to those in the sedimentary basins. We recommend further research into these discrepancies.

The presence of shallow low velocities is crucial in determining the best-fitting Q models. Figure 3.9 shows the comparison of PGV and DUR in 0.15-2.5 Hz and 2.5-5 Hz for models with

and without shallow velocity taper. In addition to the amplification on PGV due to increasing Q, the 1000 m taper lowers the shallow velocity and increase the PGVs beyond 30-40 km, where most rock sites locate. Furthermore, the desired larger ground motion amplitudes at farther distance cannot be achieved by even larger Q, which will generate substantial overprediction of DUR (Fig. 3.9); while velocity taper has minor influence on DUR and thus is preferred.

3.3.5 Small-scale heterogeneities

Figure 3.10 shows the effects of adding a von Kármán distribution of small-scale heterogeneities (SSHs) with $\sigma = 5\%$ and horizontal correlation length of 5000 m compared to a reference model without SSHs on PGV and DUR in the frequency bands 0.15-2.5 Hz and 2.5-5 Hz. Savran and Olsen (2019) studied a smaller region up to 2.5 Hz, roughly in the center of our simulated domain, found that SSH presents itself as a second-order source of misfit that yields relatively small influence on ground motions. Our results generally agree with their findings, and further show that SSHs have stronger effects at farther distance and in higher frequencies.

Przybilla *et al*. (2009) performed analysis using elastic radiative transfer theory and showed that the direction dependence of scattering can be identified by ak, where a is the correlation length and k is the wave number. For $ak \approx 1$, waves interact with heterogeneous medium most intensively because the wavelength and correlation length are in the same order. When $ak \gg 1$ waves are predominantly scattered in the forward direction, which generates geometric focusing in the early arrivals and leads to larger peak amplitudes, and vice versa for $ak \ll 1$. In the case with $a = 5000$ m, our model generally confines to the forward scattering regime and PGV is amplified, which is shown quantitatively in Figure 3.11. As the frequency increases, k and thus ak tends to increase as well, causing generally weaker scattering effects as deviating from the most intensive scattering regime, thus the median difference closer to 0 for both PGV and DUR. However, higher frequencies wavefields are capable of resolving finer

structure, and may induce larger spatial variability in scattering effects, represented by larger standard deviations. More SSH realizations with various standard deviations and correlation lengths of the random field are examined (see Figure A3.4), which shows a general trend that larger standard deviation and correlation length yield stronger SSH effects.

3.4 Discussion and Conclusions

In this study we have explored the effects of a series of different model features on the resulting ground motions for the 2014 M5.1 La Habra, CA, earthquake. Clearly, trade-offs between the parameters complicates or even inhibits determining a unique set of model parameters creating a best fit to the data. In order to quantitatively rate the performance of the different model features, we used a modified subset of the goodness-of-fit (GOF) metrics proposed by the methods of Anderson (2004) and Olsen and Mayhew (2010) developed for the comparison of broadband seismic traces (0 to 10+ Hz). The GOF score for each metric is defined as

$$G_{\text{metric}} = 10\,\text{erfc}\left(\frac{2|x-y|}{x+y}\right). \tag{3.4}$$

where x and y are two positive scalars from the selected metrics. G_{metric} is computed for each metric and combined into a weighted average using all 3 components. We used weights of 0.5, 0.5, 1, 0.5, 0.5, 1, and 1 for for PGV, PGA, DUR, AI, ENER, RS, and FAS, where reduced weights are chosen due to correlation between metrics (Olsen and Mayhew, 2010). The GOF score for the entire simulation is calculated as the average of G_{station} across all 259 stations. GOF values between two signals above 4.5 and 6.5 are considered fair and very good fit, respectively.

The GOF scores for the models (see Table 3.2) explored in this study are shown in Figure A3.6, see also Figure 3.12 and Figures A3.7 to A3.27 in Section 3.4 for results for individual models. Note that the model ID does not represent any ranking of their goodness of

fit against seismic records. The models generally achieve GOF in the range of 5.1 to 5.4 for the low frequencies (< 2.5 Hz), with the lowest values for models 15, 16 and 20, and the highest value for models 4, 6, and 11. The GOF scores for the high frequencies (> 2.5 Hz) are typically about an increment of one smaller than those for the low frequencies, caused by a combination of increased uncertainty in the source description and model parameters of the former. Among the investigated models, Models 3, 4, 6, and 21 achieve the highest GOF values for 2.5-5 Hz, while Models 9, 15, and 19 reflect the lowest values. Note that Model 9, characterized by a 350 m taper of the near-surface velocity modification, yields fair GOF values for frequencies below 2.5 Hz while sacrificing the fit for high-frequency waves, consistent with the recommendations of a 1000 m taper by Hu *et al*. (2021b). The smallest GOF value is obtained for model 15, indicating that SSH with standard deviation of 10% may be too heterogeneous. The consistently lower GOF above 2.5 Hz for Models 17-22 indicates the necessity of including mountain topography in high-frequency simulations.

Hu *et al*. (2021b) showed that reducing shallow velocities in CVM-S at poorly constrained sites in the greater Los Angeles area by a generic taper function based on V_{S30} was able to improve the fit of ground motion synthetics to data for the La Habra earthquake, particularly in regions constrained by limited geological information. However, since their tests were restricted to frequencies below 1 Hz and models with a flat free surface. Here, we examine the efficacy of the method for frequencies up to 5 Hz, while adding topography to the models from Hu *et al*. (2021b). As in their study we divided the 259 strong motion recording sites into two groups: type A sites representing sites with good geological constraints, and type B sites with poor geological constraints, characterized by unrealistically large surface V_S in the top 500-1000 m in CVM-S. Figure 3.13 shows the median FAS for both types of sites from various models (see Table 3.2 for a list of model features). As observed by Hu *et al*. (2021b), type A sites are largely unaltered by the shallow velocity tapering methodology. The original CVM-S (Model 11) significantly underpredicts the FAS at type B sites up to 5 Hz.

Topography causes generally small effects in terms of FAS (Figure 3.13, Model 1 versus Model 17), except for the increase on the vertical component for type B sites for frequencies larger than 1.5 Hz. Previous studies attempting to capture the effects of topography on ground motions and establish proxies to characterize such effects typically have used simple homogeneous models of earth material, e.g. Maufroy *et al*. (2015) and Rai *et al*. (2017). These studies found that topographic curvature is a good proxy characterizing irregular surface in evaluating topographic effects. However, assessment of topographic effects on ground motions are complicated by amplification due to the presence of shallow weathering layer of low velocities, typically present in mountain regions, omitted in these studies. Here, we re-assess these findings including the amplification effects from the modification of near-surface material at type B sites proposed by Hu *et al*. (2021b). We calculated the smoothed curvature of topography with a smoothing window of 640 m. Steeper relief is characterized by larger curvature values, while flatter regions are of curvature close to zero. Figure 3.14 shows the percent difference in PGV caused by including topography for varying curvature in the simulated region. The response of two models are shown, one with 1000 m V_S taper (Hu *et al*., 2021b) and one without (original CVM-S). The model without the near-surface low velocities introduced by the V_S taper method tends to reduce the PGVs by about up to 40% for most curvatures below 2.5 Hz, with a broader spectrum of de-amplification (up to 75%) and amplification (up to 40-100%, most pronounced for the largest curvatures) at frequencies between 2.5 and 5 Hz. These trends, however, becomes much more notable when the shallow low velocities are present, where steep topography (e.g., mountain summits and local steep hills) increases PGVs. This result may partly explain why in previous studies, omitting the near-surface model complexity, topographic effects on ground motions tend to underestimate the amplification at mountain tops compared to observations (e.g., Pischiutta *et al*., 2010; Lovati *et al*., 2011).

The accuracy of the source description is critical for obtaining reliable estimates of the parameters controlling model features such as $Q(f)$. The overprediction for near-source epicentral

distances and distance decay faster than that for data at further distances of the PGVs (see Figs. 3.8, 3.9 and 3.12) may at least partly be explained by uncertainty in the source moment and/or fault area. While the moment is likely relatively well constrained, a somewhat larger fault area would decrease near-source PGVs and facilitate propagation of additional seismic energy to further distances. We recommend using simulations with additional (ensembles of) sources, to further examine the model features in this work.

In addition to the source description, inaccuracies in the velocity structure further complicates estimation of the optimal model parameters, in particular for the Q model, as pointed out by (e.g., Savran and Olsen, 2019; Lai *et al*., 2020). Withers et al. (2015) estimated higher γ values (near 0.8) from their modeling of the Chino Hill earthquake. However, this estimate may be biased by the use of a CVM-S with near-surface rock velocities biased high, as well as smaller source-station distances and lower maximum frequency. Savran and Olsen (2019) used γ equal to 0.6, but with limited high-frequency resolution up to 2.5 Hz. Nevertheless, future improvement in community velocity models, wider access to computational resources, more efficient numerical codes and guidance from this study are bound to further constrain the ground motion models, leading to more accurate seismic hazard analysis.

Data and Resources

The UCVM program used to extract velocity meshes can be obtained from SCEC on https://github.com/SCECcode/UCVMC (last accessed 12/2020). The simulations were performed on Summit at the Oak Ridge Leadership Computing Facility in Tennessee. Most of the data-processing work was done using Python and the Generic Mapping Tools package (https://www.generic-mapping-tools.org, last accessed 04/2021).

Acknowledgements

This research was supported through the U.S. Geological Survey External Program (award #G19AS00021), as well as the Southern California Earthquake Center (SCEC; Contribution Number xx). SCEC is funded by the National Science Foundation (NSF) Cooperative Agreement EAR-1600087 and the U.S. Geological Survey (USGS) Cooperative Agreement G17AC00047. We thank Robert W. Graves for providing the source models and Fabio Silva for providing the station records of the 2014 La Habra earthquake.

Chapter 3, in full, is a reformatted version of a paper currently in preparation for submission for publication: Hu, Z., Olsen, K.B. and Day, S.M. (2021), 0-5 Hz Deterministic 3D Ground Motion Simulations for the 2014 La Habra, California, Earthquake. The dissertation author was the primary investigator and author of this paper.

Tables and Figures

Table 3.1: Simulation parameters used for the deterministic ground motion simulations of the 2014 La Habra earthquake.

Model	
Topography	Yes
Length	147.840 km
Width	140.400 km
Depth	58.000 km
Northwest corner	-118.0154409, 34.8921683
Southwest corner	-118.9774168, 33.9093124
Southeast corner	-117.7401908, 33.0695780
Northeast corner	-116.7729754, 34.0429241
Spatial resolution	
Maximum frequency	5 Hz
Minimum V_S	500 m/s
Points per minimum wavelength	5
Grid discretization	20 m
Number of cells	150,486,336,000
Number of GPU processors	1,512
Wall-clock time	5 hr
Temporal resolution	
Time discretization	0.0006 s
Simulation time	120 s
Number of timesteps	200,000

Table 3.2: Summary and main features of the models used in this study.

Model ID	Topography	$Q(f)^{*}$	SSH†	V_S Taper Depth (m)
1	Yes	$Q_S = 0.1V_S f^{0.6}$	No	1000
2	Yes	$Q_S = 0.1V_S f^{0.3}$	No	1000
3	Yes	$Q_S = 0.1V_S$	No	1000
4	Yes	$Q_S = 0.075V_S f^{0.4}$	No	1000
5	Yes	$Q_S = 0.05V_S f^{0.6}$	No	1000
6	Yes	$Q_S = Q_{seg}(V_S) f^{0.4^{**}}$	No	1000
7	Yes	$Q_S = Q_{poly}(V_S) f^{0.4^{***}}$	No	1000
8	Yes	$Q_S = 0.1V_S f^{0.6}$	No	700
9	Yes	$Q_S = 0.1V_S f^{0.6}$	No	350
10	Yes	$Q_S = 0.1V_S f^{0.6}$	No	0
11	Yes	$Q_S = 0.1V_S$	No	0
12	Yes	$Q_S = Q_{seg}(V_S) f^{0.4^{**}}$	$\sigma = 5\%$, $a = 100m$	1000
13	Yes	$Q_S = Q_{seg}(V_S) f^{0.4^{**}}$	$\sigma = 5\%$, $a = 500m$	1000
14	Yes	$Q_S = Q_{seg}(V_S) f^{0.4^{**}}$	$\sigma = 10\%$, $a = 100m$	1000
15	Yes	$Q_S = Q_{seg}(V_S) f^{0.4^{**}}$	$\sigma = 10\%$, $a = 500m$	1000
16	Yes	$Q_S = 0.1V_S f^{0.3}$	$\sigma = 5\%$, $a = 5000m$	1000
17	No	$Q_S = 0.1V_S f^{0.6}$	No	1000
18	No	$Q_S = 0.1V_S f^{0.6}$	No	700
19	No	$Q_S = 0.1V_S f^{0.6}$	No	350
20	No	$Q_S = 0.1V_S f^{0.6}$	No	0
21	No	$Q_S = 0.1V_S$	No	1000
22	No	$Q_S = 0.1V_S$	No	0

[*] $Q_P = 2Q_S$

[**] $Q_{seg}(V_S) = 0.075V_S$, for $V_S <= 1000$ m/s; $Q_S = 0.2V_S - 125$, for $V_S > 1000$ m/s

[***] $Q_{poly}(V_S) = 10.5 - 16V_S + 153V_S^2 - 103V_S^3 + 34.7V_S^4 - 5.29V_S^5 + 0.31V_S^6$, for V_S in km/s, see Taborda and Bielak (2014)

[†] When included, hurst number = 0.05, Horizontal to vertical correlation length ratio = 5

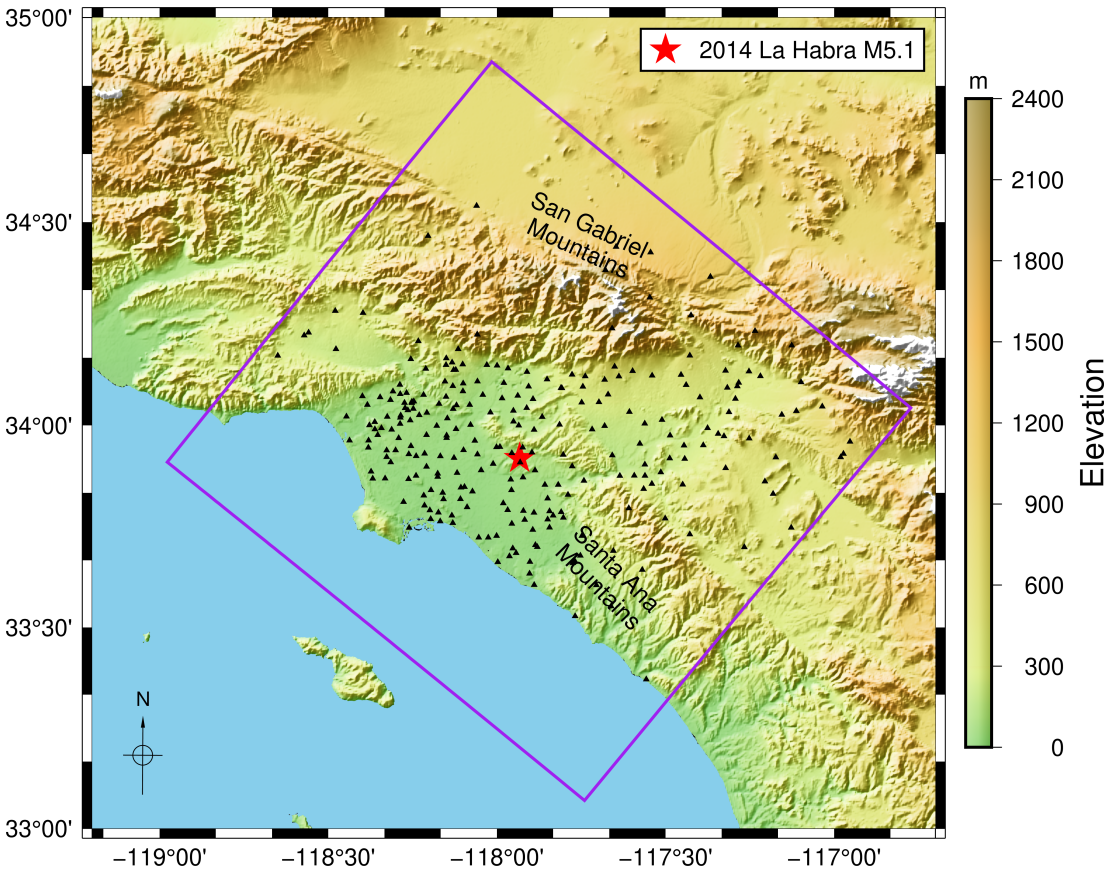

Figure 3.1: Simulation domain for the La Habra earthquake (purple solid rectangle) and locations of 259 strong motion stations (black triangles). The star denotes the epicenter. The geographical coordinates of the corners of the simulated domain is listed in Table 3.1, which is used in subsequent map views.

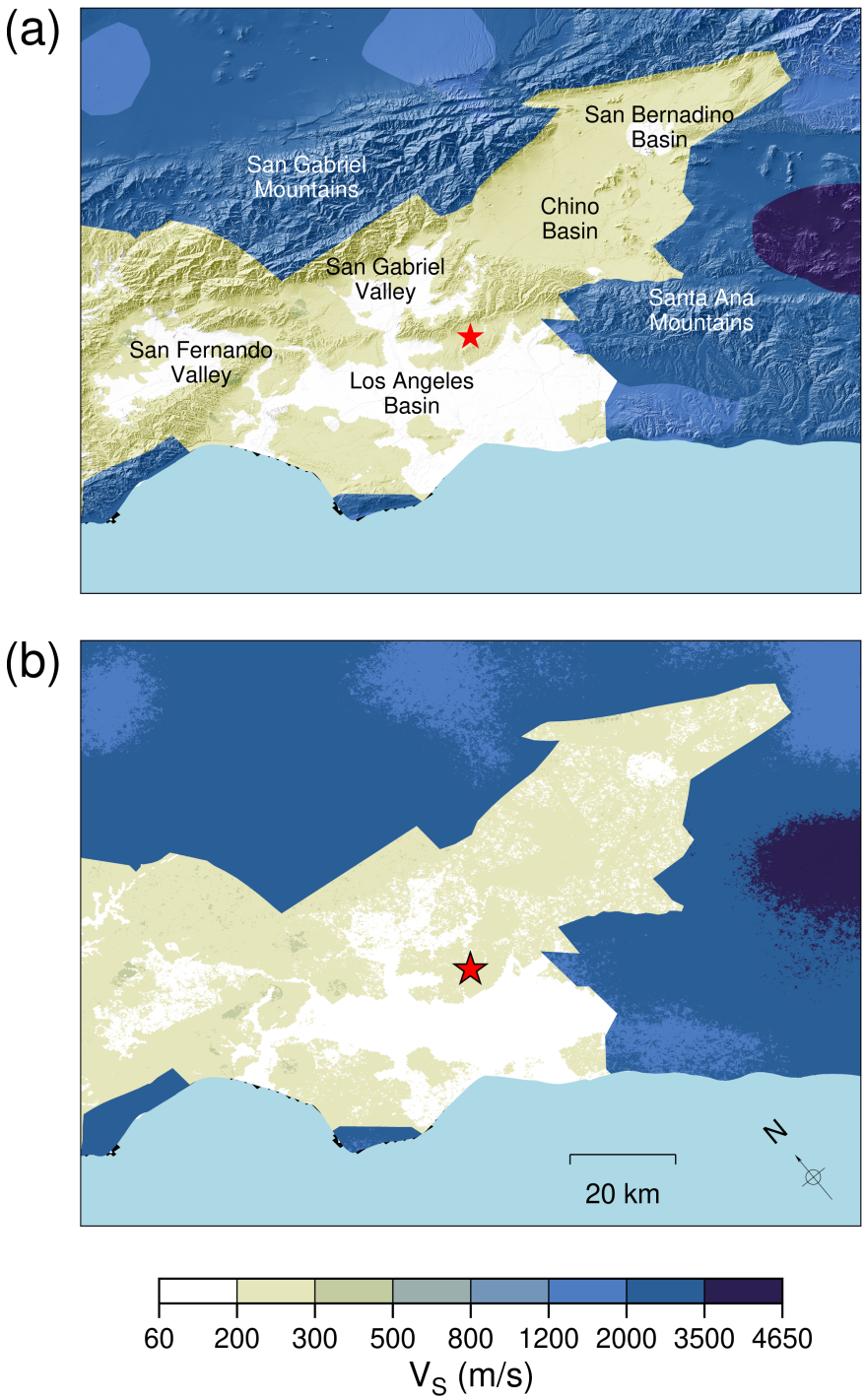

Figure 3.2: Illustration of the imprint of small-scale heterogeneities at the surface. (a) V_S extracted from the CVM-S. (b) Same as (a) but superimposed with a statistical model of heterogeneities with a correlation length of 100 m, anisotropy factor of 5, Hurst number of 0.05 and standard deviation of 5%. Topography is removed in (b) for clarity. The epicenter for the La Habra earthquake is depicted with a star.

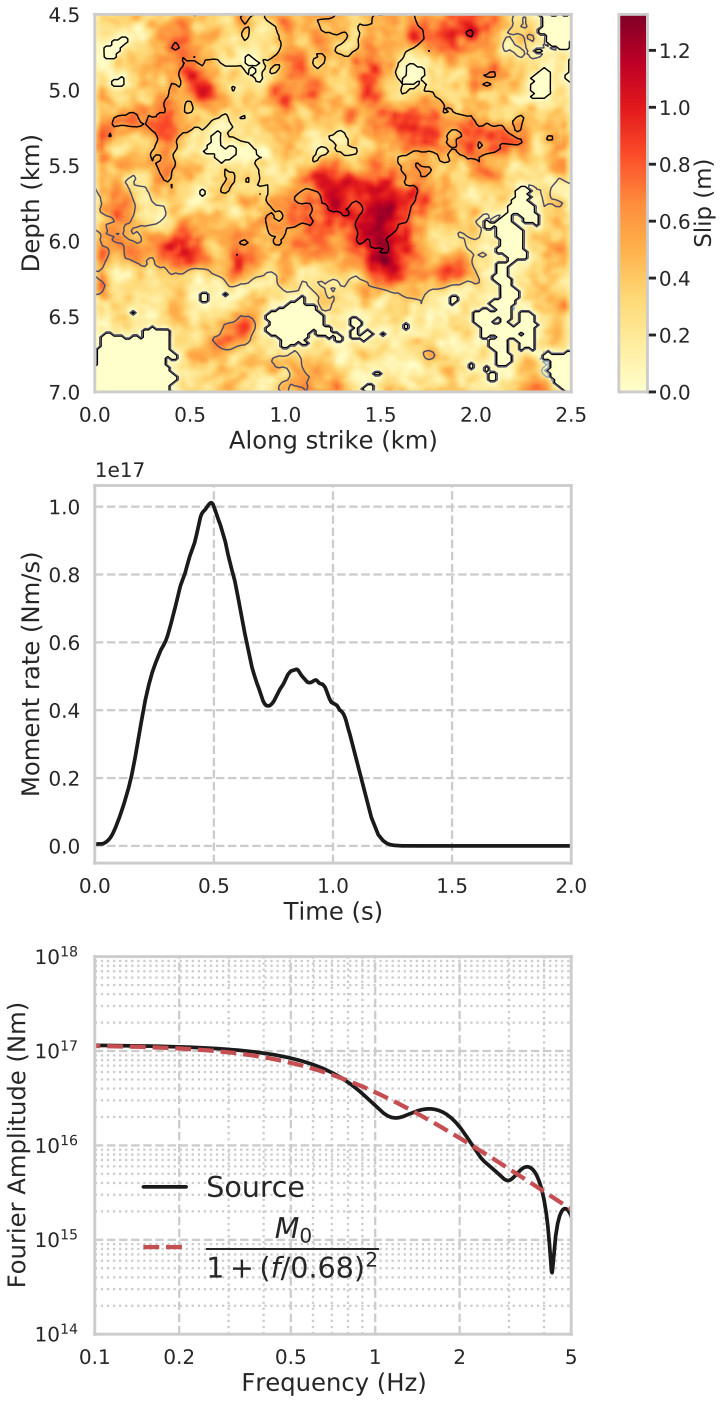

Figure 3.3: Description of the selected source model used in this study. (a) Slip distribution (shading), with contours representing rupture time at a 0.4 s interval starting from 0. (b) and (c) represent the sum of the moment rates for all subfaults and the Fourier amplitude spectrum, respectively. A Brune-type ω^{-2} decay source (Brune, 1970) that fits the source spectrum is plotted for reference.

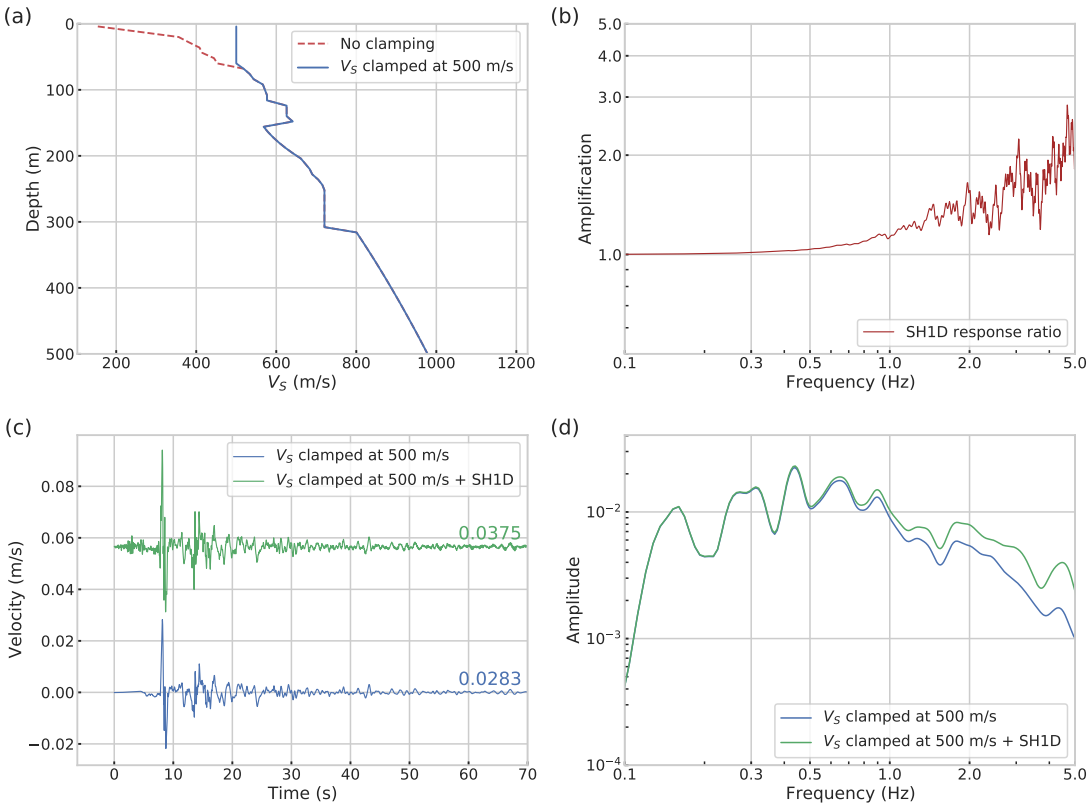

Figure 3.4: Illustration of the SH1D method used to include the effects of material with V_S less than 500 m/s in our 3D simulations for an example site. (a) V_S profile extracted from CVM-S (red dashed curve) and clamped at 500 m/s (blue). (b) SH1D response ratio between the profiles without clamping and with clamping of $V_S = 500$ m/s. (c) Synthetics from a 3D simulation using $V_S = 500$ m/s, with and without the SH1D response ratio. (d) Fourier amplitude spectra corresponding to the waveforms in (c).

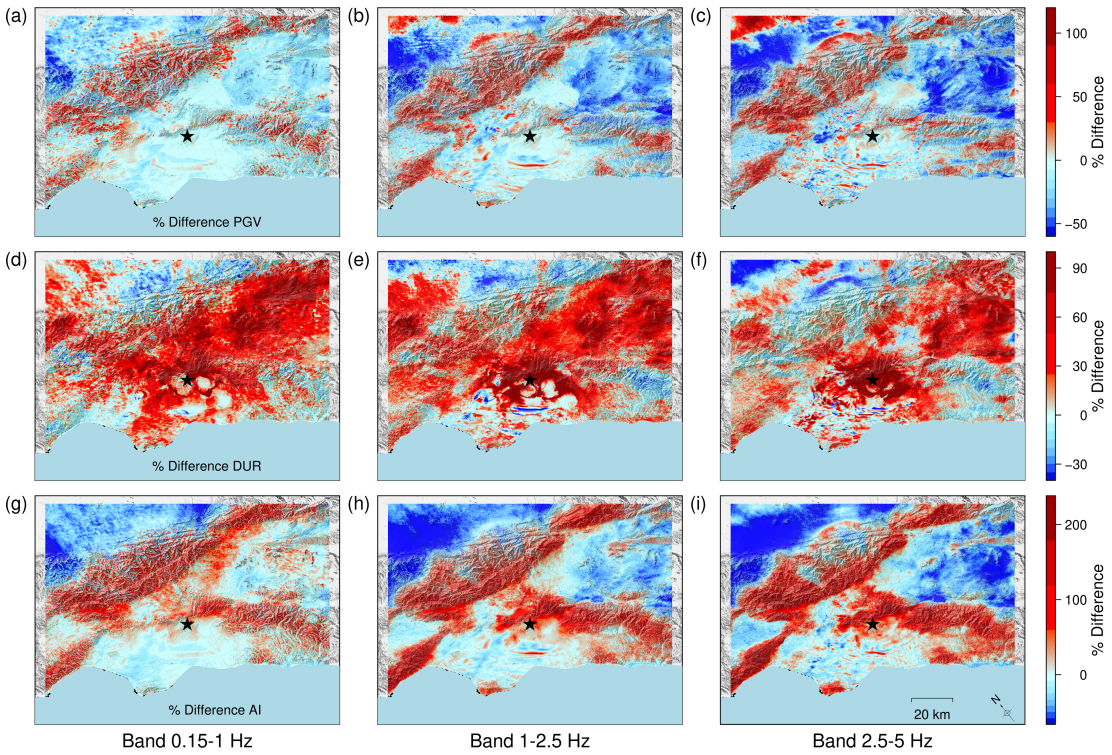

Figure 3.5: Percent difference of PGV (the first row) and DUR (the second row) at the surface determined by the model with topography and the model without topography for (left) 0.15-1 Hz, (center) 1-2.5 Hz, and (right) 2.5-5 Hz. Positive (negative) values colored in red (blue) indicate amplification (deamplification). The star denotes the epicenter.

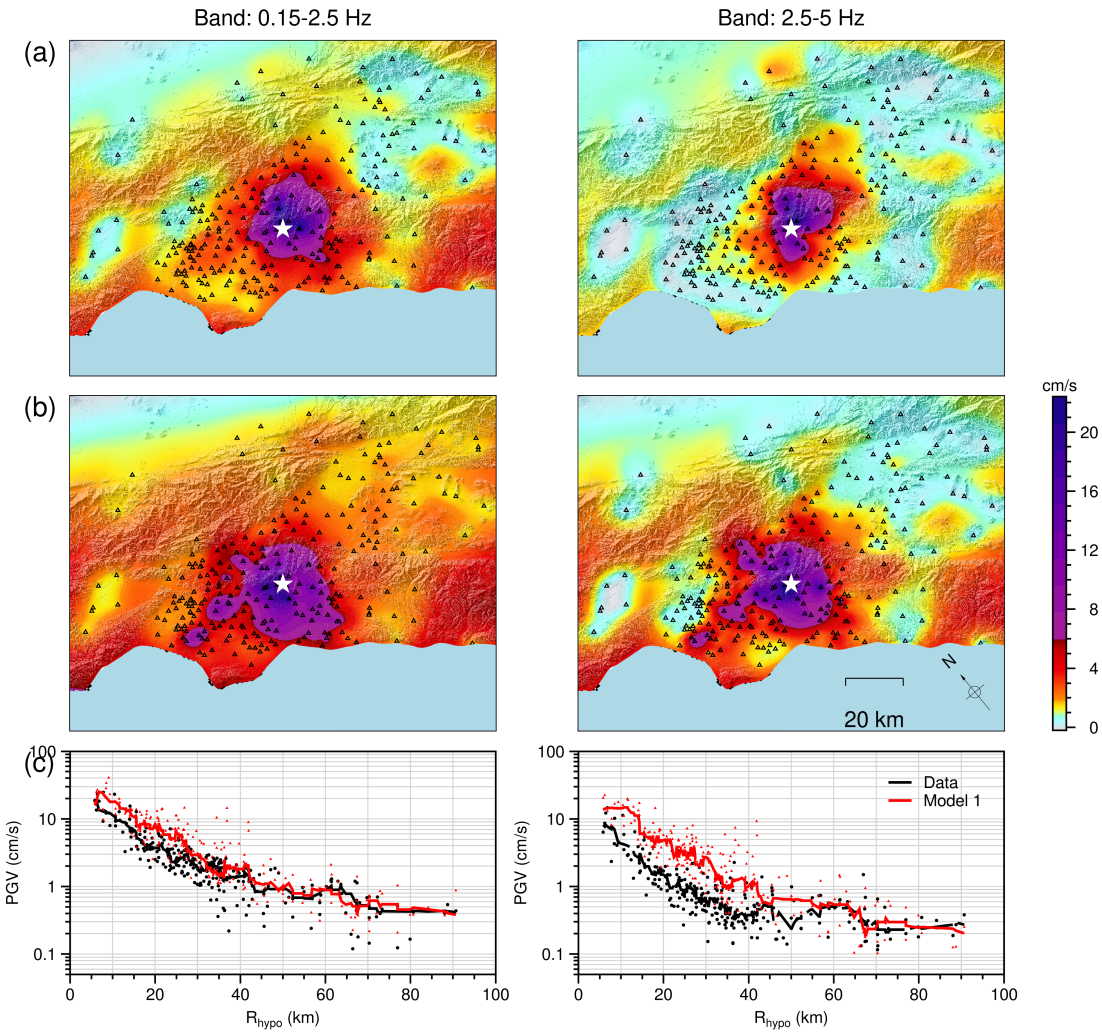

Figure 3.6: Comparison of interpolated PGVs measured at 259 stations, depicted by triangles, for (a) data and (b) synthetics using Model 1 (including topography, 1000 m shallow velocity refinement and frequency-dependent attenuation $Q_S = 0.1 V_S f^{0.6}$, $Q_P = 2Q_S$; see Table 3.2). The star denotes the epicenter. (c) PGV against R_{hypo} for data and synthetics. The left and right columns show band-limited results for 0.15-2.5 Hz, and 2.5-5 Hz, respectively.

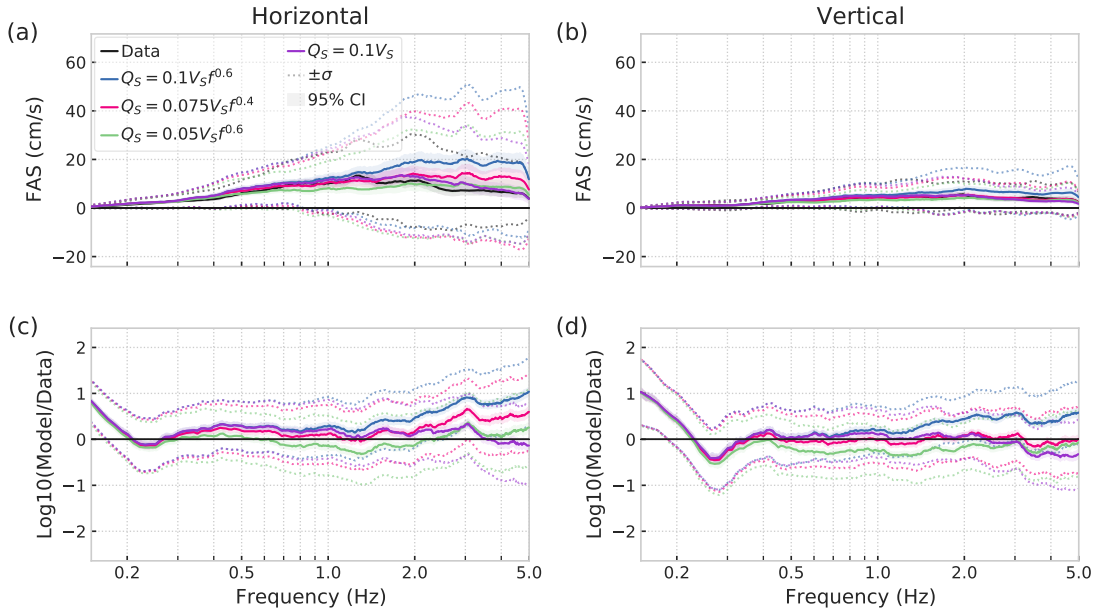

Figure 3.7: FAS computed from records and models with various attenuation models (blue: Model 1, violet: Model 3, red: Model 4, green: Model 5). The left (right) column shows results for the horizontal (vertical) components. The top row shows the FAS amplitudes and the bottom show shows the FAS bias between models and records, calculated as the 10-based log between simulations and data. The solid lines depict the median FAS over all 259 stations. The shading shows the 95% confidence interval (CI) and the dashed lines denote one standard deviation centered at the median.

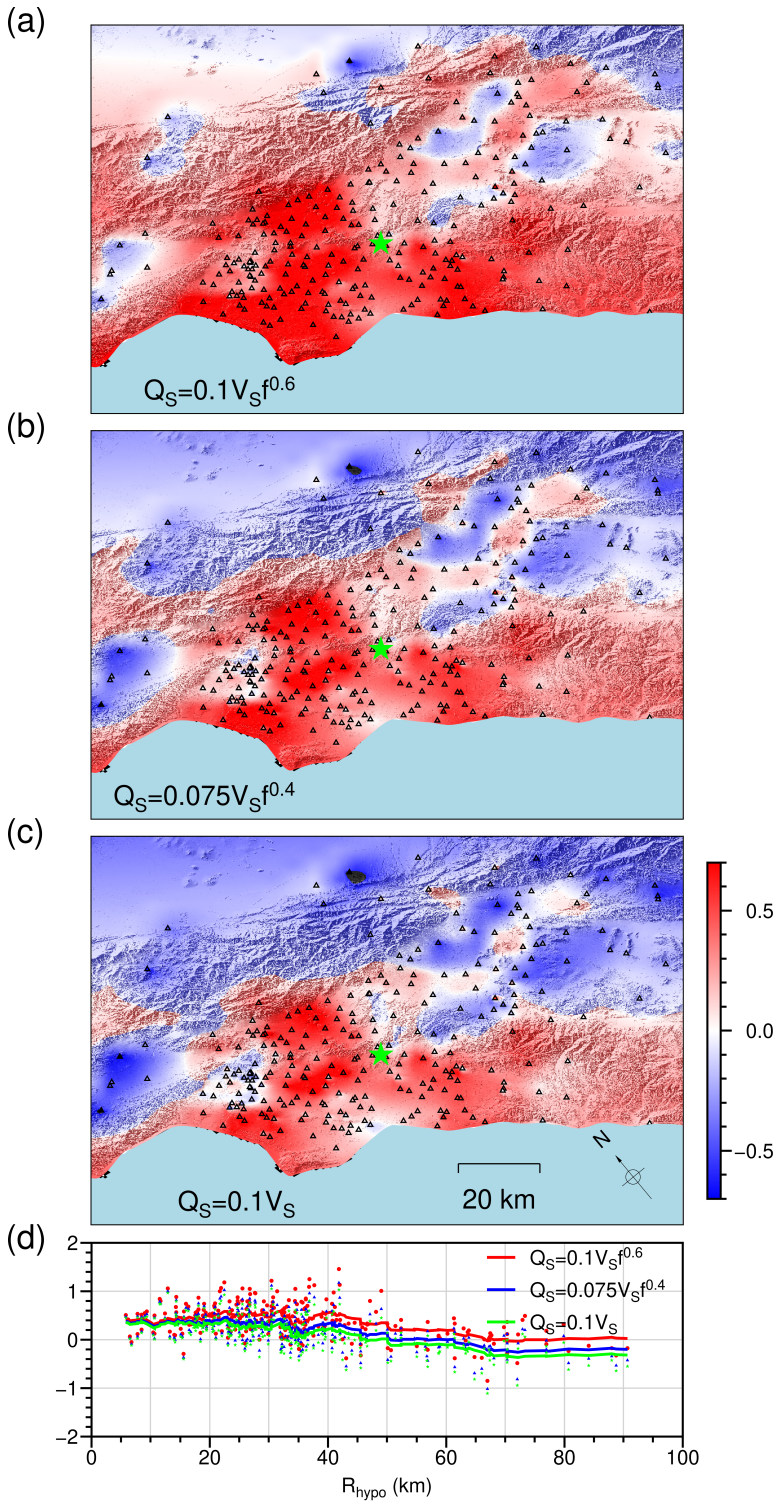

Figure 3.8: (a-c) Spatial distribution of the three-component bias for PGV, band pass filtered between 2.5 and 5 Hz. The bias values are computed as the base 10 logarithm of the ratio between simulations and records at each strong motion site. Positive (negative) values represent overprediction (underprediction). (d) Moving average of the bias of PGV using a 20-point window from the three Q models (red: Model 1, green: Model 3, blue: Model 4; see Table 3.2) shown in (a-c) versus hypocentral distance.

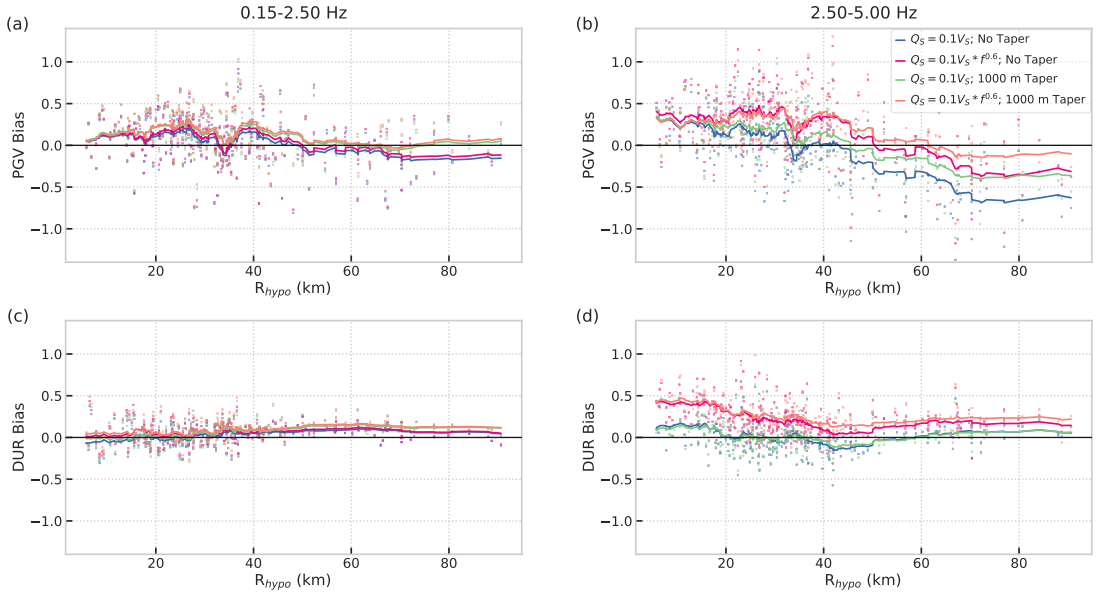

Figure 3.9: Bias of (a-b) PGV and (c-d) DUR for passbands (left) 0.15-2.5 Hz and (right) 2.5-5 Hz at all 259 stations. The bias is calculated in the same way as for Figure 3.7. The solid lines depict the moving average of the bias using a 20-point window for each of the Q models (blue: Model 11, red: Model 10, green: Model 3, orange: Model 1; see Table 3.2) versus hypocentral distance.

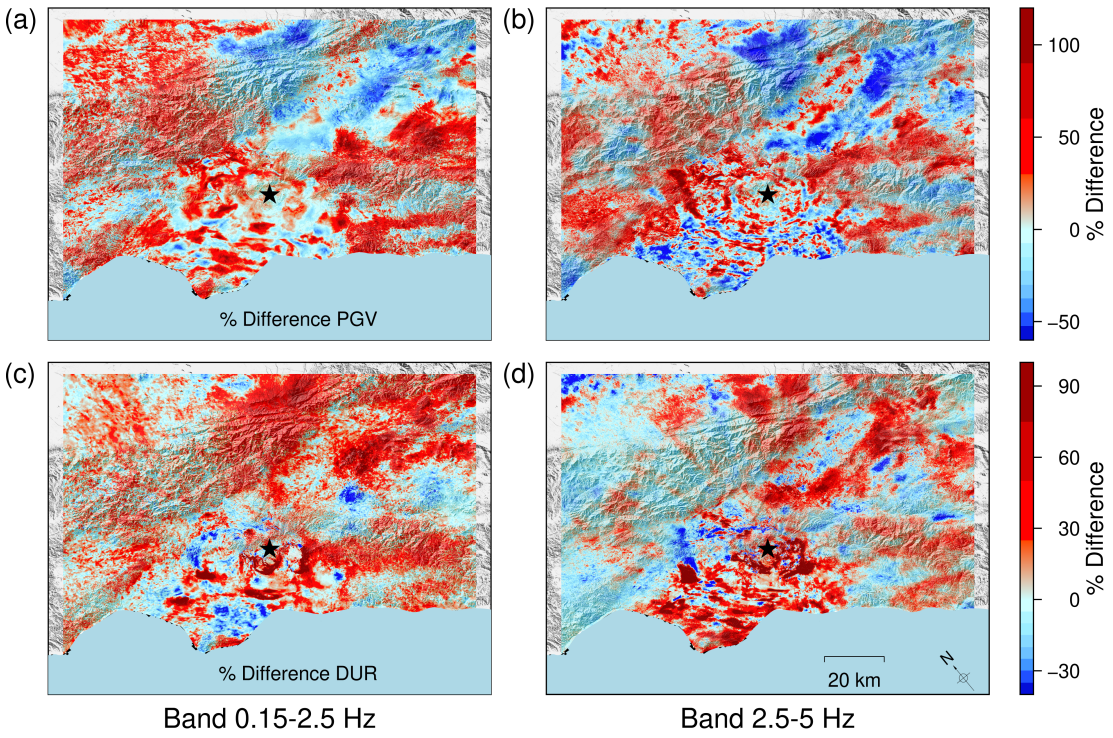

Figure 3.10: Difference in (top row) PGV and (bottom) DUR (bottom row) from Model 16, including SSH with $\sigma = 5\%$ and $a = 5000$ m, versus Model 1 (no SSHs). Left (right) columns show results for bandwidths 0.15-2.5 Hz (2.5-5 Hz). The star depicts the epicenter.

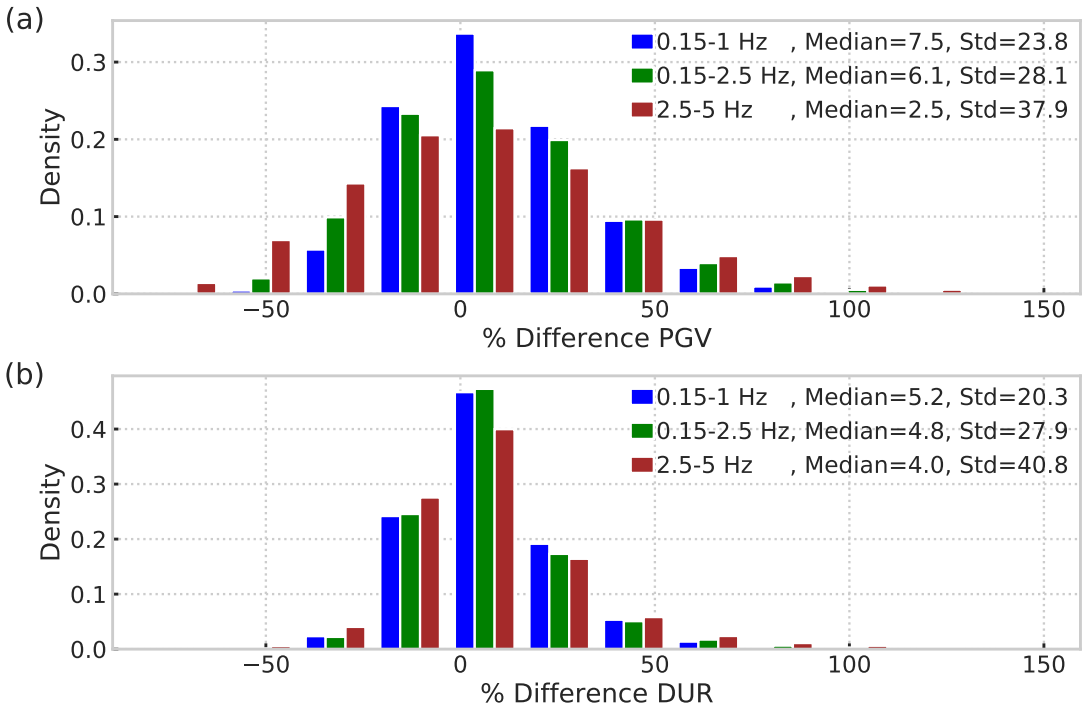

Figure 3.11: Probability density histogram of the difference between Model 16, including SSH with $\sigma = 5\%$ and $a = 5000$ m, and Model 1 (no SSHs). The definition of percent difference (x-axis) is the same as in Figure 3.5.

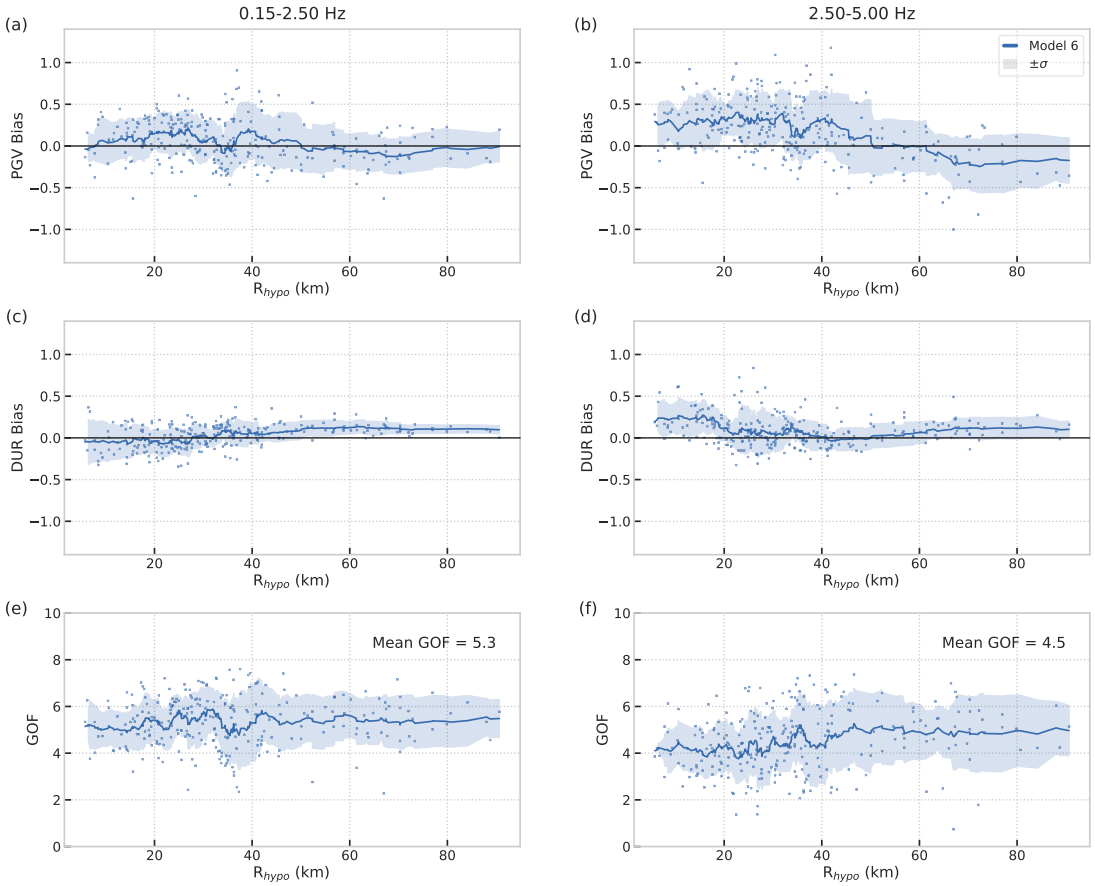

Figure 3.12: Bias of (top row) PGV and (center row) DUR and (bottom row) GOF for bandwidths (left column) 0.15-2.5 Hz and (right column) 2.5-5 Hz at all 259 stations for Model 6 (see Table 3.2 for a list of model features). The bias is calculated in the same way as for Figure 3.9. The solid line depicts the moving average using a 20-point window. The shading denotes the standard deviation centered at the mean.

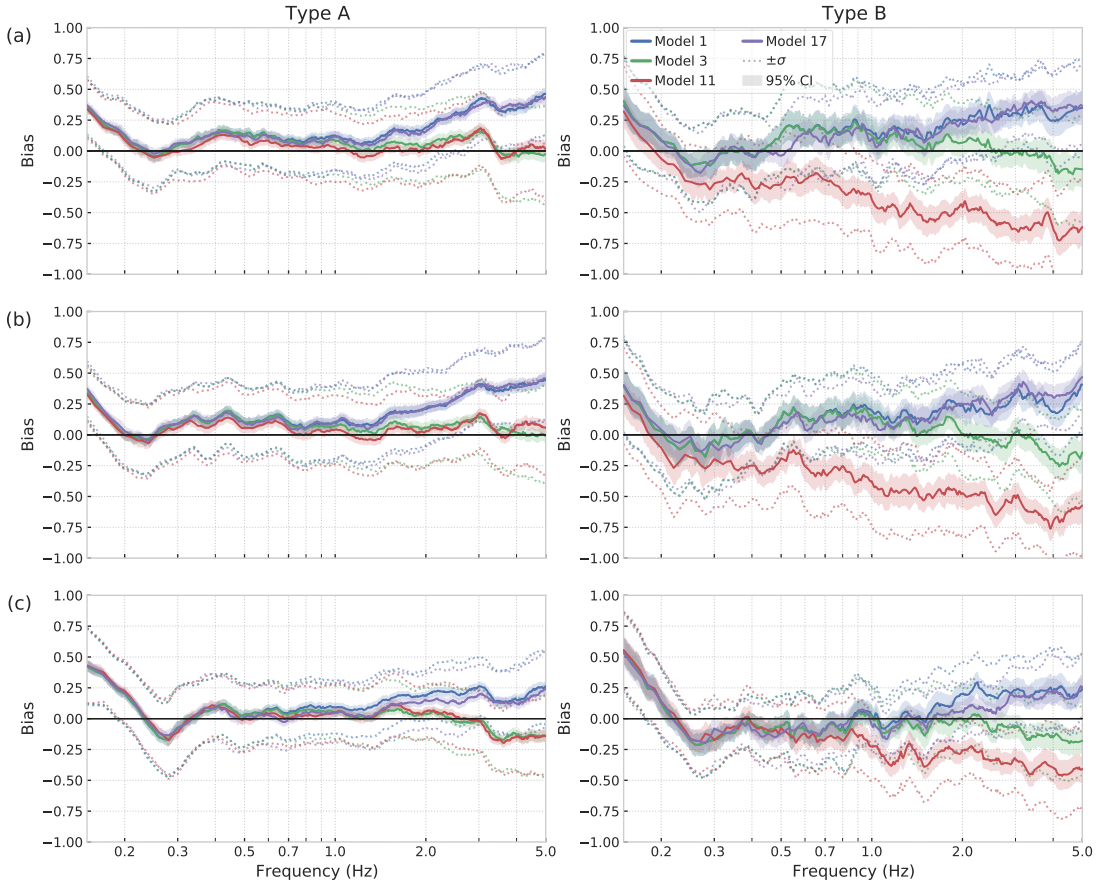

Figure 3.13: Bias of FAS on the (a) east-west, (b) north-south and (c) vertical components, calculated from models labeled by their IDs. A positive (negative) value depicts overprediction (underprediction). The left and right columns shows type A and B sites, respectively. The solid lines depict the median of FAS, where the narrow band is the 95% confidence interval of the median, and the dashed lines depict the standard deviation centered at the median.

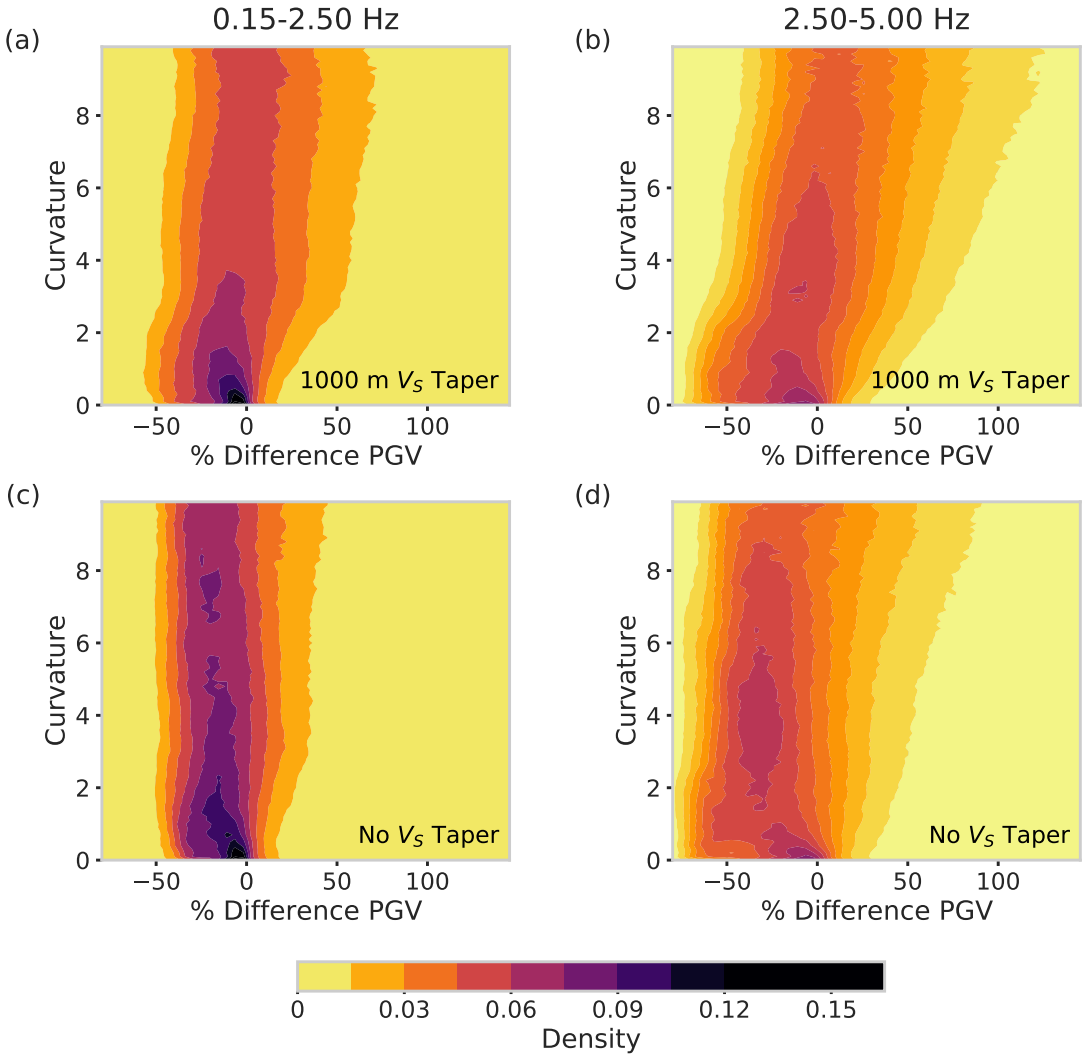

Figure 3.14: Density of PGV change for models with topography relative to models without topography for bandwidths of (left column) 0.15-2.5 Hz and (right column) 2.5-5 Hz, and models with (top row) and without (bottom row) modified shallow velocities. The y-axis depicts topographic curvature smoothed using a 2-D window of dimensions 640 m $\times$ 640 m. Values toward the top right (bottom left) denote strong amplification at steep topography (deamplification at flat topography). Note that density intervals do not correspond to constant bin sizes.

Appendix

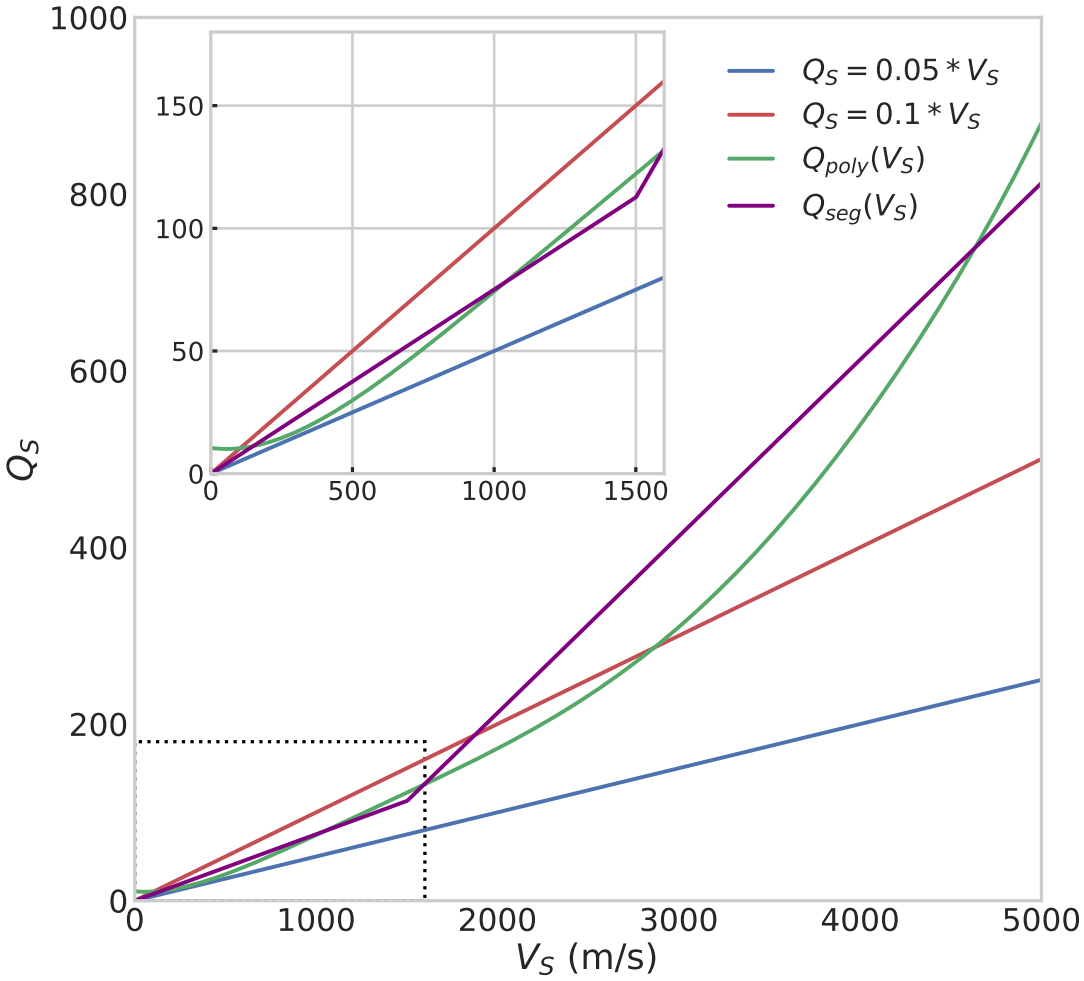

Figure A3.1: Shear-wave quality factor (Q_S) plotted against V_S (m/s) for several attenuation models widely used in the literature (e.g., Olsen *et al.*, 2003; Taborda and Bielak, 2014; Savran and Olsen, 2019; Withers *et al.*, 2019) and investigated here. The inset figure in the upper left corner zooms into $V_S <= 1600$ m/s, denoted by the dashed black box. Note that these Q_S relations are valid for constant Q models, or frequency-dependent Q models for frequencies below 1 Hz.

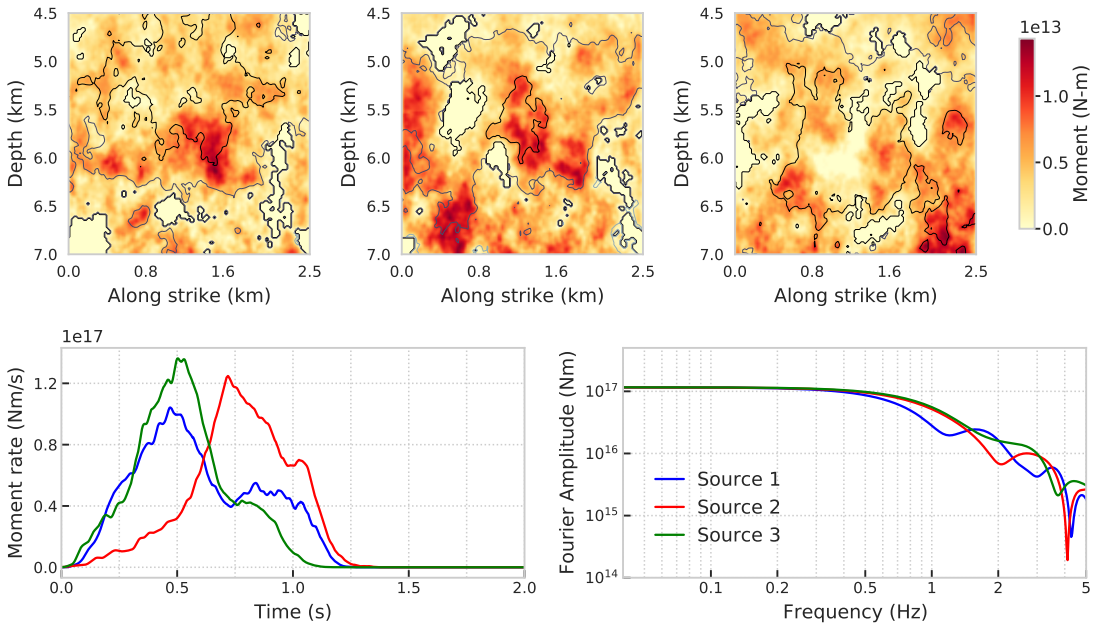

Figure A3.2: Description of three candidate source models used in this study. (top) Slip distribution (shading) for sources 1, 2 and 3 (left to right), characterized by their hypocentral depths at 5, 5.5 and 6 km, respectively. Contours depict rupture time at a 0.4 s interval starting from 0. (bottom) (left) sum of the moment rates for all subfaults and (right) Fourier amplitude spectrum, respectively. Sources 1, 2 and 3 (from left to right in the first row) are characterized by their hypocentral depths at 5, 5.5 and 6 km, respectively. The contours represent rupture time at a 0.4 s interval starting from 0. Source 1 is the default source model used elsewhere in this chapter.

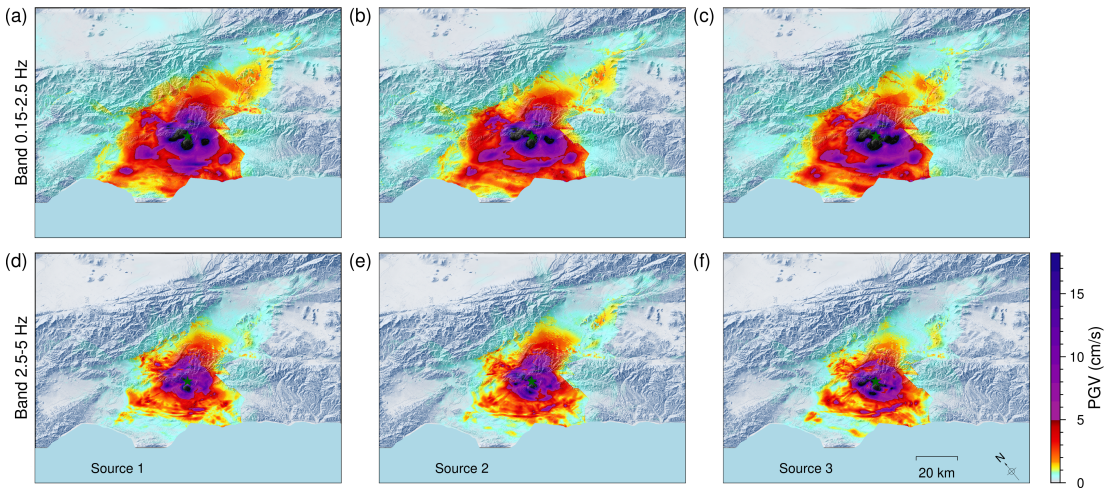

Figure A3.3: PGVs for sources 1, 2 and 3 (from left to right; see Fig. 3.3). The top and bottom rows represent the band-pass filtered results for 0.15-2.5 Hz and 2.5-5 Hz, respectively. The star denotes the epicenter.

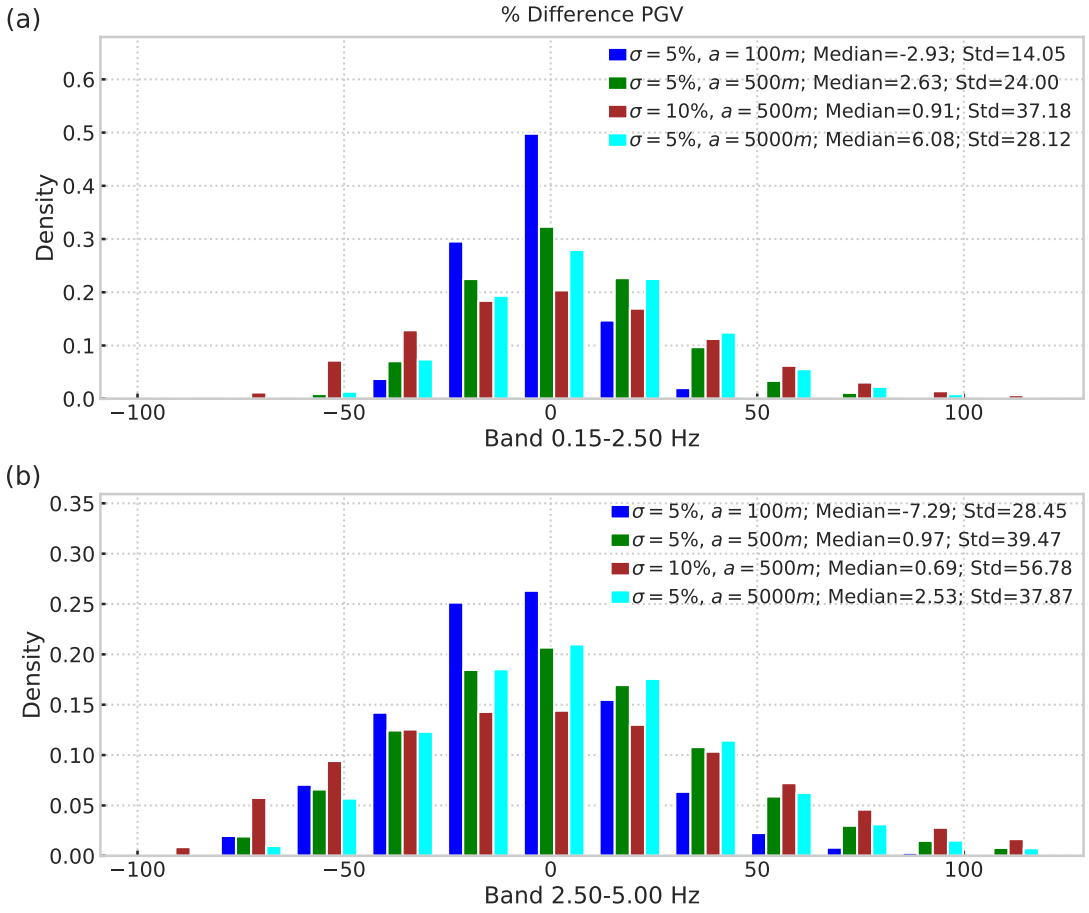

Figure A3.4: Probability density histogram of the PGV difference caused by SSH effects, between Models 12-14 with Model 6 (blue, green and red) , and Model 16 with Model 2 (cyan). The definition of percent difference (x-axis) is the same as in Figure 3.11.

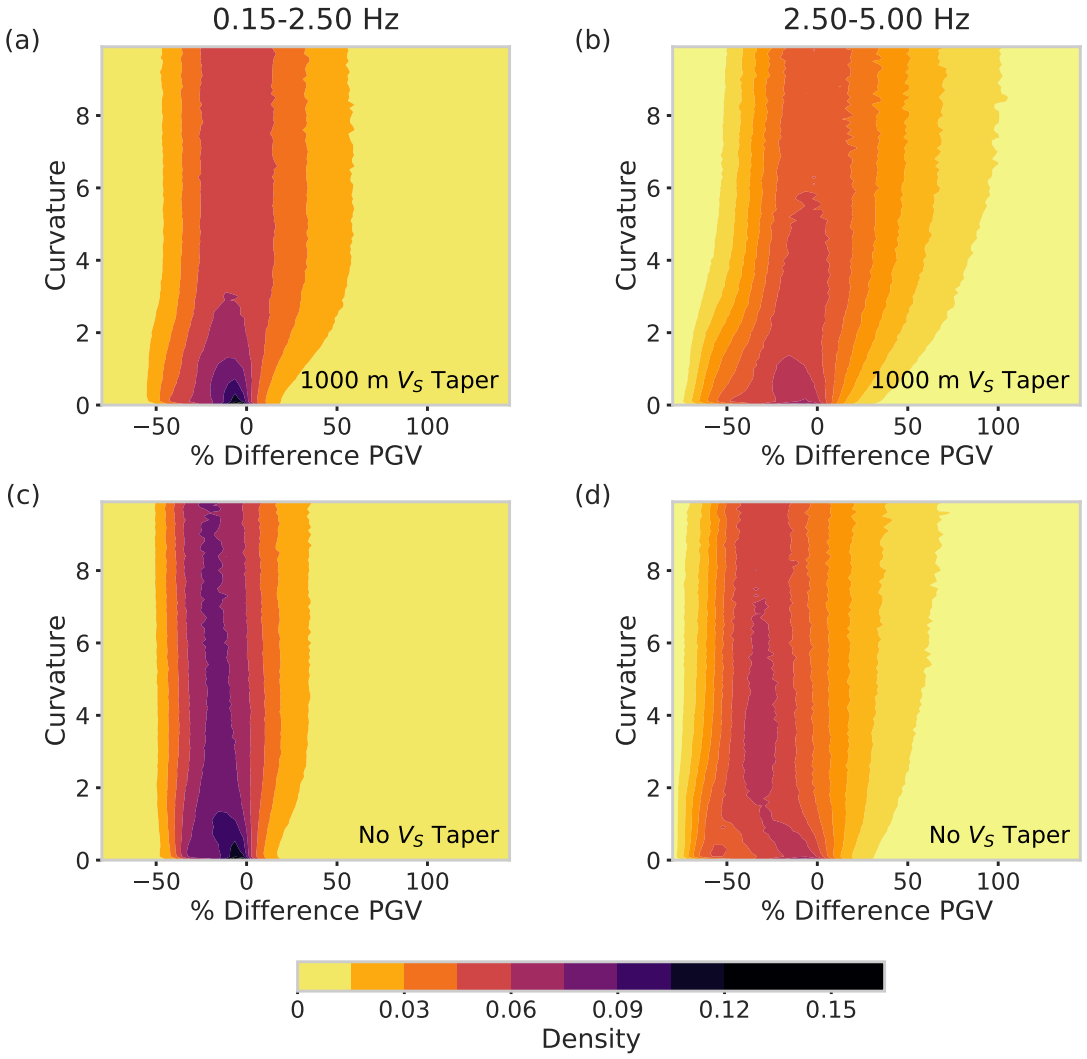

Figure A3.5: Density of PGV change for models with topography relative to models without topography for bandwidths of (left column) 0.15-2.5 Hz and (right column) 2.5-5 Hz, and models with (top row) and (bottom row) without modified shallow velocities. The y-axis depicts topographic curvature smoothed using a 2-D window of 120 m $\times$ 120 m. Values toward the top right (bottom left) denote strong amplification at steep areas (deamplification at flat areas). Note that density intervals do not correspond to constant bin sizes.

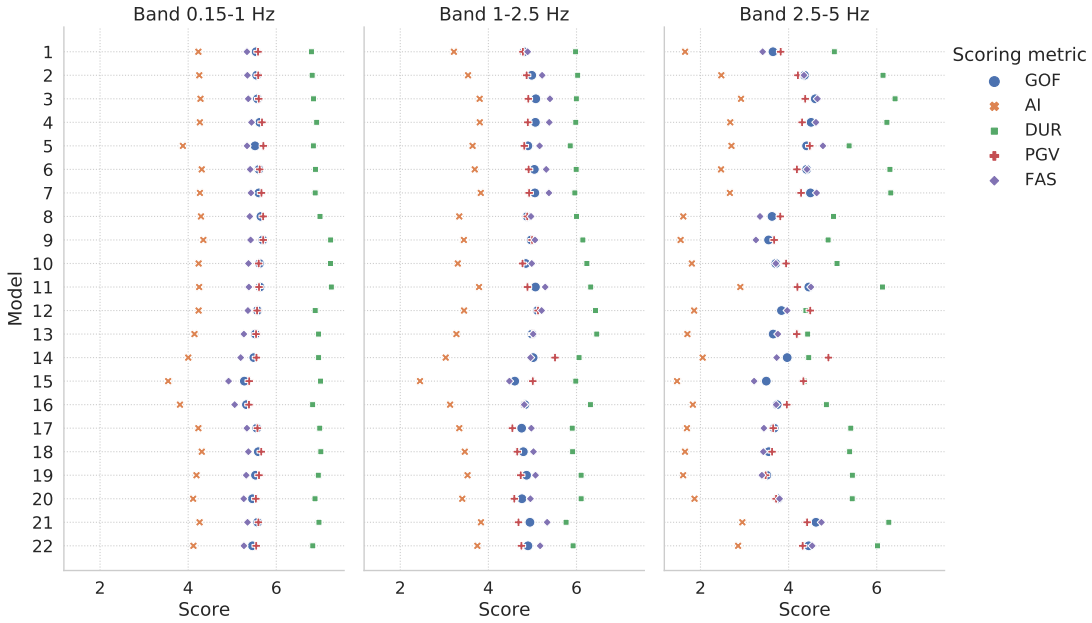

Figure A3.6: GOF scores for a subset of the metrics used in this study, for frequency bands 0.15-1 Hz, 1-2.5 Hz, and 2.5-5 Hz. Model IDs are listed in Table 3.2.

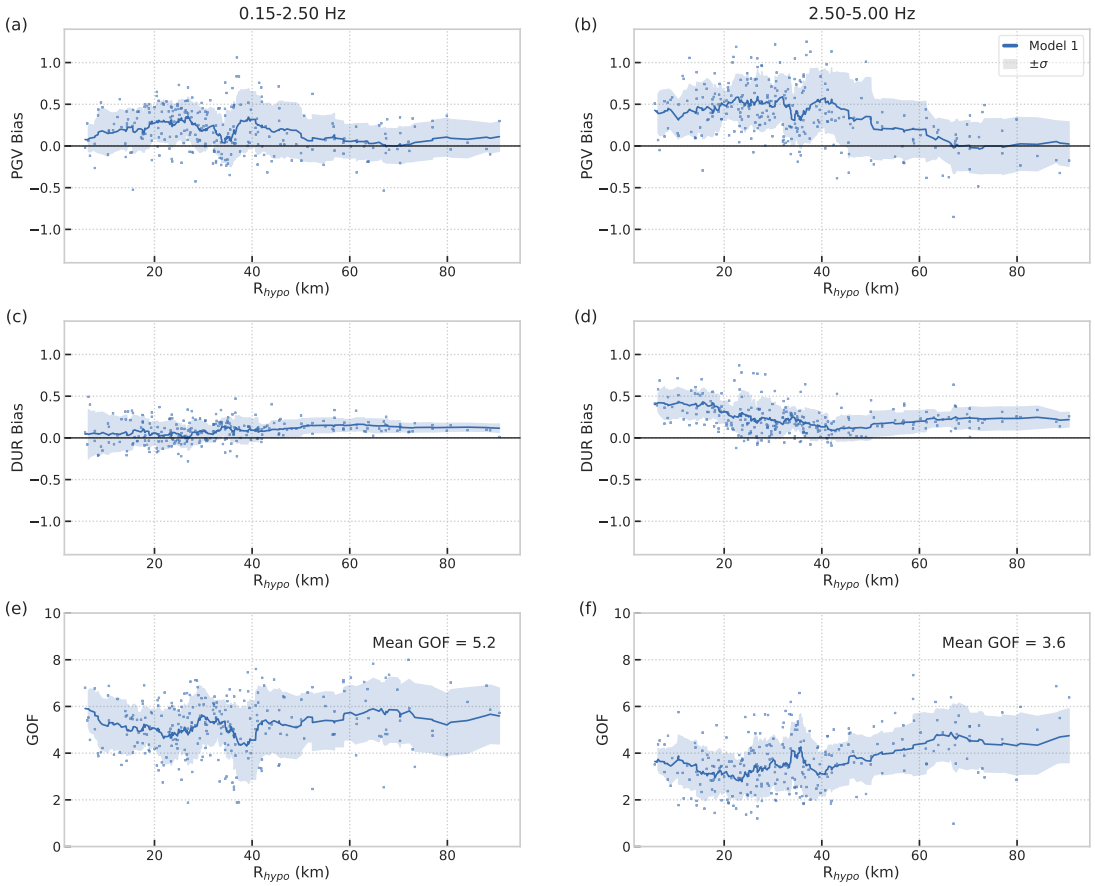

Figure A3.7: Bias of (top row) PGV and (middle row) DUR and GOF (bottom row) for bandwidths of (left column) 0.15-2.5 Hz and (right column) 2.5-5 Hz at all 259 stations for Model 1 (see Table 3.2 for model features). The bias is calculated in the same way as Figure 3.9. The solid line depicts the moving average of the bias of PGV using a 20-point window versus hypocentral distance. The shading denotes the standard deviation centered at the mean.

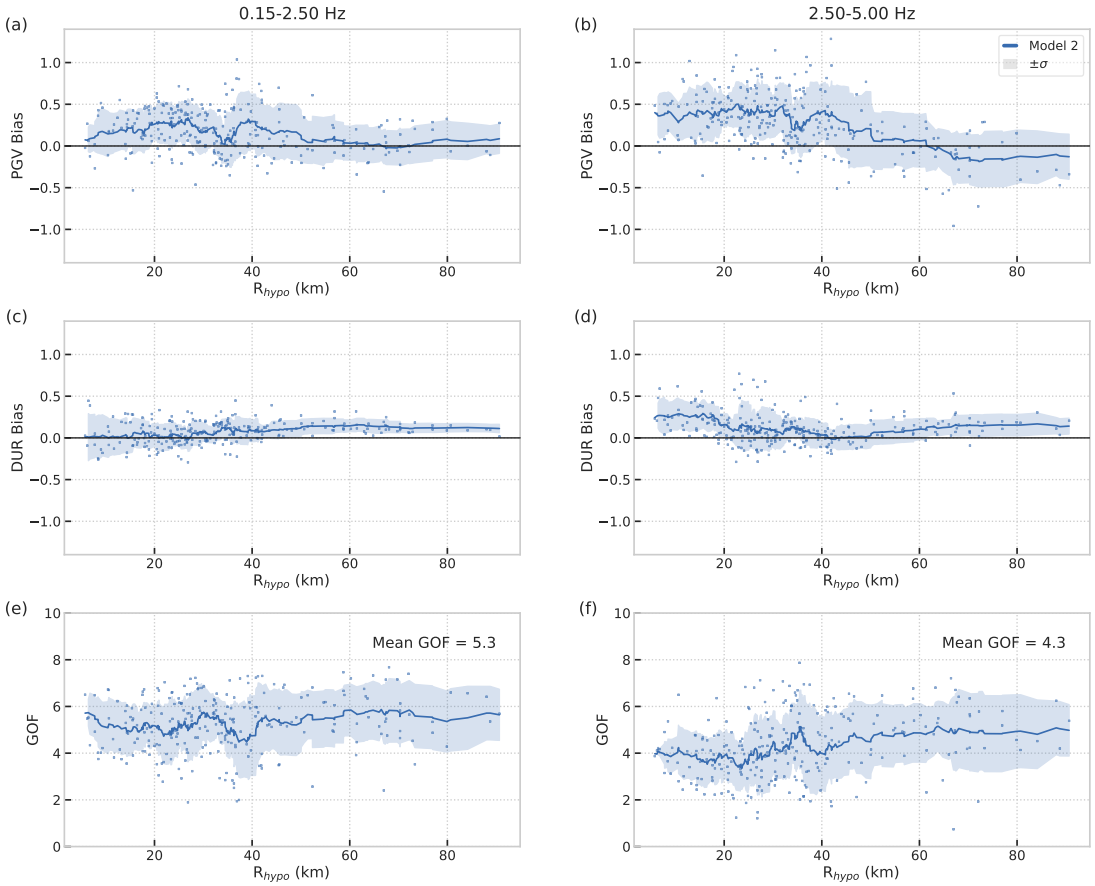

Figure A3.8: Same as Figure A3.7, but for Model 2.

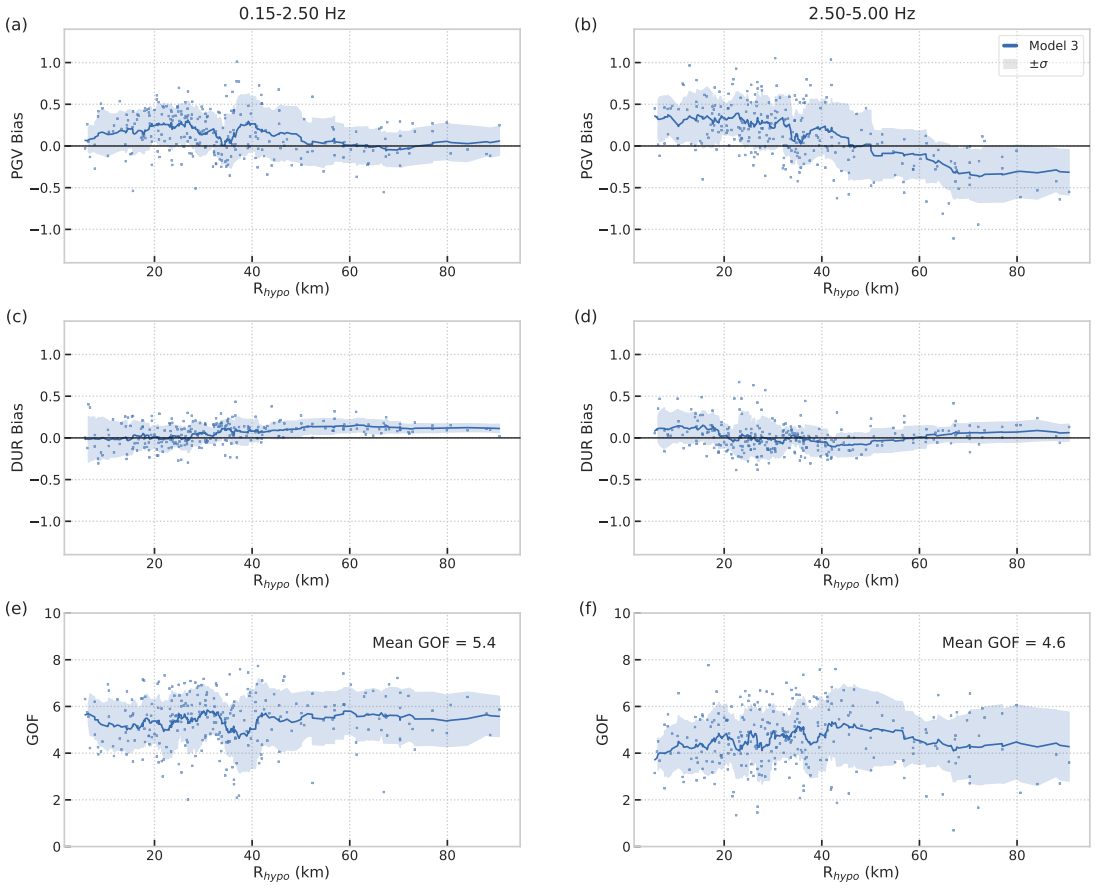

Figure A3.9: Same as Figure A3.7, but for Model 3.

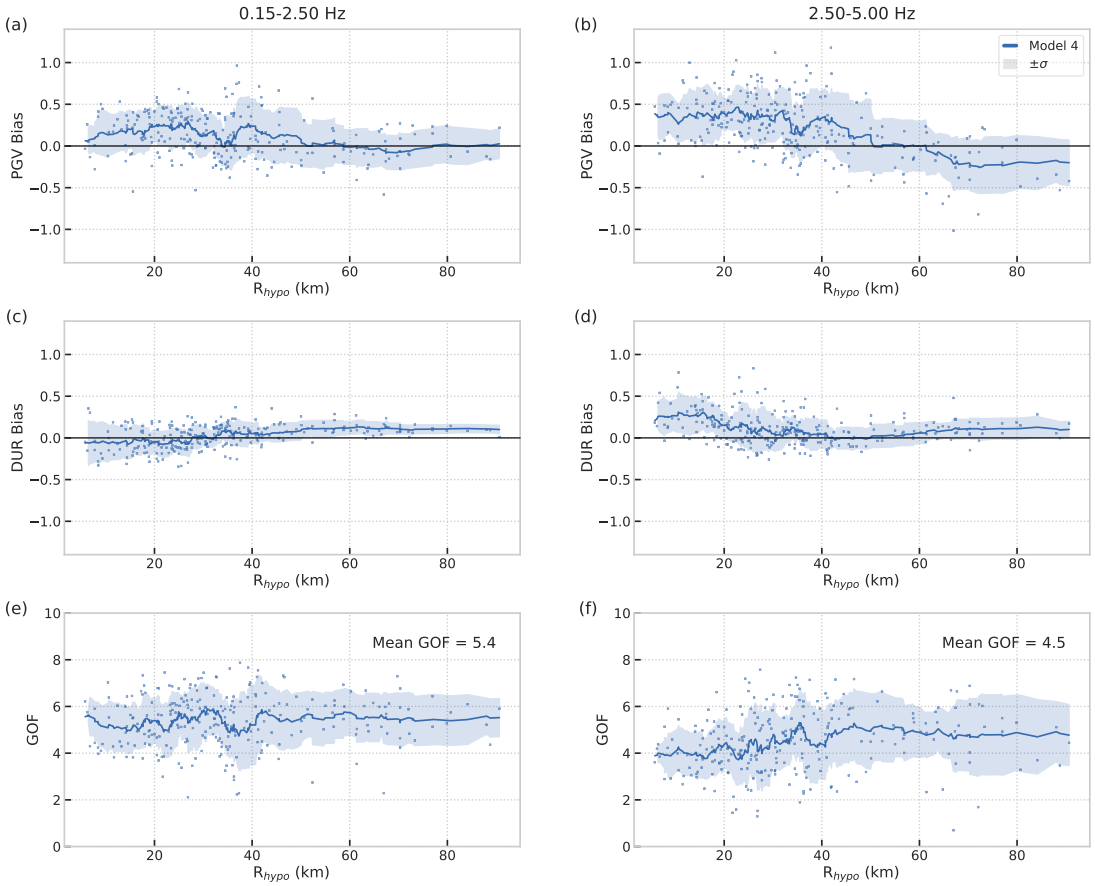

Figure A3.10: Same as Figure A3.7, but for Model 4.

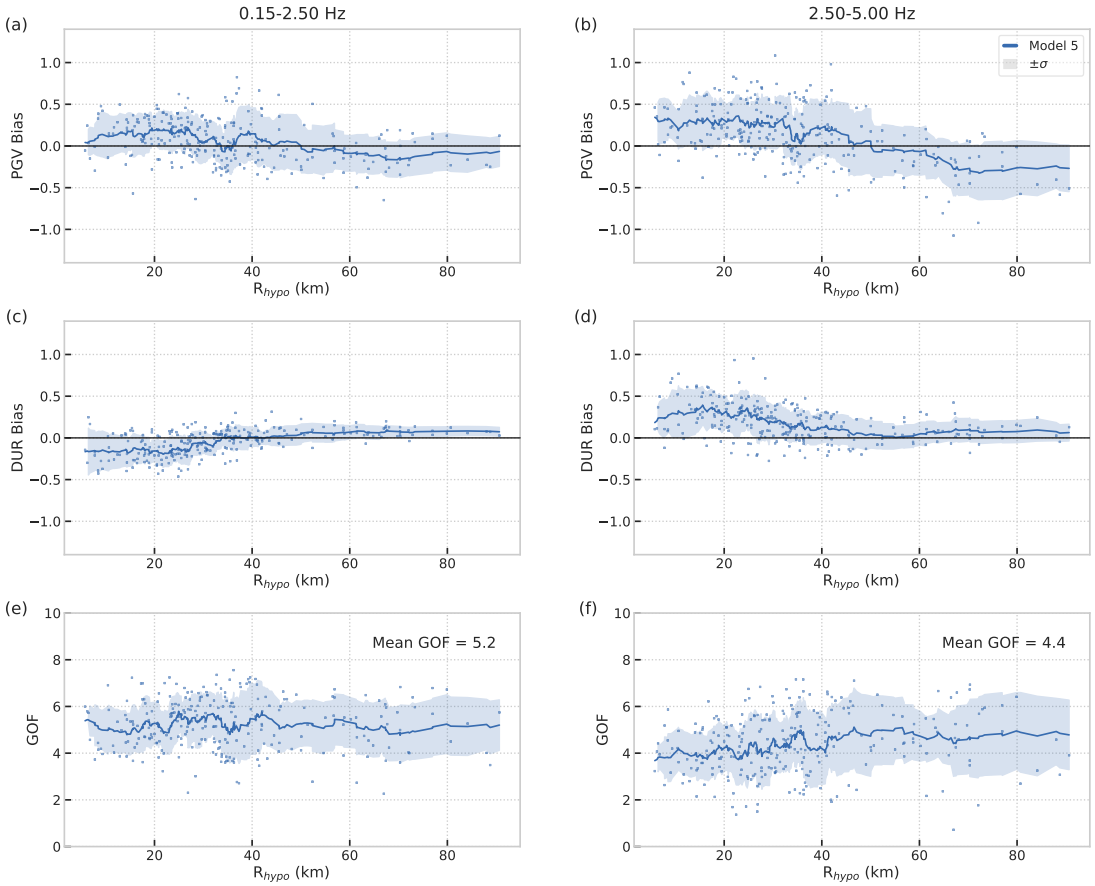

Figure A3.11: Same as Figure A3.7, but for Model 5.

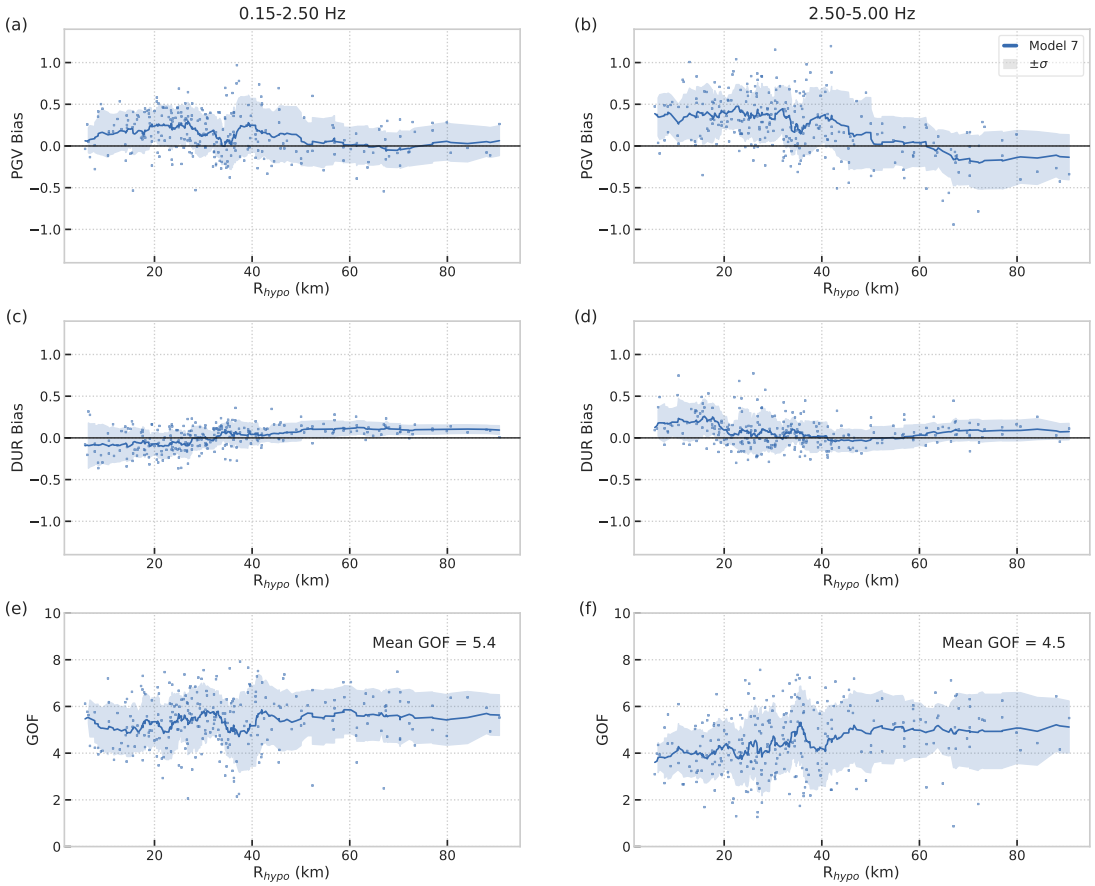

Figure A3.12: Same as Figure A3.7, but for Model 7.

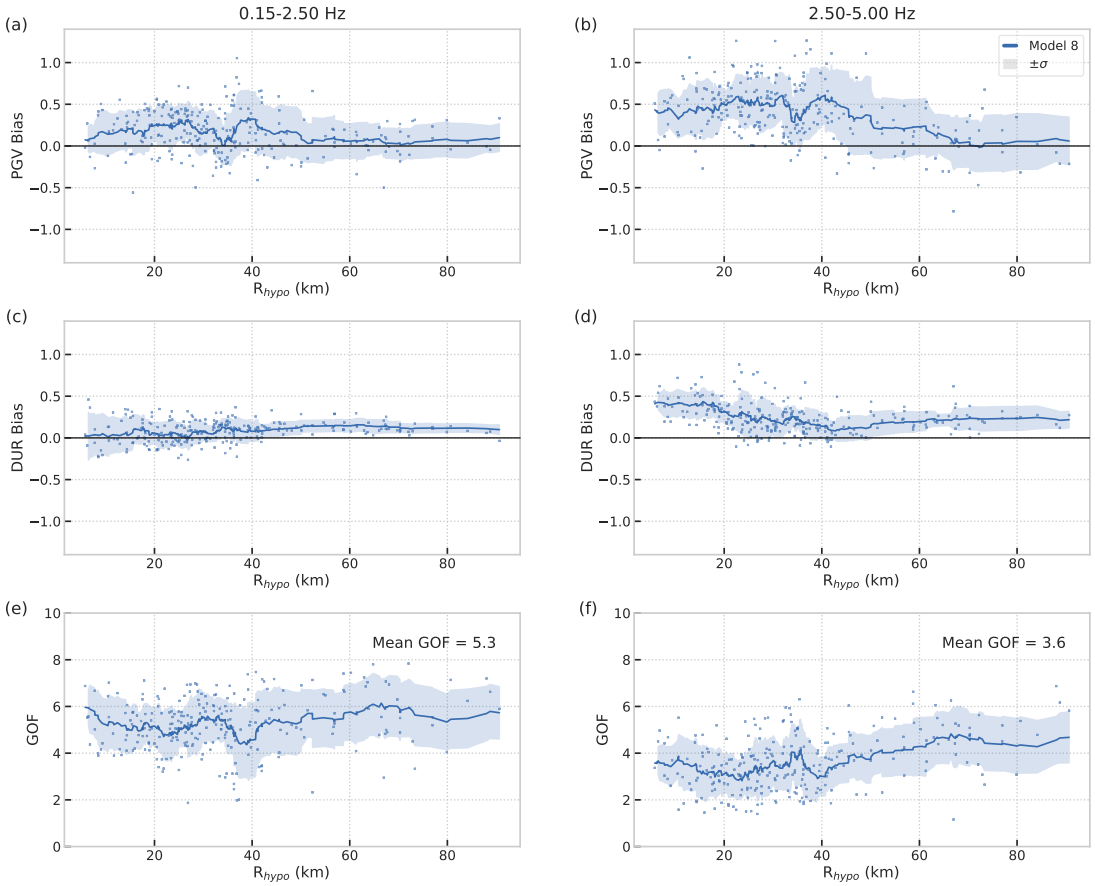

Figure A3.13: Same as Figure A3.7, but for Model 8.

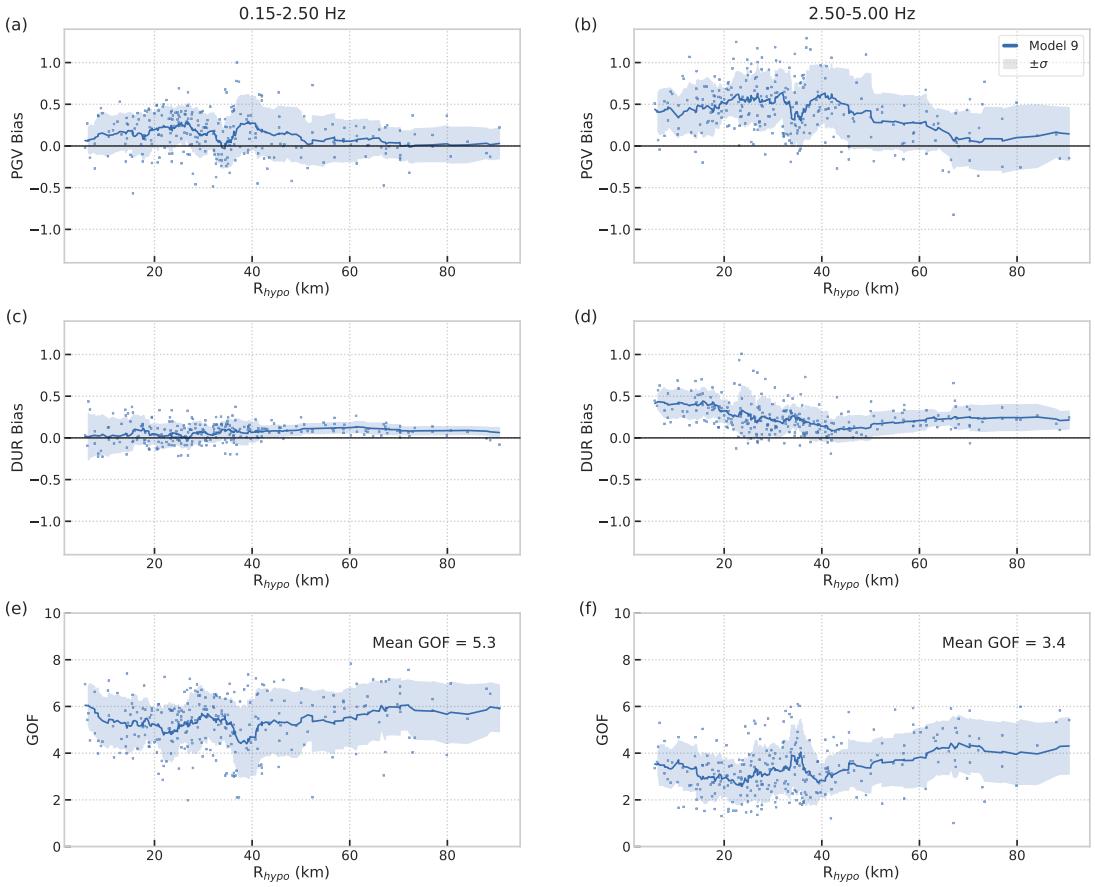

Figure A3.14: Same as Figure A3.7, but for Model 9.

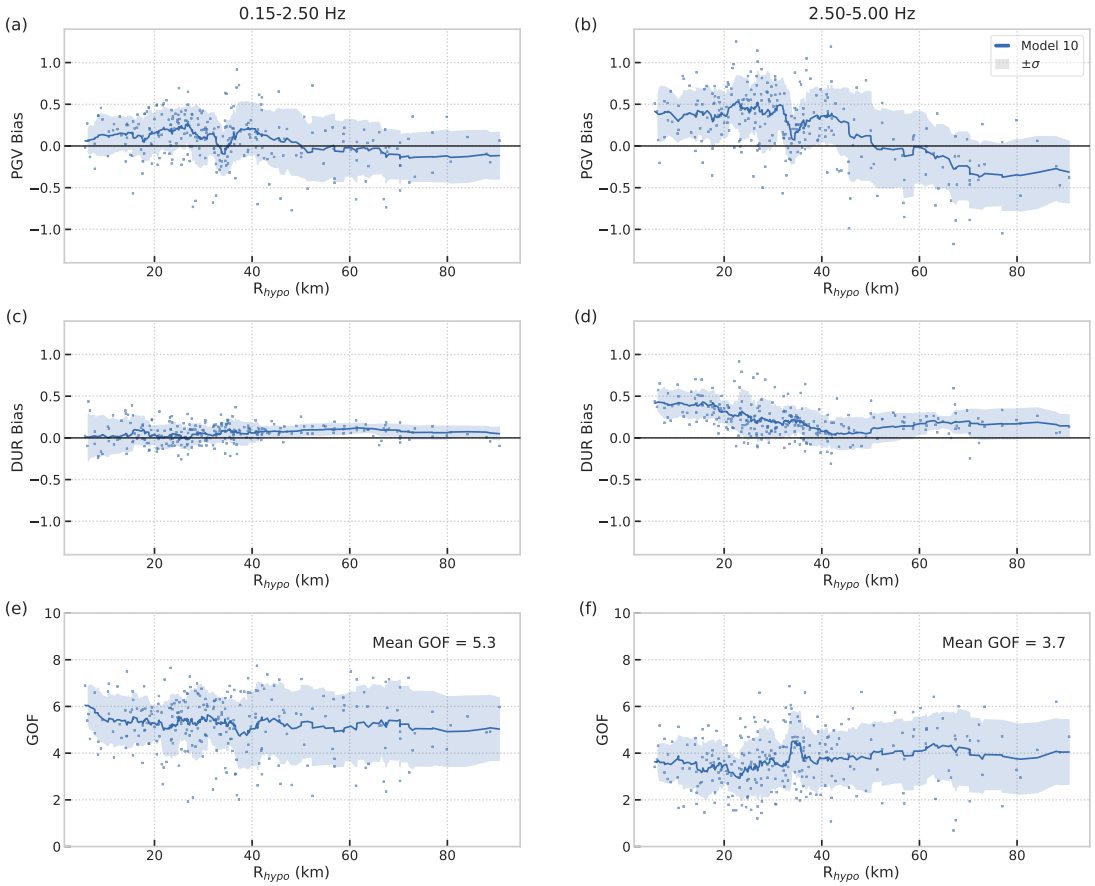

Figure A3.15: Same as Figure A3.7, but for Model 10.

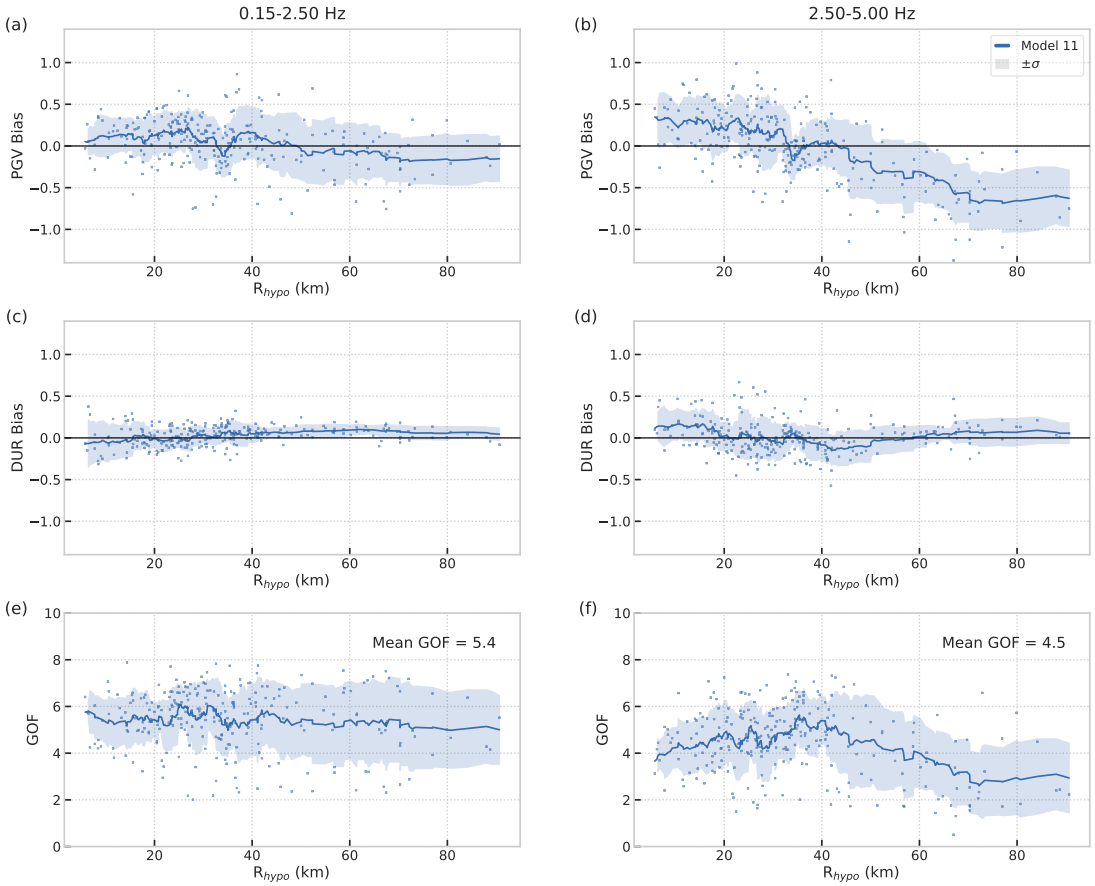

Figure A3.16: Same as Figure A3.7, but for Model 11.

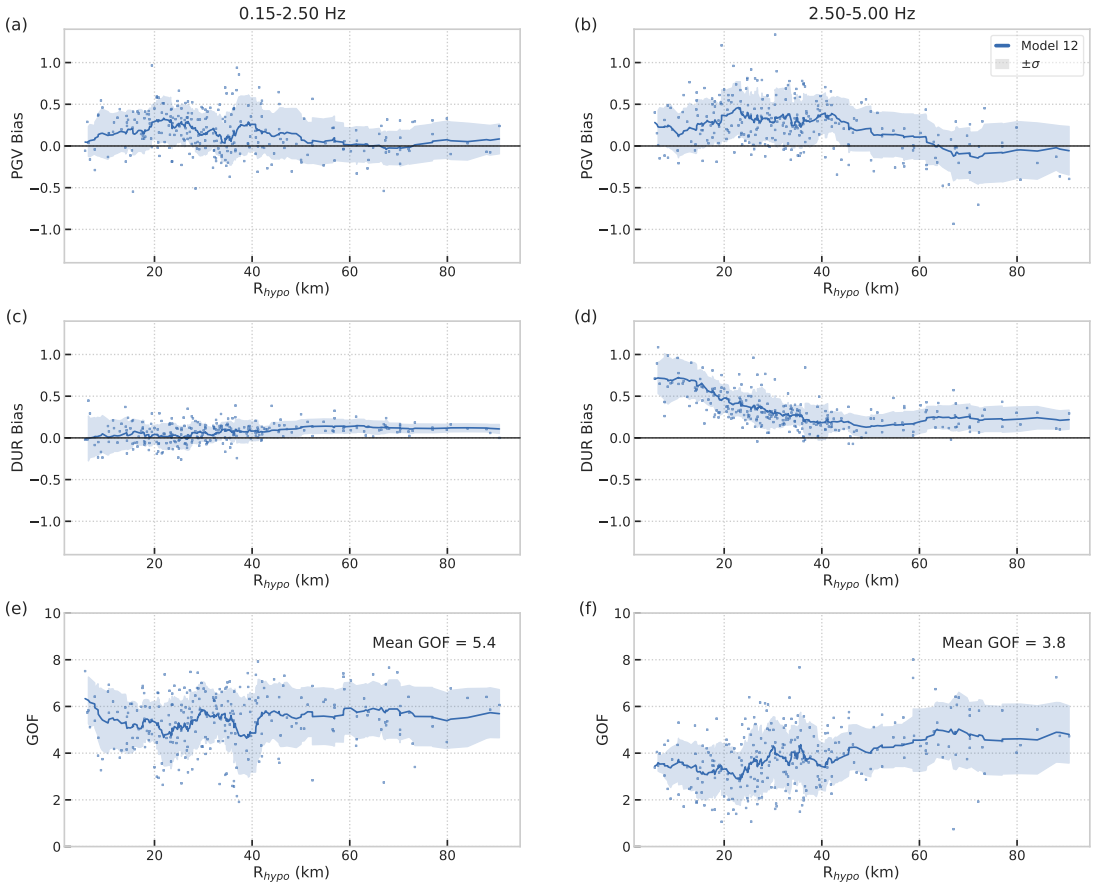

Figure A3.17: Same as Figure A3.7, but for Model 12.

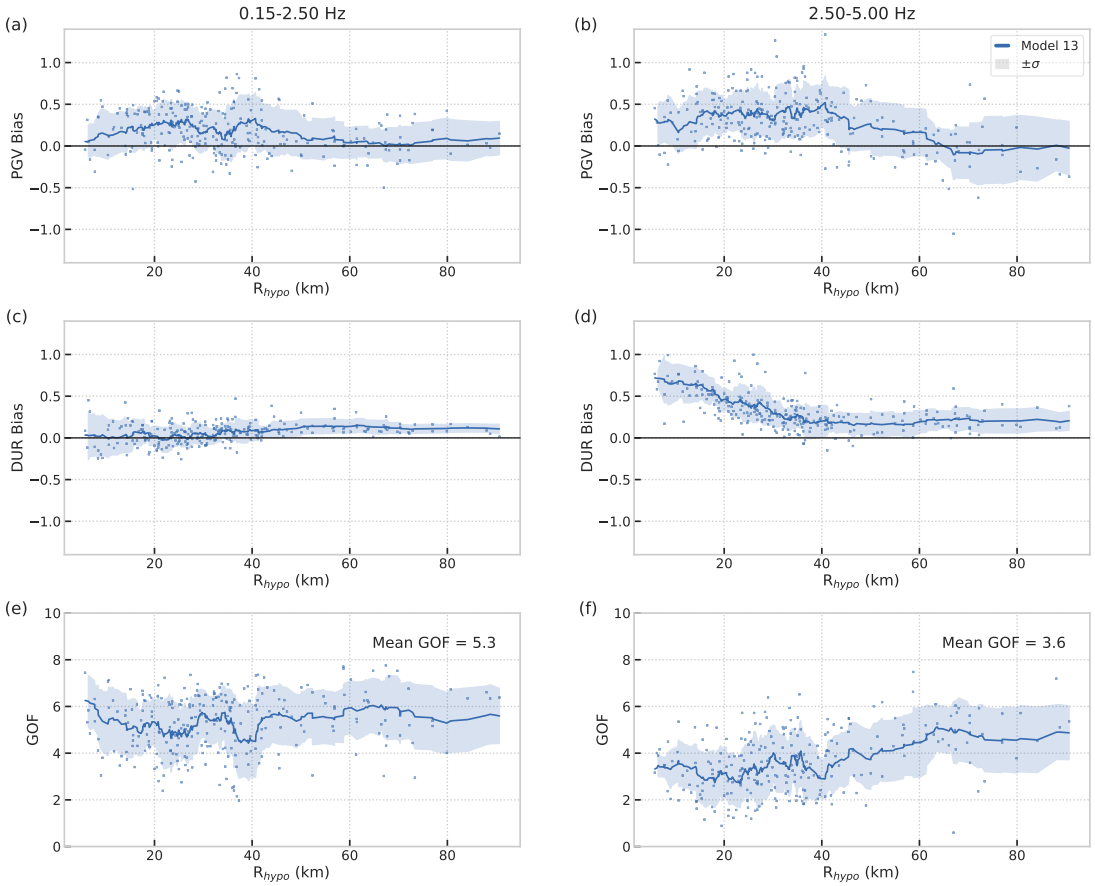

Figure A3.18: Same as Figure A3.7, but for Model 13.

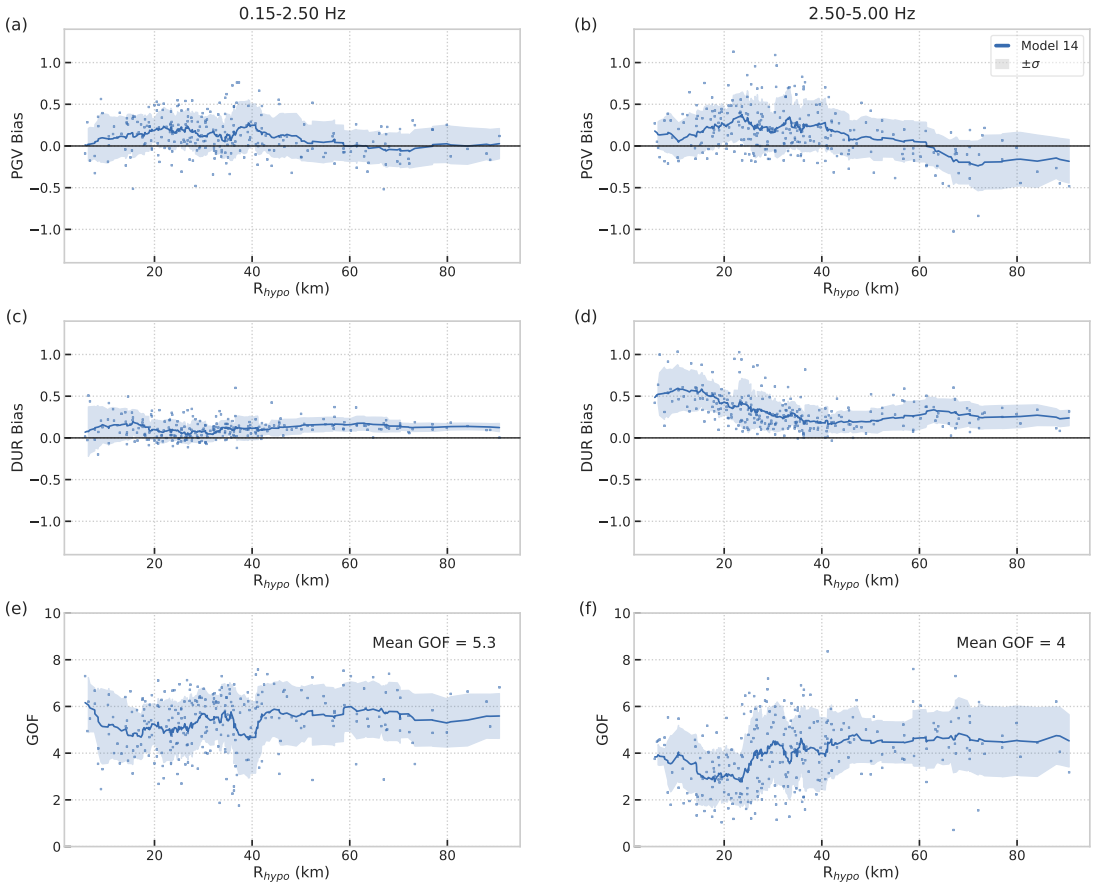

Figure A3.19: Same as Figure A3.7, but for Model 14.

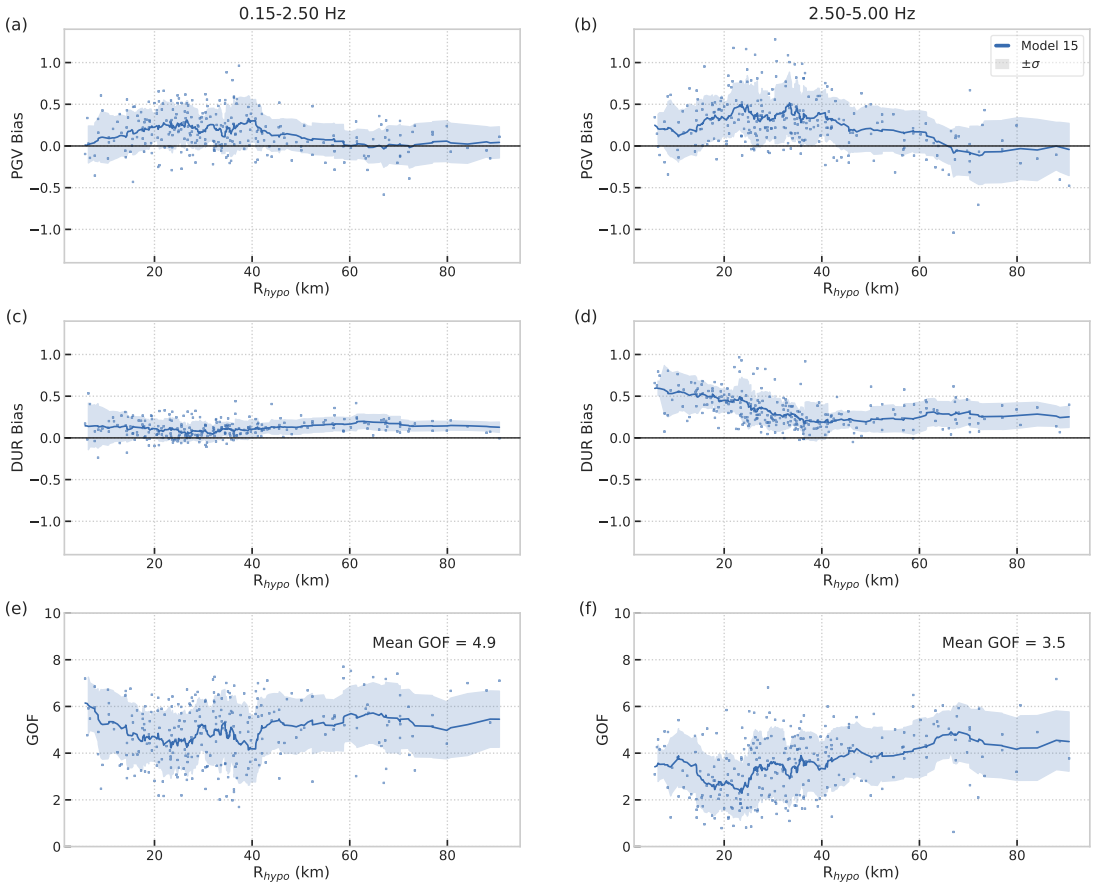

Figure A3.20: Same as Figure A3.7, but for Model 15.

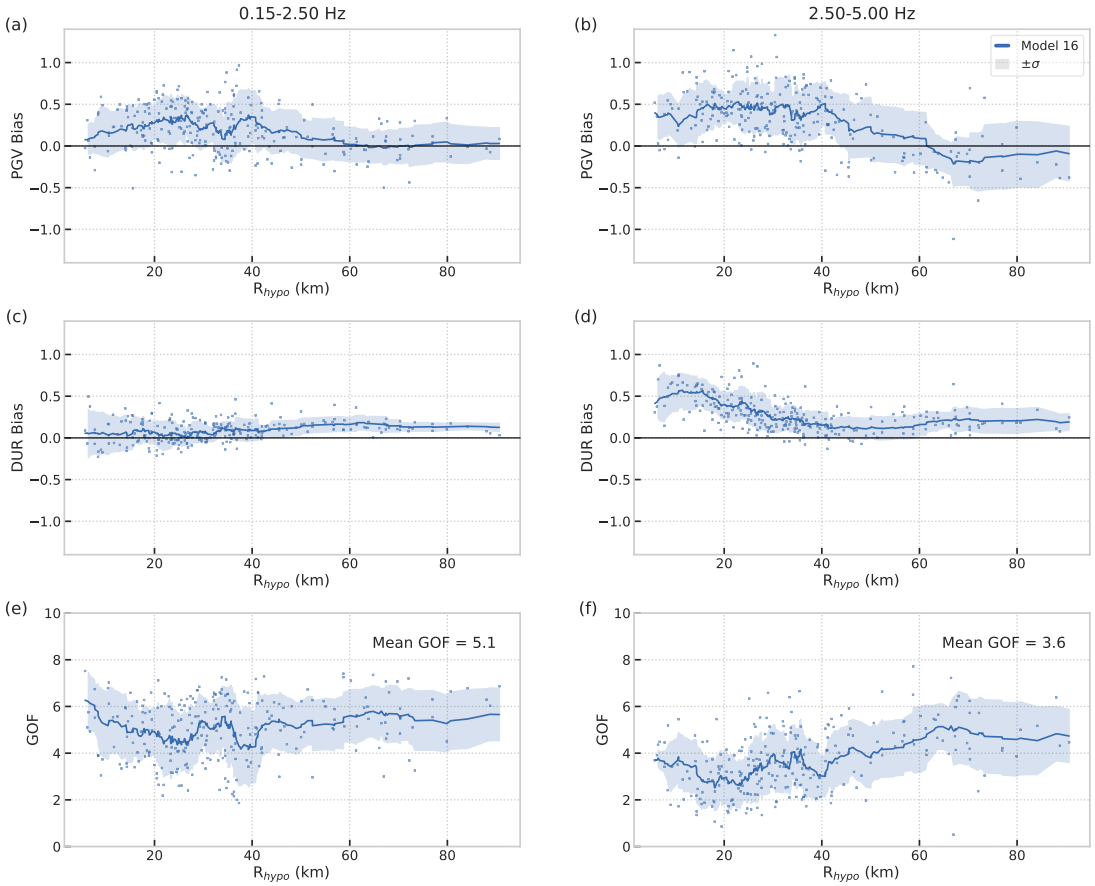

Figure A3.21: Same as Figure A3.7, but for Model 16.

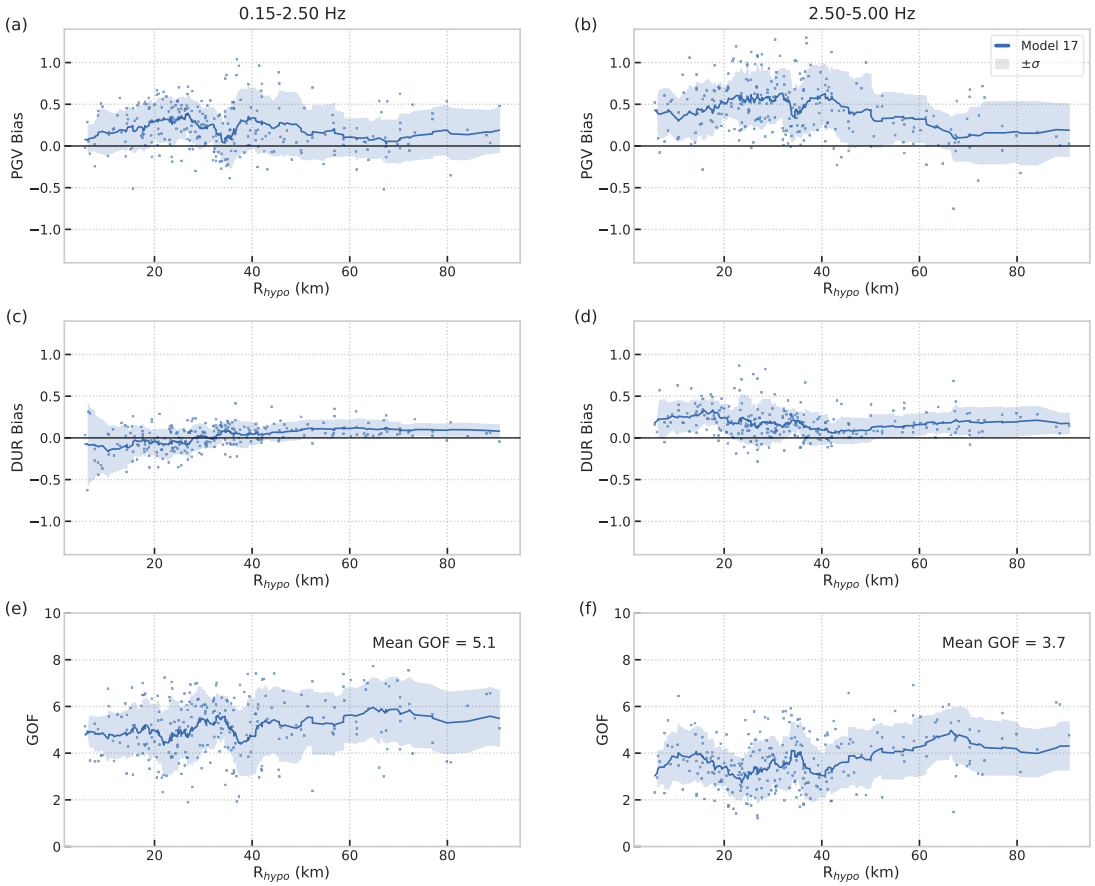

Figure A3.22: Same as Figure A3.7, but for Model 17.

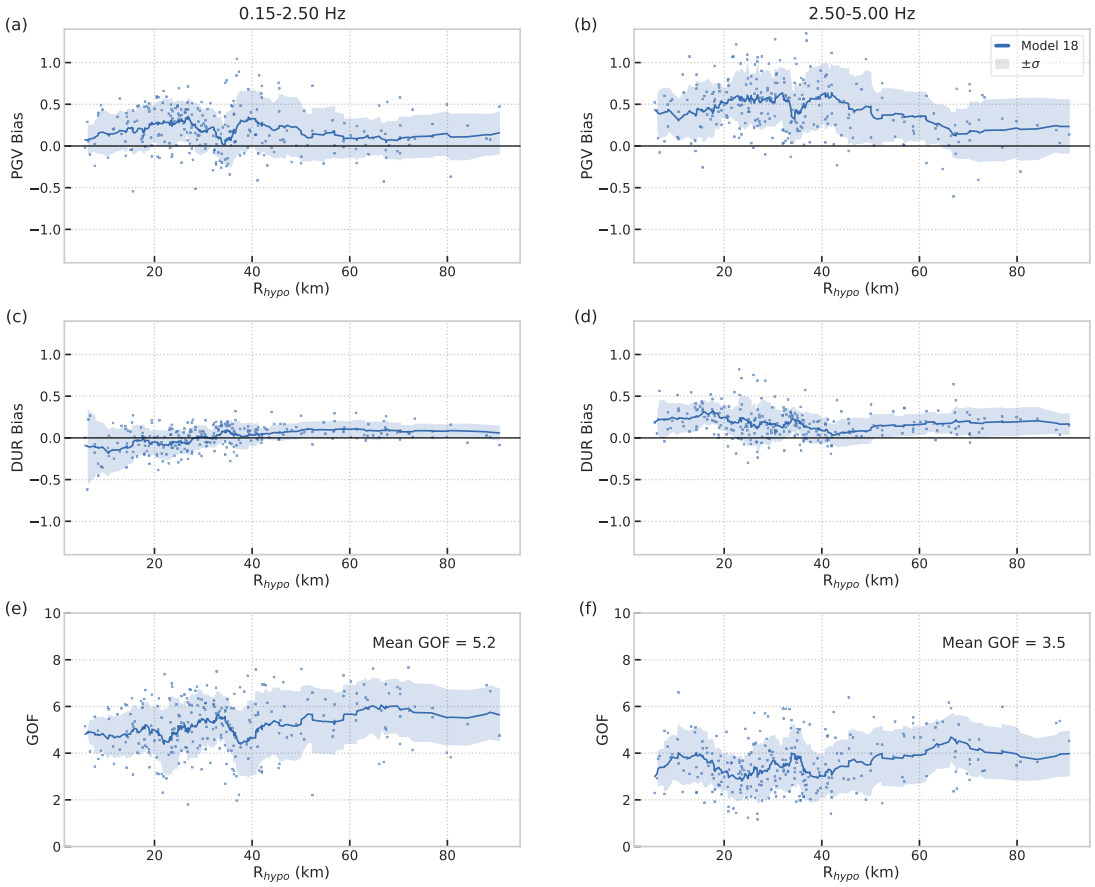

Figure A3.23: Same as Figure A3.7, but for Model 18.

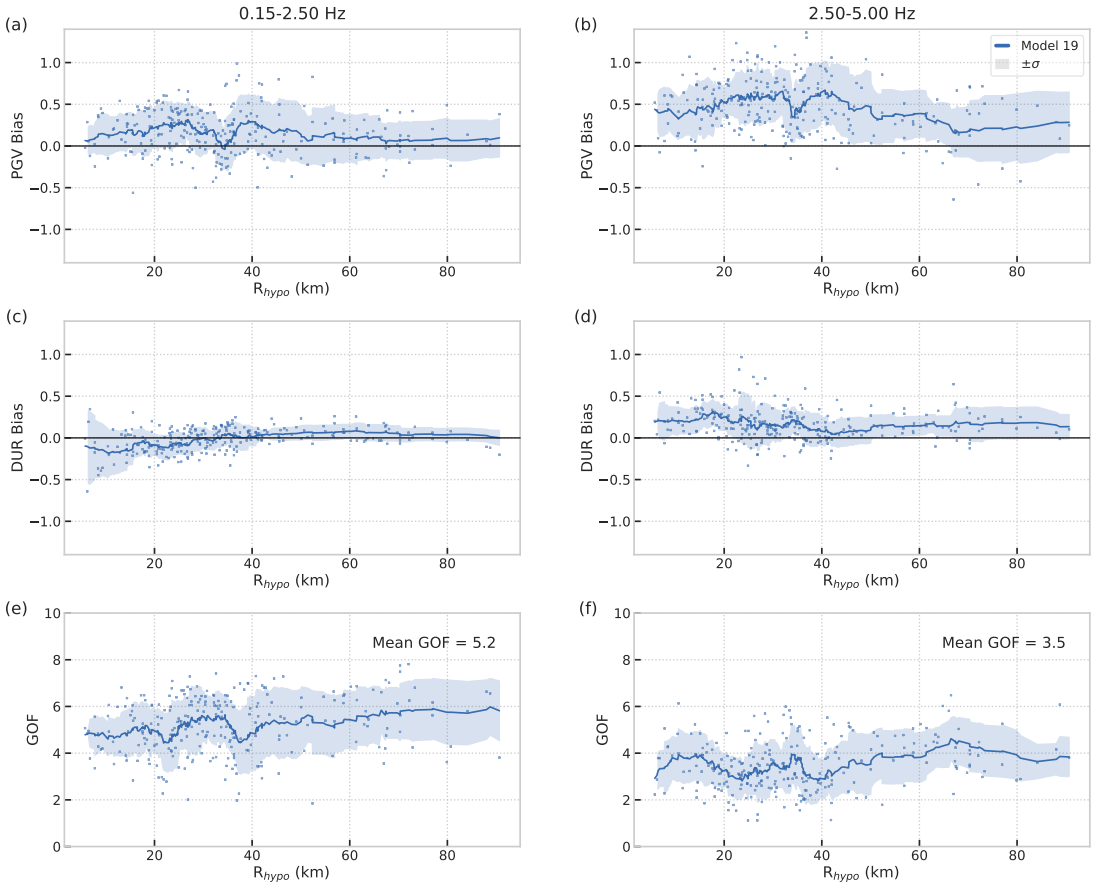

Figure A3.24: Same as Figure A3.7, but for Model 19.

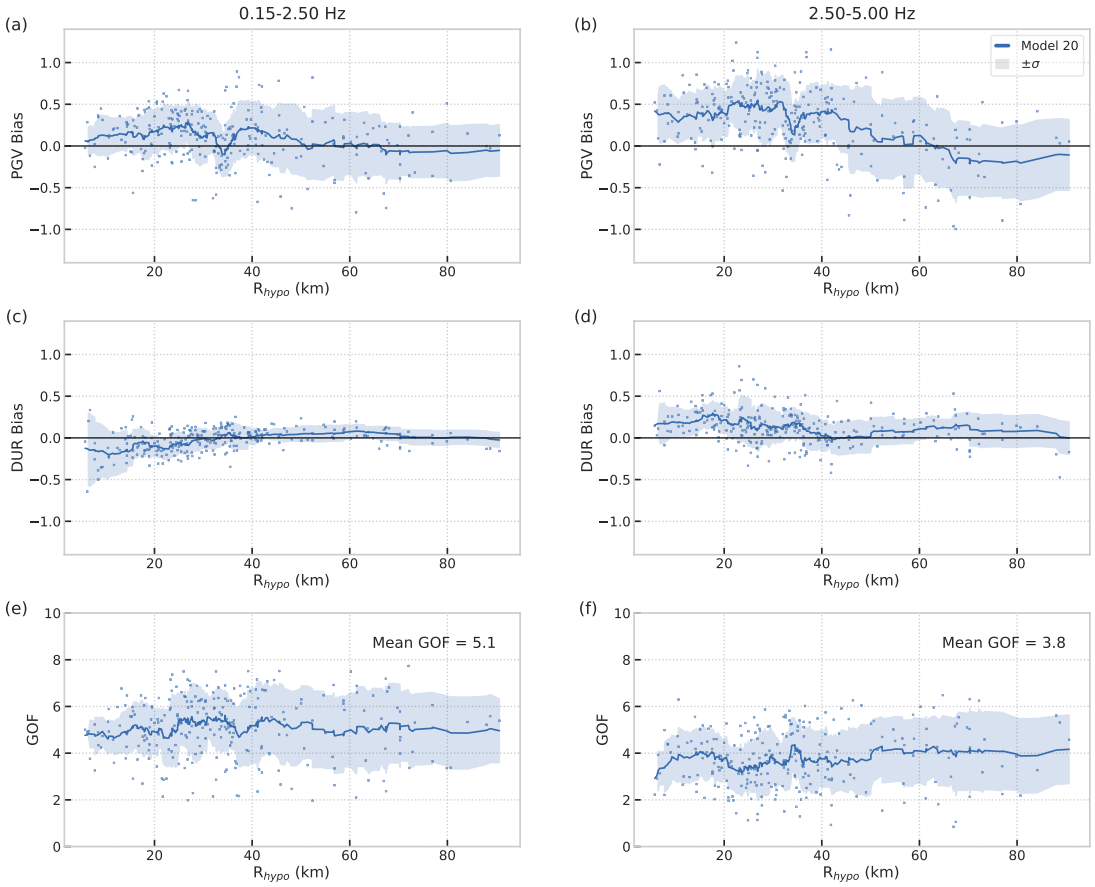

Figure A3.25: Same as Figure A3.7, but for Model 20.

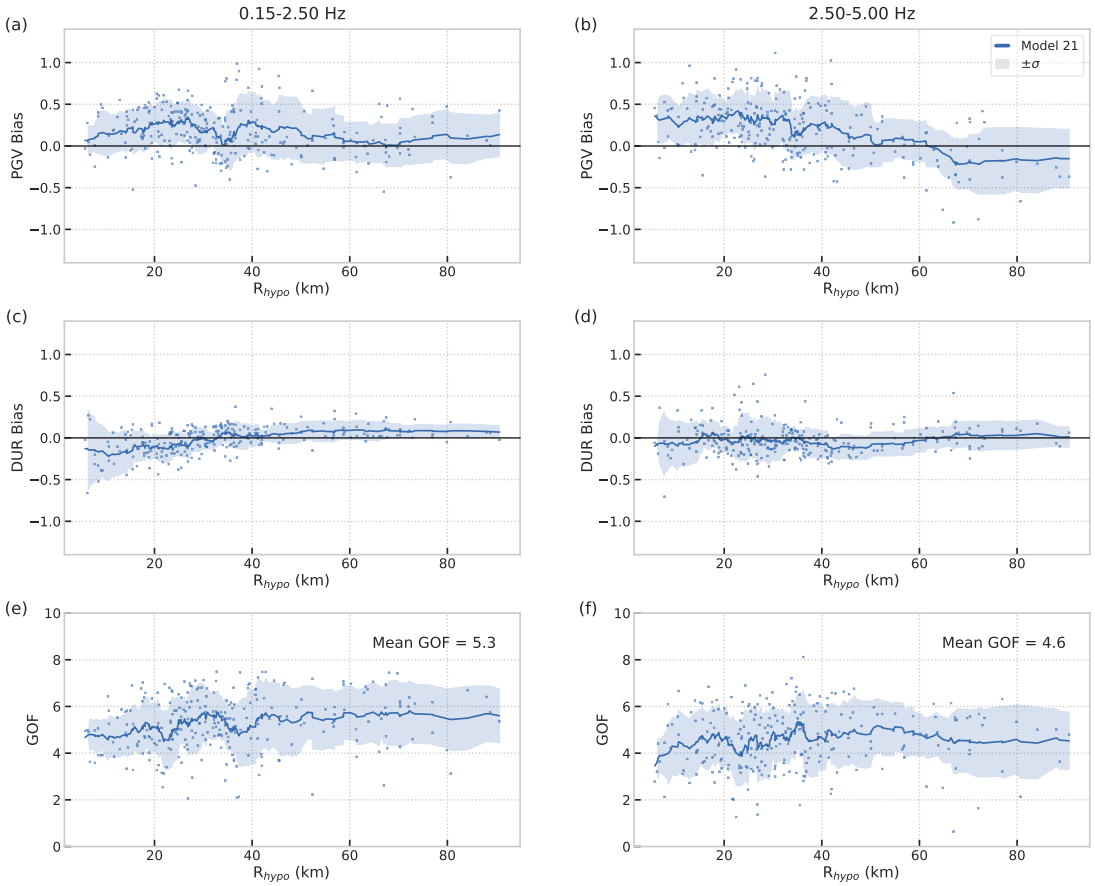

Figure A3.26: Same as Figure A3.7, but for Model 21.

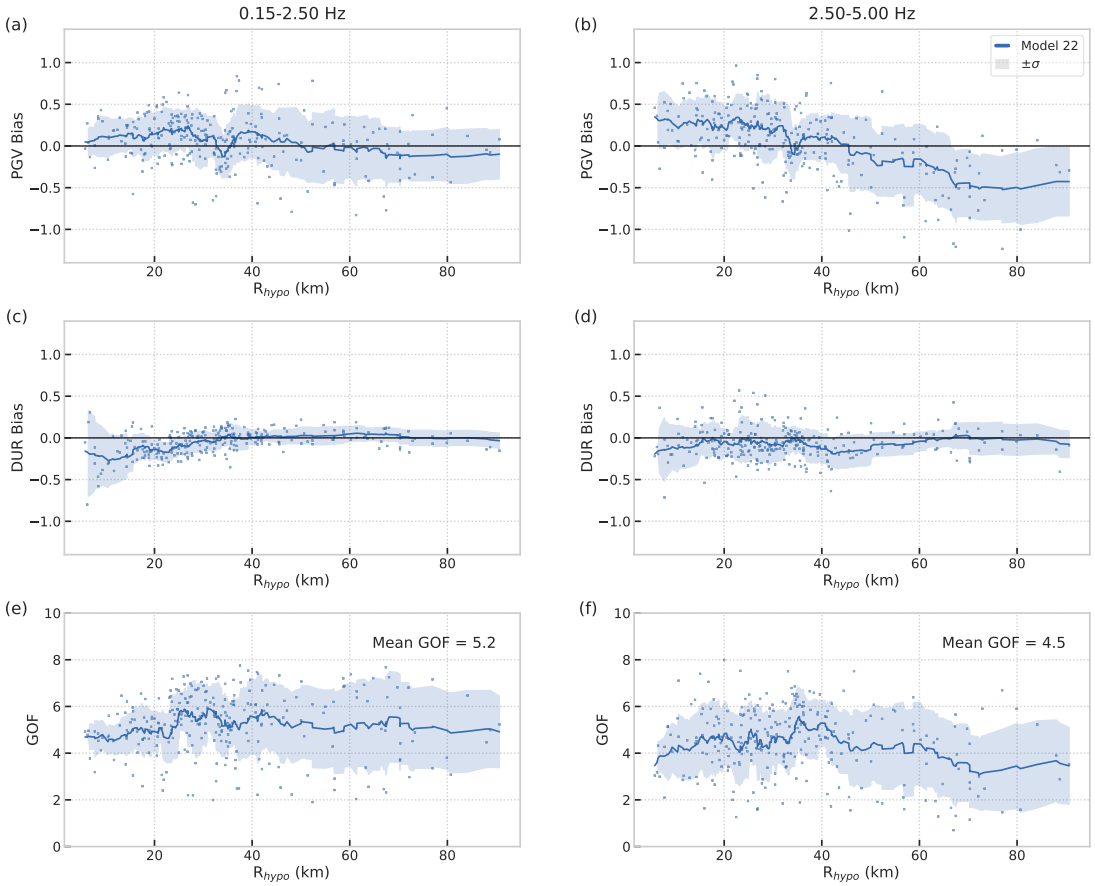

Figure A3.27: Same as Figure A3.7, but for Model 22.

Chapter 4

Modeling of Empirical Transfer Functions with 3D Velocity Structure

Empirical transfer functions (ETFs) between seismic records observed at the surface and depth represent a powerful tool to estimate site effects for earthquake hazard analysis. However, conventional modeling of site amplification, with assumptions of horizontally polarized shear waves propagating vertically through 1D layered homogeneous media, often poorly predicts the ETFs, particularly, in which large lateral variations of velocity are present. Here, we test whether more accurate site effects can be obtained from theoretical transfer functions (TTFs) extracted from physics-based simulations that naturally incorporate the complex material properties. We select two well-documented downhole sites (the KiK-net site TKCH05 in Japan and the Garner Valley site, Garner Valley Downhole Array, in southern California) for our study. The 3D subsurface geometry at the two sites is estimated by means of the surface topography near the sites and information from the shear-wave profiles obtained from borehole logs. By comparing the TTFs to ETFs at the selected sites, we show how simulations using the calibrated 3D models can significantly improve site amplification estimates as compared to 1D model predictions. The primary reason for this improvement in 3D models is redirection of scattering from vertically propagating

to more realistic obliquely propagating waves, which alleviates artificial amplification at nodes in the vertical-incidence response of corresponding 1D approximations, resulting in improvement of site effect estimation. The results demonstrate the importance of reliable calibration of subsurface structure and material properties in site response studies.

4.1 Introduction

Details of how ground shaking is affected by near-surface soil properties can help reduce the uncertainty in stochastic or empirical ground-motion models, which are important components of seismic hazard calculations. Transfer functions (TFs) are widely used to quantitatively represent site response by computing the spectral ratio of ground motions between site and reference locations in the frequency domain (e.g., Shearer and Orcutt, 1987; Steidl, 1993; Field and Jacob, 1995; Steidl *et al*., 1996; Bonilla *et al*., 2002). Assuming that the reference site, while sharing, approximately, the same path and source with the site of interest, is largely unaffected by site effects,the spectral ratio provided by the TF isolates the site response (Borcherdt, 1970). Two types of reference sites, both typically rock, have been proposed: a surface site or a downhole recording (used with the corresponding surface site). The surface downhole record pair is valuable for ensuring close proximity of the reference motions at the downhole sensor, ideally located in bedrock, whereas, it may be difficult to find an appropriate reference outcrop site within close distance to the soil site. In this article, we will only analyze TFs computed using surface-downhole site pairs.

The accuracy of site response estimates depends on the accuracy of the subsurface model used, and this is usually assumed to be controlled by the uncertainty in the site properties, in particular, the shear-wave velocity, V_S (e.g., Barani *et al*., 2013; Griffiths *et al*., 2016). V_s is the most important parameter for conventional 1D modeling of the TF, in which it is assumed that surface (and subsurface) motion consists of horizontally polarized plane S waves propagating

through a stack of homogeneous layers (e.g., Kramer, 1996). This modeling procedure (SH1D) ignores the lateral complexity of the often heterogeneous geology and subsurface structure and is, therefore, not able to include potential 2D and 3D amplification effects in the observations (e.g., Roten *et al*., 2008; Thompson *et al*., 2012). Zhu *et al*. (2018) performed numerical analysis on 2D basins and found that a constant spectral aggravation factor (Chávez-García and Faccioli, 2000), which quantifies the discrepancy between 1D and 2D/3D models, is insufficient to identify basin effects, especially, in close-to-edge regions of shallow basins. Both observations and analytical solutions suggest that 1D models lack an estimate of spatial variability, caused by complex wave propagation such as basin amplification, surface-wave generation, and scattering, and are, therefore, unable to capture spatial correlations, which may be important for understanding risk, especially, to regional-scale infrastructure (e.g., Olsen and Schuster, 1995; Boore, 2004). Although, recent approaches have attempted to reduce velocity uncertainties in site effect estimation (Matavosic and Hashash, 2012; Teague *et al*., 2018), these methods either require prohibitively complex processing or are developed for specific cases only.

It is impractical to constrain subsurface structure over a wide region to the resolution (on the order of meters to tens of meters) required for accurate ground-motion estimation to high frequencies (e.g., 10 Hz). Instead, some studies choose to use simple proxies, based on broad site classes to supplement estimates of soil properties and site spatial characteristics, for example, the National Earthquake Hazards Reduction Program (NEHRP) soil classification (BSSC, 2003; Akkar and Bommer, 2010) or a weighted average of V_S in the uppermost 30 m (V_{S30}, e.g., Abrahamson and Silva, 2008; Idriss, 2014). Thompson *et al*. (2012) proposed a scheme to classify surface-downhole site pairs by the extent of interevent variability and goodness of fit between 1D modelling and empirical site response, which can be used to calibrate the constitutive models and guide specific site studies. Despite the use of these characterizations in some generic seismic hazard estimates, for instance, via ground-motion prediction equations, recent work has pointed out the importance of considering site-to-site amplification variability (Atkinson and

Boore, 2006; Atik *et al*., 2010). These studies show that, even within a single NEHRP or V_{S30} class, the variability of site amplification and spatial correlations is strong enough to contribute significant uncertainty in ground-motion estimates.

In this chapter, we propose a method to constrain the near-surface properties using surface topography and perform high-resolution 3D numerical simulations to investigate the uncertainty in site response modeling. The simulations naturally take advantage of 3D geotechnical information and are able to incorporate complicated spatially varying amplification effects. We use two downhole array sites, namely the Garner Valley Downhole Array (GVDA) in California and the TKCH05 site from the Kiban–Kyoshin network (KiK-net) surface-downhole pairs in Japan, where detailed in situ constraints of site seismic properties (e.g., V_S and layer thicknesses) and abundant earthquake records are available, for our analysis. Both borehole sites have well-documented geological structure data, and previous studies have showed that SH1D modeling poorly predicts the ground motions without adjustments of subsurface properties or recalibration of constitutive models. Thompson *et al*. (2012) found low interevent variability and poor fit using SH1D modeling for the site TKCH05, due to omission of spatial variability around the site that scatters the downgoing waves and reduces pseudoresonance. They found that no satisfactory fit could be achieved by adjusting the velocity profile, whereas Tao and Rathje (2020) showed that modification in the top 20 m can significantly improve the site response estimate for the outcrop TF (spectral ratio between two surface sites). Bonilla *et al*. (2002) studied the wave propagation at GVDA and reported significant S-to-P conversions that led to misfit in prediction of the empirical TF (ETF; see Section 4.3) by horizontal-to-vertical spectral ratios. Teague *et al*. (2018) applied the Toro randomization model (Toro, 1995) with the spectral analysis of surface waves method, to obtain the site signature with the best match of the ETF and the theoretical TF (TTF); however, this approach suffers from the nonunique nature of inverting V_S profiles.

4.2 Data

Dependent on the strength of the input motion, site amplification and deamplification can be caused by a combination of linear and nonlinear effects. Here, we focus on linear site effects, and reserve the nonlinear analysis for subsequent research endeavors. To limit our analysis to linear ground motions, we exclude records with maximum surface accelerations larger than 0.1g (e.g., Beresnev and Wen, 1996). For each of the two site selections, we randomly picked 36 events of various azimuth and distance to the site that meets this criterion, with a minimum signal-to-noise ratio of five in their records. The goodness of fit between TTFs and ETFs from recordings is described by the variance reduction (VR) as follows:

$$\mathrm{VR} = 1 - \frac{\sum_{i=1}^{n} \left[\mathrm{TTF}\left(f_i\right) - \mathrm{ETF}_{\mathrm{med}}\left(f_i\right)\right]^2}{\sum_{i=1}^{n} \left[\mathrm{ETF}_{\mathrm{med}}\left(f_i\right)\right]^2} \tag{4.2.1}$$

in which n is the number of frequencies at which the ETFs and TTFs are computed, and ETF med is the median of the ETFs from the events that we selected. We evaluate a set of linearly spaced frequencies between 0.5 and 10 Hz, with the lower limit determined by the noise level of the data, and the upper limit from the resolution of our simulations. The VR ranges within $[-\inf, 1]$, in which VR = 1 means a perfect match, and smaller values indicate poorer fit.

4.3 TFs

We compute TFs between surface and downhole locations as follows:

$$TF = \frac{G_s(f)}{G_d(f)} \tag{4.3.1}$$

in which $G_s(f)$ and $G_d(f)$ are the root mean squares of the Fourier amplitude spectra of horizontal accelerations at the surface and downhole locations, respectively. It is worthwhile to note that the downhole recordings include the upgoing incident wavefield as well as downgoing waves that are reflected back from the free surface. This phenomenon complicates the wavefields recorded at downhole sites, and, therefore, the use of surface-downhole pairs to study site response. For records obtained at depths shallower than 200 m, as in this study, the upgoing and downgoing pulses overlap in the records, with differences in arrival times as small as 0.2 s, complicating a separation of the two contributions in the presence of extended source duration and site response (Shearer and Orcutt, 1987). For example, Bonilla *et al*. (2002) found from simulations at the GVDA site using the f-k method that the downgoing wave effect is predominant above the soil-bedrock interface and strongly degraded below that depth. Because it is almost impossible to eliminate downgoing waves from the records, we include the total wavefields at the surface and downhole sites, when calculating the TFs for both synthetics and records.

Our procedure for processing the recorded time series is similar to that documented in Tao and Rathje (2019). First, we collected acceleration time series at the surface and downhole accelerometers. Second, a fifth-order Butterworth filter, with a passband of 0.5–12 Hz, was applied to the demeaned and detrended accelerations, in which signal at frequencies below 0.5 Hz was discarded to minimize the contribution from low-frequency noise interference. Third, a second-order polynomial baseline correction was applied to the observed displacement time series, obtained by integrating the accelerations twice. Then, the ETFs were obtained as the ratio of the Fourier spectral amplitude between the surface and downhole acceleration time series for all the events. We further smoothed the TFs using the Konno–Ohmachi smoothing window in the frequency domain (Konno and Ohmachi, 1998). Although, not necessary for the synthetics, we applied the preprocessing (steps 2 and 3) to both synthetics and data for consistency.

4.4 Model Construction

It is reasonable to assume that, in the vicinity of a site of interest, bedrock depth varies in accordance with surface topography. In such models, sites located in a mountainous area have near-zero bedrock depth, whereas, sites in valley regions are characterized by larger depths to bedrock. Under this assumption, our 3D mesh is generated by mapping the topography to bedrock depth, with the constraints from borehole logging measurements. Oftentimes, bedrock depth increases rapidly from the edge toward the center of a sedimentary valley and approaches a maximum near the center of the valley, suggesting that depth to bedrock in a valley can be estimated using the topographic signature from digital elevation models. Gallant and Dowling (2003) proposed an algorithm that operates at multiple scales and combines topographic elevations into a single continuous multiresolution index of valley bottom flatness (MRVBF). Values of MRVBF below 0.5 represent areas with the steepest topography, values between 0.5 and 1.5 relate to the steep areas with few flat valley bottoms, and larger MRVBF values indicate broader and flatter valley bottoms. Here, we adopt the MRVBF technique and used the same threshold value (1.5) as in Gallant and Dowling (2003), to discriminate valley and mountainous regions. The quantitative relationship between the bedrock depth (D) and MRVBF values are assumed to obey a logarithmic formula:

$$D = max(0, \quad D_0 * log_{10}(\frac{MRVBF}{MRVBF_t})) \tag{4.4.1}$$

in which $MRVBF_t$ is the threshold MRVBF value (here, 1.5), and D_0 is a coefficient, which is calculated by substituting the MRVBF value and bedrock depth at the borehole site into the borehole equation, that is, $D_0 = D_{borehole}/log_{10}(\frac{MRVBF_{borehole}}{MRVBF_t})$.

In addition to the modifications of the velocity model from the MRVBF method, we explore the extent to which scattering effects from statistical distributions of near-surface small-scale heterogeneities (SSHs) can improve site effect estimation. Previous studies using 1D modeling show that including SSHs may improve the prediction of ETFs, likely by weakening

the downgoing wave effects (Nour *et al*., 2003; Thompson *et al*., 2012). Here, we use guidance from published studies on spectral coloring of Gaussian random numbers with von Kármán spatial correlation functions for characterizing the statistics of heterogeneities (see Appendix A; as well as, e.g., Frankel and Clayton, 1986; Withers *et al*., 2019). We use a Hurst number of 0.05, a correlation length of 100 m, a standard deviation of 5%, and a horizontal-to-vertical anisotropy of five, as constrained from sonic borehole logs in the Los Angeles basin by Savran and Olsen (2016). We include SSHs with these parameters, when generating TFs at our two selected locations, whereas, the sensitivity of the TFs to variation in the parameters is explored in the Discussion section.

4.4.1 Numerical simulations

Our goal to quantify the effects of 3D Earth structure on highfrequency (<10 Hz) TFs, using 3D modeling, is computationally challenging. We use the parallel and scalable discontinuous-mesh velocity–stress staggered-grid finite-difference code AWP-ODC-DM (Olsen, 1994; Cui *et al*., 2010; Nie *et al*., 2017) to simulate the site response. One-dimensional TTFs are computed under the SH1D assumption, in which the model consists of a stack of homogeneous layers, to provide a point of comparison for the 3D models. The model definition for the 3D TTF computation is more complicated. We include the effects of frequency-dependent attenuation using the model:

$$Q(f) = \begin{cases} Q_0 \times f_\gamma, & f > 1 \\ Q_0, & f \leq 1 \end{cases} \tag{4.4.2}$$

in which Q_0 is a frequency-independent constant attenuation proportional to the velocity, and γ is a power-law exponent describing the attenuation above 1 Hz (Withers *et al*., 2015). Here, we adopt area-specific parameters suggested in the literature; for GVDA, we use $Q_{S,0} = 0.05 \times V_S$ (V_S in meters per second), $Q_{P,0} = 2 \times Q_{S,0}$, and $\gamma = 0.6$ (Withers *et al*., 2015; for southern Calfornia),

and for TKCH05, we use a model for $Q_{P,0} = Q_{S,0} = Q_0$, given by

$$Q_0 = \begin{cases} 60, & V_S \leq 600 \\ 100, & 600 < V_S \leq 1100 \\ 150, & 1100 < V_S \leq 2100 \\ 200, & 2100 < V_S \leq 3200 \\ 300, & V_S > 3200 \end{cases} \tag{4.4.3}$$

in which V_S is in meters per second, from the Japan Seismic Hazard Information Station (J-SHIS) and $\gamma = 0.2$, following the study by Nakajima *et al*. (2013). We discretize the velocity models using two partitions in our discontinuous mesh, with grid spacings small enough to resolve the minimum V_S wavelengths (20 m and 14 m for the GVDA and TKCH05 cases, respectively), anywhere in the model with, at least, five points. In our simulations, the surface recordings at a neighboring outcrop site are deconvolved from its local subsurface property layers, up to the bottom of the simulation domain; the resulting three-component acceleration time series (converted to body forces in AWP-ODC-DM) are then distributed on the entire bottom surface of the computational domain, to generate a oneway upward propagating plane wave. We verified that such vertical-incident plane wave sources are reasonable approximations, considering our shallow simulation domains (0.4 km and 1 km deep at GVDA and TKCH05, respectively), as well as earthquake hypocenters at depths of 10 km+ and distances of tens of kilometers. We used an elastic boundary condition at the bottom grid boundary, which is transparent to downgoing waves, to avoid artificial resonance of the soil column (Roten *et al*., 2012). We part from the common way of placing the model base at the downhole site and have the input motion as the downhole motion, due to our boundary conditions. We perform the numerical simulations on the Oak Ridge National Laboratory Summit supercomputer, in which each of our simulations with the 3D model at TKCH05, including 64 million cells, requires a wall-clock time of 100 min on 32

graphic processing units for 750,000 timesteps. Similar computational requirements are needed for the 3D GVDA simulations.

4.5 GVDA

The GVDA is located in a seismically active region of California, 7 km from the San Jacinto fault and 35 km from the San Andreas fault (**archuletaGarnerValleyDownhole1992**). The site is situated in a narrow valley within the Peninsular Ranges Batholith (Bonilla *et al.*, 2002), 23 km east of Hemet and 20 km southwest of Palm Springs, California. The near-surface stratigraphy beneath GVDA consists of extensive lake-bed alluvium and decomposed crystalline rocks (Hill, 1981). Soft silty and clayey sands makes up the top 18–25 m across the site (Steidl *et al.*, 1996), followed by 50–60 m thick, decomposed, and weathered granite down to about 64–87 m, as constrained by seismic downhole testing and shallow and deep P–S velocity suspension logging (Gibbs, 1989; Steller, 1996). The GVDA site is equipped with multiple downhole accelerometers, at depths of 15, 22, 50, and 150 m that are capable of measuring accelerations from 3×10^{-6} to $2.0g$ below 100 Hz. The 150 m deep accelerometer is the only downhole sensor that penetrates the granitic rock, which is used to compute TTFs in this study.

To be able to resolve frequencies up to 10 Hz at the GVDA site, we generated a mesh of size 4 km × 4 km × 0.4 km (length × width × depth), with mesh properties compressional wave velocity (V_P), V_S and density from the 3D Community Velocity Model (CVM) S4.26.M01, which is developed and maintained by the Southern California Earthquake Center (SCEC; Small *et al.*, 2017). The borehole logs show V_S of the near-surface soft soils between 180 and 220 m/s, with the value of V_S smaller than 200 m/s only at depths between 1.4 and 2.8 m (Steller, 1996). The minimum velocity in our model was truncated at 200 m/s, which is about the average of the top 4 m, resolving frequencies up to 10 Hz, with, at least, five points per minimum S wavelength, using a smallest grid spacing of 4 m. The SCEC CVM S4.26.M01, however, fails to resolve the 3D

Garner Valley structure to the accuracy required by our analysis, and we use the MRVBF method to describe the depth to bedrock instead.

At every surface location, we first compute the MRVBF value and bedrock depth, as described in the Numerical simulations section. We then force the V_P, V_S , and densities above the bedrock to be the same as those in the measured borehole log, while keeping the seismic velocities and densities unchanged in the bedrock. Figure 4.2 illustrates how we estimate bedrock depth from the MRVBF values, using surface topography. The deeper parts of the valley are represented by larger MRVBF values. The areas with MRVBF smaller than the threshold value at 1.5 are shown in dark shading, corresponding to steeper terrain. The borehole site GVDA, at the center of the region, has a MRVBF value of 5.8 and bedrock depth of 64 m, consistent with the borehole log from Gibbs (1989). The 3D geometry inferred from the spatially varying bedrock depth is shown in the left panels of Figure 4.3, compared to the original borehole profile in the right panel.

Although we computed the ETFs for all the selected 36 events (Table 4.1 and Fig. A4.1), only one event (ID = 33) was used to generate the upgoing waves in the simulations and to compute the TTF. The selection of event ID 33 was arbitrary for two reasons: (1) the ETFs at GVDA show low interevent source variability, indicated by the narrow σ band in Figure 4.4, and (2) the modeling is constrained to linear wave propagation. The use of a realistic source allows straightforward extension to multiple sites, as well as to nonlinear analysis in the future. The source time function was obtained by deconvolving the surface recordings of this event at the neighboring outcrop site GVAR (see Fig. 4.1) to the maximum depth of our domain.

The TTFs and ETFs for GVDA are compared in Figure 4.4. The two-sigma scatter of all the ETFs is fairly narrow above 1 Hz and not sensitive to the azimuths and distances of the events, which implies that the ETFs are primarily determined by the site characteristics, and confers greater predictive power on an ETF (and presumably also on a TTF). Although the peaks for the ETFs and both 3D and 1D TTFs generally occur near the same frequencies, the goodness of fit

predicted from the 1D model (VR = 0.64) is significantly smaller compared to the 3D model (VR = 0.85). This result suggests that the shallow 3D structure contributes first-order effects to the local site amplification at GVDA (see Section 4.7).

4.6 TKCH05

The KiK-net strong-motion seismograph network in Japan provides, approximately, 700 sites, with pairs of surface and downhole seismographs installed that have recorded earthquakes with a wide range of magnitudes. KiK-net also provides geological and geophysical data, including velocity structure for each site, derived from borehole logs. Thompson *et al*. (2012) analyzed the interevent variability and goodness of fit between SH1D models and data at 100 sites from KiK-net, and identified some sites where the standard 1D site response analysis provided poor results. Among these sites, we targeted TKCH05, which is located in Honbetsu, Hokkaido, Japan, to investigate the contributions from its underlying 3D structure on site effects. Figure 4.5 shows the location of TKCH05, in a narrow valley surrounded by mountains. The large gradients of the surface topography at the valley boundaries suggest the presence of significant 3D variation of the bedrock interface below the valley. The stratigraphy at TKCH05 is, approximately, 6 m of soil and sandy gravel with V_S = 140 m/s, overlying tens of meters of sandstone over gravel stone and siltstone (see Fig. 4.6; National Research Institute for Earth Science and Disaster Resilience, 2019). Table 4.2 lists the events included in our analysis of the ETFs at TKCH05 (see Fig. A4.2 for their locations and time series), among which the event with an ID of 1 was selected to generate the incoming waves in our simulations. As we did at site GVDA, we deconvolved the surface records at the closest outcrop site, F-net site URH, which is about 21.7 km away from TKCH05 to the domain bottom.

Figure 4.6 shows the downhole profile at TKCH05, and Figure 7a shows a comparison between the corresponding 1D TTF compared to the ETFs. The 1D TTF fails to match the

frequency peaks and strongly overpredicts the amplifications at lower frequencies, producing a relatively low VR (VR = 0.35). We also considered the adjacent K-Net site HKD090, due to its proximity to TKCH05 (only 4 m relative distance), in our analysis. The available information from the measured V_S profile at HKD090 only extends to a depth of about 18 m, but, varies notably from those at TKCH05, considering the close distance. Because the top layers are as thin as 2 m, it is possible that the accuracy was degraded when the downhole logging measurements of travel time were converted to piecewise constant profiles. For this reason, we tested a simplified profile combining the two borehole logs, by replacing the TKCH05 V_S profile between 5 and 100 m, with an average value of 680 m/s. The adjustment reduces the strong discrepancy in shallow V_S values between the two borehole logs and retains the travel time from the bedrock to the surface. The SH1D model with the simplified profile produces a poorer fit to the ETF (VR = 0.181) than that obtained using the TKCH05 profile. Although, the simplified profile agrees better with the location of the second spectral peak of the ETF, the overall response compares less favorably to that obtained using the original profile due to larger amplitudes, especially at frequencies between 1 and 3 Hz.

Next, we extract our background 3D models at TKCH05 with a 1 km × 1 km × 1 km region, with the top boundary centered at TKCH05, from the Japanese national subsurface V_S model provided by J-SHIS. The J-SHIS model provides V_S and V_P and density with a horizontal spatial resolution of 1 km. Along the vertical direction, J-SHIS provides the depths of 33 layers with various thicknesses. Each layer is homogeneous and of increasing V_S with depth, ranging from 350 to 3400 m/s. Given the coarse horizontal resolution, the J-SHIS model is essentially 1D, with small stepwise discontinuities present close to the southern edge of the model (Fig. 4.8d). The bedrock depth was then estimated using the MRVBF method. The V_S below the downhole array is 1100 m/s, which increases to 1700 m/s at the bottom of our domain (Fig. 4.8). Based on the surface V_S of 140 m/s, we interpolated the initial mesh to a grid spacing of Δh = 2.5 m in the top partition of the mesh, to ensure at least 5–6 points per minimum S wavelength. In the

discontinuous mesh setup, the lower mesh partition starts at a depth of 400 m, with a grid spacing of 7.5 m. Figure 4.7a compares ETFs to TTFs, based on the 3D models generated by the MRVBF technique, as well as the soil profile at TKCH05 and our simplified profile. Compared to the 1D models, the 3D models are able to fit the ETFs much better, with VR values of 0.50 and 0.86 for the 3D models with the original and simplified profiles, respectively. The 3D models, while both producing a shift of the second peak compared with their corresponding 1D models, show remarkable improvement in the amplitudes of the first peak, especially when using the simplified profile. The results suggest that the simplified velocity profile, combining the borehole logs from the two adjacent sites, characterizes the local subsurface velocity structure below TKCH05 significantly better than the TKCH05 borehole log.

In general, a site response model can be evaluated by comparing the predicted surface ground motions (obtained by convolving the TF with the records at the reference site), with those recorded at the site of interest. We follow the traditional procedure for the calculation of TFs, neglecting the phase in the convolution process and quantifying the goodness of fit by the amplitudes only. Figure 4.7b,c compares the 1.5-8 Hz band-pass filtered surface recordings to the predicted motions from TTFs, illustrating the improvement in synthetic waveforms, as compared to data obtained at TKCH05 using the 3D as compared to the 1D model.

4.7 Discussion

We have demonstrated for two borehole sites (GVDA and TKCH05) that site amplification estimation using TTFs can be significantly improved by including effects of the underlying 3D structure. However, the 3D TTFs still leave some room for improvement. A likely important cause of the remaining misfit between TTFs computed using 3D structure and the ETFs is the uncertainty in seismic velocity estimates as a function of depth. It is common practice in soil analysis to approximate the near-surface geology as a stack of layers with constant velocity. Boore

and Thompson (2007) showed that the effects of approximating logging measurements with 10 m thick, constant-slowness layers are small for frequencies less than about 5 Hz. However, Day (1996) examined analytically the relation between site response in the frequency domain and elastic structure and found that the spectral average of bandwidth Δf is only constrained by the elastic structure up to a two-way travel-time depth of $1/\Delta f$. This means that the average TF (predominantly at higher frequencies) can be biased due to uncertainty in the shallow structure. Because the first layer is often thin, a bias in the thickness estimate can contribute relatively large error in the site effects.

The deeper structure, in particular, the bedrock depth, can also be important in determining the TFs. In conventional 1D models, the bedrock topography is simplified as a layer with fixed depth; whereas, our approach incorporates lateral variations by mapping surface topography. The subsurface structure in our model is, therefore, composed of multiple irregular interfaces, each of which is anchored to the borehole log right beneath the site of interest. In some cases, the exact depth of the soil-bedrock interface is unclear. For example, the weathered granite boundary below the GVDA site is reported at 64 m by Gibbs (1989) and 87 m by Steller Steller (1996). The two velocity profiles are similar, except for the bedrock depth (Fig. 4.9a). In the following discussion, the two models utilize their respective bedrock depth and velocity profiles. Figure 4.9b shows the TFs from two 3D models assembled with the Gibbs and Steller profiles (the latter shifted 1 m deeper than the reported value due to the 4 m spatial resolution of our model). The Steller model response matches the ETF at high frequencies better than that from the Gibbs model, whereas, the latter model fits better at 1.5–7 Hz, with a slightly better overall fit (VR = 0.85 vs. 0.82). It is noticeable that the Steller model, representing lower average velocity in the soil column, results in a shift of the peaks of the TF to the left at low frequencies. We conclude that both the lateral variation and the location of the subsurface strata are important in modeling the site response. The 3D-to-1D comparison shown in Figure 4.4 indicates that the lateral variations lead to changes in both the amplitudes and the frequency of the TF, whereas the variability of the bedrock depth

mainly results in shifts in frequency of the TF.

Another source of uncertainty in the site amplification estimates arises from unconstrained (mostly high frequency) scattering effects from crustal SSHs, and we test the effects thereof from a range of different parameters of the von Kármán autocorrelation functions. Figure 4.10 shows the 3D TTFs modeled with a nine-realization ensemble of von Kármán velocity and density perturbations, by varying the Hurst number from 0.05 to 0.15, the correlation length from 50 to 500 m, and the standard deviation of 5% and 10%, while keeping the horizontal-to-vertical anisotropy at 5. We find that the TTFs computed from these 3D models are relatively insensitive to the SSHs, except near the upper limit of our modeling bandwidth (> ~9 Hz). The median VR (0.83) of the resulting TTFs is similar to that without including the SSHs, suggesting that the random fields do not contribute first-order effects to the site amplification. However, our sensitivity study included only limited realizations for each set of von Kármán parameters due to computational limitations, and, we recommend a more thorough analysis, estimating the uncertainty of the site amplification estimates arising from additional ensembles of statistical distributions of small-scale crustal perturbations.

To better understand the reasons why the 3D models better predict the observed site amplification, as compared to their 1D counterparts, we show snapshots of wave propagation for our 3D and 1D (simplified) models of TKCH05 in Figures A4.3 and A4.4. The snapshots are extracted for frequencies between 4.5 and 5 Hz, in which the 3D TTF provides a much improved fit to the ETF, as compared to the 1D TTF. As expected, the 3D models naturally increase the complexity of the wave propagation compared to the SH1D model, for example, the presence of wave energy trapped in basins, and reflections at interfaces between geological units with different V_S (Fig. A4.3). For example, note the horizontally propagating energy in the upper tens of meters in the snapshots from the 3D model, naturally absent in the 1D results. Of course, the improvement in the site response from the 3D model depends on the accuracy of the added degrees of freedom.

To further illustrate this added complexity, we compare the horizontal and vertical cumulative energy along the borehole profile (Fig. 4.11a,b) to the theoretical (1D) response (Fig. 4.11c) for different incidence angles at TKCH05. We carry out our analysis for the bandwidth 1.6–1.9 Hz, centered on the largest SH1D ETF peak at about 1.75 Hz (see Fig. 4.7a). The depth-dependent theoretical particle velocities, with the internal reflections neglected, can be described as follows:

$$v(z,t) = \cos\left(\omega\left(t - \frac{z\cos\theta}{V_S}\right)\right) + \cos\left(\omega\left(t + \frac{z\cos\theta}{V_S}\right)\right) \tag{4.7.1}$$

in which z is the depth, t is the time, ω is the angular frequency, and θ is the incidence angle. As inferred from the SH1D solution in Figure 4.11c, the peak at ~1.75 Hz is, primarily, due to a node at the downhole sensor location in the vertical-incidence response. This theoretical solution implies that a small departure from vertical incidence, which, in practice, is caused by interactions with the 3D bedrock interface, scatters some vertically propagating seismic waves to obliquely propagating waves, and moves the node to greater depth, thereby, increasing the response at the sensor depth point. Such wave scattering changes the energy distribution along depth, including the reduced horizontal-component energy near a depth of 100 m in the 3D model compared to the 1D model (Fig. 4.11a) and the increase in vertical-component energy (Fig. 4.11b). The results indicate that at TKCH05, the site response remains a first-order 1D resonance effect, but coupled with 3D effects from horizontally propagating waves, which, when included, greatly improves the fit to the ETF compared with the SH1D model.

4.8 Summary and Conclusions

We present a method to obtain refined site effect measurements by taking into account 3D structural variation below a downhole array site and a path to refine estimates of the elastic properties of the underlying stratigraphy via the MRVBF technique. The approach requires layer

properties (e.g., S-wave velocities) along a vertical profile (typically obtained from the downhole array) as well as regional elevation data, which is widely available for most areas.

Application of the method to two sites, GVDA in southern California and TKCH05 in Japan, illustrates the extent of improvement over the conventional 1D site effect amplifications that can be expected. The relatively poor fit of the SH1D model at TKCH05 indicates that it deviates strongly from 1D behavior, supported by the complex 3D structure in the vicinity of the downhole array obtained by the MRVBF technique. Although significant improvement of the fit was obtained at GVDA as well, our results suggest that the medium below the borehole site is more horizontally stratified than is the case at TKCH05 (smaller improvements from including the effects of a MRVBFestimated 3D model). This interpretation is also supported by the horizontally stratified nature of the resulting 3D model around the GVDA site, except for smaller patches of near-surface low-velocity material produced by the method.

Thus, our method is likely to improve the prediction of site response in the presence of significant 3D structure, as well as at sites with an oversimplified or otherwise less accurate V_S profile. However, the accuracy of the site effects estimated by our proposed technique depends strongly on the fidelity of the available soil properties in the borehole, in particular at the upper end of our target bandwidth, near 10 Hz. The variability of the bedrock depth, beneath the site, as one of the controlling parameters in constructing our 3D model, can be a significant source of error in the prediction of the TF, by introducing frequency shifts at low frequencies. Finally, our results show that the improvement of the TTFs produced by incorporating small-scale crustal heterogeneities via a statistical model is secondary to that obtained by including 3D subsurface information.

Our results generally support the conclusions by Thompson *et al*. (2009) that the theoretical formulation to map soil properties to site amplification largely limits our ability to accurately model site response transfer functions, rather than the uncertainties of the soil property. However, our method provides a realistic constitutive framework, suitable for predicting site response, re-

gardless of the spatial variability in material properties across the site. Furthermore, this approach can be extended to explore nonlinear soil effects, another important component of site effects not explored here. For future work, we also recommend that the assumption of the quantitative relationship between topography and bedrock depth receive further scrutiny with 3D simulations at more sites, especially where the interevent variability is large.

Data and Resources

The seismograms and borehole log data used in this study were collected from the National Research Institute for Earth Science and Disaster Prevention (National Research Institute for Earth Science and Disaster Resilience, 2019) in Japan for TKCH05, and the Earthquake Engineering Group, Earth Research Institute at University of California, Santa Barbara (UCSB) (http://nees.ucsb.edu/) for Garner Valley Downhole Array (GVDA). The transfer functions for all earthquakes and simulations at both sites used in the analysis can be obtained from the authors upon request. Some plots were made using the Generic Mapping Tools (GMT) version 6.0.0 (https:// www.generic-mapping-tools.org/; Wessel *et al*. 2019). We used the open-source project ObsPy version 1.2.0 (https://github.com/obspy/obspy) to compute the Konno–Ohmachi smoothing window for Transfer functions (TFs). All websites were last accessed in June 2020. We included figures on the event locations and recorded accelerations, as well as snapshots of the 3D and 1D simulations, for GVDA and TKCH05 in the supplemental material to this article.

Acknowledgements

Computations in this project were performed on Rhea and Summit, which are part of the Oak Ridge Leadership Facility at the Oak Ridge National Laboratory. This research was supported by the Southern California Earthquake Center (SCEC; Contribution Number 10885) and by the

National Science Foundation under Grant Number EAR-1664203. SCEC is funded by National Science Foundation (NSF) Cooperative Agreement EAR-1600087 and U.S. Geological Survey (USGS) Cooperative Agreement G17AC00047. Figure 4.6a is reprinted from Thompson *et al*. (2012). The authors thank two anonymous reviewers and the Associate Editor Jim Kaklamanos for valuable suggestions that helped to improve this article.

Chapter 4, in full, is a reformatted version of the material as it appears in Bulletin of the Seismological Society of America: Hu, Z., Roten, D., Olsen, K.B. and Day, S.M. (2020). Modeling of Empirical Transfer Functions with 3D Velocity Structure. *Bulletin of the Seismological Society of America*. The dissertation author was the primary investigator and author of this paper.

Tables and Figures

Table 4.1: Earthquakes Used to Compute the Empirical Transfer Functions at Garner Valley Downhole Array (GVDA)

ID	Date (yy/mm/dd)	Time (hh:mm:ss)	M_L	Latitude (°)	Longitude (°)	Depth (km)	Distance (km)	Azimuth (°)
1	7/6/02	05:11:26	4.3	33.872	-116.212	5	48	242
2	7/6/13	14:50:34	3.4	33.697	-116.042	12	59	267
3	8/7/29	18:42:16	5.4	33.953	-117.761	15	106	108
4	8/12/06	04:18:43	5.1	34.813	-116.419	7	130	190
5	9/3/13	03:42:22	3	34.016	-117.197	15	62	129
6	9/11/15	07:54:23	3.3	33.914	-117.059	14	45	127
7	10/3/13	16:32:32	4.2	32.991	-116.358	6	81	339
8	10/6/15	04:26:58	5.7	32.7	-115.921	5	129	327
9	10/7/08	01:07:11	3	33.445	-116.406	12	35	315
10	10/11/17	09:46:15	3.2	33.987	-117.159	15	57	128
11	11/6/14	08:25:41	3.6	33.69	-116.74	18	7	111
12	11/11/19	20:32:21	3.9	33.245	-116.265	10	61	321
13	12/3/30	06:09:27	3.3	33.304	-116.879	15	45	25
14	12/5/18	10:37:12	3.6	33.319	-116.402	8	46	327
15	12/8/08	16:33:22	4.5	33.904	-117.791	10	107	105
16	12/8/27	04:41:37	4.9	33.021	-115.519	4	129	304
17	12/10/02	08:28:15	4.1	32.805	-116.144	10	108	333
18	13/03/11	16:56:06	4.7	33.502	-116.457	13	27	313
19	13/03/27	17:50:29	3.4	33.495	-116.445	8	29	312
20	14/01/16	07:40:06	3.6	33.829	-117.687	10	95	101
21	14/03/29	04:09:42	5.1	33.932	-117.917	5	119	105
22	14/05/19	20:08:52	3.8	34.253	-116.825	8	66	168
23	14/07/10	20:41:44	3.2	33.505	-116.507	15	24	320
24	14/11/03	08:53:35	3.3	34.017	-117.232	18	65	127
25	14/12/04	16:53:21	3.6	33.963	-116.635	16	33	186
26	15/05/31	13:02:56	3.6	33.313	-116.282	13	54	317
27	16/01/09	11:43:11	3.3	33.66	-116.774	14	9	84
28	16/02/14	09:01:10	3.4	33.892	-117.118	14	48	121
29	16/06/10	08:04:39	5.2	33.431	-116.443	12	34	321
30	16/09/26	14:31:08	4.3	33.298	-115.714	2	98	295
31	17/06/25	13:53:25	3.5	34.001	-116.903	14	43	150
32	17/12/09	20:45:24	3.5	33.4987	-116.801	5	22	32
33	18/04/23	00:46:09	3.9	33.921	-116.322	8	43	229
34	18/05/19	19:26:51	3.5	33.4958	-116.808	3	23	33
35	18/08/04	13:48:49	3.1	33.9323	-116.828	6	33	154
36	18/09/01	16:50:29	3.1	33.4878	-116.807	2	24	31

Table 4.2: Earthquakes Used to Compute the Empirical Transfer Functions at TKCH05

ID	Date (yy/mm/dd)	Time (hh:mm:ss)	M_w	Latitude (°)	Longitude (°)	Depth (km)	Distance (km)	Azimuth (°)
1	8/8/29	23:41:00	4.1	42.935	144.035	96	40	301
2	8/11/09	09:11:00	3.8	42.712	143.698	93	46	352
3	9/1/11	14:57:00	4.7	42.593	143.415	68	61	16
4	9/2/28	09:36:00	5.3	42.583	142.188	113	131	63
5	9/3/20	15:52:00	5	42.6	144.535	64	95	307
6	9/6/05	12:30:00	6.4	41.812	143.62	31	145	360
7	10/1/15	03:46:00	5	42.352	143.117	51	95	26
8	10/4/09	03:41:00	4.8	42.917	144.722	57	93	284
9	10/7/08	21:23:00	4.7	42.573	144.528	59	96	309
10	10/7/28	08:06:00	4.5	42.337	143.798	56	88	350
11	10/10/14	22:59:00	5.5	42.312	143.068	53	101	27
12	12/3/11	17:33:00	4.4	42.537	143.265	63	71	24
13	12/3/14	19:49:00	6	40.68	144.967	69	293	337
14	12/7/22	13:42:00	5.1	42.488	143.025	61	85	35
15	12/8/22	10:33:00	5.2	42.347	143.052	53	98	29
16	12/10/26	19:52:00	3.7	42.702	143.212	104	57	36
17	12/11/19	10:37:00	4.1	42.773	143.942	103	47	326
18	13/03/09	21:16:00	5	43.13	144.77	101	94	269
19	13/05/17	04:20:00	4.3	42.672	143.417	74	53	18
20	13/08/22	15:53:00	4.8	42.318	142.995	54	103	30
21	13/10/21	12:33:00	4.6	42.32	143.047	50	101	28
22	14/04/21	16:46:00	4.2	42.492	143.563	77	70	4
23	15/03/25	09:34:00	5	42.352	143.095	50	96	27
24	15/08/14	13:43:00	5.1	42.752	143.112	80	58	45
25	15/09/26	18:49:00	4.5	42.212	141.957	94	170	54
26	15/11/11	00:50:00	3.9	42.955	143.758	116	22	328
27	16/07/24	11:51:00	4.9	42.873	143.173	96	46	53
28	16/09/07	18:42:00	4.7	42.493	142.68	110	104	48
29	16/10/09	03:36:00	3.9	42.877	143.923	115	37	317
30	16/10/12	04:02:00	5	42.325	143.042	50	100	28
31	17/02/27	18:10:00	4.7	42.348	143.048	52	98	29
32	17/03/14	12:57:00	4.7	42.815	142.7	82	82	66
33	17/04/30	23:42:00	5.4	42.322	143.07	53	99	27
34	17/09/10	17:44:00	5.6	41.758	142.877	43	163	22
35	17/11/03	12:45:00	5	42.563	143.748	66	63	350
36	18/04/14	04:00:00	5.4	43.175	145.737	53	172	267

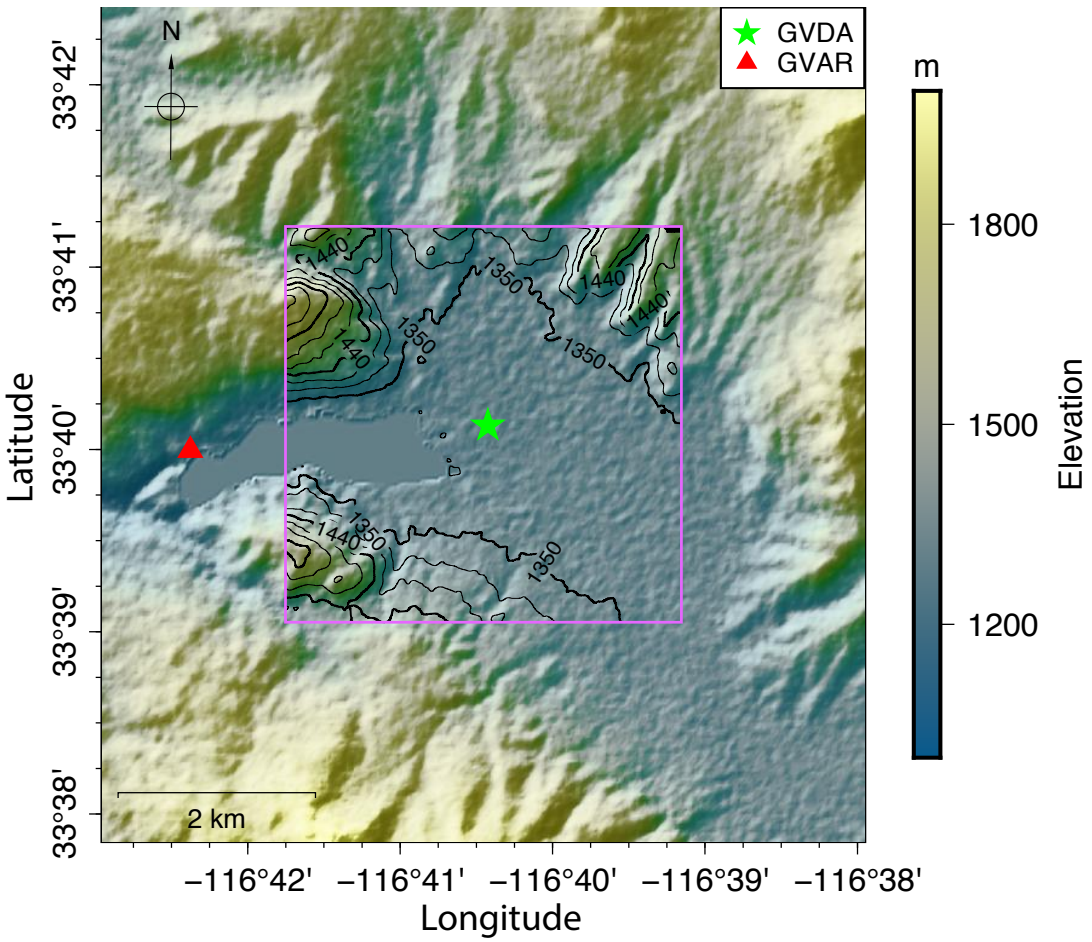

Figure 4.1: Site map of Garner Valley Downhole Array (GVDA), denoted by the star. The rectangle depicts the extent of the modeling domain, where the contours depict elevation in meters. The triangle denotes a nearby outcrop site GVAR. The color version of this figure is available only in the electronic edition.

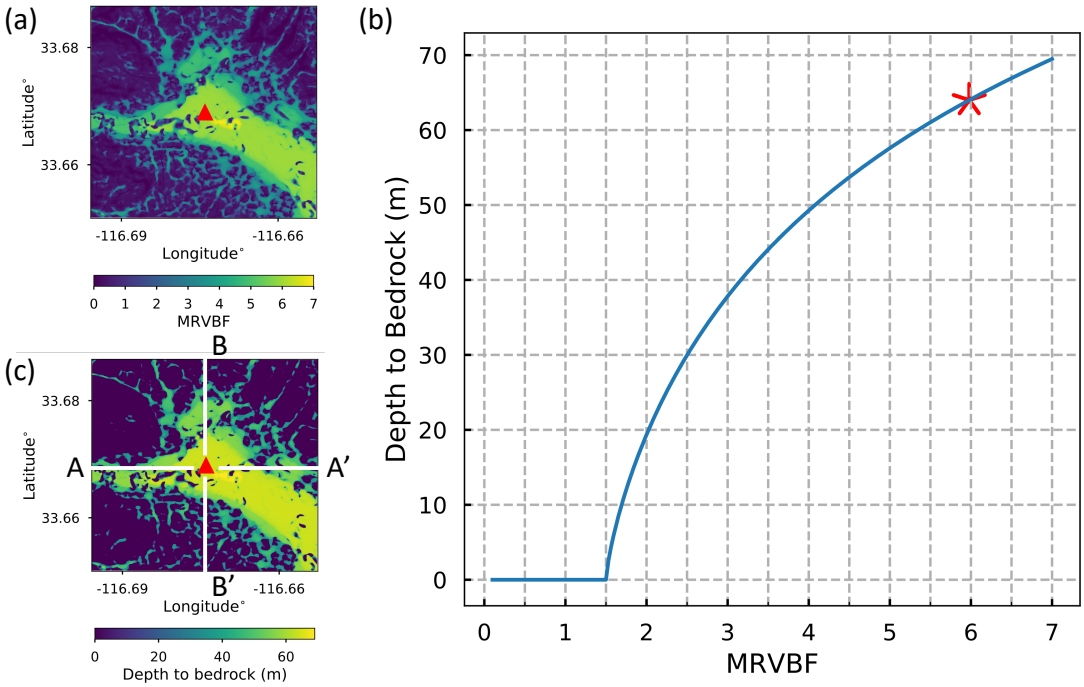

Figure 4.2: (a) Multiresolution index of valley bottom flatness (MRVBF) and (b) the bedrock depth map surrounding GVDA, which is depicted by a triangle in both figures. (c) The mapping function from MRVBF to bedrock depth, with GVDA marked with an asterisk. The color version of this figure is available only in the electronic edition.

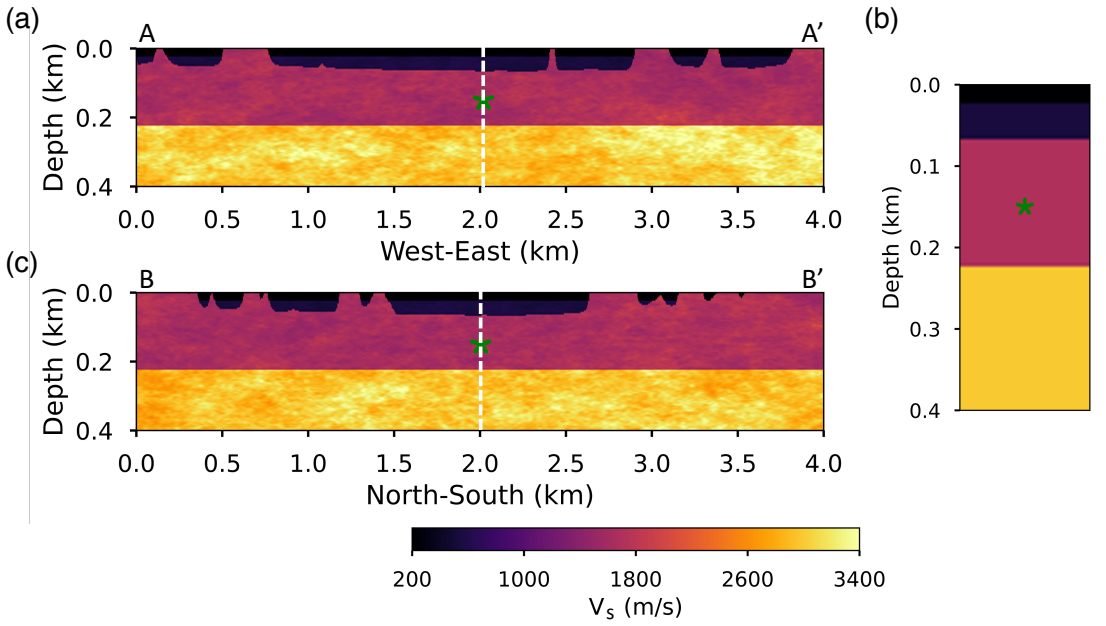

Figure 4.3: Cross sections of V_S in the 3D mesh (see Fig. 4.2) intersecting GVDA along (a) A–A' and (c) B–B'; the downhole accelerometer is denoted with the asterisk. (b) The 1D V_S profile, with its location denoted by the dashed line in the left panels, obtained from the borehole log, and used in the SH1D model. The color version of this figure is available only in the electronic edition.

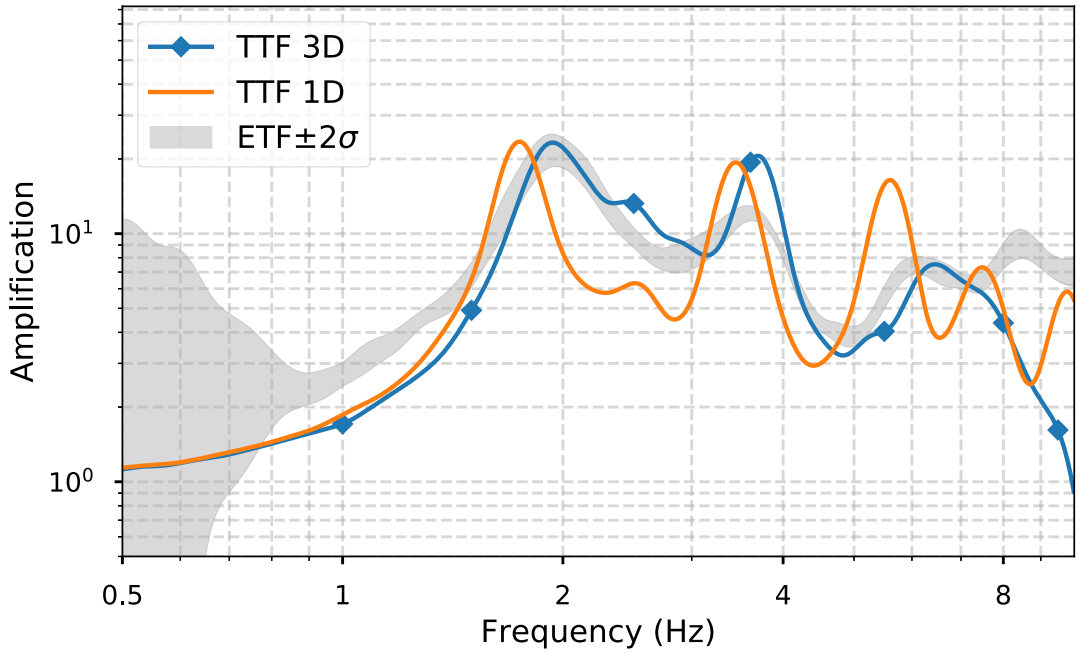

Figure 4.4: Comparison between the theoretical transfer functions (TTFs) computed using the 3D model and the SH1D model at GVDA, with the two-sigma scatter of empirical transfer functions (ETFs) shaded in gray. The color version of this figure is available only in the electronic edition.

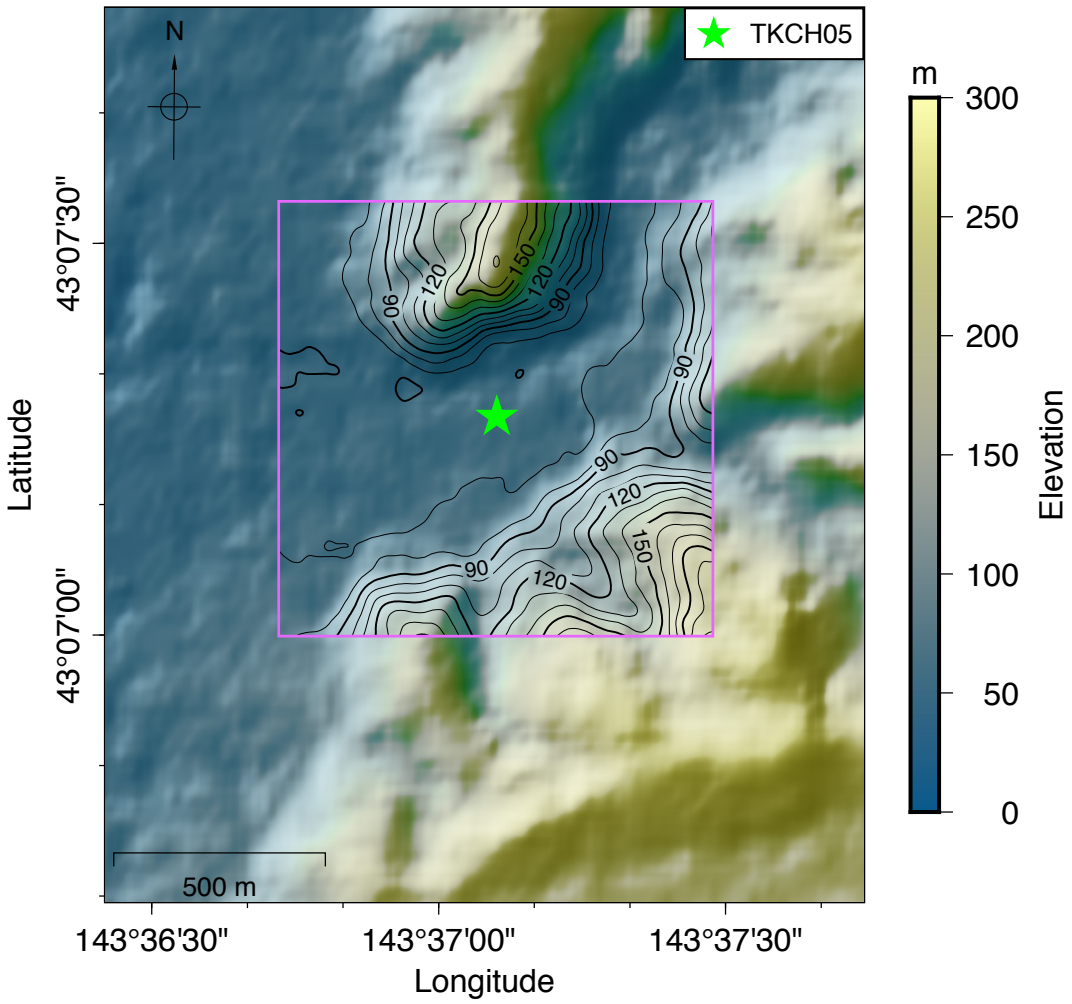

Figure 4.5: Site map of TKCH05, denoted by the star. The rectangle depicts the extent of the modeling domain, where the contours depict elevation in meters. The color version of this figure is available only in the electronic edition.

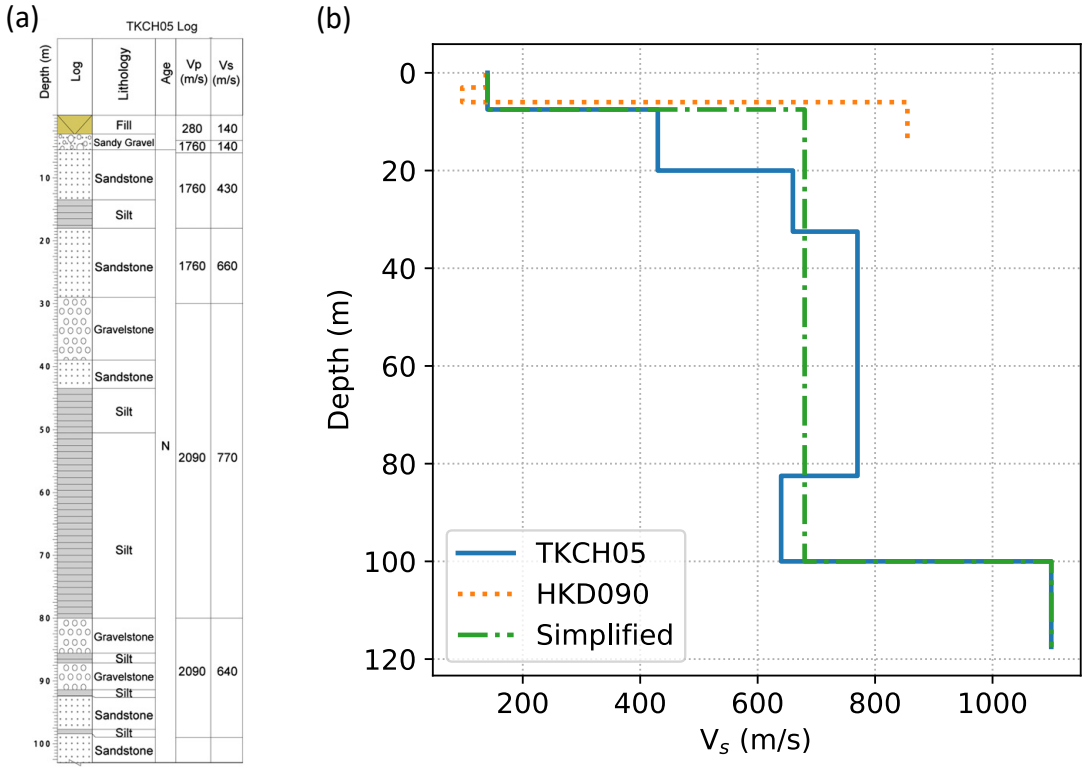

Figure 4.6: (a) Borehole log at TKCH05 (from Thompson *et al*. 2012). (b) Borehole V_S profiles at TKCH05 and HKD090, as well as for our simplified 1D model. The color version of this figure is available only in the electronic edition.

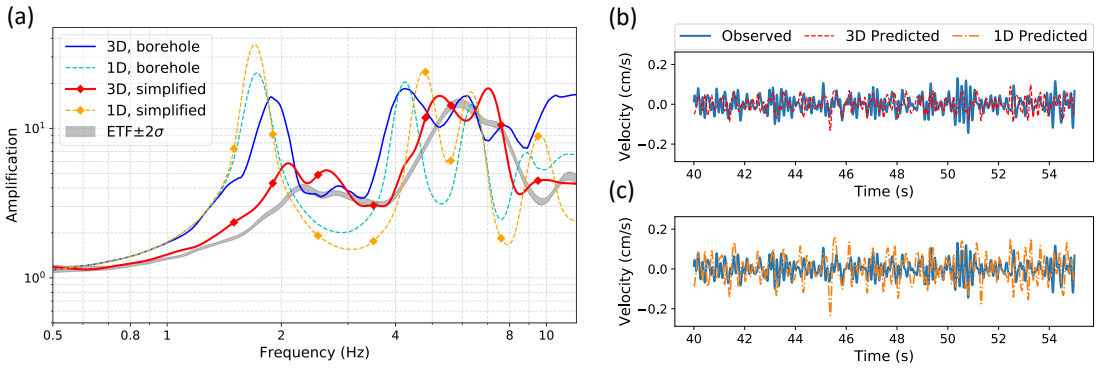

Figure 4.7: (a) Comparison between TTFs and the two-sigma scatter of the ETF for 3D and 1D models at TKCH05. Solid and dashed lines without markers are the 3D and 1D models based on the borehole log profile, respectively; solid and dashed lines with diamond markers depict the 3D and 1D models, based on the simplified downhole profile. (b,c) Comparison of 1.5–8 Hz observed east–west component surface ground motions with those obtained from convolution of the downhole records with the TTFs from models using the simplified profile for the (b) 3D model and (c) 1D model. The color version of this figure is available only in the electronic edition.

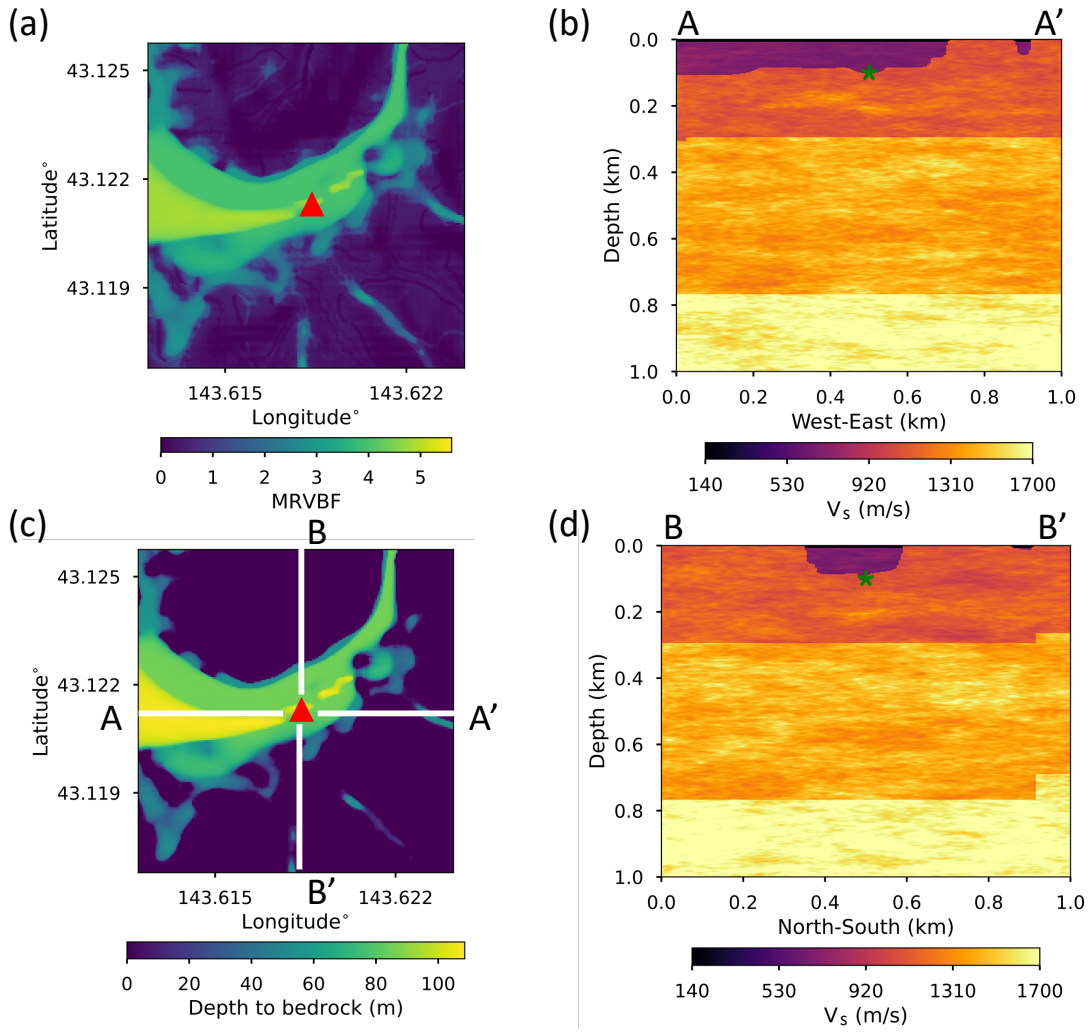

Figure 4.8: (a) MRVBF and (c) depth to bedrock in the vicinity of TKCH05, with the site location denoted by the triangle. (b) West–east A–A’ and (d) north–south B–B’ cross sections intersecting TKCH05, the downhole sensor is marked with the asterisk. The color version of this figure is available only in the electronic edition.

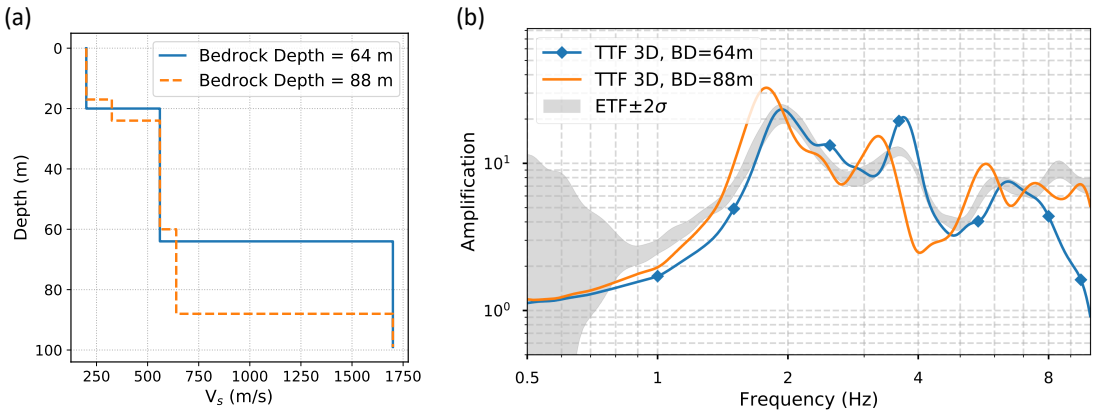

Figure 4.9: (a) The Gibbs and Steller velocity profiles at GVDA, in which the bedrock depth is 64 (solid line) and 88 m (dashed line), respectively. (b) Comparison between the two-sigma scatter of the ETFs (gray shaded) and the TTFs from the 3D models assembled with the Gibbs and Steller profiles, respectively. The color version of this figure is available only in the electronic edition.

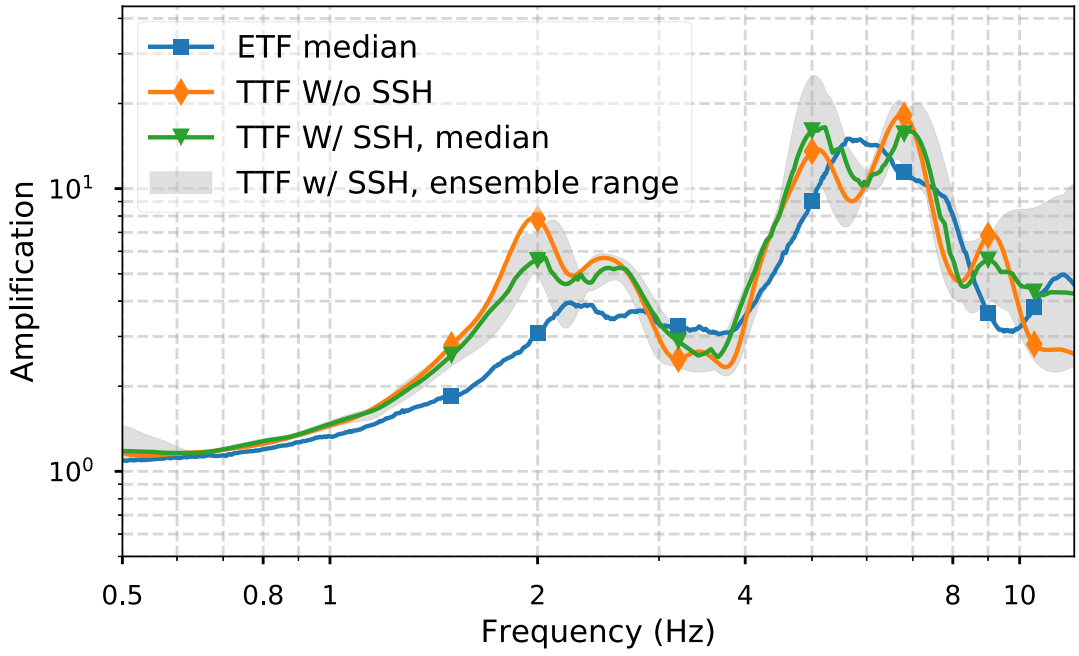

Figure 4.10: Comparison between the median ensemble ETF, the TTF from the 3D model without and with small-scale heterogeneities (SSHs) at TKCH05. The gray shaded region is the range of maximum and minimum values encountered in TTFs from these realizations of SSHs. The color version of this figure is available only in the electronic edition.

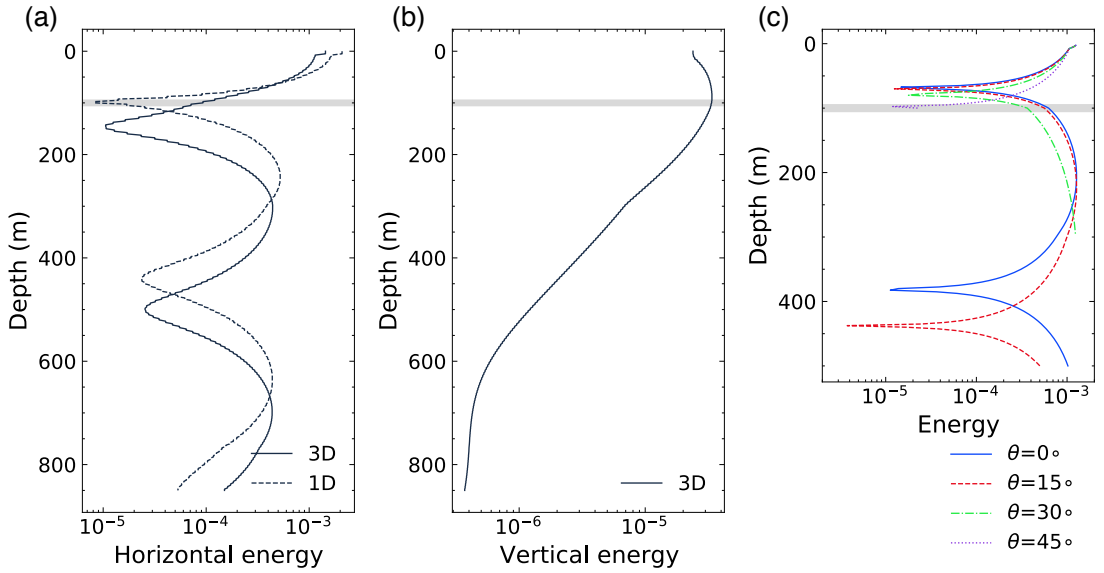

Figure 4.11: Energy on the (a) horizontal and (b) vertical components at the site TKCH05. (c) Total energy along depth using the simplified velocity profile at TKCH05 with different incidence angles. The gray horizontal line, at around 100 m depth, depicts the downhole site depth. The color version of this figure is available only in the electronic edition.

Appendix

This appendix includes one figure (Figure A4.1) showing the location of the events used in the GVDA study and recorded accelerations at a subset of events, one figure (Figure A4.2) showing the locations of the events used in the TKCH05 study and recorded accelerations at a subset of events, and two figures (Figures A4.3 and A4.4) showing the comparison of snapshots generated in 3D and 1D models at the TKCH05 site in Japan.

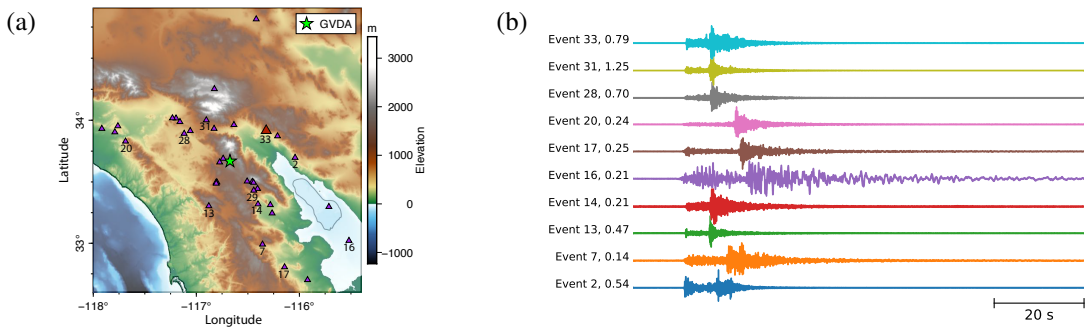

Figure A4.1: (a) Map of events (purple triangles) used for computing the ETFs at GVDA. The red triangle depicts the event used in simulations. (b) Recorded accelerations (normalized) along West-East direction at 10 randomly selected sites. The maximum amplitude is shown to the left of each line.

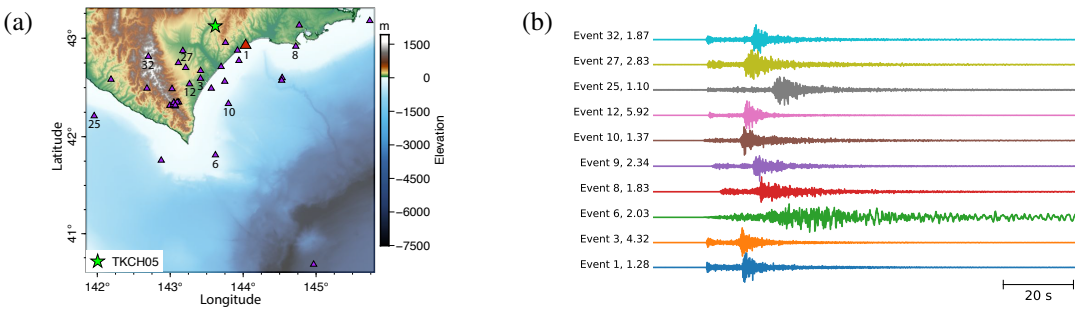

Figure A4.2: (a) Map of events (purple triangles) used for computing the ETFs at TKCH05. The red triangle depicts the event used in simulations. (b) Recorded accelerations (normalized) along West-East direction at 10 randomly selected sites. The maximum amplitude is shown to the left of each line.

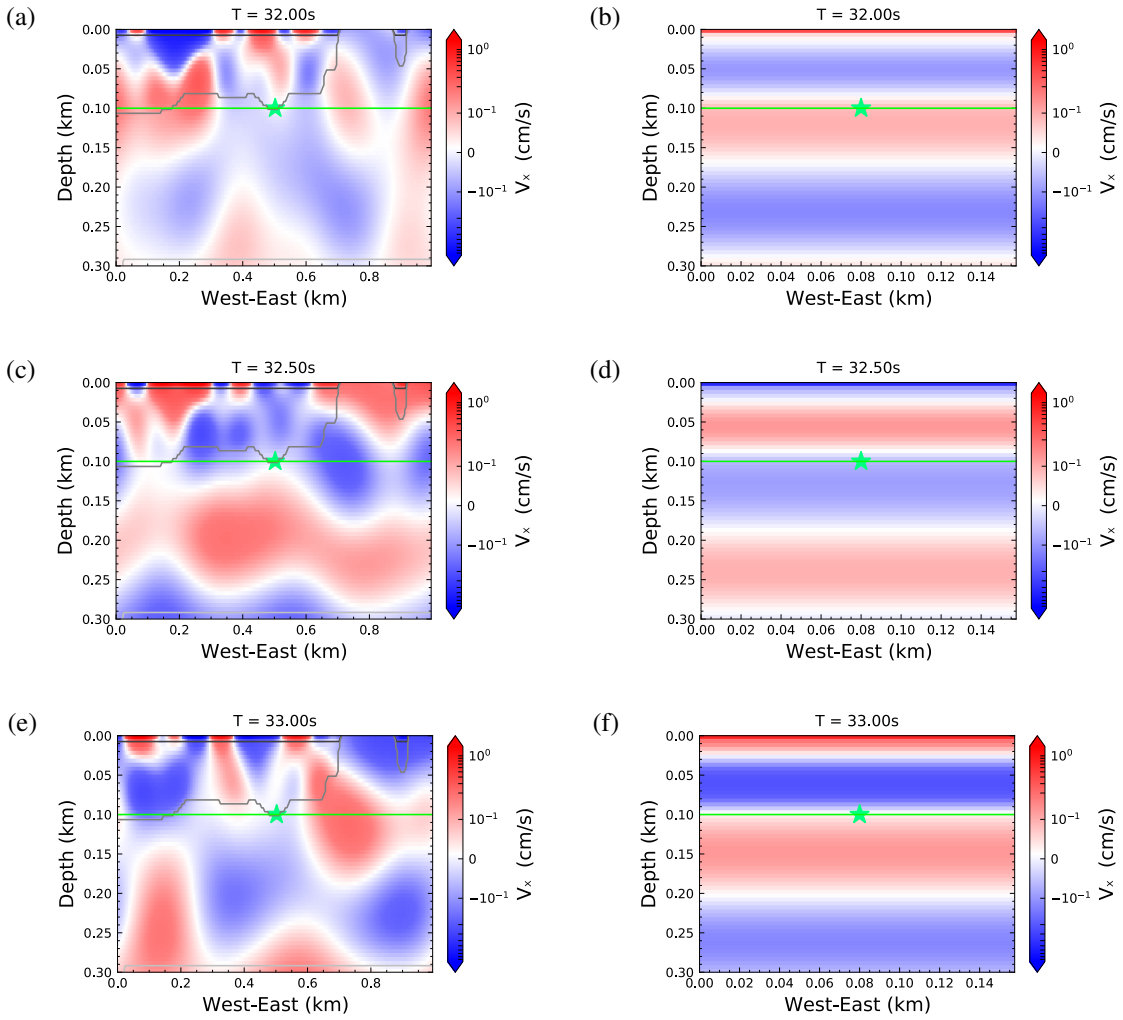

Figure A4.3: Snapshots of V_X at TKCH05 along the A-A' cross section in Figure 4.8c, bandpass filtered between 4.5 and 5 Hz. (a), (c) and (e) display snapshots of the 3D model, where the gray contour lines represent interfaces between bulks with difference Vs; the green star denotes the downhole site and the green line marks its depth. (b), (d) and (f) are for the 1D model.

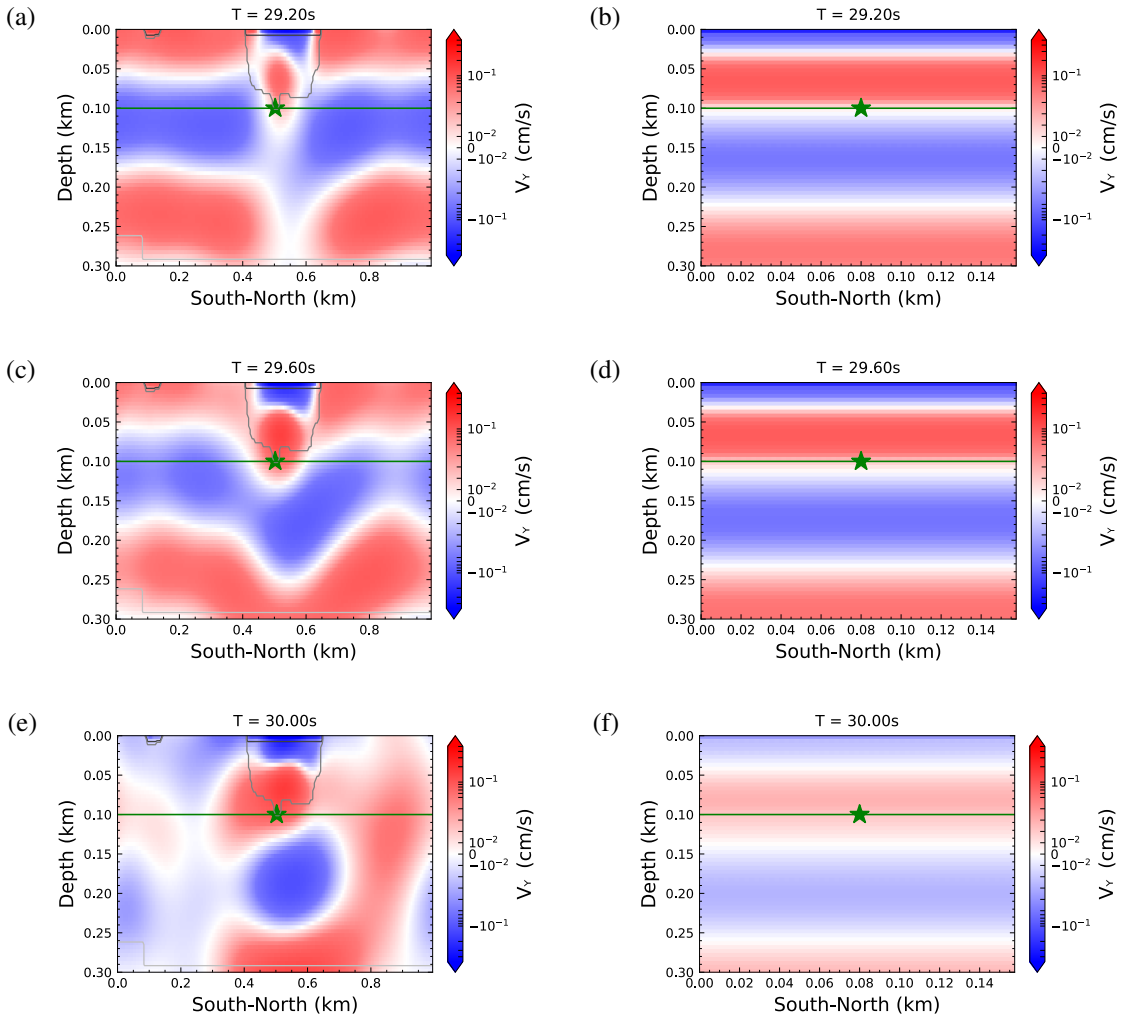

Figure A4.4: Same as Figure A4.3, except along the B-B' cross section in Figure 4.8c.

Chapter 5

Kinematic Source Models for Earthquake Simulations with Fault-zone Plasticity

Fault slip and surface deformation patterns are essential factors in seismic hazard assessment. However, slip inversions reveal a widely observed shallow slip deficit (SSD) which has not yet been clearly explained. One possible cause of the SSD is distributed plastic deformation in the fault damage zone near the surface. Roten *et al*. (2017a) performed 3D dynamic rupture simulations of the 1992 M_w 7.3 Landers earthquake in a medium governed by Drucker-Prager plasticity. The study showed that while linear simulations tend to underpredict SSD and off-fault deformation (OFD), nonlinear simulations with moderately fractured rock mass can properly reproduce results that are consistent with the 30-60% SSD and around 46% OFD reported in geodetic observations. Analysis of the Roten *et al*. (2017a) results shows that discrepancies between linear and nonlinear simulations are only significant in the top few hundreds of meters of the surface-rupturing fault. Although inelastic response in the fault damage zone provides more realistic representations of earthquake physics, it can be computationally expensive or numerically unfeasible (e.g., in adjoint methods) to include nonlinear effects in ground motion simulations. One solution proposed here is to use an equivalent kinematic source (EKS) model that mimics

the fault-zone plastic effects. This method generates source-time-functions by modifying the slip rate time histories based on comparisons of linear and non-linear dynamic rupture models, which are then used as input to kinematic simulations. The EKS model generally reproduces the reduction of ground motions observed in dynamic simulations with fault-zone plasticity. In spite of its simple formula, the EKS model is relatively robust in the presence different stress drop, rock strength and rupture directions for a M_w 7.8 earthquake scenario on the San Andreas Fault. Further verification of the method and comparison with the output from kinematic rupture generators are needed before the anticipated use in practical applications such as the SCEC CyberShake and Broadband platforms.

5.1 Introduction

Dynamic and kinematic earthquake simulations of fault rupture processes and wave propagation have been widely used as a complimentary approach to predict ground motions, especially for near-source regions where observed data is sparse. Numerical models are also used to establish physical limits to ground motions caused by plastic yielding in crustal rocks (e.g., Andrews *et al*., 2007; Duan and Day, 2010). Roten *et al*. (2014) simulated the M_w 7.8 ShakeOut earthquake scenario on the southern San Andreas fault and found that plastic yielding in the fault zone can reduce peak ground velocities (PGVs) at periods longer than 1 s, which somewhat contradicts the typical assumption that non-linear effects are only relevant at higher frequencies. A successive study (Roten *et al*., 2017a) on the 1992 M_w 7.3 Landers Earthquake further showed that simulations with fault-zone plasticity can reproduce off-fault deformations and shallow slip deficit that are consistent with previous studies and observations; however linear simulations fail to capture such phenomenon.

Although many recent studies on rupture dynamics have focused on the absorption of rupture energy by inelastic response of near-fault materials and pointed out its importance in

numerical simulations (e.g., Andrews, 2005; Ma, 2008; Dunham *et al*., 2011b; Dunham *et al*., 2011a; Gabriel *et al*., 2013), linear simulations with viscoelastic models are still widely adopted for seismic hazard analysis considering their efficiency. This work aims to further explore fault-zone non-linearity due to plastic yielding and develop a kinematic source model to emulate plasticity in linear simulations.

5.2 Method

We set up a number of dynamic simulations using the AWP-ODC 3D finite-difference code (Olsen *et al*., 1995; Day and Bradley, 2001; Cui *et al*., 2010), which simulates spontaneous rupture with the staggered-grid split-node formulation (Dalguer and Day, 2007) and includes Drucker-Prager plasticity following the return-map algorithm (Roten *et al*., 2017a). The code has been verified against several finite-difference and finite-element methods for both visco-elastic and visco-plastic material properties within the Southern California Earthquake Center (SCEC) dynamic rupture code verification project (Harris *et al*., 2009; Harris *et al*., 2011).

5.2.1 Simulations of Dynamic Rupture

We performed dynamic simulations of a M_w 7.8 earthquake scenario rupturing the southern San Andreas Fault. The planar fault was embedded in a 3-D heterogeneous velocity mesh (SCEC CVM4; Magistrale *et al*., 2000) with a 450-m wide low-velocity zone, where the peak amplitudes of the shear wave are reduced by 30%, based on the model by Roten *et al*. (2017a).

The Drucker-Prager plasticity was implemented in terms of cohesion c and friction angle φ:

$$Y(\tau) = \max\left(0, c\cos\varphi - \left(\tau_m + P_f\right)\sin\varphi\right), \tag{5.2.1}$$

where $Y(\tau)$ is the yield stress, τ_m the mean stress (negative in compression) and P_f the fluid

pressure. Although cohesions and friction angles can be measured from small samples in the laboratory, rock strength tends to decrease with sample size, as smaller samples are less likely to include pre-existing fractures on which failure may occur (Wyllie, 2017). This issue is addressed by the generalized Hoek-Brown failure criterion, which describes the strength of intact rock with the unconfined compressive strength and the material constant m_i, which is provided in tables for various rock types. The reduced value mb is evaluated from the material constant m_i using the Geological Strength Index (GSI) of the rock (Hoek and Brown, 1980; Hoek and Brown, 1997). The value of the GSI ranges from 0 to 100 and is used to reflect different geologic conditions, related to the degree of fracturing and weathering. For example, a GSI above about 80 indicates intact, undisturbed rock; a GSI of 50 describes a blocky/disturbed rock, while a GSI value of 30 characterizes a mostly disintegrated, heavily broken/tectonically deformed rock mass. The Hoek-Brown model (Evert *et al*., 2002) is used to approximate the Hoek-Brown failure criterion and derive the equivalent cohesions and friction angles for two different rock models, sandstone and shale, with GSI values of 50 and 30, respectively.

We performed dynamic rupture simulations for several different realizations of the random stress field and selected a representative case for different media (Fig. 5.1). Linear and non-linear models show similar spatial patterns of the peak slip rates (PSRs), while the site-specific amplitudes can show considerable variation between the two distributions, in particular near the surface. In the linear case, surface PSRs are about 7 m/s for most parts of the fault and reach peak values in excess of 14 m/s in the right portion of the fault. These surface PSR values are reduced to less than 4 m/s in the non-linear simulation for the sandstone model, and even less for the shale model. Overall reduction in PSRs is produced by non-linear effects, and it is most pronounced in the shallow zone, which is consistent with the findings from Roten *et al*. (2014). We also use simulations with different stress drop (7, 8 and 10 MPa), as was found by Roten *et al*. (2017a) to significantly affect the magnitude of nonlinear reduction of ampliutudes, as well as with different rupture directions.

5.2.2 Peak Slip Rate–Depth Profile

Since permanent deformations concentrate near the fault, plastic yielding of crustal rock in fault zones is assumed to produce the majority of the difference in ground motions. We averaged the slip rates along depth for linear and non-linear simulations using the SCEC CVM4. The linear models excite high PSRs near the surface ($<$ 3 km depth), which can be as large as twice the PSRs for sandstone models, while both models generate almost identical PSRs in the deeper part of the fault. This result is also shown through the ratio of PSRs between non-linear and linear models, which gradually increases from about 0.4-0.5 on the surface to close to 1 near the bottom of the fault (Fig. 5.2).

Including non-linearity caused by fault-zone plasticity can greatly increase the computational cost in dynamic simulations, while kinematic simulations using linear models are much more efficient. The similar pattern of PSR ratio profiles motivates the design of a depth-dependent 'shape' function, which can be applied to the linear PSR profile to replicate the non-linear PSR profile, and therefore produce similar ground motions without the added computational cost of the nonlinear rheology. We adopted the shape function in the form of $r_{fit} = A + B * \exp(f(depth))$, and used regression of a large ensemble of realizations to produce a best-fit function (see red dashed curves in Fig. 5.2):

$$r_{fit} = 0.97 - \left(0.97 - \frac{GSI}{100}\right) * \exp\left(\frac{-d}{d_{norm}}\right), \tag{5.2.2}$$

where d is the depth and d_{norm} is a normalization depth, above which the reduction of PSRs in non-linear cases becomes pronounced. We approximated d_{norm} with the depth where the PSR profile for the linear model first produces near constant values. Note that this depth is closely related to the fault zone rock strengths, as further discussed in Section 5.4. The shape function mentioned above is therefore only a function of depth and rock strength (represented by GSI values). Moreover, the plastic yielding mainly occurs when strain is large, so the difference

in source time functions (STFs) between non-linear and linear models generally exists in a short period around the failure time. Equation (5.2.2) only describes the ratio of PSR and we therefore decide to use a narrow Gaussian shape window centered at the subfault peak failure time, i.e. the width of the Gaussian window at each subfualt is double of the time interval between the time when rupture starts (defined as reaching 1% of PSR) and the time reaching PSR.

5.2.3 Kinematic Source Model

In the proposed method, given any STF for a linear model, its corresponding non-linear PSR-depth profile can be retrieved by multiplying the shape function introduced in Equation (5.2.2) with the PSR profile from the linear model. The process to modify a STF to obtain the converted STF is demonstrated in Figure 5.3. The modification is applied to all subfaults and generates an equivalent kinematic source (EKS) model. The PSR profile describes the slip rate distribution along fault strike with individual STFs on each subfault at the same average depth. Using the methodology, some detailed rupture information is inevitably lost. However, the converted STF is reasonably close to that for the non-linear model, suggesting that it is reasonable to expect that the EKS model is able to reproduce reasonably similar ground motions to that from the non-linear model, which we demonstrate in the following section.

5.3 Comparison of Ground Motion Simulations for Linear, Nonlinear and EKS models

5.3.1 Comparison of Ground Motions

Figure 5.4 shows peak ground velocities for example scenarios of the M_w 7.8 ShakeOut scenario with linear, plastic, and EKS models. In the linear case, strong shaking (PGV > 3

m/s) occurs near the fault, in particular at Palm Springs, at the intersection of the fault and the San Bernardino Basin, and near Lake Hughes; some small patches of strong ground motions (PGVs larger than 1.5 m/s) also appear in the Los Angeles (LA) Basin and Oxnard Plain. These patterns have been reported in previous simulations (Olsen *et al*., 2009) and confirmed by ambient noise measurements (Denolle *et al*., 2014), which can be attributed to wave guide effects. The non-linear model predicts significantly smaller PGVs near the fault, where PGVs are reduced to about 2 m/s or smaller. The reduction is relatively less pronounced in the areas near Palm Springs. The EKS model, as expected, generally produces lower PGVs compared to the linear model, though slightly higher those from the nonlinear model.

5.3.2 Nonlinear Reduction of Ground Motion Extremes

The reduction of ground motion extremes in the nonlinear models can be seen in the cumulative distribution of PGVs (Fig. 5.5). For example, at an occurrence frequency of 10^{-4}, PGVs decrease from 4.5 m/s in the linear simulation to 3.5 m/s in the nonlinear simulation, which is well reproduced in the EKS model. The results are consistent for different rock types including sandstone and shale, with the latter yielding slightly more reduction than sandstone due to its weaker strength.

In order to analyze the effects of plasticity and the efficacy of the EKS model at different frequencies, Figs. 5.6 to 5.8) compares the distributions of spectral acceleration (SA) at 5 s (SA-5s), 3 s (SA-3s), and 2 s (SA-2s). The nonlinear reductions of SAs are generally similar to those for PGVs, with relatively larger reduction of the most infrequent SAs (up to 40-50% for SA-3s and even more for SA-2s). The nonlinear reduction of SA-5s is relatively smaller than that at shorter periods, and the EKS tends to overestimate the SA-5s for the high stress drop model.

5.3.3 Rupture Direction

The rupture direction can play an important role in the resulting ground motions due to directivity, and in connection with waveguide channels (e.g., Olsen *et al*., 2006). We also tested how robust the EKS method performs for different rupture directions. Figure 5.8 and 5.9 show linear, nonlinear and EKS ground motions for the ShakeOut scenario with fault ruptures in the northwestward and southeastward directions, respectively. The distribution of SA-2s in the lower stress drop case (7 MPa) is similar for the two rupture directions. The large stress drop scenario (10 MPa) for the NW-SE rupture direction generates smaller extreme SA-2s values as compared to those for the SE-NW rupture, triggering weaker non-linear effects. For all scenarios, the EKS method tends to reduce the linear ground motions to levels of about 100-150% of the nonlinear results. However, more simulations with different stress drops are needed to assess the efficacy of the method in general.

5.3.4 Off-Fault Regions

Even though the EKS model can reproduce similar overall ground motion reduction features to nonlinear models, its efficacy in regions away from the fault remains a challenge. As shown in Figure 5.4, the EKS model fails to reduce extreme PGVs in some areas from the linear results, which is however present in the nonlinear simulations. Figure 5.10 shows the distribution of PGVs in the LA basin for linear, nonlinear and EKS models. The EKS model works reasonably well to reproduce the PGV patterns from the nonlinear models for shale but overpredicts the PGVs for sandstone. This may be explained by the fact that the sandstone models generate PGVs in the LA basin comparable with the shale model, instead of stronger shaking due to greater rock strength and less inelastic absorption of seismic energy.

5.4 Discussion and Conclusions

Our simulations of an M_w 7.8 strike slip scenario show that slip rates and the resulting ground motions are reduced, as expected, in the presence of plastic yielding in fault-zone crustal rocks. We attempt to emulate the plastic effects by equivalent kinematic sources (EKS), modifying the source time functions in linear models. The EKS model generates amplitude reduction in the range of 100-150% of that seen from nonlinear (plastic) simulations. Considering its reasonable robust performance for different rock strengths and rupture directions along with its simple formula, the EKS model is suitable to be applied in kinematic rupture generators.

The EKS model proposed here only depends on rock strength and depth. It is likely that more advanced formulation of the method, e.g. with dependency on lateral variation of the source-time function and magnitude, initial stress, and stress drop can produce more accurate ground motion features. More simulations with different realizations of these parameters will have to be carried out, which is recommended for future work. These simulations should also include non-surface-rupturing scenarios.

Acknowledgements

Chapter 5, in full, is a reformatted version of a report to the Southern California Earthquake Center: Hu, Z., Roten, D., Olsen, K.B., and Day, S.M. (2021). Kinematic Source Models for Earthquake Simulations with Fault-zone Plasticity. The dissertation author was the primary investigator and author of this manuscript.

Tables and Figures

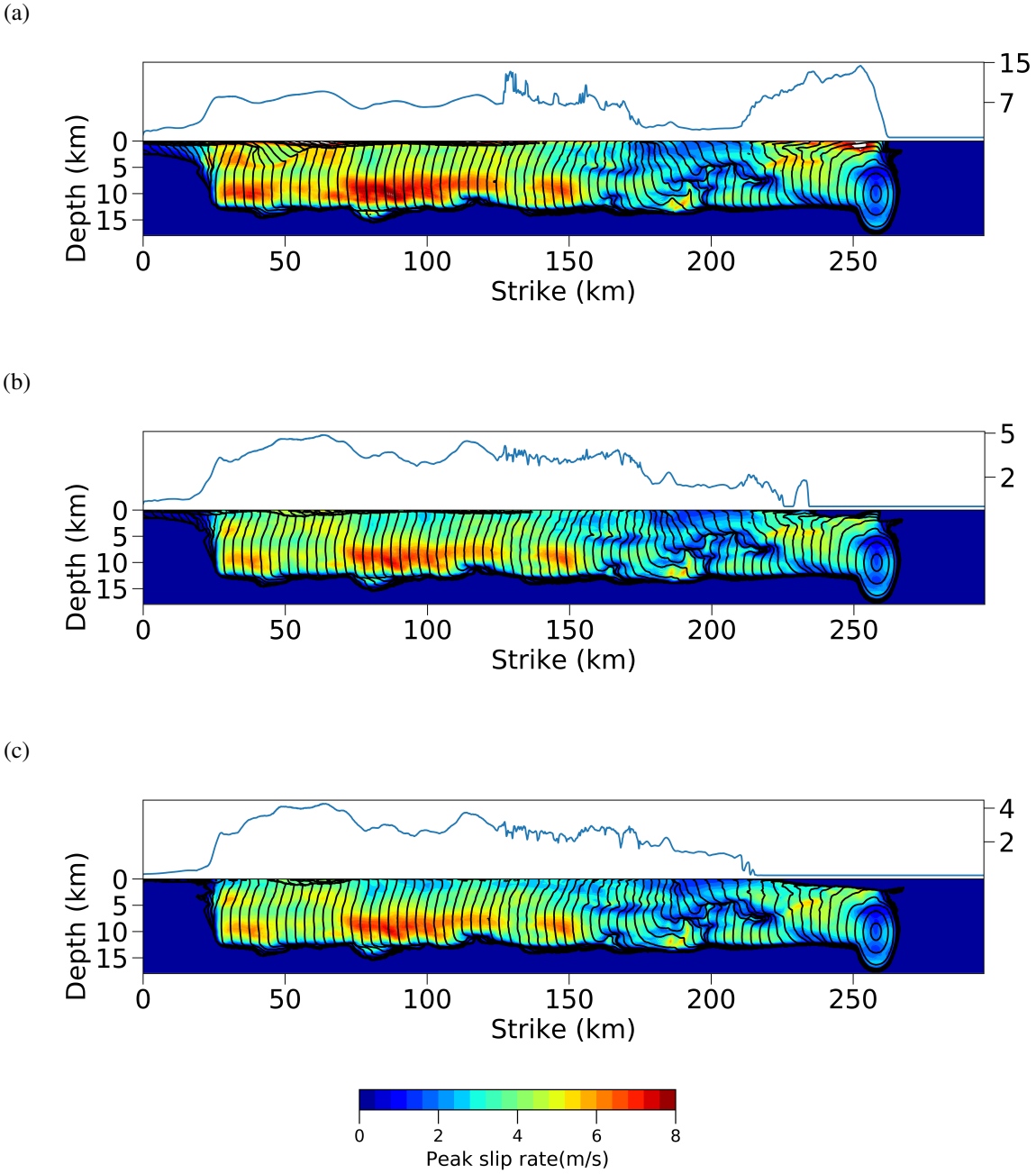

Figure 5.1: Peak slip rate (PSR) simulated on the fault for ShakeOut scenario, with the surface PSR (in m/s) shown in the panel above each subplot. (a) linear, (b) sandstone (nonlinear), and (c) shale (nonlinear) results. Black contours indicate rupture time in 1 s intervals from 0.

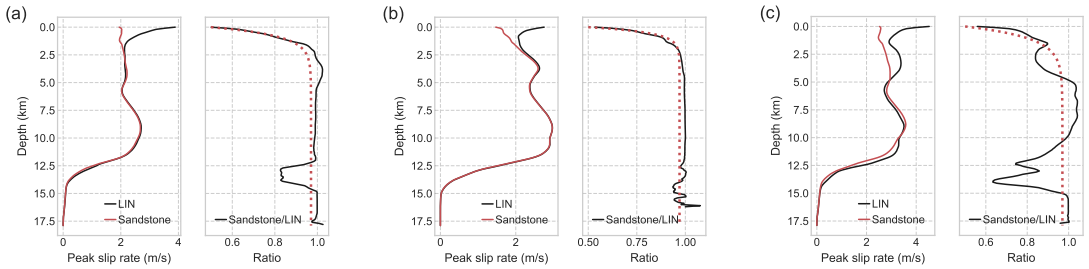

Figure 5.2: Peak slip rate (PSR) averaged along strike against depth (left panel of each subplot) for sandstone (nonlinear) and linear models and their ratio (right panel of each subplot). (a)-(c) depit three realizations for the sandstone models with stress drop of 7, 8, and 10 MPa, respectively. Dashed red lines indicate the curves fitting the nonlinear to linear PSR ratios using Equation (5.2.2).

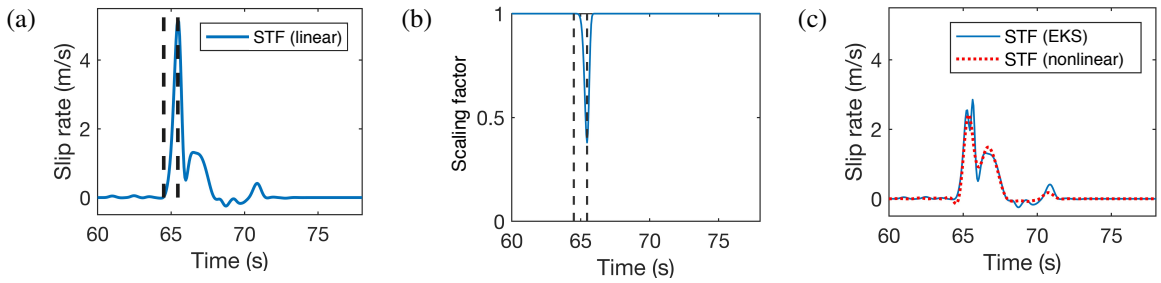

Figure 5.3: (a) STF on a representative subfault from the linear model. (b) Time-domain scaling factors from the shape function computed by Equation (5.2.2). (c) STFs for the nonlinear model and EKS model. The black dashed lines in (a) and (b) indicate the peak time of the STF and shape functions.

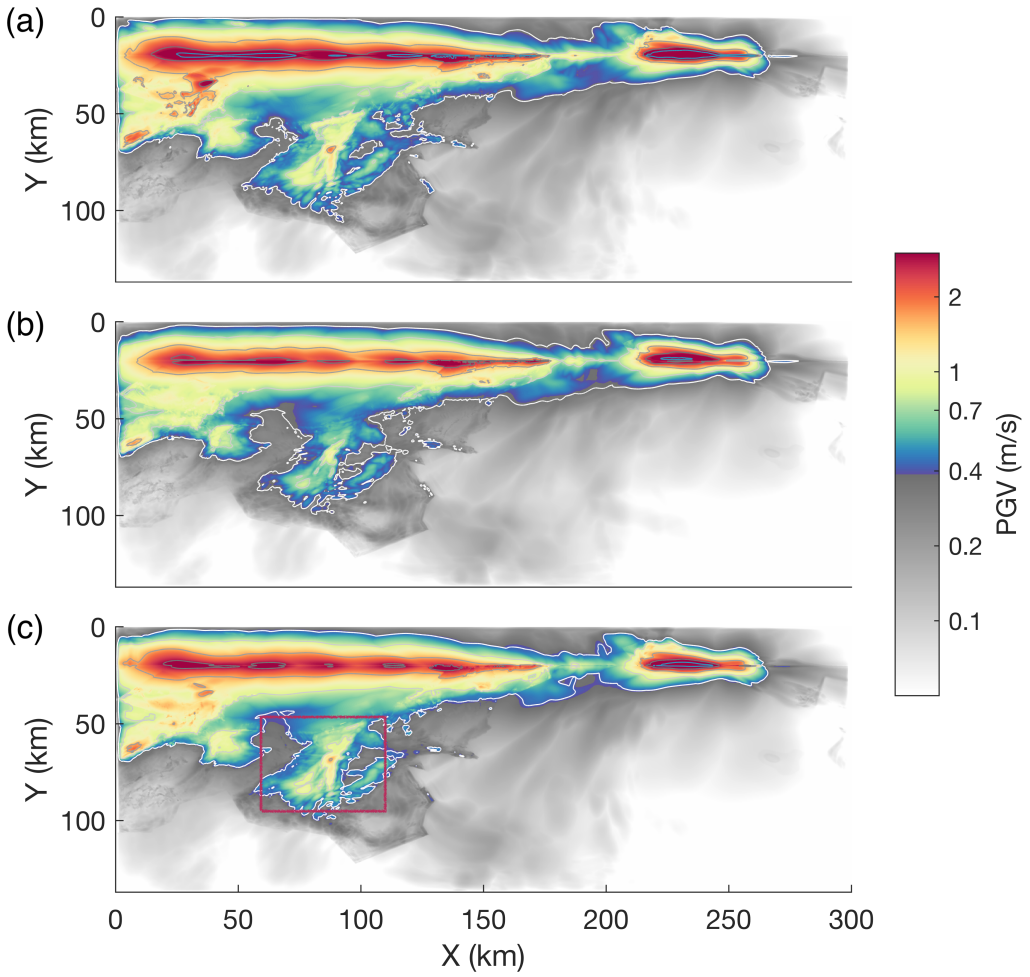

Figure 5.4: PGV distribution for the southern San Andreas fault region, obtained for (a) linear, (b) sandstone and (c) EKS model. The red rectangle depicts the LA basin region for further ground motion comparisons in Figure 5.10.

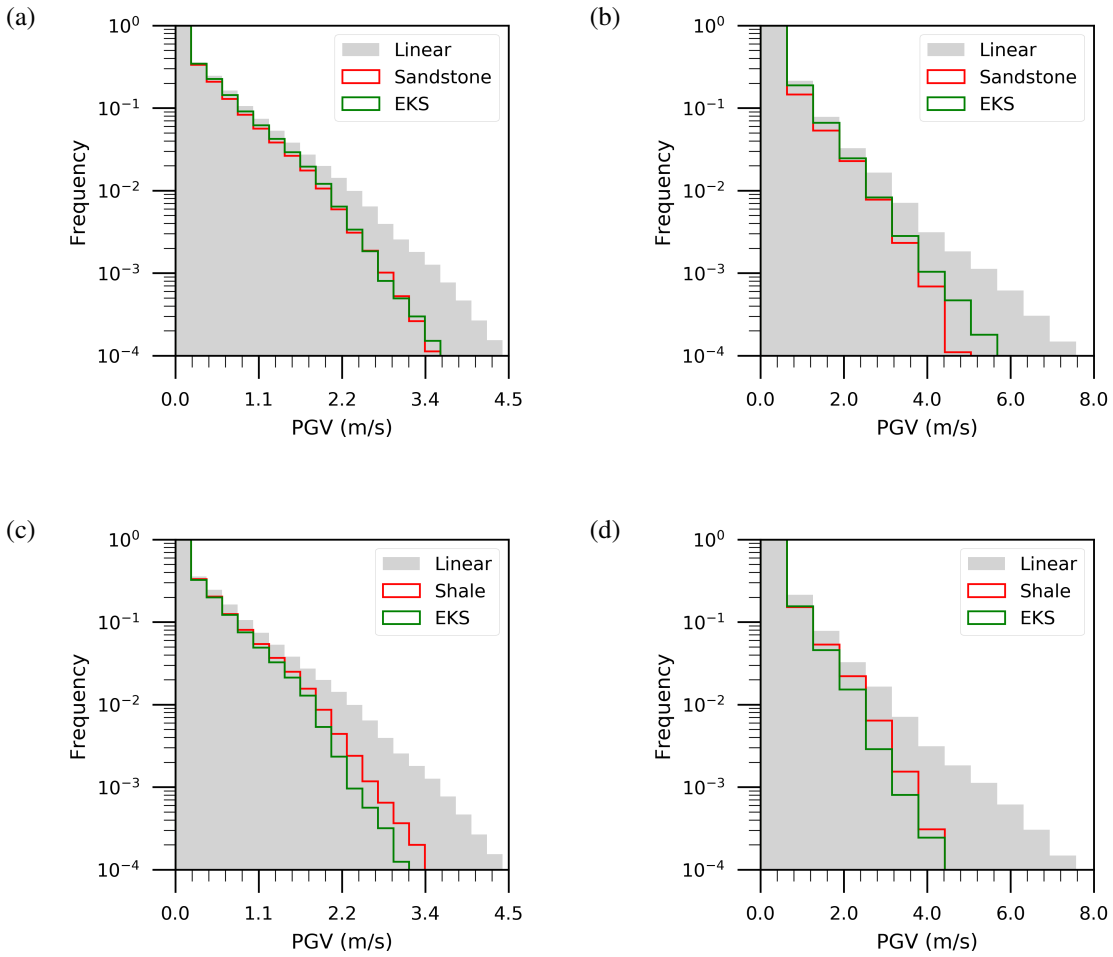

Figure 5.5: Cumulative distribution of PGVs for linear models with stress drop of 7 (a and c) and 10 (b and d) MPa, as well as nonlinear models and the corresponding EKS models. The top row (a and b) depicts models with sandstone and the bottom row (c and d) shows models with shale.

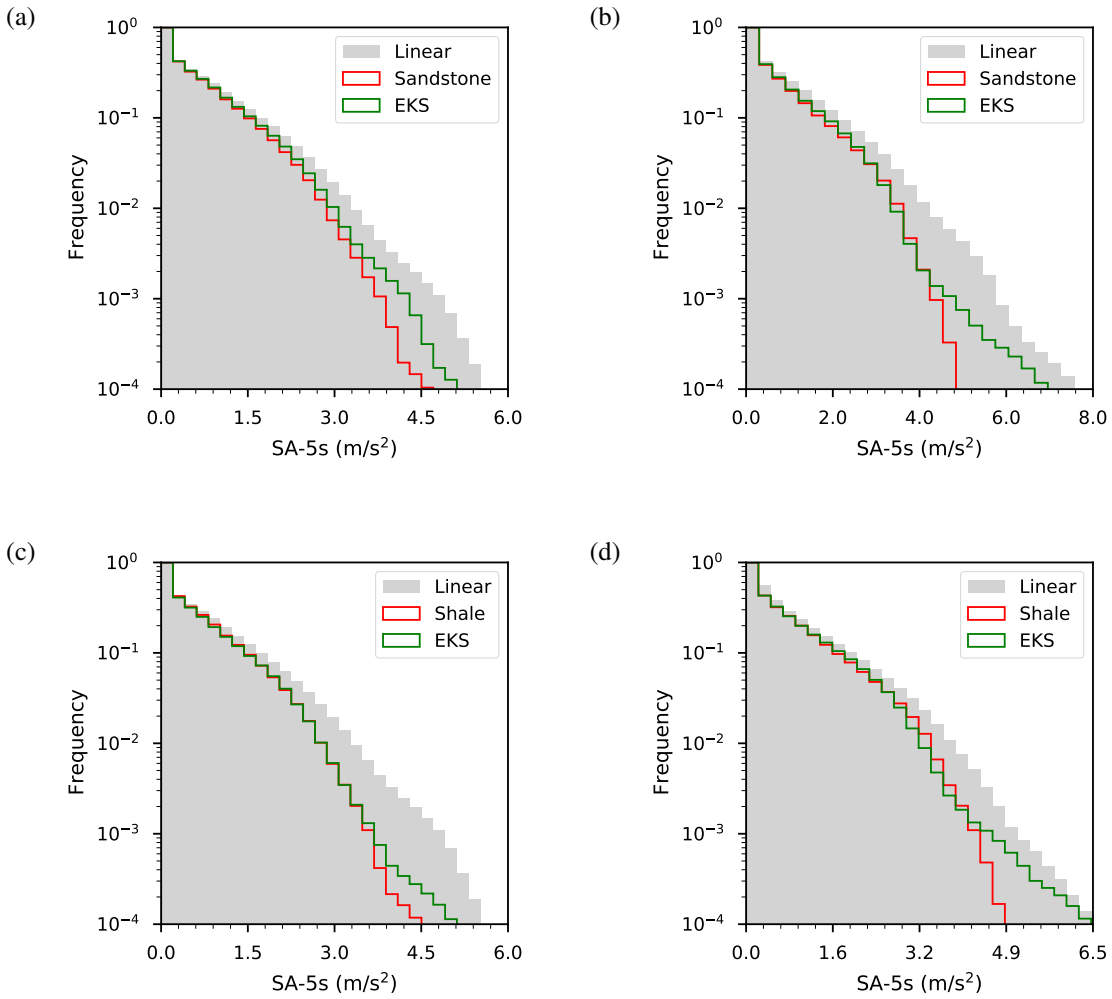

Figure 5.6: Same as Figure 5.5, but for SA-5s comparisons.

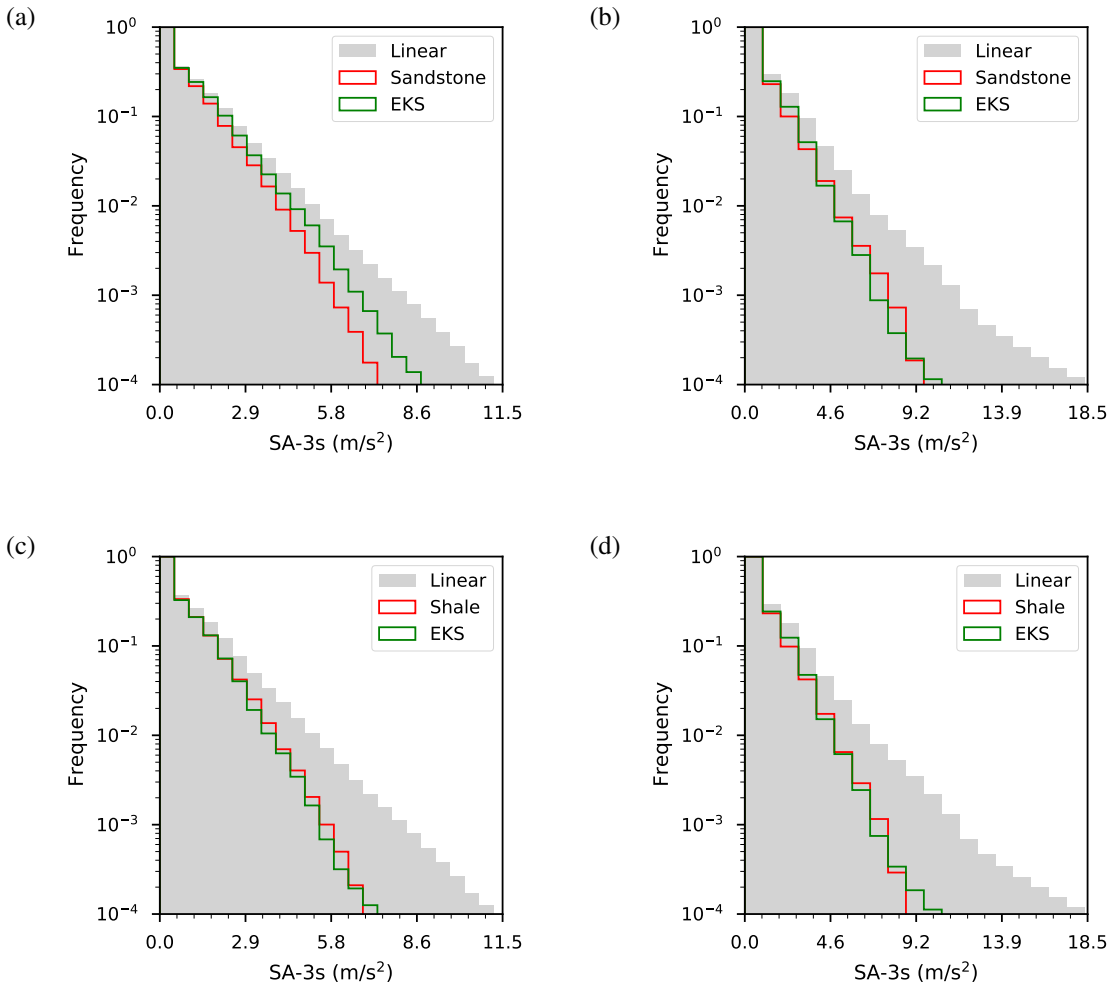

Figure 5.7: Same as Figure 5.5, but for SA-3s comparisons.

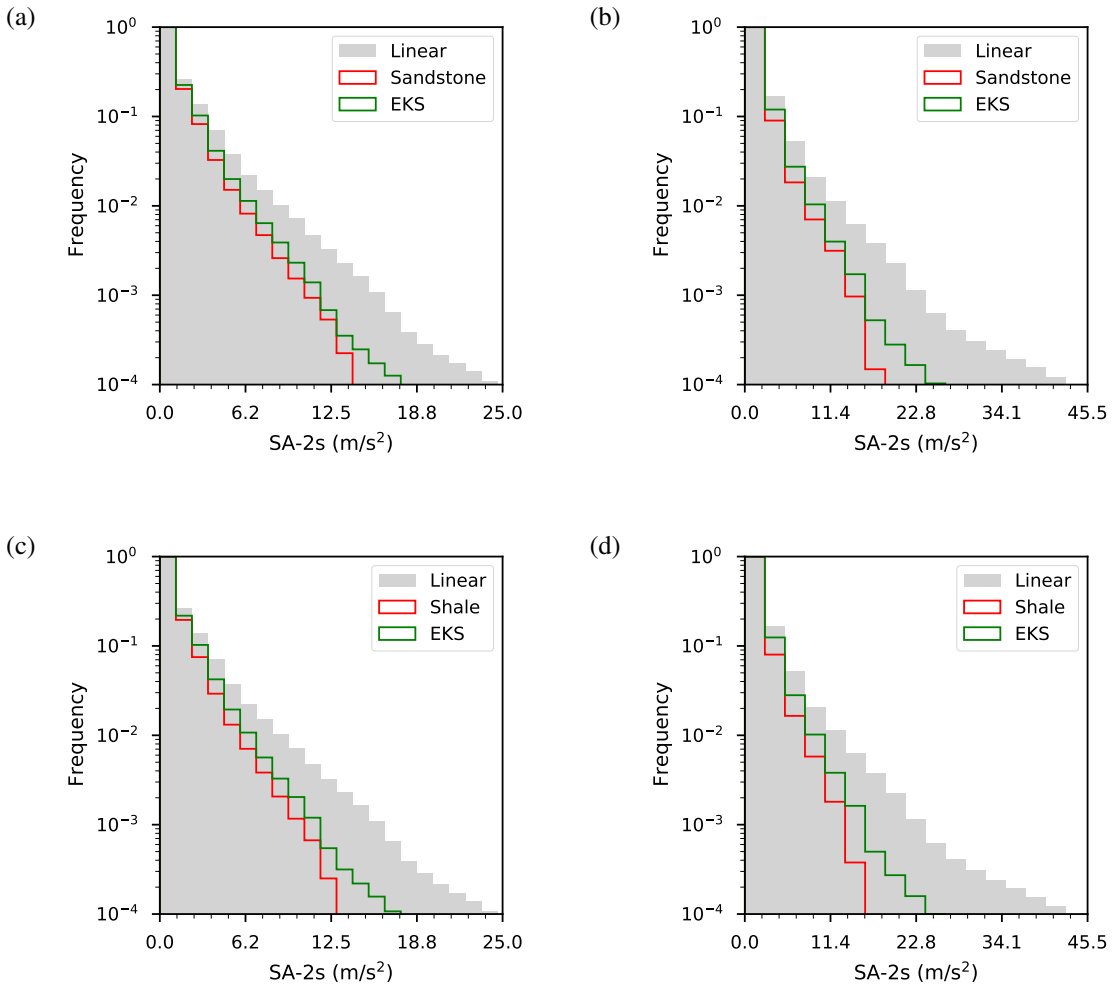

Figure 5.8: Same as Figure 5.5, but for SA-2s comparisons.

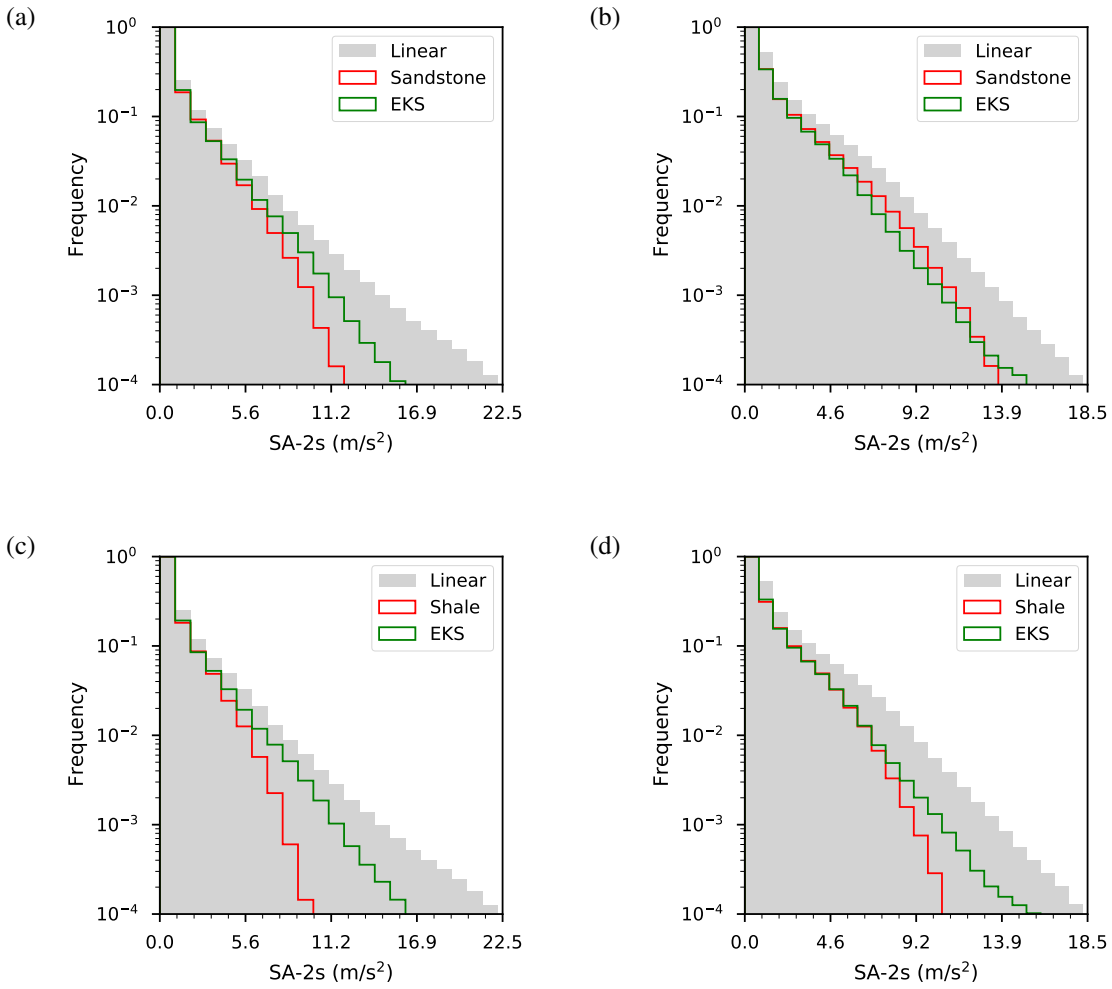

Figure 5.9: Same as Figure 5.8, but the rupture direction is reversed to NW-SE for all models.

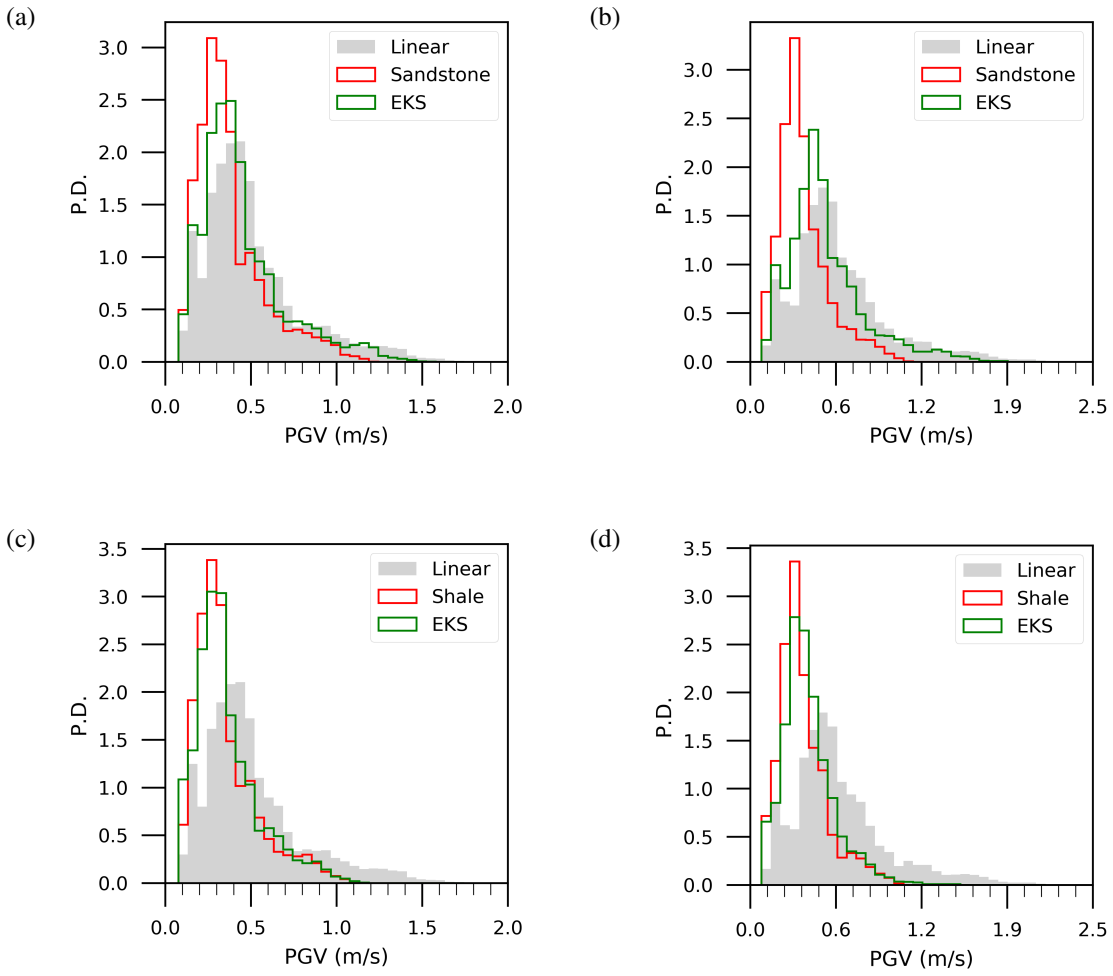

Figure 5.10: Probability density (P.D.) histograms of PGVs in the Los Angeles Basin area. The models for each subfigure are the same as in Figure 5.8

Appendix

A Von Kármán Autocorrelation Function

The stochastic nature of the medium, with the assumption that the randomness is spatially homogeneous or isotropic, can be characterized using an autocorrelation function (ACF) as a function of spatial lag ($R(\mathrm{x})$). The power spectral density function characterizing the random medium can be calculated from the Fourier transform of the ACF over three (for 3D simulations) spatial coordinates:

$$P(k_x, k_y, k_z) = \iiint_{-\infty}^{\infty} R(x, y, z) \mathrm{e}^{-k_x x - k_y y - k_z z} \, \mathrm{d}x \, \mathrm{d}y \, \mathrm{d}z \tag{A1}$$

where k_x, k_y and k_z are the wavenumbers in each direction, respecitvely. For wave propagation problems in geophysical applications, the von Kármán ACF is commonly used and found superior to Gaussian or exponential formulations (Frankel and Clayton, 1986), with the form of:

$$\Phi_{v,a}(r) = \sigma^2 \frac{2^{1-v}}{\Gamma(v)} \left(\frac{r}{a}\right)^v K_v \left(\frac{r}{a}\right) \tag{A2}$$

in which ν is the Hurst component, a is the correlation length, K_ν is the modified Bessel function of order ν, $\Gamma(\nu)$ is the gamma function, and σ^2 is the variance, with Fourier transform:

$$P(k) = \frac{\sigma^2 (2\sqrt{\pi}a)^E \Gamma(v + E/2)^{v+E/2}}{\Gamma(v)\,(1 + k^2 a^2)} \tag{A3}$$

in which k is the wave number and E is the Euclidean dimension.

The von Kármán model follows a power law in its power spectral density function when the wavenumber k is large ($ak \gg 1$). In addition, it has a low-cut frequency filter and thus non-fractal large-scale heterogeneities. The von Kármán model is widely adopted in many independent studies due to its ability to capture the laterallly correlated heterogeneities as well as the self-similar small-scale heterogeneities, and good fit with experiments (Ru-Shan, 1982; Carpentier and Roy-Chowdhury, 2009; Nakata and Beroza, 2015). Nevertheless, the parameters remain uncertain due to diferent sources of data or the analysis methods used in indivisual studies. In general, Hurst exponents were reported between 0.0 and 0.5, and horizontal to vertical anisotropy ratios between 2 and 5 and the vertical correction lengths between 30 and 300 m in previous studies from digital geological maps, sonic logs and seismic reflection data (e.g., Nakata and Beroza, 2015; Savran and Olsen, 2016; and the references therein).

Bibliography

Abercrombie, R. E. (1997). "Near-Surface Attenuation and Site Effects from Comparison of Surface and Deep Borehole Recordings". In: *Bulletin of the Seismological Society of America* 87.3, pp. 731–744. ISSN: 0037-1106.

Abrahamson, N. and Silva, W. (2008). "Summary of the Abrahamson & Silva NGA Ground-Motion Relations". In: *Earthquake Spectra* 24.1, pp. 67–97. ISSN: 8755-2930, 1944-8201.

Abrahamson, N. A., Silva, W. J., and Kamai, R. (2014). "Summary of the ASK14 Ground Motion Relation for Active Crustal Regions". In: *Earthquake Spectra* 30.3, pp. 1025–1055. ISSN: 8755-2930, 1944-8201.

Aki, K. and Richards, P. G. (2002). *Quantitative Seismology*. 2nd ed. Sausalito, CA: University Science Books. ISBN: 0-935702-96-2.

Aki, K. (1969). "Analysis of the Seismic Coda of Local Earthquakes as Scattered Waves". In: *Journal of Geophysical Research (1896-1977)* 74.2, pp. 615–631. ISSN: 2156-2202.

— (1980). "Attenuation of Shear-Waves in the Lithosphere for Frequencies from 0.05 to 25 Hz". In: *Physics of the Earth and Planetary Interiors* 21.1, pp. 50–60. ISSN: 00319201.

— (1993). "Local Site Effects on Weak and Strong Ground Motion". In: *Tectonophysics*. New Horizons in Strong Motion: Seismic Studies and Engineering Practice 218.1, pp. 93–111. ISSN: 0040-1951.

Aki, K. and Chouet, B. (1975). "Origin of Coda Waves: Source, Attenuation, and Scattering Effects". In: *Journal of Geophysical Research (1896-1977)* 80.23, pp. 3322–3342. ISSN: 2156-2202.

Akkar, S. and Bommer, J. J. (2010). "Empirical Equations for the Prediction of PGA, PGV, and Spectral Accelerations in Europe, the Mediterranean Region, and the Middle East". In: *Seismological Research Letters* 81.2, pp. 195–206. ISSN: 0895-0695.

Anderson, J. G. (2004). "Quantitative Measure Of The Goodness-Of-Fit of Synthetic Seismograms". In: The 13th World Conference on Earthquake Engineering. Vancouver, B.C., Canada: Earthquake Engineering Research Institute, p. 243.

Anderson, J. G. and Hough, S. E. (1984). "A Model for the Shape of the Fourier Amplitude Spectrum of Acceleration at High Frequencies". In: *Bulletin of the Seismological Society of America* 74.5, pp. 1969–1993.

Anderson, J. G., Lee, Y., Zeng, Y., and Day, S. (1996). "Control of Strong Motion by the Upper 30 Meters". In: *Bulletin of the Seismological Society of America* 86.6, pp. 1749–1759. ISSN: 0037-1106.

Andrews, D. J. (2005). "Rupture Dynamics with Energy Loss Outside the Slip Zone". In: *Journal of Geophysical Research* 110.B1, B01307. ISSN: 0148-0227.

Andrews, D. J., Hanks, T. C., and Whitney, J. W. (2007). "Physical Limits on Ground Motion at Yucca Mountain". In: *Bulletin of the Seismological Society of America* 97.6, pp. 1771–1792. ISSN: 0037-1106.

Arias, A. (1970). *Measure of Earthquake Intensity.* Massachusetts Inst. of Tech., Cambridge. Univ. of Chile, Santiago de Chile.

Ashford, S. A. and Sitar, N. (1997). "Analysis of Topographic Amplification of Inclined Shear Waves in a Steep Coastal Bluff". In: *Bulletin of the Seismological Society of America* 87.3, pp. 692–700. ISSN: 0037-1106.

Assimaki, D., Kausel, E., and Gazetas, G. (2005). "Soil-Dependent Topographic Effects: A Case Study from the 1999 Athens Earthquake". In: *Earthquake Spectra* 21.4, pp. 929–966. ISSN: 8755-2930.

Aster, R. C. and Shearer, P. M. (1991). "High-Frequency Borehole Seismograms Recorded in the San Jacinto Fault Zone, Southern California. Part 1. Polarizations". In: *Bulletin of the Seismological Society of America* 81.4, pp. 1057–1080. ISSN: 0037-1106.

Atik, L. A., Abrahamson, N., Bommer, J. J., Scherbaum, F., Cotton, F., and Kuehn, N. (2010). "The Variability of Ground-Motion Prediction Models and Its Components". In: *Seismological Research Letters* 81.5, pp. 794–801. ISSN: 0895-0695.

Atkinson, G. M. and Boore, D. M. (2006). "Earthquake Ground-Motion Prediction Equations for Eastern North America". In: *Bulletin of the Seismological Society of America* 96.6, pp. 2181–2205. ISSN: 0037-1106.

Atkinson, G. M. (1995). "Attenuation and Source Parameters of Earthquakes in the Cascadia Region". In: *Bulletin of the Seismological Society of America* 85.5, pp. 1327–1342. ISSN: 0037-1106.

Bao, H., Bielak, J., Ghattas, O., Kallivokas, L. F., O'Hallaron, D. R., Shewchuk, J. R., and Xu, J. (1998). "Large-Scale Simulation of Elastic Wave Propagation in Heterogeneous Media on Parallel Computers". In: *Computer Methods in Applied Mechanics and Engineering*.

Containing Papers Presented at the Symposium on Advances in Computational Mechanics 152.1, pp. 85–102. ISSN: 0045-7825.

Barani, S., De Ferrari, R., and Ferretti, G. (2013). "Influence of Soil Modeling Uncertainties on Site Response". In: *Earthquake Spectra* 29.3, pp. 705–732. ISSN: 8755-2930, 1944-8201.

Bard, P.-Y. (1982). "Diffracted Waves and Displacement Field over Two-Dimensional Elevated Topographies". In: *Geophysical Journal International* 71.3, pp. 731–760. ISSN: 0956-540X.

Bean, C. J., Marsan, D., and Martini, F. (1999). "Statistical Measures of Crustal Heterogeneity from Reflection Seismic Data: The Role of Seismic Bandwidth". In: *Geophysical Research Letters* 26.21, pp. 3241–3244. ISSN: 1944-8007.

Beresnev, I. A. and Wen, K.-L. (1996). "Nonlinear Soil Response a Reality?" In: *Bulletin of the Seismological Society of America* 86.6, pp. 1964–1978.

Bielak, J., Taborda, R., Olsen, K., Graves, R., Silva, F., Khoshnevis, N., Savran, W., Roten, D., Shi, Z., Goulet, C., *et al*. (2016). "Verification and Validation of High-Frequency (f Max= 5 Hz) Ground Motion Simulations of the 2014 M 5.1 La Habra, California, Earthquake". In: *AGU Fall Meeting Abstracts*. Vol. 2016, S33G–04.

Bielak, J., Graves, R. W., Olsen, K. B., Taborda, R., RamÃrez-GuzmÃ¡n, L., Day, S. M., Ely, G. P., Roten, D., Jordan, T. H., Maechling, P. J., Urbanic, J., Cui, Y., and Juve, G. (2010). "The ShakeOut Earthquake Scenario: Verification of Three Simulation Sets". In: *Geophysical Journal International* 180.1, pp. 375–404. ISSN: 0956540X, 1365246X.

Bommer, J. J. and Abrahamson, N. A. (2006). "Why Do Modern Probabilistic Seismic-Hazard Analyses Often Lead to Increased Hazard Estimates?" In: *Bulletin of the Seismological Society of America* 96.6, pp. 1967–1977. ISSN: 0037-1106.

Bonilla, L. F., Steidl, J., Gariel, J.-C., and Archuleta, R. (2002). "Borehole Response Studies at the Garner Valley Downhole Array, Southern California". In: *Bulletin of the Seismological Society of America* 92.8, pp. 3165–3179. ISSN: 0037-1106.

Bonilla, L. F., Steidl, J. H., Lindley, G. T., Tumarkin, A. G., and Archuleta, R. J. (1997). "Site Amplification in the San Fernando Valley, California: Variability of Site-Effect Estimation Using the S-Wave, Coda, and H/V Methods". In: 87.3, pp. 710–730.

Boore, D. M. (1972). "A Note on the Effect of Simple Topography on Seismic SH Waves". In: *Bulletin of the Seismological Society of America* 62.1, pp. 275–284.

— (1986). "Short-Period P- and S-Wave Radiation from Large Earthquakes: Implications for Spectral Scaling Relations". In: *Bulletin of the Seismological Society of America* 76.1, pp. 43–64. ISSN: 0037-1106.

Boore, D. M. (2004). “Can Site Response Be Predicted?” In: *Journal of Earthquake Engineering* 8 (sup001), pp. 1–41. ISSN: 1363-2469, 1559-808X.

Boore, D. M. and Joyner, W. B. (1991). “Estimation of Ground Motion at Deep-Soil Sites in Eastern North America”. In: *Bulletin of the Seismological Society of America* 81.6, pp. 2167–2185. ISSN: 0037-1106.

— (1997). “Site Amplifications for Generic Rock Sites”. In: *Bulletin of the Seismological Society of America* 87.2, pp. 327–341. ISSN: 0037-1106.

Boore, D. M., Stewart, J. P., Seyhan, E., and Atkinson, G. M. (2014). “NGA-West2 Equations for Predicting PGA, PGV, and 5% Damped PSA for Shallow Crustal Earthquakes”. In: *Earthquake Spectra* 30.3, pp. 1057–1085. ISSN: 8755-2930.

Boore, D. M. and Thompson, E. M. (2007). “On Using Surface-Source Downhole-Receiver Logging to Determine Seismic Slownesses”. In: *Soil Dynamics and Earthquake Engineering* 27.11, pp. 971–985. ISSN: 02677261.

Borcherdt, R. D. (1970). “Effects of Local Geology on Ground Motion near San Francisco Bay”. In: *Bulletin of the Seismological Society of America* 60, pp. 29–61.

Borcherdt, R. D. (1994). “Estimates of Site-Dependent Response Spectra for Design (Methodology and Justification)”. In: *Earthquake Spectra* 10.4, pp. 617–653. ISSN: 8755-2930, 1944-8201.

Bouchon, M. and Barker, J. S. (1996). “Seismic Response of a Hill: The Example of Tarzana, California”. In: *Bulletin of the Seismological Society of America* 86 (1A), pp. 66–72. ISSN: 0037-1106.

Bouckovalas, G. D. and Papadimitriou, A. G. (2005). “Numerical Evaluation of Slope Topography Effects on Seismic Ground Motion”. In: *Soil Dynamics and Earthquake Engineering*. 11th International Conference on Soil Dynamics and Earthquake Engineering (ICSDEE): Part 1 25.7, pp. 547–558. ISSN: 0267-7261.

Bozorgnia, Y., Abrahamson, N. A., Atik, L. A., Ancheta, T. D., Atkinson, G. M., Baker, J. W., Baltay, A., Boore, D. M., Campbell, K. W., Chiou, B. S.-J., Darragh, R., Day, S., Donahue, J., Graves, R. W., Gregor, N., Hanks, T., Idriss, I. M., Kamai, R., Kishida, T., Kottke, A., Mahin, S. A., Rezaeian, S., Rowshandel, B., Seyhan, E., Shahi, S., Shantz, T., Silva, W., Spudich, P., Stewart, J. P., Watson-Lamprey, J., Wooddell, K., and Youngs, R. (2014). “NGA-West2 Research Project”. In: *Earthquake Spectra* 30.3, pp. 973–987. ISSN: 8755-2930, 1944-8201.

Brocher, T. M. (2005). “Empirical Relations between Elastic Wavespeeds and Density in the Earth’s Crust”. In: *Bulletin of the Seismological Society of America* 95.6, pp. 2081–2092. ISSN: 0037-1106.

Brocher, T. M. (2008). "Compressional and Shear-Wave Velocity versus Depth Relations for Common Rock Types in Northern California". In: *Bulletin of the Seismological Society of America* 98.2, pp. 950–968.

Brune, J. N. (1970). "Tectonic Stress and the Spectra of Seismic Shear Waves from Earthquakes". In: *Journal of geophysical research* 75.26, pp. 4997–5009.

BSSC (2003). *The 2003 NEHRP Recommended Provisions for New Buildings and Other Structures. Part 1: Provisions (FEMA 450)*.

Burjánek, J., Edwards, B., and Fäh, D. (2014). "Empirical Evidence of Local Seismic Effects at Sites with Pronounced Topography: A Systematic Approach". In: *Geophysical Journal International* 197.1, pp. 608–619. ISSN: 0956-540X.

Campbell, K. W. and Bozorgnia, Y. (2014). "NGA-West2 Ground Motion Model for the Average Horizontal Components of PGA, PGV, and 5% Damped Linear Acceleration Response Spectra". In: *Earthquake Spectra* 30.3, pp. 1087–1115. ISSN: 8755-2930.

Carpentier, S. and Roy-Chowdhury, K. (2009). "Conservation of Lateral Stochastic Structure of a Medium in Its Simulated Seismic Response". In: *Journal of Geophysical Research: Solid Earth* 114.B10.

Çelebi, M. (1987). "Topographical and Geological Amplifications Determined from Strong-Motion and Aftershock Records of the 3 March 1985 Chile Earthquake". In: *Bulletin of the Seismological Society of America* 77.4, pp. 1147–1167. ISSN: 0037-1106.

Cerjan, C., Kosloff, D., Kosloff, R., and Reshef, M. (1985). "A Nonreflecting Boundary Condition for Discrete Acoustic and Elastic Wave Equations". In: *GEOPHYSICS* 50.4, pp. 705–708. ISSN: 0016-8033, 1942-2156.

Chaljub, E., Komatitsch, D., Vilotte, J., Capdeville, Y., and Festa, G. (2006). *Spectral Element Analysis in Seismology. Advances in Wave Propagation in Heterogeneous Earth, Ru-Shan Wu and Valerie Maupin, Etds., in the Series Advances*.

Chávez-García, F. J. and Faccioli, E. (2000). "Complex Site Effects and Building Codes: Making the Leap". In: *Journal of Seismology* 4.1, pp. 23–40. ISSN: 13834649.

Chiou, B. S.-J. and Youngs, R. R. (2014). "Update of the Chiou and Youngs NGA Model for the Average Horizontal Component of Peak Ground Motion and Response Spectra". In: *Earthquake Spectra* 30.3, pp. 1117–1153. ISSN: 8755-2930, 1944-8201.

Cui, Y., Moore, R., Olsen, K., Chourasia, A., Maechling, P., Minster, B., Day, S., Hu, Y., Zhu, J., and Jordan, T. (2009a). "Toward Petascale Earthquake Simulations". In: *Acta Geotechnica* 4.2, pp. 79–93. ISSN: 1861-1133.

Cui, Y., Olsen, K., Chourasia, A., Moore, R., Maechling, P., and Jordan, T. (2009b). "The TeraShake Computational Platform for Large-Scale Earthquake Simulations". In: *Advances in Geocomputing*. Ed. by H. Xing. Lecture Notes in Earth Sciences. Berlin, Heidelberg: Springer, pp. 229–277. ISBN: 978-3-540-85879-9.

Cui, Y., Olsen, K. B., Jordan, T. H., Lee, K., Zhou, J., Small, P., Roten, D., Ely, G., Panda, D. K., Chourasia, A., Levesque, J., Day, S. M., and Maechling, P. (2010). "Scalable Earthquake Simulation on Petascale Supercomputers". In: *2010 ACM/IEEE International Conference for High Performance Computing, Networking, Storage and Analysis*. 2010 SC - International Conference for High Performance Computing, Networking, Storage and Analysis. New Orleans, LA, USA: IEEE, pp. 1–20. ISBN: 978-1-4244-7557-5.

Cui, Y., Poyraz, E., Olsen, K. B., Zhou, J., Withers, K., Callaghan, S., Larkin, J., Guest, C., Choi, D., Chourasia, A., *et al*. (2013). "Physics-Based Seismic Hazard Analysis on Petascale Heterogeneous Supercomputers". In: *SC'13: Proceedings of the International Conference on High Performance Computing, Networking, Storage and Analysis*. IEEE, pp. 1–12.

Dalguer, L. A. and Day, S. M. (2007). "Staggered-Grid Split-Node Method for Spontaneous Rupture Simulation". In: *Journal of Geophysical Research: Solid Earth* 112.B2.

Davis, L. L. and West, L. R. (1973). "Observed Effects of Topography on Ground Motion". In: *Bulletin of the Seismological Society of America* 63.1, pp. 283–298. ISSN: 0037-1106.

Day, S. M. (1996). "RMS Response of a One-Dimensional Half-Space to SH". In: *Bulletin of the Seismological Society of America* 86.2, pp. 363–370. ISSN: 0037-1106.

Day, S. M. and Bradley, C. R. (2001). "Memory-Efficient Simulation of Anelastic Wave Propagation". In: *Bulletin of the Seismological Society of America* 91.3, pp. 520–531. ISSN: 0037-1106.

Day, S. M., Graves, R., Bielak, J., Dreger, D., Larsen, S., Olsen, K. B., Pitarka, A., and Ramirez-Guzman, L. (2008). "Model for Basin Effects on Long-Period Response Spectra in Southern California". In: *Earthquake Spectra* 24.1, pp. 257–277. ISSN: 8755-2930, 1944-8201.

Denolle, M., Dunham, E., Prieto, G., and Beroza, G. (2014). "Strong Ground Motion Prediction Using Virtual Earthquakes". In: *Science* 343.6169, pp. 399–403.

Dodge, D. A. and Beroza, G. C. (1997). "Source Array Analysis of Coda Waves near the 1989 Loma Prieta, California, Mainshock: Implications for the Mechanism of Coseismic Velocity Changes". In: *Journal of Geophysical Research: Solid Earth* 102.B11, pp. 24437–24458.

Dolan, S. S. and Bean, C. J. (1997). "Some Remarks on the Estimation of Fractal Scaling Parameters from Borehole Wire-Line Logs". In: *Geophysical Research Letters* 24.10, pp. 1271–1274. ISSN: 1944-8007.

Duan, B. and Day, S. M. (2010). "Sensitivity Study of Physical Limits on Ground Motion at Yucca Mountain". In: *Bulletin of the Seismological Society of America* 100.6, pp. 2996–3019. ISSN: 0037-1106.

Dunham, E. M., Belanger, D., Cong, L., and Kozdon, J. E. (2011a). "Earthquake Ruptures with Strongly Rate-Weakening Friction and Off-Fault Plasticity, Part 1: Planar Faults". In: *Bulletin of the Seismological Society of America* 101.5, pp. 2296–2307. ISSN: 0037-1106.

— (2011b). "Earthquake Ruptures with Strongly Rate-Weakening Friction and Off-Fault Plasticity, Part 2: Nonplanar Faults". In: *Bulletin of the Seismological Society of America* 101.5, pp. 2308–2322. ISSN: 0037-1106.

Durand, S., Gaffet, S., and Virieux, J. (1999). "Seismic Diffracted Waves from Topography Using 3-D Discrete Wavenumber-Boundary Integral Equation Simulation". In: *Geophysics* 64.2, pp. 572–578.

Eberhart-Phillips, D., Thurber, C., and Fletcher, J. B. (2014). "Imaging p and s Attenuation in the Sacramento–San Joaquin Delta Region, Northern California". In: *Bulletin of the Seismological Society of America* 104.5, pp. 2322–2336.

Ely, G., Small, P., Jordan, T. H., Maechling, P. J., and Wang, F. (2010). "A Vs30-Derived Near-Surface Seismic Velocity Model". In: AGU. No. S51A-1907. San Francisco, California, p. 1.

Erickson, D., McNamara, D. E., and Benz, H. M. (2004). "Frequency-Dependent Lg Q within the Continental United States". In: *Bulletin of the Seismological Society of America* 94.5, pp. 1630–1643. ISSN: 0037-1106.

Evert, H., Carranza-Torres, C., and Corkum, B. (2002). "Hoek-Brown Failure Criterion". In: *NARMS-TAC Conference. Toronto*.

Fehler, M., Hoshiba, M., Sato, H., and Obara, K. (1992). "Separation of Scattering and Intrinsic Attenuation for the Kanto-Tokai Region, Japan, Using Measurements of S-Wave Energy versus Hypocentral Distance". In: *Geophysical Journal International* 108.3, pp. 787–800.

Field, E. H. (2000). "A Modified Ground-Motion Attenuation Relationship for Southern California That Accounts for Detailed Site Classification and a Basin-Depth Effect". In: *Bulletin of the Seismological Society of America* 90 (6B), S209–S221. ISSN: 0037-1106.

Field, E. H., Kramer, S., Elgamal, A.-W., Bray, J., Matasovic, N., Johnson, P., Cramer, C., Roblee, C., Wald, D., Bonilla, L., Dimitriu, P., and Anderson, J. (1998). "Nonlinear Site Response: Where We're At (A Report from a SCEC/PEER Seminar and Workshop)". In: *Seismological Research Letters* 69.3, pp. 230–234. ISSN: 0895-0695.

Field, E. H. and Jacob, K. H. (1995). “A Comparison and Test of Various Site-Response Estimation Techniques, Including Three That Are Not Reference-Site Dependent”. In: *Bulletin of the Seismological Society of America* 85.4, pp. 1127–1143.

Flatté, S. M. and Wu, R.-S. (1988). “Small-Scale Structure in the Lithosphere and Asthenosphere Deduced from Arrival Time and Amplitude Fluctuations at NORSAR”. In: *Journal of Geophysical Research: Solid Earth* 93.B6, pp. 6601–6614. ISSN: 2156-2202.

Frankel, A. and Clayton, R. W. (1986). “Finite Difference Simulations of Seismic Scattering: Implications for the Propagation of Short-Period Seismic Waves in the Crust and Models of Crustal Heterogeneity”. In: *Journal of Geophysical Research* 91.B6, p. 6465. ISSN: 0148-0227.

Frankel, A., McGarr, A., Bicknell, J., Mori, J., Seeber, L., and Cranswick, E. (1990). “Attenuation of High-Frequency Shear Waves in the Crust: Measurements from New York State, South Africa, and Southern California”. In: *Journal of Geophysical Research: Solid Earth* 95.B11, pp. 17441–17457. ISSN: 2156-2202.

Frankel, A. and Vidale, J. (1992). “A Three-Dimensional Simulation of Seismic Waves in the Santa Clara Valley, California, from a Loma Prieta Aftershock”. In: *Bulletin of the Seismological Society of America* 82.5, pp. 2045–2074. ISSN: 0037-1106.

Fujiwara, H., Kawai, S., Hao, K. X., Morikawa, N., and Azuma, H. (2017). “J-SHIS - AN INTEGRATED SYSTEM FOR SHARING INFORMATION ON NATIONAL SEISMIC HAZARD MAPS FOR JAPAN”. In: 16 WCEE. Santiago Chile, p. 7.

Gabriel, A.-A., Ampuero, J.-P., Dalguer, L. A., and Mai, P. M. (2013). “Source Properties of Dynamic Rupture Pulses with Off-Fault Plasticity: RUPTURE WITH OFF-FAULT PLASTICITY”. In: *Journal of Geophysical Research: Solid Earth* 118.8, pp. 4117–4126. ISSN: 21699313.

Gaffet, S., Cultrera, G., Dietrich, M., Courboulex, F., Marra, F., Bouchon, M., Caserta, A., Cornou, C., Deschamps, A., Glot, J.-P., and Guiguet, R. (2000). “A Site Effect Study in the Verchiano Valley during the 1997 Umbria-Marche (Central Italy) Earthquakes”. In: *Journal of Seismology* 4.4, pp. 525–541. ISSN: 1573-157X.

Gallant, J. C. and Dowling, T. I. (2003). “A Multiresolution Index of Valley Bottom Flatness for Mapping Depositional Areas”. In: *Water Resources Research* 39.12, p. 1347. ISSN: 00431397.

Geli, L., Bard, P.-Y., and Jullien, B. (1988). “The Effect of Topography on Earthquake Ground Motion: A Review and New Results”. In: *Bulletin of the Seismological Society of America* 78.1, pp. 42–63. ISSN: 0037-1106.

Gibbs, J. (1989). *Near-Surface P- and S-Wave Velocities from Borehole Measurements near Lake Hemet, California*. Report 89-630.

Gilbert, G. K., Holmes, J., Humphrey, R. L., Sewell, J., and Soule, F. (1907). *The San Francisco Earthquake and Fire of April 18, 1906, and Their Effects on Structures and Structural Materials*. USGS Numbered Series 324. Govt. Print. Off., pp. 1–13.

Graves, R. W. and Pitarka, A. (2010). "Broadband Ground-Motion Simulation Using a Hybrid Approach". In: *Bulletin of the Seismological Society of America* 100 (5A), pp. 2095–2123. ISSN: 0037-1106.

Graves, R. and Pitarka, A. (2016). "Kinematic Ground-Motion Simulations on Rough Faults Including Effects of 3D Stochastic Velocity Perturbations". In: *Bulletin of the Seismological Society of America* 106.5, pp. 2136–2153. ISSN: 0037-1106, 1943-3573.

Graves, R. W. (1995). "Preliminary Analysis of Long-Period Basin Response in the Los Angeles Region from the 1994 Northridge Earthquake". In: *Geophysical research letters* 22.2, pp. 101–104.

Graves, R. W. and Wald, D. J. (2004). "Observed and Simulated Ground Motions in the San Bernardino Basin Region for the Hector Mine, California, Earthquake". In: *Bulletin of the Seismological Society of America* 94.1, pp. 131–146.

Graves, R. W. (1996). "Simulating Seismic Wave Propagation in 3D Elastic Media Using Staggered-Grid Finite Differences". In: *Bulletin of the Seismological Society of America* 86.4, pp. 1091–1106. ISSN: 0037-1106.

Graves, R. W., Aagaard, B. T., Hudnut, K. W., Star, L. M., Stewart, J. P., and Jordan, T. H. (2008). "Broadband Simulations for M $_{w}$ 7.8 Southern San Andreas Earthquakes: Ground Motion Sensitivity to Rupture Speed". In: *Geophysical Research Letters* 35.22, p. L22302. ISSN: 0094-8276.

Griffiths, S. C., Cox, B. R., Rathje, E. M., and Teague, D. P. (2016). "Mapping Dispersion Misfit and Uncertainty in Vs Profiles to Variability in Site Response Estimates". In: *Journal of Geotechnical and Geoenvironmental Engineering* 142.11, p. 04016062. ISSN: 1090-0241, 1943-5606.

Gülerce, Z. and Abrahamson, N. A. (2011). "Site-Specific Design Spectra for Vertical Ground Motion". In: *Earthquake Spectra* 27.4, pp. 1023–1047. ISSN: 8755-2930, 1944-8201.

Gusev, A. A. and Abubakirov, I. R. (1996). "Simulated Envelopes of Non-Isotropically Scattered Body Waves as Compared to Observed Ones: Another Manifestation of Fractal Heterogeneity". In: *Geophysical Journal International* 127.1, pp. 49–60. ISSN: 0956-540X.

Gutenberg, B. (1957). "Effects of Ground on Earthquake Motion". In: *Bulletin of the Seismological Society of America* 47.3, pp. 221–250. ISSN: 0037-1106.

Hanks, T. C., Abrahamson, N., Board, M., Boore, D. M., Brune, J., and Cornell, C. (2005). "Observed Ground Motions, Extreme Ground Motions, and Physical Limits to Ground

Motions". In: *Directions in Strong Motion Instrumentation*. Ed. by P. Gülkan and J. G. Anderson. Nato Science Series: IV: Earth and Environmental Sciences. Dordrecht: Springer Netherlands, pp. 55–59. ISBN: 978-1-4020-3812-9.

Harris, R. A., Barall, M., Andrews, D. J., Duan, B., Ma, S., Dunham, E. M., Gabriel, A.-A., Kaneko, Y., Kase, Y., Aagaard, B. T., *et al*. (2011). "Verifying a Computational Method for Predicting Extreme Ground Motion". In: *Seismological Research Letters* 82.5, pp. 638–644.

Harris, R. A., Barall, M., Archuleta, R., Dunham, E., Aagaard, B., Ampuero, J. P., Bhat, H., Cruz-Atienza, V., Dalguer, L., Dawson, P., *et al*. (2009). "The SCEC/USGS Dynamic Earthquake Rupture Code Verification Exercise". In: *Seismological Research Letters* 80.1, pp. 119–126.

Hartzell, S., Harmsen, S., and Frankel, A. (2010). "Effects of 3D Random Correlated Velocity Perturbations on Predicted Ground Motions". In: *Bulletin of the Seismological Society of America* 100.4, pp. 1415–1426. ISSN: 0037-1106.

Hartzell, S., Ramírez-Guzmán, L., Meremonte, M., and Leeds, A. (2017). "Ground Motion in the Presence of Complex Topography II: Earthquake Sources and 3D Simulations". In: *Bulletin of the Seismological Society of America* 107.1, pp. 344–358. ISSN: 0037-1106, 1943-3573.

Hartzell, S. H., Carver, D. L., and King, K. W. (1994). "Initial Investigation of Site and Topographic Effects at Robinwood Ridge, California". In: *Bulletin of the Seismological Society of America* 84.5, pp. 1336–1349.

Hauksson, E. and Shearer, P. M. (2006). "Attenuation Models (Q_P and Q_S) in Three Dimensions of the Southern California Crust: Inferred Fluid Saturation at Seismogenic Depths: Q_P AND Q_S 3-D MODELS OF SOUTHERN CALIFORNIA". In: *Journal of Geophysical Research: Solid Earth* 111.B5, n/a–n/a. ISSN: 01480227.

Heath, D. C., Wald, D. J., Worden, C. B., Thompson, E. M., and Smoczyk, G. M. (2020). "A Global Hybrid $V_{S\ 30}$ Map with a Topographic Slope–Based Default and Regional Map Insets". In: *Earthquake Spectra* 36.3, pp. 1570–1584. ISSN: 8755-2930, 1944-8201.

Hedlin, M. A. H., Shearer, P. M., and Earle, P. S. (1997). "Seismic Evidence for Small-Scale Heterogeneity throughout the Earth's Mantle". In: *Nature* 387.6629 (6629), pp. 145–150. ISSN: 1476-4687.

Helffrich, G. R. and Wood, B. J. (2001). "The Earth's Mantle". In: *Nature* 412.6846 (6846), pp. 501–507. ISSN: 1476-4687.

Hill, R. (1981). "Geology of Garner Valley and Vicinity". In: *South Coast Geol. Soc.*, pp. 90–99.

Hoek, E. and Brown, E. T. (1980). "Empirical Strength Criterion for Rock Masses". In: *Journal of the geotechnical engineering division* 106.9, pp. 1013–1035.

— (1997). "Practical Estimates of Rock Mass Strength". In: *International journal of rock mechanics and mining sciences* 34.8, pp. 1165–1186.

Holliger, K. (1996). "Upper-Crustal Seismic Velocity Heterogeneity as Derived from a Variety of P-Wave Sonic Logs". In: *Geophysical Journal International* 125.3, pp. 813–829. ISSN: 0956-540X.

Hough, S. E., Anderson, J. G., Brune, J., Vernon, F., Berger, J., Fletcher, J., Haar, L., Hanks, L., and Baker, L. (1988). "Attenuation near Anza, California". In: *Bulletin of the Seismological Society of America* 78.2, pp. 672–691. ISSN: 0037-1106.

Hu, Z., Olsen, K. B., and Day, S. M. (2021a). "0-5 Hz Deterministic 3D Ground Motion Simulations for the 2014 La Habra, California, Earthquake". In: *Manuscript in preparation*.

— (2021b). "Calibration of the Near-Surface Seismic Structure in the SCEC Community Velocity Model Version 4". In: *Manuscript in preparation*.

Idriss, I. M. (2014). "An NGA-West2 Empirical Model for Estimating the Horizontal Spectral Values Generated by Shallow Crustal Earthquakes". In: *Earthquake Spectra* 30.3, pp. 1155–1177. ISSN: 8755-2930, 1944-8201.

Imperatori, W. and Mai, P. M. (2013). "Broad-Band near-Field Ground Motion Simulations in 3-Dimensional Scattering Media". In: *Geophysical Journal International* 192.2, pp. 725–744. ISSN: 0956-540X.

— (2015). "The Role of Topography and Lateral Velocity Heterogeneities on Near-Source Scattering and Ground-Motion Variability". In: *Geophysical Journal International* 202.3, pp. 2163–2181. ISSN: 0956-540X, 1365-246X.

International Code Council (2014). *2015 IBC International Building Code, International Code Council*.

Jones, L. M., Bernknopf, R. L., Cox, D. A., Goltz, J., Hudnut, K. W., Mileti, D. S., Perry, S., Ponti, D., Porter, K. A., Reichle, M. S., *et al*. (2008). *The ShakeOut Scenario: Effects of a Potential M7. 8 Earthquake on the San Andreas Fault in Southern California*. US Geological Survey.

Joyner, W. B., Warrick, R. E., and Fumal, T. E. (1981). "The Effect of Quaternary Alluvium on Strong Ground Motion in the Coyote Lake, California, Earthquake of 1979". In: *Bulletin of the Seismological Society of America* 71.4, pp. 1333–1349. ISSN: 0037-1106.

Käser, M. and Dumbser, M. (2006). "An Arbitrary High-Order Discontinuous Galerkin Method for Elastic Waves on Unstructured Meshes — I. The Two-Dimensional Isotropic Case

with External Source Terms". In: *Geophysical Journal International* 166.2, pp. 855–877. ISSN: 0956-540X.

Kawase, H. and Aki, K. (1990). "Topography Effect at the Critical SV-Wave Incidence: Possible Explanation of Damage Pattern by the Whittier Narrows, California, Earthquake of 1 October 1987". In: *Bulletin of the Seismological Society of America* 80.1, pp. 1–22. ISSN: 0037-1106.

Kohler, M. D. (2003). "Mantle Heterogeneities and the SCEC Reference Three-Dimensional Seismic Velocity Model Version 3". In: *Bulletin of the Seismological Society of America* 93.2, pp. 757–774. ISSN: 0037-1106.

Komatitsch, D. and Tromp, J. (2002). "Spectral-Element Simulations of Global Seismic Wave Propagation-I. Validation". In: *Geophysical Journal International* 149.2, pp. 390–412. ISSN: 0956540X, 1365246X.

Konno, K. and Ohmachi, T. (1998). "Ground-Motion Characteristics Estimated from Spectral Ratio between Horizontal and Vertical Components of Microtremor". In: *Bulletin of the Seismological Society of America* 88.1, pp. 228–241. ISSN: 0037-1106.

Kramer, S. L. (1996). *Geotechnical Earthquake Engineering*. PrenticeHall, Englewood Cliffs, N. J.

Lai, V. H., Graves, R. W., Yu, C., Zhan, Z., and Helmberger, D. V. (2020). "Shallow Basin Structure and Attenuation Are Key to Predicting Long Shaking Duration in Los Angeles Basin". In: *Journal of Geophysical Research: Solid Earth* 125.10. ISSN: 2169-9313, 2169-9356.

Lee, E. J., Chen, P., and Jordan, T. H. (2014a). "Testing Waveform Predictions of 3D Velocity Models against Two Recent Los Angeles Earthquakes". In: *Seismological Research Letters* 85.6, pp. 1275–1284. ISSN: 0895-0695, 1938-2057.

Lee, E.-J., Chen, P., Jordan, T. H., Maechling, P. B., Denolle, M. A. M., and Beroza, G. C. (2014b). "Full-3-D Tomography for Crustal Structure in Southern California Based on the Scattering-Integral and the Adjoint-Wavefield Methods". In: *Journal of Geophysical Research: Solid Earth* 119.8, pp. 6421–6451. ISSN: 2169-9356.

Lee, E.-J., Chen, P., Jordan, T. H., and Wang, L. (2011). "Rapid Full-Wave Centroid Moment Tensor (CMT) Inversion in a Three-Dimensional Earth Structure Model for Earthquakes in Southern California: Rapid Full-Wave CMT Inversion". In: *Geophysical Journal International* 186.1, pp. 311–330. ISSN: 0956540X.

Lee, S.-J., Chan, Y.-C., Komatitsch, D., Huang, B.-S., and Tromp, J. (2009a). "Effects of Realistic Surface Topography on Seismic Ground Motion in the Yangminshan Region of Taiwan Based Upon the Spectral-Element Method and LiDAR DTM". In: *Bulletin of the Seismological Society of America* 99 (2A), pp. 681–693. ISSN: 0037-1106.

Lee, S.-J., Komatitsch, D., Huang, B.-S., and Tromp, J. (2009b). "Effects of Topography on Seismic-Wave Propagation: An Example from Northern Taiwan". In: *Bulletin of the Seismological Society of America* 99.1, pp. 314–325. ISSN: 0037-1106.

Lee, V. W. and Trifunac, M. D. (2010). "Should Average Shear-Wave Velocity in the Top 30m of Soil Be Used to Describe Seismic Amplification?" In: *Soil Dynamics and Earthquake Engineering* 30.11, pp. 1250–1258. ISSN: 02677261.

Levander, A., Hobbs, R. W., Smith, S. K., England, R. W., Snyder, D. B., and Holliger, K. (1994). "The Crust as a Heterogeneous "Optical" Medium, or "Crocodiles in the Mist"". In: *Tectonophysics*. Seismic Reflection Probing of the Continents and Their Margins 232.1, pp. 281–297. ISSN: 0040-1951.

Levander, A. R. and Holliger, K. (1992). "Small-Scale Heterogeneity and Large-Scale Velocity Structure of the Continental Crust". In: *Journal of Geophysical Research: Solid Earth* 97.B6, pp. 8797–8804. ISSN: 2156-2202.

Lin, G., Shearer, P. M., Hauksson, E., and Thurber, C. H. (2007). "A Three-Dimensional Crustal Seismic Velocity Model for Southern California from a Composite Event Method". In: *Journal of Geophysical Research: Solid Earth* 112.B11. ISSN: 2156-2202.

Liu, H.-P., Anderson, D. L., and Kanamori, H. (1976). "Velocity Dispersion Due to Anelasticity; Implications for Seismology and Mantle Composition". In: *Geophysical Journal International* 47.1, pp. 41–58.

Liu, P., Archuleta, R. J., and Hartzell, S. H. (2006). "Prediction of Broadband Ground-Motion Time Histories: Hybrid Low/High- Frequency Method with Correlated Random Source Parameters". In: *Bulletin of the Seismological Society of America* 96.6, pp. 2118–2130. ISSN: 0037-1106.

Liu, Z., Shang, C., Huang, L., Liang, J., and Li, J. (2020). "Scattering of Seismic Waves by Three-Dimensional Large-Scale Hill Topography Simulated by a Fast Parallel IBEM". In: *Earthquake Engineering and Engineering Vibration* 19.4, pp. 855–873. ISSN: 1671-3664, 1993-503X.

Lovati, S., Bakavoli, M., Massa, M., Ferretti, G., Pacor, F., Paolucci, R., Haghshenas, E., and Kamalian, M. (2011). "Estimation of Topographical Effects at Narni Ridge (Central Italy): Comparisons between Experimental Results and Numerical Modelling". In: *Bulletin of earthquake Engineering* 9.6, pp. 1987–2005.

Ludwig, W., Nafe, J., and Drake, C. (1970). *Seismic Refraction*. Vol. 4. 1 vols. The Sea. New York. 53-84.

Ma, S. and Beroza, G. C. (2008). "Rupture Dynamics on a Bimaterial Interface for Dipping Faults". In: *Bulletin of the Seismological Society of America* 98.4, pp. 1642–1658. ISSN: 0037-1106.

Ma, S. (2008). "A Physical Model for Widespread Near-Surface and Fault Zone Damage Induced by Earthquakes". In: *Geochemistry, Geophysics, Geosystems* 9.11. ISSN: 1525-2027.

Ma, S., Archuleta, R. J., and Page, M. T. (2007). "Effects of Large-Scale Surface Topography on Ground Motions, as Demonstrated by a Study of the San Gabriel Mountains, Los Angeles, California". In: *Bulletin of the Seismological Society of America* 97.6, pp. 2066–2079. ISSN: 0037-1106.

Magistrale, H., Day, S., Clayton, R. W., and Graves, R. (2000). "The SCEC Southern California Reference Three-Dimensional Seismic Velocity Model Version 2". In: *Bulletin of the Seismological Society of America* 90 (6B), S65–S76. ISSN: 0037-1106.

Magistrale, H., McLaughlin, K., and Day, S. (1996). "A Geology-Based 3D Velocity Model of the Los Angeles Basin Sediments". In: *Bulletin of the Seismological Society of America* 86.4, pp. 1161–1166. ISSN: 0037-1106.

Mai, P. M., Imperatori, W., and Olsen, K. B. (2010). "Hybrid Broadband Ground-Motion Simulations: Combining Long-Period Deterministic Synthetics with High-Frequency Multiple S-to-S Backscattering". In: *Bulletin of the Seismological Society of America* 100 (5A), pp. 2124–2142. ISSN: 0037-1106.

Marafi, N. A., Eberhard, M. O., Berman, J. W., Wirth, E. A., and Frankel, A. D. (2019). "Impacts of Simulated M9 Cascadia Subduction Zone Motions on Idealized Systems". In: *Earthquake Spectra* 35.3, pp. 1261–1287. ISSN: 8755-2930.

Massa, M., Barani, S., and Lovati, S. (2014). "Overview of Topographic Effects Based on Experimental Observations: Meaning, Causes and Possible Interpretations". In: *Geophysical Journal International* 197.3, pp. 1537–1550. ISSN: 0956-540X, 1365-246X.

Massa, M., Lovati, S., D'Alema, E., Ferretti, G., and Bakavoli, M. (2010). "An Experimental Approach for Estimating Seismic Amplification Effects at the Top of a Ridge, and the Implication for Ground-Motion Predictions: The Case of Narni, Central Italy". In: *Bulletin of the Seismological Society of America* 100.6, pp. 3020–3034. ISSN: 0037-1106.

Matavosic, N. and Hashash, Y. (2012). *Practices and Procedures for Site-Specific Evaluations of Earthquake Ground Motions*. Washington, D.C.: Transportation Research Board. ISBN: 978-0-309-22355-3.

Maufroy, E., Cruz-Atienza, V. M., Cotton, F., and Gaffet, S. (2015). "Frequency-Scaled Curvature as a Proxy for Topographic Site-Effect Amplification and Ground-Motion Variability". In: *Bulletin of the Seismological Society of America* 105.1, pp. 354–367. ISSN: 0037-1106, 1943-3573.

Mitchell, T. M. and Faulkner, D. R. (2009). "The Nature and Origin of Off-Fault Damage Surrounding Strike-Slip Fault Zones with a Wide Range of Displacements: A Field Study

from the Atacama Fault System, Northern Chile". In: *Journal of Structural Geology* 31.8, pp. 802–816. ISSN: 0191-8141.

Molnar, S., Cassidy, J. F., Olsen, K. B., Dosso, S. E., and He, J. (2014). "Earthquake Ground Motion and 3D Georgia Basin Amplification in Southwest British Columbia: Shallow Blind-Thrust Scenario Earthquakes". In: *Bulletin of the Seismological Society of America* 104.1, pp. 321–335.

Nakajima, J., Hada, S., Hayami, E., Uchida, N., Hasegawa, A., Yoshioka, S., Matsuzawa, T., and Umino, N. (2013). "Seismic Attenuation beneath Northeastern Japan: Constraints on Mantle Dynamics and Arc Magmatism". In: *Journal of Geophysical Research: Solid Earth* 118.11, pp. 5838–5855. ISSN: 21699313.

Nakata, N. and Beroza, G. C. (2015). "Stochastic Characterization of Mesoscale Seismic Velocity Heterogeneity in Long Beach, California". In: *Geophysical Supplements to the Monthly Notices of the Royal Astronomical Society* 203.3, pp. 2049–2054.

National Research Institute for Earth Science and Disaster Resilience (2019). *NIED K-NET, KiK-Net*. National Research Institute for Earth Science and Disaster Resilience.

Nguyen, K.-V. and Gatmiri, B. (2007). "Evaluation of Seismic Ground Motion Induced by Topographic Irregularity". In: *Soil Dynamics and Earthquake Engineering* 27.2, pp. 183–188. ISSN: 0267-7261.

Nie, S., Wang, Y., Olsen, K. B., and Day, S. M. (2017). "Fourth-order Staggered-grid Finite-difference Seismic Wavefield Estimation Using a Discontinuous Mesh Interface (Wedmi)". In: *Bulletin of the Seismological Society of America* 107.5, pp. 2183–2193. ISSN: 0037-1106, 1943-3573.

Nielsen, L. and Thybo, H. (2006). "Identification of Crustal and Upper Mantle Heterogeneity by Modelling of Controlled-Source Seismic Data". In: *Tectonophysics*. The Heterogeneous Mantle 416.1, pp. 209–228. ISSN: 0040-1951.

Noda, H., Dunham, E. M., and Rice, J. R. (2009). "Earthquake Ruptures with Thermal Weakening and the Operation of Major Faults at Low Overall Stress Levels". In: *Journal of Geophysical Research: Solid Earth* 114.B7. ISSN: 2156-2202.

Nour, A., Slimani, A., Laouami, N., and Afra, H. (2003). "Finite Element Model for the Probabilistic Seismic Response of Heterogeneous Soil Profile". In: *Soil Dynamics and Earthquake Engineering* 23.5, pp. 331–348. ISSN: 02677261.

O'Connell, R. J. and Budiansky, B. (1978). "Measures of Dissipation in Viscoelastic Media". In: *Geophysical Research Letters* 5.1, pp. 5–8. ISSN: 1944-8007.

O'Reilly, O., Yeh, T.-Y., Olsen, K. B., Hu, Z., Breuer, A., Roten, D., and Goulet, C. (2021). "A High-Order Finite Difference Method on Staggered Curvilinear Grids for Seismic Wave

Propagation Applications with Topography". In: *Bulletin of the Seismological Society of America* accpeted for publication, p. 43.

Olsen, K. B., Day, S. M., and Bradley, C. R. (2003). "Estimation of Q for Long-Period (>2 Sec) Waves in the Los Angeles Basin". In: *Bulletin of the Seismological Society of America* 93.2, pp. 627–638. ISSN: 0037-1106.

Olsen, K. B., Day, S. M., Minster, J. B., Cui, Y., Chourasia, A., Faerman, M., Moore, R., Maechling, P., and Jordan, T. (2006). "Strong Shaking in Los Angeles Expected from Southern San Andreas Earthquake". In: *Geophysical Research Letters* 33.7, p. L07305. ISSN: 0094-8276.

Olsen, K. B. and Mayhew, J. E. (2010). "Goodness-of-Fit Criteria for Broadband Synthetic Seismograms, with Application to the 2008 Mw 5.4 Chino Hills, California, Earthquake". In: *Seismological Research Letters* 81.5, pp. 715–723. ISSN: 0895-0695.

Olsen, K., Day, S., Dalguer, L., Mayhew, J., Cui, Y., Zhu, J., Cruz-Atienza, V., Roten, D., Maechling, P., Jordan, T., *et al*. (2009). "ShakeOut-D: Ground Motion Estimates Using an Ensemble of Large Earthquakes on the Southern San Andreas Fault with Spontaneous Rupture Propagation". In: *Geophysical Research Letters* 36.4.

Olsen, K. and Takedatsu, R. (2015). "The SDSU Broadband Ground-Motion Generation Module BBtoolbox Version 1.5". In: *Seismological Research Letters* 86.1, pp. 81–88.

Olsen, K. B., Begnaud, M., Phillips, S., and Jacobsen, B. H. (2018). "Constraints of Crustal Heterogeneity and Q (f) from Regional (¡ 4 Hz) Wave Propagation for the 2009 North Korea Nuclear Test". In: *Bulletin of the Seismological Society of America* 108 (3A), pp. 1369–1383.

Olsen, K. B., Stephenson, W. J., and Geisselmeyer, A. (2008). "3D Crustal Structure and Long-Period Ground Motions from a M9. 0 Megathrust Earthquake in the Pacific Northwest Region". In: *Journal of Seismology* 12.2, pp. 145–159.

Olsen, K. B. (1994). "Simulation of Three Dimensional Wave Propagation in the Salt Lake Basin". Salt Lake City, Utah: The University of Utah.

Olsen, K. B., Archuleta, R. J., and Matarese, J. R. (1995). "Three-Dimensional Simulation of a Magnitude 7.75 Earthquake on the San Andreas Fault". In: *Science* 270.5242, pp. 1628–1632. ISSN: 0036-8075, 1095-9203.

Olsen, K. B. and Schuster, G. T. (1995). "Causes of Low-Frequency Ground Motion Amplification in the Salt Lake Basin: The Case of the Vertically Incident P Wave". In: *Geophysical Journal International* 122.3, pp. 1045–1061. ISSN: 0956540X, 1365246X.

Pischiutta, M., Cultrera, G., Caserta, A., Luzi, L., and Rovelli, A. (2010). "Topographic Effects on the Hill of Nocera Umbra, Central Italy: Topographic Effects on Nocera Umbra Hill". In: *Geophysical Journal International* 182.2, pp. 977–987. ISSN: 0956540X, 1365246X.

Pitarka, A. and Ichinose, G. (2009). "Simulating Forward and Backward Scattering in Viscoelastic 3D Media with Random Velocity Variations and Basin Structure". In: *US Geol. Surv. Tech. Rep.*

Plesch, A., Suess, M., Munster, J., Shaw, J. H., Hauksson, E., Tanimoto, T., and Members of the USR, Working Group (2007). "A New Velocity Model for Southern California: CVM-H 5.0". In: Proceedings of SCEC Annual Meeting. Palm Springs, CA.

Plesch, A., Tape, C., Graves, R. W., Shaw, J. H., and Ely, G. P. (2017). "Updates for the CVM-H Including New Representations of the Offshore Santa Maria and San Bernardino Basin and a New Moho Surface". In: Proceedings of SCEC Annual Meeting. B-128. Palm Springs, CA.

Plesch, A., Tape, C., Shaw, J. H., and Members of the USR, Working Group (2009). "CVM-H 6.0: Inversion Integration, the San Joaquin Valley and Other Advances in the Community Velocity Model". In: *SCEC Annual Meeting*. Proceedings of SCEC Annual Meeting.

Poggi, V., Edwards, B., and Fah, D. (2011). "Derivation of a Reference Shear-Wave Velocity Model from Empirical Site Amplification". In: *Bulletin of the Seismological Society of America* 101.1, pp. 258–274. ISSN: 0037-1106.

Przybilla, J., Korn, M., and Wegler, U. (2006). "Radiative Transfer of Elastic Waves versus Finite Difference Simulations in Two-Dimensional Random Media". In: *Journal of Geophysical Research: Solid Earth* 111.B4. ISSN: 2156-2202.

Przybilla, J., Wegler, U., and Korn, M. (2009). "Estimation of Crustal Scattering Parameters with Elastic Radiative Transfer Theory". In: *Geophysical Journal International* 178.2, pp. 1105–1111. ISSN: 0956540X, 1365246X.

Qiu, H., Lin, F.-C., and Ben-Zion, Y. (2019). "Eikonal Tomography of the Southern California Plate Boundary Region". In: *Journal of Geophysical Research: Solid Earth* 124.9, pp. 9755–9779. ISSN: 2169-9356.

Rai, M., Rodriguez-Marek, A., and Chiou, B. S. (2017). "Empirical Terrain-Based Topographic Modification Factors for Use in Ground Motion Prediction". In: *Earthquake Spectra* 33.1, pp. 157–177. ISSN: 8755-2930, 1944-8201.

Raoof, M., Herrmann, R., and Malagnini, L. (1999). "Attenuation and Excitation of Three-Component Ground Motion in Southern California". In: *Bulletin of the Seismological Society of America* 89.4, pp. 888–902.

Reid, H. F. (1910). *The California Earthquake of April 18, 1906*. 2, pp. 16–18.

Rodgers, A. J., Pitarka, A., Petersson, N. A., Sjögreen, B., and McCallen, D. B. (2018). "Broadband (0-4 Hz) Ground Motions for a Magnitude 7.0 Hayward Fault Earthquake With Three-Dimensional Structure and Topography: An *M* 7 Hayward Fault Earthquake". In: *Geophysical Research Letters* 45.2, pp. 739–747. ISSN: 00948276.

Roten, D., Fäh, D., Olsen, K. B., and Giardini, D. (2008). "A Comparison of Observed and Simulated Site Response in the Rhône Valley". In: *Geophysical Journal International* 173.3, pp. 958–978. ISSN: 0956540X, 1365246X.

Roten, D., Olsen, K. B., and Day, S. M. (2017a). "Off-Fault Deformations and Shallow Slip Deficit from Dynamic Rupture Simulations with Fault Zone Plasticity: OFF-FAULT DEFORMATION FROM SIMULATION". In: *Geophysical Research Letters* 44.15, pp. 7733–7742. ISSN: 00948276.

Roten, D., Olsen, K. B., Day, S. M., and Cui, Y. (2017b). "Quantification of Fault-Zone Plasticity Effects with Spontaneous Rupture Simulations". In: *Pure and Applied Geophysics* 174.9, pp. 3369–3391. ISSN: 0033-4553, 1420-9136.

Roten, D., Olsen, K. B., Day, S. M., Cui, Y., and Fäh, D. (2014). "Expected Seismic Shaking in Los Angeles Reduced by San Andreas Fault Zone Plasticity". In: *Geophysical Research Letters* 41.8, pp. 2769–2777. ISSN: 00948276.

Roten, D., Olsen, K. B., and Pechmann, J. C. (2012). "3D Simulations of M 7 Earthquakes on the Wasatch Fault, Utah, Part Ii: Broadband (0-10 Hz) Ground Motions and Nonlinear Soil Behavior". In: *Bulletin of the Seismological Society of America* 102.5, pp. 2008–2030. ISSN: 0037-1106.

Roth, M. and Korn, M. (1993). "Single Scattering Theory Versus Numerical Modelling In 2-D Random Media". In: *Geophysical Journal International* 112.1, pp. 124–140. ISSN: 0956-540X.

Saito, T., Sato, H., and Ohtake, M. (2002). "Envelope Broadening of Spherically Outgoing Waves in Three-Dimensional Random Media Having Power Law Spectra". In: *Journal of Geophysical Research: Solid Earth* 107.B5, ESE 3-1-ESE 3–15. ISSN: 2156-2202.

Sánchez-Sesma, F. J. and Campillo, M. (1991). "Diffraction of P, SV, and Rayleigh Waves by Topographic Features: A Boundary Integral Formulation". In: *Bulletin of the Seismological Society of America* 81.6, pp. 2234–2253. ISSN: 0037-1106.

Sánchez-Sesma, F. J., Herrera, I., and Avilés, J. (1982). "A Boundary Method for Elastic Wave Diffraction: Application to Scattering of SH Waves by Surface Irregularities". In: *Bulletin of the seismological Society of America* 72.2, pp. 473–490.

Sato, H. (1989). "Broadening of Seismogram Envelopes in the Randomly Inhomogeneous Lithosphere Based on the Parabolic Approximation: Southeastern Honshu, Japan". In: *Journal of Geophysical Research: Solid Earth* 94.B12, pp. 17735–17747. ISSN: 2156-2202.

Sato, H., Fehler, M. C., and Maeda, T. (2012). *Seismic Wave Propagation and Scattering in the Heterogeneous Earth*. Vol. 496. Springer.

Sato, H. and Fehler, M. C. (2009). *Seismic Wave Propagation and Scattering in the Heterogeneous Earth*. Berlin, Heidelberg: Springer Berlin Heidelberg. ISBN: 978-3-540-89623-4.

Savran, W. H. and Olsen, K. B. (2019). "Ground Motion Simulation and Validation of the 2008 Chino Hills Earthquake in Scattering Media". In: *Geophysical Journal International* 219.3, pp. 1836–1850. ISSN: 0956-540X, 1365-246X.

— (2016). "Model for Small-Scale Crustal Heterogeneity in Los Angeles Basin Based on Inversion of Sonic Log Data". In: *Geophysical Journal International* 205.2, pp. 856–863. ISSN: 0956-540X, 1365-246X.

Sawazaki, K., Sato, H., and Nishimura, T. (2011). "Envelope Synthesis of Short-Period Seismograms in 3-D Random Media for a Point Shear Dislocation Source Based on the Forward Scattering Approximation: Application to Small Strike-Slip Earthquakes in Southwestern Japan". In: *Journal of Geophysical Research: Solid Earth* 116.B8. ISSN: 2156-2202.

Seriani, G. (1998). "3-D Large-Scale Wave Propagation Modeling by Spectral Element Method on Cray T3E Multiprocessor". In: *Computer Methods in Applied Mechanics and Engineering*. Exterior Problems of Wave Propagation 164.1, pp. 235–247. ISSN: 0045-7825.

Ru-Shan, W. (1982). "Attenuation of Short Period Seismic Waves Due to Scattering". In: *Geophysical Research Letters* 9.1, pp. 9–12.

Shapiro, S. A. and Kneib, G. (1993). "Seismic Attenuation By Scattering: Theory and Numerical Results". In: *Geophysical Journal International* 114.2, pp. 373–391. ISSN: 0956-540X.

Shaw, J. H., Plesch, A., Tape, C., Suess, M. P., Jordan, T. H., Ely, G., Hauksson, E., Tromp, J., Tanimoto, T., Graves, R., Olsen, K., Nicholson, C., Maechling, P. J., Rivero, C., Lovely, P., Brankman, C. M., and Munster, J. (2015). "Unified Structural Representation of the Southern California Crust and Upper Mantle". In: *Earth and Planetary Science Letters* 415, pp. 1–15. ISSN: 0012-821X.

Shearer, P. M. and Orcutt, J. S. (1987). "Surface and Near-Surface Effects on Seismic Waves—Theory and Borehole Seismometer Results". In: *Bulletin of the Seismological Society of America* 77.4, pp. 1168–1196.

Shingaki, Y., Goto, H., and Sawada, S. (2018). "Evaluation Performance for Site Amplification Factors: S-Wave Impedance vs. V30". In: *Soils and Foundations* 58.4, pp. 911–927. ISSN: 00380806.

Silva, W. and Darragh, R. B. (1995). *Engineering Characterization of Strong Ground Motion Recorded at Rock Sites. Final Report*. EPRI-TR-102262. Electric Power Research Inst.

(EPRI), Palo Alto, CA (United States); Pacific Engineering and Analysis, Inc., El Cerrito, CA (United States).

Singh, S. K. and Ordaz, M. (1993). "On the Origin of Long Coda Observed in the Lake-Bed Strong-Motion Records of Mexico City". In: *Bulletin of the Seismological Society of America* 83.4, pp. 1298–1306.

Small, P., Gill, D., Maechling, P. J., Taborda, R., Callaghan, S., Jordan, T. H., Olsen, K. B., Ely, G. P., and Goulet, C. (2017). "The SCEC Unified Community Velocity Model Software Framework". In: *Seismological Research Letters* 88.6, pp. 1539–1552. ISSN: 0895-0695, 1938-2057.

Spudich, P., Hellweg, M., and Lee, W. H. K. (1996). "Directional Topographic Site Response at Tarzana Observed in Aftershocks of the 1994 Northridge, California, Earthquake: Implications for Mainshock Motions". In: *Bulletin of the Seismological Society of America* 86 (1B), S193–S208. ISSN: 0037-1106.

Steidl, J. H. (2000). "Site Response in Southern California for Probabilistic Seismic Hazard Analysis". In: *Bulletin of the Seismological Society of America* 90 (6B), S149–S169. ISSN: 0037-1106.

Steidl, J. H. (1993). "Variation of Site Response at the UCSB Dense Array of Portable Accelerometers". In: *Earthquake Spectra* 9.2, pp. 289–302. ISSN: 8755-2930, 1944-8201.

Steidl, J. H., Tumarkin, A. G., and Archuleta, R. J. (1996). "What Is a Reference Site?" In: *Bulletin of the Seismological Society of America* 86.6, pp. 1733–1748. ISSN: 0037-1106.

Steller, R. (1996). *New Borehole Geophysical Results at GVDA*. UCSB Internal Report.

Stephenson, W. J., Reitman, N. G., and Angster, S. J. (2017). *Cascadia Subduction Zone for 3D Earthquake Ground Motion Simulations, Version 1.6*. 2007–1348. U.S. Geological Survey.

Süss, M. P. and Shaw, J. H. (2003). "*P* Wave Seismic Velocity Structure Derived from Sonic Logs and Industry Reflection Data in the Los Angeles Basin, California: 3-D VELOCITY STRUCTURE IN LOS ANGELES BASIN". In: *Journal of Geophysical Research: Solid Earth* 108.B3. ISSN: 01480227.

Taborda, R., Azizzadeh-Roodpish, S., Khoshnevis, N., and Cheng, K. (2016). "Evaluation of the Southern California Seismic Velocity Models through Simulation of Recorded Events". In: *Geophysical Journal International* 205.3, pp. 1342–1364.

Taborda, R. and Bielak, J. (2014). "Ground-Motion Simulation and Validation of the 2008 Chino Hills, California, Earthquake Using Different Velocity Models". In: *Bulletin of the Seismological Society of America* 104.4, pp. 1876–1898.

Takemura, S., Furumura, T., and Maeda, T. (2015). "Scattering of High-Frequency Seismic Waves Caused by Irregular Surface Topography and Small-Scale Velocity Inhomogeneity". In: *Geophysical Journal International* 201.1, pp. 459–474.

Tao, Y. and Rathje, E. (2019). "Insights into Modeling Small-Strain Site Response Derived from Downhole Array Data". In: *Journal of Geotechnical and Geoenvironmental Engineering* 145.7, p. 04019023. ISSN: 1090-0241, 1943-5606.

— (2020). "Taxonomy for Evaluating the Site-Specific Applicability of One-Dimensional Ground Response Analysis". In: *Soil Dynamics and Earthquake Engineering* 128, p. 105865. ISSN: 02677261.

Tape, C., Liu, Q., Maggi, A., and Tromp, J. (2009). "Adjoint Tomography of the Southern California Crust". In: *Science* 325.5943, pp. 988–992. ISSN: 0036-8075, 1095-9203. pmid: 19696349.

— (2010). "Seismic Tomography of the Southern California Crust Based on Spectral-Element and Adjoint Methods". In: *Geophysical Journal International* 180.1, pp. 433–462. ISSN: 0956540X, 1365246X.

Teague, D. P., Cox, B. R., and Rathje, E. M. (2018). "Measured Vs. Predicted Site Response at the Garner Valley Downhole Array Considering Shear Wave Velocity Uncertainty from Borehole and Surface Wave Methods". In: *Soil Dynamics and Earthquake Engineering* 113, pp. 339–355. ISSN: 02677261.

Templeton, E. L., Bhat, H. S., Dmowska, R., and Rice, J. R. (2010). "Dynamic Rupture through a Branched Fault Configuration at Yucca Mountain, and Resulting Ground Motions". In: *Bulletin of the Seismological Society of America* 100.4, pp. 1485–1497. ISSN: 0037-1106.

Thompson, E. M., Baise, L. G., Kayen, R. E., and Guzina, B. B. (2009). "Impediments to Predicting Site Response: Seismic Property Estimation and Modeling Simplifications". In: *Bulletin of the Seismological Society of America* 99.5, pp. 2927–2949. ISSN: 0037-1106.

Thompson, E. M. (2018). *An Updated Vs30 Map for California with Geologic and Topographic Constraints*. U.S. Geological Survey.

Thompson, E. M., Baise, L. G., Tanaka, Y., and Kayen, R. E. (2012). "A Taxonomy of Site Response Complexity". In: *Soil Dynamics and Earthquake Engineering* 41, pp. 32–43. ISSN: 02677261.

Thompson, E. M., Wald, D. J., and Worden, C. B. (2014). "A VS30 Map for California with Geologic and Topographic Constraints". In: *Bulletin of the Seismological Society of America* 104.5, pp. 2313–2321. ISSN: 0037-1106.

Thybo, H., Nielsen, L., and Perchuc, E. (2003). "Seismic Scattering at the Top of the Mantle Transition Zone". In: *Earth and Planetary Science Letters* 216.3, pp. 259–269. ISSN: 0012-821X.

Toro, G. (1995). *Probabilistic Models of Site Velocity Profiles for Generic and Site-Specific Ground-Motion Amplification Studies*. Technical Report No. 779574. Upton, N.Y.: Brookhaven National Laboratory, p. 147.

Trifunac, M. D. and Hudson, D. E. (1971). "Analysis of the Pacoima Dam Accelerogram—San Fernando, California, Earthquake of 1971". In: *Bulletin of the Seismological Society of America* 61.5, pp. 1393–1411. ISSN: 0037-1106.

Umeda, Y., Kuroiso, A., Ito, K., and Muramatu, I. (1987). "High Accelerations Produced by the Western Nagano Prefecture, Japan, Earthquake of 1984". In: *Tectonophysics* 141.4, pp. 335–343. ISSN: 0040-1951.

USGS (2014). *Earthquake Events, Focal Mechanism*. URL: https://earthquake.usgs.gov/earthquakes/eventpage/ci15481673/focal-mechanism (visited on 2020).

— (2020). *National Seismic Hazard Maps - Elevation Products (3DEP)*. URL: https://apps.nationalmap.gov/downloader/#/ (visited on 2020).

Vernon, F. L., Pavlis, G. L., Owens, T. J., McNamara, D. E., and Anderson, P. N. (1998). "Near-Surface Scattering Effects Observed with a High-Frequency Phased Array at Pinyon Flats, California". In: *Bulletin of the Seismological Society of America* 88.6, pp. 1548–1560.

Wald, D. J. and Allen, T. I. (2007). "Topographic Slope as a Proxy for Seismic Site Conditions and Amplification". In: *Bulletin of the Seismological Society of America* 97.5, pp. 1379–1395. ISSN: 0037-1106.

Wang, W. and Shearer, P. M. (2017). "Using Direct and Coda Wave Envelopes to Resolve the Scattering and Intrinsic Attenuation Structure of Southern California: RESOLVE THE ATTENUATION STRUCTURE". In: *Journal of Geophysical Research: Solid Earth* 122.9, pp. 7236–7251. ISSN: 21699313.

Wessel, P., Luis, J. F., Uieda, L., Scharroo, R., Wobbe, F., Smith, W. H. F., and Tian, D. (2019). "The Generic Mapping Tools Version 6". In: *Geochemistry, Geophysics, Geosystems* 20.11, pp. 5556–5564. ISSN: 1525-2027, 1525-2027.

Wills, C. J. and Clahan, K. (2006). "Developing a Map of Geologically Defined Site-Condition Categories for California". In: *Bulletin of the Seismological Society of America* 96 (4A), pp. 1483–1501. ISSN: 0037-1106.

Wills, C. J., Gutierrez, C. I., Perez, F. G., and Branum, D. M. (2015). "A Next Generation V_{S30} Map for California Based on Geology and Topography". In: *Bulletin of the Seismological Society of America* 105.6, pp. 3083–3091. ISSN: 0037-1106, 1943-3573.

Withers, K. B., Olsen, K. B., and Day, S. M. (2015). "Memory-efficient Simulation of Frequency-dependent q". In: *Bulletin of the Seismological Society of America* 105.6, pp. 3129–3142. ISSN: 0037-1106, 1943-3573.

Withers, K. B., Olsen, K. B., Day, S. M., and Shi, Z. (2019). "Ground Motion and Intraevent Variability from 3D Deterministic Broadband (0–7.5 Hz) Simulations along a Nonplanar Strike-slip Fault". In: *Bulletin of the Seismological Society of America* 109.1, pp. 229–250. ISSN: 0037-1106, 1943-3573.

Wood, H. (1908). *Distribution of Apparent Intensity in San Francisco, in the California Earthquake of April 18, 1906*. Washington, DC: Carnegie Institute of Washington, pp. 220–245.

Wu, R.-S. (1985). "Multiple Scattering and Energy Transfer of Seismic Waves — Separation of Scattering Effect from Intrinsic Attenuation — I. Theoretical Modelling". In: *Geophysical Journal International* 82.1, pp. 57–80. ISSN: 0956-540X.

Wyllie, D. C. (2017). *Rock Slope Engineering: Civil Applications*. CRC Press.

Zeng, Y. (1993). "Theory of Scattered P- and S-Wave Energy in a Random Isotropic Scattering Medium". In: *Bulletin of the Seismological Society of America* 83.4, pp. 1264–1276. ISSN: 0037-1106.

Zeng, Y., Anderson, J. G., and Su, F. (1995). "Subevent Rake and Random Scattering Effects in Realistic Strong Ground Motion Simulation". In: *Geophysical Research Letters* 22.1, pp. 17–20. ISSN: 1944-8007.

Zeng, Y., Su, F., and Aki, K. (1991). "Scattering Wave Energy Propagation in a Random Isotropic Scattering Medium: 1. Theory". In: *Journal of Geophysical Research: Solid Earth* 96.B1, pp. 607–619. ISSN: 2156-2202.

Zhang, W., Zhang, Z., and Chen, X. (2012). "Three-Dimensional Elastic Wave Numerical Modelling in the Presence of Surface Topography by a Collocated-Grid Finite-Difference Method on Curvilinear Grids". In: *Geophysical Journal International* 190.1, pp. 358–378. ISSN: 0956-540X.

Zhu, C., Riga, E., Pitilakis, K., Zhang, J., and Thambiratnam, D. (2018). "Seismic Aggravation in Shallow Basins in Addition to One-Dimensional Site Amplification". In: *Journal of Earthquake Engineering* 24.9, pp. 402–412. ISSN: 1363-2469, 1559-808X.